Uncovering the Complexity of a Simple Retrovirus: A Study of Glycosylated Gag and Flow Virometry

Tyler Renner

This thesis is submitted to the Faculty of Medicine in partial fulfillment of the requirements for the degree of Doctorate in Philosophy with specialization in Microbiology & Immunology.

Department of Biochemistry, Microbiology and Immunology

Faculty of Medicine

University of Ottawa

Abstract

Murine leukemia virus (MLV), classified as a gammaretrovirus, has been studied extensively to enhance our understanding of the biology and replication of retroviral infection. Typically referred to as a simple retrovirus, its usefulness as a model is highlighted owing to its minimal genome. The genetic material for MLV was thought to only code the basic and essential defining features of a retrovirus. Through the understanding developed from the use of simple retroviruses, the clinical and research communities were immeasurably more prepared to combat the more complex and decidedly infamous human immunodeficiency virus (HIV). Interestingly, a scenario of convergent evolution has directed MLV to encode an accessory protein, termed Glycosylated Gag (gGag), that shares functionality reminiscent of several HIV proteins. Herein, I present a dissection of a novel function of this enigmatic protein, paired with an improved understanding of the biology of MLV that was revealed by the development of small particle flow cytometry performed on viruses, also known as flow virometry. Initially, we elucidated that gGag is responsible for the resistance of MLV towards the restriction factor murine APOBEC3 (mA3). I showed that even endogenous mA3 from primary cells exhibited an enhanced enzymatic activity towards MLV with mutant gGag proteins which have lost glycosylation sites. In our following study, I illustrated that these mutants displayed a reduced viral core stability, the severity of which was correlated directly with susceptibility to mA3. These results are in line with the hypothesis that viral core stability and APOBEC3-susceptibility are directly linked. Furthermore, I showed for the first time that unprocessed gGag was associated with viral particles released from producer cells in the orientation of a type I membrane protein, with the structural regions directed within the viral core. This may be the direct evidence of how gGag improves capsid stability, a mechanism which is still unresolved. On the flip side, gGag as a type II membrane protein was observed exclusively on virus-like particles devoid of detectable envelope glycoprotein (Env). This marks a potential new function for gGag in the context of infection. Given the ubiquitous necessity of an optimized core stability for any virus, combined with the

overlapping function of gGag with HIV accessory proteins, continuation of this work represents an as of yet clinically unexplored avenue for the development of HIV therapeutics. At the same time, in order to characterize individual viral particles, I played an instrumental role in developing the technique of flow virometry within our core facility. I illustrated that the Env of MLV does not significantly accumulate on extracellular vesicles (EVs) and acts as an effective marker for viral particles. With this evidence in hand, the enumeration of MLV virions was made possible. By correlating this information with an absolute viral genome determination, I was able to estimate the packaging efficiency for MLV in a quantitative manner. This information suggests that roughly 80-85% of MLV particles are missing their essential genetic information. These findings may implicate the disease progression of MLV infection may be enhanced by the use of defective-interfering particles, a theory that has been suggested for HIV. This work highlighted the fact that flow virometry is uniquely capable to discriminate viral particles from other cell-derived membraned vesicles in a highly sensitive manner. Overall, my work has unveiled new complexities of a simple retrovirus, while laying the groundwork towards both diagnostics and therapeutics for the ongoing battle with HIV.

Acknowledgements

Each of us are exposed to our own unique challenges and handle them as only we can. Though it is my name on this dissertation, this challenge was not mine alone, as I could not have pushed through without the support and generosity of many others. Too many to mention within this section, I apologize for excluding anyone. Even in the face of 'burn out' or hardships, there has always been a foundation holding me up.

First, my family has been at my side through everything. Especially my parents (Landy and Phil) and siblings (Tasha, Jordan, Sheri and Phil Jr.), who have shown me nothing but love and encouragement in my pursuit of an education. Even when it has led and kept me far from home. Our visits, even the surprise ones, have meant the world to me over the years. Next, my Ottawa family has made adapting to a new life so much easier than I thought possible. Alan, Maureen & Kate especially, you have adopted me as one of your own in a fashion that seems unbelievable. Thank you for everything you have and continue to do.

Second, my friends and colleagues have been with me through many hardships, both personal and professional. Especially Sammy, who is more like a sister to me. You have been the one family member that has physically been with me through everything. George, you paved this path for me, made it both interesting and fun. Tara, Kasandra, Maria and Mathieu, you have each taught me and inspired the scientist I am becoming. Mark, Cindy, Joanne, Laura, Anna, Matt, Mariam and Andrew, I won't forget the role you've played as well. Thank you all for putting up and being there with me. A special thanks for your contributions within this thesis and your friendship as we all develop and grow.

Third, my mentors have each imparted wisdom onto me to varying degrees, all of which are appreciated. My thesis advisory committee, Dr. Andrew Makrigiannis, Dr. Martin Pelchat and Dr. Robin Parks, thank you each for your input, advice and support over the years. Dr. Subash Sad for your valued

advice and direction at this point in my life. Dr. Vera Tang, you and I have cooperated and commiserated for so long, I hope we can stay in touch. Last, but not least, Dr. Marc-André Langlois, you had taken me in as an undergraduate student and gave me a shot. You have shaped my abilities to think critically over years of mentorship. True to your word, now you are helping me reach my career goals, whatever they may be. Thank you for everything.

Finally, my unwavering, patient, inspirational wife, Laura. You have tethered me to our reality, opening my eyes to what is truly important in life. While this document marks the end of an era, you and I begin a new one together. Thank you for always standing up with me through thick and thin, helping me practice presentations time and time again, and lighting up any room you enter. We are partners in everything, this work is as much yours as it is mine.

List of Abbreviations

- strand: minus strand
+ strand: positive strand
µm: micrometer
3D-PCR: differential DNA denaturation PCR

A: alanine (amino acid) or adenine (nucleotide)
A1: apolipoprotein B mRNA editing enzyme, catalytic polypeptide-1
A2: apolipoprotein B mRNA editing enzyme, catalytic polypeptide-like 2
A3A: apolipoprotein B mRNA editing enzyme, catalytic polypeptide-like 3A
A3B: apolipoprotein B mRNA editing enzyme, catalytic polypeptide-like 3B
A3C: apolipoprotein B mRNA editing enzyme, catalytic polypeptide-like 3C
A3D: apolipoprotein B mRNA editing enzyme, catalytic polypeptide-like 3DE
A3F: apolipoprotein B mRNA editing enzyme, catalytic polypeptide-like 3F
A3G: apolipoprotein B mRNA editing enzyme, catalytic polypeptide-like 3G
A3H: apolipoprotein B mRNA editing enzyme, catalytic polypeptide-like 3H
AKV: AKR mouse-derived virus
ALV: avian leukosis virus
APOBEC3: apolipoprotein B mRNA editing enzyme, catalytic polypeptide-like 3
ASLV: avian sarcoma / leukosis virus
Asn: Asparagine

BAF: Barrier to autointegration factor
bp: base pairs
BST-2: bone marrow stromal antigen 2

C: cysteine (amino acid) or cytosine (nucleotide)
CA: capsid
cDNA: complementary DNA
cGAS: cyclic GMP-AMP synthase
Ch25H: cholesterol 25-hydroxylase

D: aspartic acid / aspartate
DDX41: DEAD-box helicase 41
DIPs: defective, interfering particles
DNA: deoxyribonucleic acid
dNTPs: deoxyribonucleotide triphosphate
dsDNA: double stranded DNA
dTTP: deoxythymidine triphosphate
dUTP: deoxyuridine triphosphate

E: glutamic acid
ELISA: enzyme linked immunosorbent assay
Env: Envelope glycoprotein
ERManI: endoplasmic reticulum mannosidase I
ERVs: Endogenous retroviruses

ESCRT: endosomal sorting complex required for transport
EVs: Extracellular vesicles
Exo1: Exonuclease 1

F: phenylalanine
FCM: flow cytometry
Fv1 or 4: Friend virus susceptibility protein 1 or 4
FVM: flow virometry

G: glycine (amino acid) or guanine (nucleotide)
Gag: Group antigen
GBP5: guanylated-binding protein 5
gDNA: genomic DNA
gGag / Glyco-Gag / gPr80: glycosylated Gag
gRNA: genomic RNA

H: histidine
hA3: human APOBEC3
HERC5: HECT domain and RCC1-like domain-containing protein 5
HIV: human immunodeficiency virus
HyperHRM: hypermutation-analysis by HRM
HRM: high resolution melt
HTLV: human T-lymphotropic virus

I: isoleucine
IFI203: interferon activated gene 203
IFITM: interferon-induced transmembrane protein
IFN: interferon
IN: integrase
IRES: internal ribosomal entry site
ISG15: interferon-stimulated gene 15

K: lysine
kb: kilobases
KO: knock-out
KRAB-ZFP: Kruppel-associated box domain-containing zinc finger proteins

L: leucine
LINE-1: long interspersed element 1
LTR: long terminal repeat

M: methionine
mA3: murine apolipoprotein B mRNA editing enzyme, catalytic polypeptide-like 3
MA: matrix
MHC: major histocompatibility complex
(M-)MLV: (Moloney) Murine leukemia virus
MOV10: Moloney leukemia virus 10

mRNA: messenger RNA
MVBs: multivesicular bodies
Mx2: myxovirus resistance protein 2

N: asparagine
NC: nucleocapsid
nm: nanometer
Nef: Negative factor
NGS: next-generation sequencing
NTA: nanoparticle tracking analysis

P: proline
PBS: primer binding site
PCR: polymerase chain reaction
PIC: pre-integration complex
Pol: polymerase
PPT: polypurine tract
Pro: proline
Psi (ψ): packaging signal
Psi+ (ψ+): extended packaging signal

Q: glutamine

R: arginine
Rmcf(2): resistance to mink cell focus-forming virus (2)
RNA: ribonucleic acid
RNase H: ribonuclease H
RSV: Rous sarcoma virus
RT: reverse transcriptase
RTC: reverse transcription complex

S: serine
SAMHD1: SAM and HD domain-containing protein 1
SERINC: serine incorporator
SDS-PAGE: sodium dodecyl sulphate polyacrylamide gel electrophoresis
SSC: side scattered light
ssDNA: single stranded DNA
ssRNA: single stranded RNA
STING: stimulator of interferon genes
SU: surface (subunit of Env)

T: threonine (amino acid) or thymine (nucleotide)
TIM: T cell immunoglobulin and mucin domain proteins
TM: transmembrane (subunit of Env)
TREX1: three-prime repair exonuclease 1
TRIM: tripartite motif-containing protein
tRNA: transfer RNA
TSPO: translocator protein

TU: transducing unit

U: uracil (nucleotide)
UNG2: uracil DNA glycosylase 2, nuclear localization

V: valine
Vif: Viral infectivity factor
VLPs: virus-like particles
Vpr: Viral protein R
Vpu: Viral protein U
Vpx: Viral protein X
VSV: vesicular stomatitis virus

W: tryptophan

Y: tyrosine

ZAP: zinc finger CCCH-type antiviral protein 1

Table of Contents

List of Figures & Tables

Chapter 1: General Introduction

The Dawn of Virology

Seeing is believing

The discovery of bacteria has been accredited to Antony van Leeuwenhoek late in the 17th century, though at the time he referred to them as "animalcules" (1). He accomplished this with a microscope of his own design, describing the appearance, mobility and multiplication of these creatures. Even with this, it was Louis Pasteur in the mid 19th century that truly demonstrated the pathological implications of microorganisms (2). Within this aforementioned work, Pasteur identified that "furuncles" or boils may contain a microbe with the ability to proliferate in culture and propagate disease in lab animals. Furthermore, in the same work Pasteur identifies that several organisms are responsible for the development of puerperal fever, which was symptomatically defined. This work was pivotal for Pasteur and colleague, Charles Chamberland, to develop a water filtration device that was capable of filtering bacteria from solution. These filters were made widely available and became common practice among researchers to establish bacteria as the causal agent of infection.

Pasteur and Chamberland's work laid the foundation for the concept of viruses, referred to at the time as filterable infectious agents. The first documented discovery of a viral infection is debatably attributed to Ivanoski in 1892 or Beijerinck in 1898 (3). While Ivanoski was the first to identify that a filterable compound was responsible for the observed pathology of mosaic disease, it was Beijerinck that characterized the virus. As viral discovery continued, some research was dedicated to the permeability of these filter devices for ruling out bacteria in the context of infection (4). Reassurance was brought forth through the invention and adaptation of electron microscopy within the scope of bacteriophage research (5). The importance of bacteriophage research cannot be stressed enough, as

Renato Dulbecco adapted his knowledge on this front for the development of a plaque assay for use with animal viruses (6). Variations of this assay are still used today as a standard in quantification of a multitude of viruses (7). In brief, a virus will form 'plaques' when it is propagated on a monolayer of suitable target cells. This method circumvents the need of a microscope, as these 'plaques' are discernible by the human eye. This was truly revolutionizing for the animal virology field, as this enabled researchers to quantify the infectivity of a biological sample.

The aforementioned work, and much more, has been instrumental to our current understanding of viruses. These pathogens are cellular parasites, incapable of independent replication without a suitable host. Their discovery has led scientists to numerous arguments about the very definition of life (8). The comparative simplicity of their replication cycle has also raised debates about their origin with respect to cellular life – which came first, the virus or the cell (9)? Despite these interesting avenues of philosophical deliberation, researchers have agreed upon the need for classification of the many emerging viruses. As new viral species were being rigorously documented, David Baltimore presented the idea of categorizing viruses based on genome and replication characteristics (10). This classification system is still in use today, with some minor modifications. However, the development of new technologies, such as Next Generation Sequencing (NGS) and metagenomics, is responsible for the discovery of thousands of new viruses and a newfound appreciation for viral phylogeny (11, 12).

Retroviruses

Throughout the 20th century, scientists were discovering filterable pathogens that were transmitting forms of cancer. Early on, the group of avian sarcoma / leukosis viruses (ASLV), specifically Rous sarcoma virus (RSV) and avian leukosis virus (ALV), were discovered by two independent researchers (13, 14). This was followed up by numerous discoveries of mammalian tumor-causing agents: feline leukemia virus, gibbon ape leukemia virus, simian sarcoma virus, mouse mammary tumor virus and a diverse number of murine leukemia and sarcoma viruses, to name a few (15-22). At this

point it was undeniable; contagious agents could lead to cancer formation. Genetics research into some of these viruses identified potential oncogenes that were highly homologous with host proteins (23, 24). While others were missing oncogenes, they were found to modulate levels of similar host-encoded genes to transform cells (25-27). This work unlocked a diverse field of cancer research. Another unexpected avenue was brought forth with serology testing and defective viruses. Screening of chickens for this potentially leukosis-causing virus, it was discovered that asymptomatic birds may contain defective virus (28). The Bryan high titer strain of RSV, for example, was found to only be infectious when coproduced with a helper virus due to a defect in cellular entry (29). While transformation of a cell with this defective virus typically yielded no infectious progeny, there were some demonstrations to the contrary (30, 31). This was the first evidence to support the notion that pre-existing viral components are present within seemingly uninfected cells.

Alone, these previous findings would have been thought preposterous. However, there was some groundwork already in place. Howard Temin initially postulated the highly provocative theory, challenging the accepted dogma of the time, that RSV, an RNA virus, maintains a DNA intermediate to impose a more stable and heritable phenotype on progeny of infected cells (32, 33). At this point, a search had begun to identify if virus could be produced from 'uninfected' cells. An example being that of AKR mice, which were identified to produce virus during embryonic development (34). This phenomenon was also observed *in vitro* for BALB/c-derived embryonic cells after prolonged cultivation (35). Chemical induction of these viruses could be observed in putatively uninfected cells, across species (36, 37). Around the same time, Baltimore and Temin had independently discovered a virus-derived reverse transcriptase, also referred to as an RNA-dependent DNA Polymerase (38, 39). The knowledge of the relative stability of RNA and DNA, combined with Dulbecco's Nobel Prize winning research that showed the capability of a viral DNA genome to stably integrate into a host, furthered the narrative that

these transforming RNA viruses must be integrating a DNA-intermediate (40). This theory was later proven with the discovery of the essential functions of the viral integrase (41).

This cumulation of research brings us to our current understanding of retroviruses, a diverse class of pathogens that aim to permanently guarantee their genetic survival by integrating viral nucleic acids into the genome of a host. As is their namesake, these viruses are *retro*, or backwards, to the typical dogma, using a reverse transcriptase to convert a RNA genome into dsDNA that is primed for that essential integration step. The family of *Retroviridae* is divided into two very different subfamilies: O*rthoretrovirinae* and *Spumaretrovirinae*. The latter being termed "foamy" due to the impacts they have on the infected cells, while being relatively non-pathogenic (42). These viruses can also be recognized by their distinct stage of reverse transcription, allowing them to deliver a fully synthesized dsDNA genome when entering a new target cell (42, 43). *Orthoretrovirinae*, on the other hand, are the more commonly thought of group of retroviruses due to their pathogenicity, potentially causing immunodeficiency or cancer. While the reverse transcription process is conserved across subfamilies, the timing differs from *Spumaretrovirinae*, as these retroviruses maintain an RNA genome until entering a new target cell.

Endogenous Retroelements

There are many features of the human genome that resemble or share characteristics of viruses. In fact, there is a large amount of evidence suggesting that approximately half of the human genome is accounted for by transposable elements or derivatives thereof (44). The only forms of transposable elements still active today are endogenous retroviruses (ERVs) and retrotransposons, such as long interspersed element 1 (LINE-1). Retrotransposons are clearly related to retroviruses, as they share the definable quality of reverse transcribing an RNA genome intermediate prior to integration into a new position in the host. In fact, one theory of the derivation of the first retroviruses is proposed to have progressively evolved the ability to move between cells, originating from a retrotransposon (9).

As briefly touched upon in the previous section, researchers were identifying the presence of endogenous retroviruses without realizing the full implications at the time. Given the unique ability of a retrovirus to permanently modify the genome of an infected cell, it is unsurprising to see historical footprints of retroviral infection within the genetic material of hosts. Obviously, a somatic cell infection does not provide a heritable footprint, but infected germ cells may lead to the ubiquitous and continued survival of a virus by virtue of its integration into the host genome. One can speculate this as the 'goal' of a retrovirus, guaranteeing that the host's survival will ensure viral propagation. In this regard, the most successful retroviruses are those without oncogenes, typically simple in nature, and foamy viruses. This is likely linked to the reduced pathogenicity of these particular viruses, lengthening the survival and therefore chances of offspring for infected hosts.

ERVs are undeniably present in all vertebrate species to various degrees. This longstanding relationship between animals and retroviruses implies that there has been a great deal of co-evolution. Indeed, ERVs have played a remarkable role in our evolution as placental mammals. Though distantly related animal species have had different genetically tractable retroviral encounters over the millenia, there is a surprising amount of convergent evolution (45). It seems probable that a retroviral infection event is the very factor responsible for the evolution away from our closest egg-laying relative, the monotremes. There is a strong amount of evidence that supports independent gene captures of retroviral envelope genes among mammalian lineages; the family of syncytin genes is responsible for proper placental formation. Other implications for the effects of ERVs are reviewed by Grandi & Tramontano (46). ERVs also have been recognized to modulate the transcriptional regulation of neighbouring genes. Additionally, both the transcription and translation of ERVs can trigger immune sensors, potentially leading to autoimmunity (46, 47). While avian and mammalian retroviruses are commonly studied as model systems, it does not come as a surprise that many other species have similarly co-evolved with retroviruses (48). The latter work exposed the possibility of several animal

reservoirs for zoonotic transmission, even across water-land barriers. Clearly, we have only reached the tip of the iceberg to understand the historical relevance, levels of coevolution and origin of ERVs.

A Model Retrovirus: Murine Leukemia Virus

Retrovirology, a New Field

A number of murine leukemia viruses (MLVs) have been identified as ERVs within a variety of mouse strains. As a member of the gammaretrovirus genus, MLVs are representatively simple retroviruses, though there are a few examples of MLVs that contain oncogenes (19, 49-51). The term 'simple' is quite relative, as we still do not have a complete understanding of their biology. This virus has been studied extensively and has been recognized as a useful tool. Our improved understanding of the elements controlling genome packaging and integration have allowed scientists to develop multicomponent retroviral vectors to create stable cell lines, transgenic mice and even gene therapy vectors. Furthermore, the uncovering of the replication cycle of an archetypal retrovirus in a mouse model system has better prepared us for the investigations and clinical developments necessary when facing the human retroviral threats, such as HIV-1, HTLV-1 and to a lesser extent HIV-2. Herein, we describe the foundation of MLV biology available while this dissertation was in preparation.

The MLV Genome

Within the genome of an infected cell, the dsDNA coding material for MLV acts as a 'provirus'. The boundaries of a replication-competent provirus consist of long-terminal repeats (LTRs), potentially indistinguishable from one another. The subunits of these regions are termed: U3, R and U5 regions. At the 5' end of the LTR lies the U3, which is understood to act mainly as an enhancer / promoter. This area contains the expected consensus signals for transcription initiation, while some MLVs encode tandem

enhancer regions (52). These enhancer regions play an important role in determining the effective replicative cellular range of a provirus (53). Immediately following the U3 is the R region, which marks the beginning of the RNA transcripts. In addition, the R region also contains the polyadenylation signal (54). Despite this, there are very few short polyadenylated RNAs detected within the context of MLV transcription – indicating that the 3' R region is the key contributor of the polyadenylation signal (55). Finally, it is the U5 region that marks the end of the LTR. Once transcription has completed, RNA processing, such as polyadenylation, transcription termination and cleavage, is regulated by sequences within the 3' U3 region in MLV; this role is played within the 3' U5, which immediately follows the R region, in similar family members (56, 57). By making use of these recognizable elements commonly found within the cell, retroviruses take advantage of cellular replication machinery to transcribe the genome as any other cellular gene. Given the nature of a typical retrovirus, there is a possibility the U3 at the 3' end of the viral genome may act as an independent promoter, modulating transcription of downstream cellular genes. Cellular gene modulation was considered to be a rare event, occurring due to readthrough of the transcription termination signals in the 3' LTR (58). However, with new technology available, it has become apparent that both LTRs may impact cellular transcription initiation levels in a bidirectional fashion (59). Thus, the main product of LTR driven transcription is a full-length MLV viral transcript that resembles a cellular mRNA with a viral R region at both termini (**Figure 1.1**).

The MLV mRNA has several functional elements. Firstly, there are several coding sequences (CDS) that are translated and post-translationally processed. The mRNAs containing these CDS have been identified to contain a functional internal ribosomal entry site (IRES) which ensures their translation through all stages of mitosis, though the relevance of these sites during the viral replication cycle is still unclear (60, 61). The structural proteins are translated as a single polyprotein known as Gag, or Group-specific antigen. This region is solely responsible for viral assembly, as virus-like particles (VLPs) can acquire a host-derived phospholipid bilayer and egress with the exclusive expression of Gag (62).

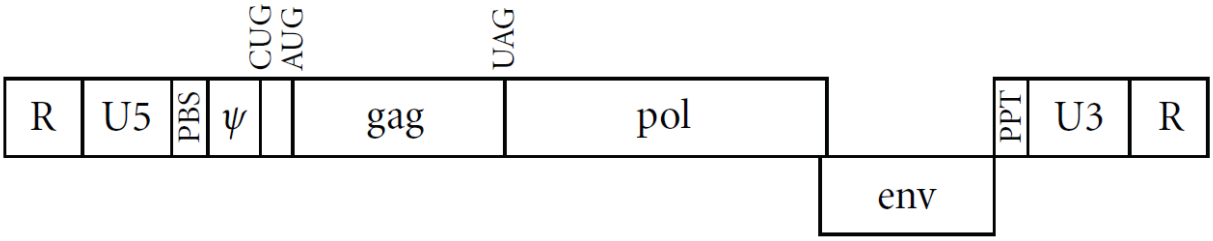

Figure 1.1. Architecture of the MLV RNA genome.

The unique regions described in the text are illustrated within the MLV genome. Each terminus is flanked by an R region and maintains a portion of the LTR. Immediately following U5 is the leader sequence, which contains the PBS and ψ. The leader sequence also contains the alternative start codon, CUG, for gGag. Following are each of the coding sequences for Gag, Pol and Env. Between the CDS for Gag and Pol is a UAG termination codon, which is readthrough on occasion due to the pseudoknot structure of the RNA. Upstream of the U3 is the PPT, essential for reverse transcription. Abbreviations: PBS: primer binding site; ψ: packaging signal; CDS: coding sequence; PPT: polypurine tract.

.

There is a stop codon that typically terminates translation at the end of the Gag coding sequence, however a read-through event occasionally occurs resulting in the translation of a Gag-Pol polyprotein (64, 65). This is due to a pseudoknot structure in the mRNA that forms a conformation suitable for read-through only about 6% of the time, ensuring a nearly 20:1 ratio of Gag : Gag-Pol (66). Recent evidence has shed some light on the importance of this ratio of translation to reach maximal virus production, with minor impacts on individual virion infectivity (67). The Pol, or Polymerase, was named after a translational product, the RNA-dependent DNA polymerase – also known as reverse transcriptase. This region contains the viral protease genes and the necessary components to complete reverse transcription and integration steps of the retrovirus replication cycle. The protease is responsible for cleaving the Gag and Gag-Pol polyproteins into their functional subunits at the necessary recognition sites during a process known as virus maturation (64, 68). The final prototypical gene product is the envelope glycoprotein (Env). In MLV, the coding region for Env leaves only an approximately 50bp gap on non-coding region between Env and the 3' LTR (54). This protein is responsible for the entry phase of the viral replication cycle; it represents the only essential viral protein on the membrane of a virus particle, with the majority of the protein exposed on the surface (69). Similar to Gag and Pol, the relative levels of produced Env protein is controlled by the virus. This regulation is mediated by the coordination of a splicing event, which removes much upstream of Env, leading to its efficient translation (70). Improving the splice efficiency modifies both the ratio of Gag : Gag-Pol : Env and the ratio of full to spliced RNA, which has a drastic impact of MLV infectivity (71). Additionally, some strains of MLV recognize a CUG codon, that is located approximately 88 amino acids upstream of the Gag initiation site, as a start codon. These strains produce a protein that is in the same reading frame of Gag, but is post-translationally modified in the endoplasmic reticulum, referred to as Glycosylated Gag (72). The specific functions of these proteins will be discussed in more detail in a later section.

In addition to the aforementioned coding and regulatory elements of the MLV transcript, the RNA must incorporate itself as a genome into newly produced viral particles. As retroviruses contain positive (+) stranded RNA genomes, no further modification to the RNA is required prior to packaging to distinguish it from these other functions. It was initially discovered that retrovirus family members maintain a dimeric genome that is linked by an interaction in the 5' region of the RNA, which has been termed a 'kissing loop' (73). For MLV, this region was identified to be within the 350bp of non-coding region found between the 5' LTR and the initiation codon of Gag (74). While this region is solely sufficient for genome dimerization and packaging, further evidence has shown an improved efficiency when containing a small section of the Gag RNA (75). These regions are referred to as the packaging signal (Psi, ψ) or extended packaging signal (Psi+, ψ+), respectively. Integrating these signals with cellular mRNA showed favourable viral incorporation and dimerization within viral particles (76). Incorporation of these mRNAs occurred as dimers, similar to the viral genomes (77). This provided the first evidence that the packaging signal and dimerization are directly linked. To confirm the link between dimerization and genome packaging, a structurally-based analysis visualizing the stem-loop conformations of monomeric and dimeric MLV genomes identified key interacting nucleotides that are only accessible in a dimeric state (78). Dimerization of Psi was then recognized to be involved in the nuclear export of the unspliced viral genome (79, 80). This is further supported by heterodimerization studies of distinct MLV transcripts (81, 82). Though the specificities behind genome packaging are discussed later, it is still unclear if Gag captures this viral genomic dimer in the nucleus or the cytoplasm, due to the presence of Gag in both regions of the cell (83). In summary, through dimerization events mediated by a highly conserved region of the MLV genome, the unspliced viral transcripts can be trafficked in a directed mechanism towards virus particle encapsidation.

A final major function of the viral RNA is that of a pre-mRNA. It is recognized by host splicing factors which results in the regulation of Env translation. Several elements within the MLV genome

regulate the splicing event, some of which were discussed previously. Additionally, a cytoplasmic accumulation element has been identified within the coding sequence for Pol, exemplifying another facet of this complex regulation (84). As a definitive property of a simple retrovirus, the MLV RNA was thought to be singly spliced, solely for Env expression. However, there have been multiple studies that have identified additional splice donor and acceptor sites that lead to biologically relevant spliced RNA species (85, 86). Furthermore, at least one such RNA maintains the ability to be packaged into virions and has been recognized to integrate into the genomes of infected cells (87). Though the functions of these different types of spliced RNA are not yet clear, they have been associated with the relative oncogenesis in MLV infection (85). This 'simple' retrovirus exhibits regulation of the splicing events through secondary structures in the RNA, some of which are in the leader sequence between the 5' LTR and the Gag coding sequence (70). The complexities of the level of control exhibited by and over the MLV transcripts are not comprehensively described in this text, however this review does them more justice (88). Due to the positioning of the splice sites, as of yet there are no identified variants of the MLV transcript that contain a Psi without an Env, though there are some variants without Psi that do not package efficiently.

MLV Viral Assembly

As briefly mentioned in the earlier section, Gag alone is sufficient for the generation of VLPs. This gave researchers some insight when initiating studies into the requirements for viral assembly, indicating that retroviruses do not depend on Env for the signals required for the generation of viral particles. As mentioned earlier, the retroviral Gag is a polyprotein. It contains subunits that are denoted matrix (MA), p12, capsid (CA) and nucleocapsid (NC). Initially, the Gag polyprotein was recognized to contain myristoylation sites in the MA domain which targets Gag molecules to the cell surface (89). Disruption of this modification prevented both membrane association and viral structure formation by Gag. Further studies showed that a polybasic region in MA also coordinates interactions with

phospholipids, independently of the myristoylation (90). Mutational analysis also suggests that MA coordinates the trafficking of Gag through cytoskeleton linked interactions (91). The importance of MA in localizing Gag towards a cellular membrane is clear, and one would speculate that this domain likely coordinates specific incorporation of the Env towards viral particles. This would seem a likely option, as MLV Env does preferentially organize with viral particles and there seems to be an interaction with MA and Env (92, 93). However, MLV Gag still out competes HIV-1 for MLV Env incorporation even when the MA domain of MLV is swapped for that of HIV-1 (93). This indicates it may be a more complex recruitment mechanism than originally thought.

Whereas the localization of Gag to the lipid membrane is clearly a responsibility of the MA domain, there is evidence to suggest the assembly of the viral core structure is shared between the p12 and CA domains. Though, perhaps the word 'share' is too strong, as p12 plays a minor role in core structure and assembly when compared to CA. There are some regions of p12 that seem indispensable for viral assembly, however some deletions do not impact this stage of the virus replication cycle (94). Seemingly, these are the same regions that are responsible for subtle intermolecular interactions with CA, suggesting some ability to contribute to the multimerization of Gag (95). On the other hand, there are many examples of CA mutations that disrupt viral assembly. Regions in the N-terminal domain had a minor influence on viral assembly, but did impact the morphology of the viral cores (96). Other point mutations in CA will entirely prevent Gag-Gag interactions, and therefore viral assembly (97). A more complex study, involving homodimerization and heterodimerization of mutant and wild-type Gag, illustrated potential interaction sites by use of single point mutants (98). The carboxy tail of CA is also deemed important for viral assembly (99). This region was later deemed the charged assembly helix motif due to its role in multimerization of Gag (100). It is unsurprising that many regions of CA are involved in the oligomerization of Gag, given the predominantly homohexameric composition of the viral capsid lattice (101).

The final component of the Gag polyprotein is the NC, which was named after its strong affinity for the viral genome. The MLV NC is a 10kDa subunit with a high proportion of proline and basic residues (102). This region is hypothesized to tightly interact with nucleic acids based on charge, which explains some lack of specificity for the RNA incorporation into virions (103). It also contains a CCHC motif which forms a zinc finger that has been shown as an essential structure in recognizing and packaging the viral genomic RNA (104). A detailed analysis of NC and Psi dimeric interface showed the interaction along the zinc knuckle of this structure (78). The NC has been implicated to some degree in multimerization of Gag required for virion assembly (105). This may be due to its strong nucleic acid binding affinity, as it has been shown that viral cores require RNA as a structural element, regardless if it is viral or host origin (106). Furthermore, NC recognition of dimeric Psi is best achieved as a set of 12 assembled Gag or Gag-Pol polyproteins, indicating this may be a sufficient milestone for virion assembly (107). Direct visualization studies suggest that this interaction occurs within endosomal vesicles (108). However, while the high affinity of NC for Psi does favour its encapsidation, the abundance of other RNA in the cytosol all but guarantees the packaging of some non-viral nucleic acids. On this front, it was discovered that most cellular mRNA species are incorporated into the viral particles at random, but there is some specificity observed as some mRNAs are equally as abundant as the viral genome (109). Total RNA within a viral sample, however, was calculated to be roughly 7-8 bases per Gag molecule.

Given the polyprotein form of Gag and its inherent requirement for the structural assembly of a viral particle, each of these aforementioned subunits will be in relatively equal abundance. This is on the order of 2000 Gag molecules (101). Pol, on the other hand, is incorporated stochastically with a strong dependence on its relative abundance within the cell (67). This implies the Gag-Gag interaction is incapable of discriminating Gag or Gag-Pol as a binding partner. As it is translated with approximately 6% of the efficiency of Gag, there should be a roughly 20:1 Gag : Gag-Pol ratio (66).

Representative of other members of the family, MLV Env is translated and processed through the endoplasmic reticulum and trans-Golgi network for glycosylation and insertion as a trimeric transmembrane protein. On its route to the cellular membrane, Env is cleaved by a furin or furin-like protease to separate the protein into surface (SU) and transmembrane (TM) subunits which are covalently linked by disulphide bridging (110). There is evidence that suggests that this furin-like protease cleavage is important for selective incorporation of MLV Env into sites of viral assembly (111). Other research supports that this protease cleavage event potentiates, but is not essential for, Env activity during viral entry (112). Though not essential for viral assembly, Env does specifically associate with MLV through an interaction with multiple domains of Gag and the intracellular tail of Env (93, 111). Along these lines, there is evidence to support the colocalization of Env and Gag, even within the endosomal protein sorting machinery (108, 113, 114). These interactions support a relatively consistent and specific level of Env incorporation into each budding virion, which is assumed to be somewhere between 80-120 trimeric 'spikes' per viral particle (115).

The final event of viral budding, also known as egress and depicted in **Figure 1.2**, is mediated through the ESCRT-I and ESCRT-III that are recruited mainly by the p12 and MA domains of Gag (116). This has been confirmed by the analysis of viral particle composition, indicating the presence of several of these factors (117). Removal of the common motif responsible for Nedd4 binding (PPPY) prevented endosomal sorting of Gag in producer cells (118). The same phenotype can be rescued through Itch ubiquitination, this highlights the importance of ubiquitination, and not exclusively Nedd4, for endosomal sorting and viral budding (119). Presumably through the interactions with these pathways, MLV and HIV have both been recognized to assemble through the endosomal compartment and bud using multivesicular bodies (120). Mutants lacking these interactions are strikingly reminiscent to the previously described MA mutants that are unable to incorporate into the cellular membrane. It is likely that the membrane association of Gag is indispensable for recruitment of these ESCRT family members,

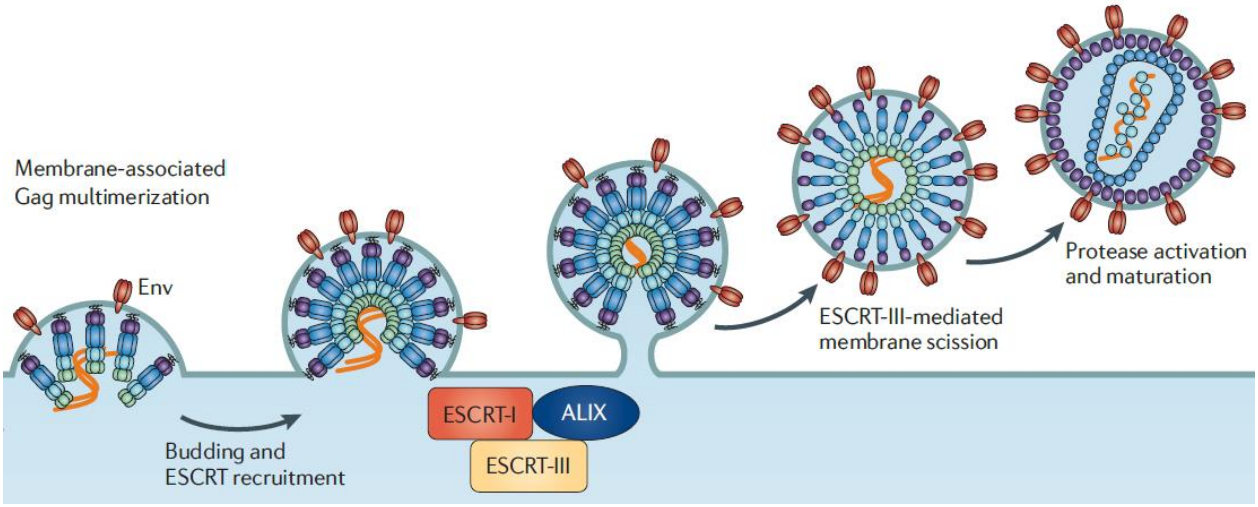

Figure 1.2. Multimerization and budding of retroviral Gag.

Retroviral structural proteins are directed towards the cell membrane for oligomerization and encapsidation of the viral RNA genome. Host proteins (i.e. ESCRT-I, ESCRT-III & ALIX) are attracted by conserved domains within Gag to mediate the egress of assembled virions. This image adapted from the original, which was reproduced under License: 4674930178483, and is Copyright © Springer Nature (121).

ensuring proper cellular localization for CA-mediated oligomerization and NC-mediated RNA packaging. Altogether, it is clear that Gag has a number of functions that act in a concerted effort towards the goal of viral assembly and egress.

Maturation

Now that the viral particles have egressed, a maturation event has to occur before they become infectious (122). It was recognized that the protease is located immediately following the NC on Gag-Pol polyproteins (64). This region is required for maturation and infectivity, but surprisingly immature particles are still capable of reverse transcription (123). Based on homology with other retroviral family members, a dimer of the MLV Gag-Pol polyproteins is assumed to initiate this process through an autocatalytic cleavage event that releases the protease, which is functional as a dimer (124). At this point, the unhindered protease will actively cleave the Gag and Gag-Pol polyproteins into their functional subunits by recognition of specific cleavage sites separating each domain (125). Surprisingly, though the mature virus contains stronger intermolecular interactions, the immature virus is more structurally sound (126). Increased intermolecular interactions as subunits has also been observed between NC and viral RNA (127). This difference in rigidity is likely due to the polymeric nature of Gag at this stage, enforcing a covalent interaction between all subunits. Since the CA and NC proteins are the main intermolecular forces, while p12 and MA contribute only minorly, one can conceptually understand the loss of structural strength. The protease is also required for cleavage of the intraviral tail of the Env, referred to as the R-peptide. This cleavage is essential for Env functionality and therefore infectivity (128). This timing is essential, as the uncleaved R-peptide was previously essential for selective recruitment of MLV Gag to budding sites (111).

The final structure of the mature virus maintains the designated orientation that was imposed by the Gag polyprotein: MA, p12, CA, NC. While the MA subunits are not likely providing much structural support, they remain associated with the membrane envelope of the virion. The p12 subunits seemingly

interact to some degree with CA, providing an added stability to the viral core. CA forms a complex structure through mainly homohexameric interactions. This structure encompasses the ribonucleic acid protein complex, which consists of the NC, viral and host RNA, as well as the Pol subunits.

MLV Entry

Once virions are released from a cell, there is a limited time available to seek and infect a new host. To put this into perspective, for MLV at a body temperature of 37°C, the half-life is between 4 and 5 hours (129). However, this is irrelevant for viral particles that are transferred at points of cell-to-cell contact, which clearly is a directed method for MLV to spread infection; the relative role of each type of infection event *in vivo* is still unclear. (92). Nonetheless, a significant amount of effort has gone into characterizing the functionality of cell-free viral particles. For example, it is known that host proteins, in addition to the viral Env, are incorporated in the membrane of MLV. While Env is actively incorporated, other membrane proteins may be passively associated as viruses bud from a cell (62). There may be some selectivity, however, given the accumulation of Env in cholesterol-rich microdomains within the plasma membrane (113, 114). Some of these host proteins have been identified to include: CD9, CD63, CD81, integrin β1, HMFG-E8 and Lamp-2 (117). This was the first identification that MLV incorporates cellular adhesion proteins on the viral membrane surface, which likely play an auxiliary role in directing the viral particles to new target cells. Though this may enhance attraction between cells, the involvement of Env in receptor binding is paramount for infection. It is understood that the Env undergoes a major conformational shift upon interaction with its receptor (130). In the case of the MLV Env, it seemingly extends an additional 40% of its original height. After initial interactions, MLV is endocytosed in a dynamin-dependent, caveolin-based, pathway that involves cathepsin activation (131). It has previously been reported that the cathepsin protease cleavage of the SU domain potentiates virus entry into the cytoplasm of a cell (132). At this point sequential isomerization of each SU-TM disulphide

linkage occurs, followed by removal of the SU region (133). This function of SU is essential for the refolding of TM and exposure of the fusion peptide, which actively incorporates itself into the opposing membrane (134). For a short time, the virus has two lipid bilayers before fusion occurs in a similar mechanism to other viral Envs, releasing the viral core structure into the cell (135).

After shedding its lipid bilayer, the structural elements of the virus retain their formation to act as a protective shell for the viral nucleic acids, thus avoiding innate sensors within the cytoplasm of the cell (136). Core stability is very important for this complex to remain intact, as mutants in the CA domain are incapable of producing intracellular reverse transcripts (97). This may be due to either core degradation within the acidified compartment, which is common during the endocytic entry of MLV, or premature uncoating within the cytosol of the cell. In either case, these mutants were incapable of forming a functional reverse transcription complex (RTC). The RTC is permeable to small molecules, like dNTPs, but not large proteins or complexes (137). Given the open nature of the MLV capsid structure, a cytosolic uncoating event may not be necessary to achieve this permeability (101). This allows for the progression of reverse transcription while protecting the viral genome from degradation or sensing. Once reverse transcription is complete and a dsDNA viral genome has been generated, this is now referred to as a pre-integration complex (PIC). These complexes of MLV have been established to travel upon the cytoskeleton and microtubule network to reach the nucleus of the cell (91, 138). It is theorized that the PIC waits at the periphery of the nucleus until mitosis events allows for nuclear entry (139). Recent evidence suggests that this is regulated by the post-translational modification of CA, specifically its SUMOylation (140). Once within the nucleus of a cell, the p12 subunit interacts with the host nucleosome in order to proximally associate the PIC for genomic integration (141). This function has long been suspected due to the high level of homology of MLV p12 with histone proteins (142). Currently it is theorized that a mitotic shift releases p12 from chromatin, initiating uncoating of the viral

core and triggering integration (143). The virus then directs the integration of its dsDNA genome into the host chromatin, enforcing the permanent and heritable incorporation of an MLV provirus.

Reverse Transcription

The reverse transcriptase is a unique enzyme responsible for converting ssRNA into dsDNA and has been extensively studied. As briefly discussed in an earlier section, the essential tools for this process are encoded within the Pol region of the genome and encapsidated into a budding virion as the Gag-Pol polyprotein. This ensures there is a consistent level of Pol proteins, roughly an equivalent of $1/20^{th}$ the levels of Gag. Though it seems in terms of retroviral infectivity, MLV can withstand a large variation of Gag : Gag-Pol ratios (67). The feature of packaging polyproteins ensures that the domains of Pol, which consists of reverse transcriptase (RT), RNase H and integrase, are all present within equimolar ratios. The functions of RT and RNase H are so tightly intertwined that these are not separated by protease cleavage (144). Given the nucleic acid binding affinity of each component, and the orientation of Gag-Pol in the capsid, Pol polyproteins and subunits are all within the confines of the capsid structure.

The process of reverse transcription is dependent upon priming and is directed in a 5' to 3' direction, similar to many other polymerases. The entire process from RNA to dsDNA is outlined in **Figure 1.3**. It was first identified that a cellular component, typically the host $tRNA^{Pro}$, was used for priming and initiation of reverse transcription (145). The exact primer binding site (PBS) was identified in the leader sequence of MLV, whereby a strong RNA duplex would occur (146). At the time, it was theorized that the viral genome specifically incorporated the tRNA due to their strong affinity for one another inside the viral particle. However, it was later shown that the genome was dispensable for this recruitment (147). It has been recently shown that precursors to tRNAs, not mature forms, are specifically recruited from the cytoplasm prior to their planned degradation (148). Though the exact mechanism is still not clear, the RT has long been implicated in this recruitment (150). This is further

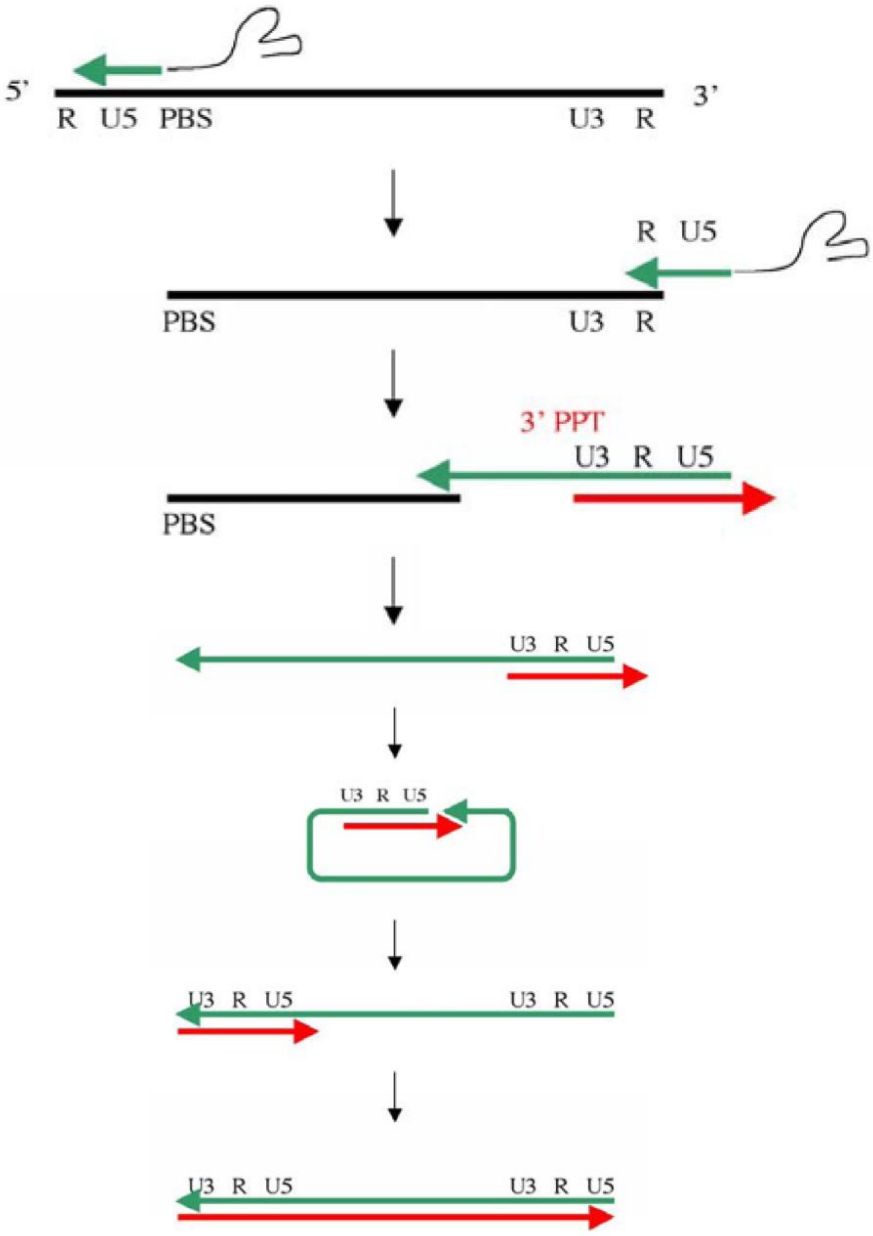

Figure 1.3. The mechanism of reverse transcription.

1) DNA synthesis is primed via the annealing of tRNA to the appropriate PBS on the viral genome. 2) After RNase H-mediated degradation of the template, the strong stop DNA undergoes strand transfer to act as a primer. 3) As the PPT is resistant to degradation, it acts as a primer to initiate plus (+) strand synthesis. This may occur simultaneously to completion of the minus (-) strand. 4) Each termini of ssDNA contains a complementary PBS, these sites anneal to form a circular intermediate. 5) Extension of the + strand dissociates the intermediate. 6) Extension of the - strand finishes the process. Abbreviations: PBS: primer binding site; PPT: polypurine tract. This image is adapted from the original, which was reproduced from (149) and Copyright © 2011 Nathalie Arhel in accordance with the Creative Commons Attribution License (https://creativecommons.org/licenses/by/2.0).

supported by the relationship between tRNA packaging and Gag-Pol translation (151). Thus, within MLV particles there would be a direct molar correlation between RT and necessary primer for initiation of DNA synthesis. Surprisingly, however, the initiation of reverse transcription is the responsibility of NC, and not RT. This is due it its chaperone function, whereby the tRNA is directed as a primer to initiate reverse transcription (152). The exact mechanism of NC involvement in this process was recently uncovered, illustrating that the PBS, which is just downstream of the Psi, is made accessible to tRNA binding by NC (153). At this point, NC directs tRNA binding and initiates DNA synthesis. By this model, NC is also important for elongation, which has been a suggested role based on mutagenesis (154). The zinc finger of NC has also been recognized as important for chaperoning properties during this process (155, 156). Thus, the necessity of NC for reverse transcription is two-fold: 1) Providing the RNA template and 2) Initiating, stabilizing and chaperoning DNA synthesis.

Once primed for extension, the functional monomer RT extends from the PBS in a 5' to 3' direction, until reaching the terminal R region (157). This short extension step, often referred to as minus-strand strong-stop DNA, only consists of the 5' terminal R-U5 region. The RNase H functions to eliminate the RNA from DNA : RNA hybridizations, thus freeing the strong-stop DNA (158). At this point, the R, or repeat, region earns its namesake. Similarly to the tRNA, NC chaperones this as a primer to initiate the first strand-transfer event, bringing the strong-stop ssDNA to the 3' terminal region of the viral RNA genome (159). Reverse transcription continues along, generating a nearly full-length DNA copy of the viral genome, heteroduplexed with its RNA complement, terminating at the original site of tRNA binding, the PBS. The RNase H activity removes the majority of the complementary RNA strand, leaving behind a small fragment that is resistant to degradation, known as the polypurine tract (PPT) (160). This region is located in the non-coding sequence between Env and the 3' LTR. The PPT acts as a primer for plus-strand DNA synthesis, generating a longer strong-stop DNA than the first step. This strong-stop DNA contains U3-R-U5-PBS, as the tRNA was still bound. Once the tRNA is removed by RNase H, the NC is

thought to chaperone the strand-transfer of this region to homoduplex with the terminal PBS on the minus strand, creating a circular intermediate (161). The RT extends both the minus-strand and plus-strand, creating a dsDNA genome that is terminated with a potentially identical U3-R-U5 or LTR.

Though this process is well-understood as a linear procedure, the multitude of enzymes within a viral particle and the nature of retroviruses to package two RNA genomes, increases the level of complexity therein. For instance, there are presumably ~100 RTs present within a single viral particle with only two ssRNA genomes. Though even ~20 RTs per particle achieves the same level of infectivity, indicating an overabundance of these enzymes (67). This leaves one to question, how many RTs can act to generate a single dsDNA genome? How many are essential? A more pressing concern with reverse transcription is the rate of recombination, as this leads to increased genetic diversity. Given the presence of dual RNA templates, a phenomenon referred to as 'template switching' occurs in which the RT jumps between each RNA template to generate a single DNA strand. This is a recombination event only if the virion has packaged two distinct viral RNA genomes. Template switching is seemingly driven by the competition of RNase H and RT activities within the functional monomer (162). This is also mediated by complex RNA structures, inducing pauses in RT elongation (163). Similar to many RNA-dependent polymerases, MLV RT is relatively error prone, introducing an error approximately 1 in 30000 bases (164). This means that roughly half of all reverse transcription events incorporate a mismatch. Understandably, mutations influencing the recognition of dNTPs by the RT have a drastic impact on this mutation rate (165). With all of this in mind, it is easy to recognize that MLV has a high level of evolutionary drive. This has led each component of the virus to have comprehensive and multifaceted roles in its replication cycle, that we are still uncovering to date.

Integration

It has long been recognized that reverse transcription functions independently of integration, but the mere generation of dsDNA viral genomes is not sufficient for a productive infection (41). Herein

lies the importance of the integrase (IN). As mentioned previously, the RTC completes dsDNA synthesis and awaits nuclear envelope degradation. The PIC is translocated into the nucleus and brought into proximity to the chromatin via p12, initiating uncoating of the viral core. Upon completion of reverse transcription, the IN recognizes a site-specific dsDNA sequence that enables it to perform a cleavage, leaving a small overhang on the 3' terminus of each DNA strand (166). With these overhangs, the IN can use the free 3' OH groups to form a new linkage with a targeted site within the host genome. This function is solely dependent upon IN (167). The ligation of the 5' ends of the proviral genome is performed by cellular repair machinery (168). This highlights the successful replication of a retrovirus.

IN does function in a site-specific manner to cleave the termini of an MLV genome, however it does not specifically recognize substrates for integration. An autointegration event can occur which would result in a defective, circularized viral genome. This is clustered into the group of defective 1-LTR circles, which also contain recombined and ligated reverse transcription products (169). These abortive end products are exclusively found in the nucleus. A host protein was identified to prevent MLV from performing these suicidal integration events, earning the name *barrier to autointegration factor* (BAF) (170, 171). The interaction of BAF with the dsDNA viral genome compacts its overall structure, reducing accessibility for an intramolecular integration (172). There is a high likelihood that BAF is also involved in the recruitment of the PIC to the chromatin, given its tendency to form multimers, interact with cellular DNA and many nuclear proteins (173). An alternative end point for the dsDNA viral genome is non-homologous end joining, which results in the formation of 2-LTR circles (174). These abortive products are even detectable in the cytosol of cells, indicating they may occur prior to nuclear translocation (175). All aforementioned products are illustrated in **Figure 1.4**. To put this into perspective, an intermolecular integration event for MLV was approximated to occur between 0.75-2 times for every autointegration event *in vitro* (176). Though this is undoubtedly more complicated within a cell, as there are several guiding factors, such as the BET family of proteins, that promote intermolecular interactions (177).

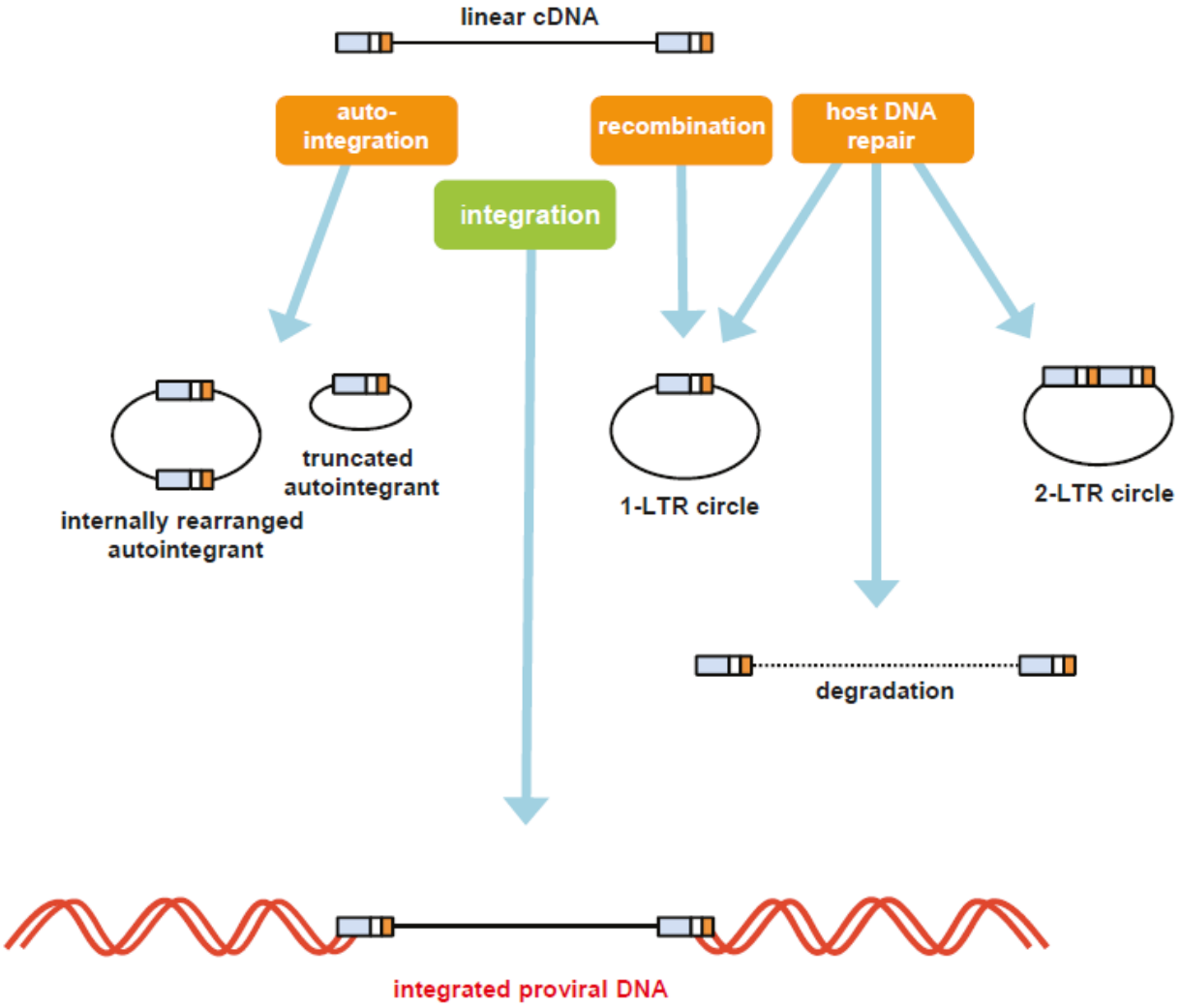

Figure 1.4. End products of retroviral nucleic acids.

Autointegration, recombination and host DNA repair (i.e. non-homologous end joining) may result in various circular abortive products of retroviral dsDNA. Alternatively, some host proteins may directly degrade the provirus before integration occurs. A productive infection, on the other hand, only occurs when intermolecular integration is achieved with the host chromatin. This image was reproduced from (169) and Copyright © 2011 Richard D. Sloan & Mark A. Wainberg in accordance with the Creative Commons Attribution License (http://creativecommons.org/licenses/by/2.0).

These factors guide the PIC to what was originally thought to be near transcription start sites, but have been clarified to active chromatin regions, such as strong enhancers (178). Evidence suggests these site-specific preferences of MLV integration may be due to more favourable structural formations (179). Indeed, MLV has a preference to integrate within dense and stable nucleosome structures (180). An analysis for the interaction partners of MLV IN has identified a variety of chromatin remodeling proteins, transcriptional activators, DNA repair proteins and even members of the spliceosome (181). This implies that IN may be functioning independently to identify integration sites and recruit the necessary repair machinery for ligation of the 5' termini of the provirus. However, one cannot exclude a further role for p12 at this stage of the infection cycle, given its affinity for histones (141). As a result, the integration site preferences of MLV seem to promote its inevitable transcription (182). Therefore, MLV has evolutionarily developed an integration site targeting mechanism towards structurally favourable and transcriptionally active regions within the genome. At this point, the replication cycle will inevitably repeat itself, potentially generating a heritable ERV that may persist within the host for millennia.

Restriction Factors

Intrinsic Retroviral Restriction Factors

Originally it was thought that permissiveness of a cell to infection was solely determined by the ability of the virus to recognize a receptor on its surface, however this is not always the case. After countless generations of coevolution between retroviruses and hosts, a number of defence mechanisms have been developed. It is now understood that entry is not the only feature averting a productive infection, but there is a constant struggle between pathogen and host. Cells have developed several blockades, which are typically interferon inducible, to target various conserved and crucial regions of the viral replication cycle. Variations in cellular expression and viral toleration to these blockades will govern the permissiveness of a host cell. This section will overview the variety of intracellular resistance factors

that have developed to counteract retrovirus infection. Keeping in mind that this list is in no way comprehensive, as there are undoubtedly a large number of yet to be identified restriction factors.

The first barrier to infection is entry. Cells missing the appropriate receptor for the Env of MLV are inherently protected from infection (183). On this front, a number of restriction factors have been evolved to inhibit viral entry. The simplest example of this stems from the well-described phenomenon of receptor interference. Retroviruses tend to prevent the superinfection of a cell by retaining or occupying their respective receptors (184). To imitate this, some evolutionary events have taken advantage of ERV Env coding sequences. Prevention of MLV infection by this mechanism is accomplished by Fv4, while the remainder of this particular ERV is not translated (185). Fv4 is not the only one of its kind, as Rmcf and Rmcf2 are other examples of similar ERV-dependent receptor interference mechanisms (186, 187). Even the syncytin family, discussed earlier as responsible for proper fusogenic activity during placental development, has been implicated in this type of protection (188). Even if the receptor is not interfered with, entry can still be blocked by the IFITM family of proteins. While HIV seems susceptible, MLV may circumvent these restriction factors by an as of yet unknown mechanism (189, 190). Alternatively, viral membranes that contain cholesterol may be susceptible to Ch25H, which modifies cholesterol on the incoming plasma membrane to prevent fusion (191, 192). The SERINC family of restriction factors, discussed in more detail later on, also play a substantial role in entry, if they are acquired during the egress of the producer cell (193). Unsurprisingly, these steps are not 100% efficient at preventing retroviral entry. Luckily, the cell has further road blocks in store.

With the knowledge of the viral replication cycle, it is clear that MLV must shield its replication intermediates while in the cytosol. Cytosolic DNA or RNA:DNA hybrids can be eliminated by TREX1, detected by cGAS, DDX41 and IFI203, leading to an activation of STING leading to a strong Type I IFN response from the cell (136, 194, 195). This reaction not only prevents the infection of this individual

cell, but the secretion of Type I IFNs will upregulate these and other antiviral genes, preventing further infections. Avoiding detection in this manner, the PIC must enter the nucleus and effectively disassemble to integrate into the genome. Thus, the regulated stability and disassembly of the viral core represents a highly targeted avenue for known restriction factors. Similarly to the aforementioned receptor interference mechanisms, ERV coding sequences have been host-adapted to interfere with the viral core. Fv1 is a notable example of exactly this situation for MLV restriction; being derived from an ERV Gag, it directly interacts with the MLV CA protein and prevents infection through a yet unknown mechanism (196, 197). TRIM5α is another example of a CA binding protein, the net result of which is viral core destabilization (197). As one of over 60 TRIM family members with potential antiviral activities, it directly interacts with capsid resulting in the prevention of dsDNA synthesis (198). MX2 has also recently been identified to function in a similar way, inhibiting HIV-1 but not MLV (199). Similarly to the aforementioned mutational analyses within the p12 or CA, which seemingly allow for assembly and entry but not infection, these restriction factors emphasize the importance of the capsid structural integrity. Clearly successful retroviruses have evolved to exclude these factors and retain core stability until reaching the safety of the nucleus.

Throughout reverse transcription, even structurally sound viral cores are not entirely protected. This is in part due to the inclusion of several host proteins during Gag assembly. One such example is the APOBEC3 family of restriction factors, discussed in more detail later on, which exhibit both a mutagenic and inhibitory role at the level of reverse transcription (200). Another incorporated protein, MOV10, is an RNA helicase and presumably acts to inhibit reverse transcription (201). In the absence of these other factors, the core must be at least partially permeable to allow for dNTPs to enter. Herein lies the target of SAMHD1, which acts to restrict the flow of dNTPs to the RTC, hindering synthesis of a dsDNA genome (202). If a retrovirus can surpass all of these hurdles and avoid some of the abortive products of its own replication, it may successfully infect a cell.

Although, winning a battle does not necessarily change the tide of a war. Especially in hosts that have coevolved with retroviruses, both endogenous and exogenous, for many generations, there are several other restriction factors that exert a blockade preventing retroviral egress and spread. The family of KRAB-ZFP have a transcriptionally suppressive function, some of which prevent proviral transcription (203). ZAP was identified to post-transcriptionally reduce the levels of cytoplasmic, but not nuclear, MLV mRNA (203). HERC5 has been shown to conjugate a small protein, ISG15, to Gag of both MLV and HIV, thereby inhibiting its multimerization and therefore viral assembly (204). GBP5 functions to inhibit Env processing and membrane incorporation for both MLV and HIV glycoproteins (205). TSPO works to direct HIV Env towards ERManI which cleaves glycosylated sites on Env to enhance its degradation, leading to viral particles lacking sufficient Env for infectivity (206, 207). Restrictive effects of TSPO and ERManI on MLV have yet to be reported. Tetherin/BST-2 is well-characterized as an anchoring protein, preventing viral release and inducing endocytosis of viral particles (208, 209). The TIM family of proteins have been identified to share a tetherin-like phenotype, preventing the liberation of viral particles from the cell surface (210). It is clear that the coevolution of host and retroviruses have led to a large repertoire of intrinsic, inducible, factors that prevent infection. This may be one major hurdle to the limited collection of successful retroviruses that are currently identified.

SERINC

The members of the SERINC family earned their namesake through the function of serine incorporation into membranes (211). However, this seemingly has nothing to do with their recently discovered antiviral activity, as the lipid composition of a viral particle is not impacted by SERINC (212). Furthermore, only SERINC3 and SERINC5 have exhibited significant antiviral activities so far (213). Expression of SERINC directly correlates with levels of the protein found on viral particles, and the downstream inhibition of infection (214). Once associated with the membrane of virions, it is theorized that SERINC directly inactivates Env, blocking any conformational change, preventing its fusogenic

activity and entry into the target cell (215). Indeed, SERINC inhibition prevents any cytoplasmic accumulation of viral structural components, consistent with this theory (216). Interestingly, the antiviral effects of SERINC are correlated with an increased sensitivity of Env to antibody-mediated neutralization (213, 215). This is likely due to the conformational hold it places on the glycoprotein. As an auxiliary function, SERINC seems to play a role in stabilizing the levels of TIM, a tetherin-like restriction factor (217). Thus, SERINC function to prevent the infection of new target cells by impairing egress and blocking fusion of the virus and target cell membranes.

APOBEC3

The APOBEC3 family of proteins are named as such due to their homology and functional similarities to the apolipoprotein B mRNA editing catalytic protein (APOBEC1), which is well known for its ability to act on RNA as a cytidine deaminase (218, 219). All members of this family share a well-defined zinc binding motif that enabled homology-based identification of the APOBEC3 proteins (220). While some APOBEC3 family members only have one zinc coordinating domain, the most studied have two separate domains. This homology enabled quick characterization for APOBEC3 proteins as deoxycytidine deaminases, with a specificity for ssDNA substrates (221). With the knowledge of mutations imposed by APOBEC3 at the level of the proviral genome, it did not take long to determine that ssDNA substrate was the minus (-) strand reverse transcription intermediate (222). Thus, these restriction factors were hypothesized to inhibit retroviral infection by inflicting damaging mutagenesis on the minus strand of ssDNA during reverse transcription, corresponding to a G → A mutation profile on the coding strand.

In order to gain access to the RTC, the APOBEC3 proteins must either be assembled into budding viral particles or be allowed access through the viral core structure in the target cell. While there is some evidence that APOBEC3 may act in the cytoplasm of a target cell to prevent its infection, this is not seen as the main mechanism of action of these proteins (136, 223-225). Through an association with the

structural Gag proteins, specifically the NC region, APOBEC3 will be incorporated into the viral core of budding particles (226). The encapsidation of APOBEC3 was found to depend on zinc coordination motifs and RNA binding (227). Unsurprisingly, the ability of NC to interact strongly with RNA was found to be necessary for the interaction between these two proteins (228). In fact, without RNA these proteins do not form a detectable interaction. The basic region of the NC, and not the zinc finger, was implicated as the main requirement for this RNA-dependent interaction (229). Interestingly, the coevolution of murine APOBEC3 (mA3) and MLV has pushed the MLV NC to inefficiently interact with mA3, leading to an incomplete inactivation (230). Though this seems to be specific to mA3 and MLV, as human APOBEC3G (A3G, originally called CEM15 in the early studies) was similarly incorporated into both MLV and HIV. While this was originally thought to be a function of the NC, it was later discovered that the Gag of MLV was dispensable for resisting mA3 (231). The function of NC to specifically interact with the viral genomic RNA acted to exclude APOBEC3 from viral particles (232). This is directly corroborated by other studies that imply cellular RNA, and not viral RNA, more efficiently coordinates the incorporation of APOBEC3 into budding viral particles (228). Thus, APOBEC3 gains efficient access to the RTC of retroviruses by first hitching a ride into the viral assembly line, mediated by a strong affinity for RNA. This is often referred to as a post-entry block mechanism of restriction, due to the nature of preventing a secondary infection.

Initially controversial, the restriction by APOBEC3 does not seem to be solely dependent upon their deaminase activity. This alternative mode of inhibition is referred to as deaminase-independent restriction. An example of this comes from the mild influence mA3 has on MLV infection, which rarely imposes any mutagenesis (233). Convincing evidence of this phenotype came from chimera studies, dissecting the contribution of each zinc coordinating domain in the overall mutation rate while relating this to the overall inhibition of retroviral infection (234). Further research indicated that APOBEC3F (A3F), and to a much lesser extent A3G, can impose a strong barrier to retroviral infection even in the

absence of any mutagenic potential (235). However, there is some controversy about the role of deaminase-independent activity when considering endogenous levels of these restriction factors. Even when employing an A3F catalytic mutant, it could not independently inhibit the spread of infection (236). Studies using primary cells have implicated the importance of both mechanisms (237). Notably, deaminase-inactive mA3 has proven to be a functional restriction factor against MLV *in vivo* (238). This highlights the relevance of the deaminase-independent restriction pathway, at least for some APOBEC3 proteins. Several models have been proposed for the blockades imposed by APOBEC3 that are independent of catalytic activity. This includes inhibiting the initiation of reverse transcription by blocking primer binding, preventing strand transfer, sequestering the viral RNA from the RT, physically stalling the RT and/or inhibiting integration (239-243). Evidence suggests that this activity is independent of NC, which is surprising given the competitive affinity APOBEC3 and NC have for the RNA within the viral core (244). Therefore, deaminase-independent activity of APOBEC3 proteins does pose a functional and relevant threat to the replication of retroviruses.

In the case of retroviral restriction, however, it is more relevant to consider both of these actions working together in a concerted mechanism. While intriguing mathematical modelling has illustrated that deaminase activity accounts for 99.3% of A3G-mediated restriction, but only 69.8% of A3F-mediated restriction of retroviral infection (245). This high gene inactivation potential of A3G compared to other APOBEC3 proteins is due to its unique context of deamination, increasing the likelihood of a premature stop codon (246). Thereby each APOBEC3 may have a different balance of activities that govern its restriction on retroviral replication. Successful inhibition with the deaminase-independent activity of these proteins would prevent integration of any proviral DNA, protecting the cell from much of the potential damage of infection. If this activity were to fail, however, deamination clearly imposes a mutagenic attempt to inactivate the provirus. This mutagenic tactic is not limited by deamination, as incorporation of APOBEC3 into MLV particles has been associated with a reduced

fidelity of the reverse transcriptase (247). This phenomenon has also been observed with human APOBEC3 proteins on HIV-1 (248). Ultimately, this may allow for the integration of inactivated provirus. However, there has been significant research towards the mutagenic influence of APOBEC3 with regards to the high level of evolutionary escape observed for retroviruses, especially HIV-1 (249). Sublethal mutagenesis, whether originating from deamination or reduced RT fidelity, has been associated with immune escape and development of drug resistant strains (248, 250, 251). Indeed the genetic variability of both HIV and MLV is undoubtedly enhanced by suboptimal deamination by APOBEC3 (252-255). On the other hand, a compelling study has demonstrated that APOBEC3-mediated deamination minimally contributes to genetic variability when compared to RT error (256). Furthermore, at least in the co-expression of A3F and A3G, deaminase activity more frequently led to inactivation of provirus with a minimal contribution to genetic variability (248). These latter two studies emphasize that the majority of viruses are ideally inactivated by this family of restriction factors, however the surviving fraction has an enhanced evolutionary rate with genetic imprints of the influence of APOBEC3.

Retroviral Coevolution with Restriction Factors

HIV-1 and HIV-2

Among the family of retroviruses, HIV is the most well-studied due to the pathology and mortality exerted in humans. A great deal of the success of this virus is attributed to the wide array of accessory proteins that have evolved mechanisms to inhibit restriction factors within the host. Though there is no doubt that the development of these accessory proteins is due to the imposed pressures on SIV, the parental relative of HIV (257). In fact, several of the examples of restriction factors provided in this report would not have been identified if it were not for the function of the accessory proteins of HIV. The roles of restriction factors within the context of HIV infection are depicted in **Figure 1.5**.

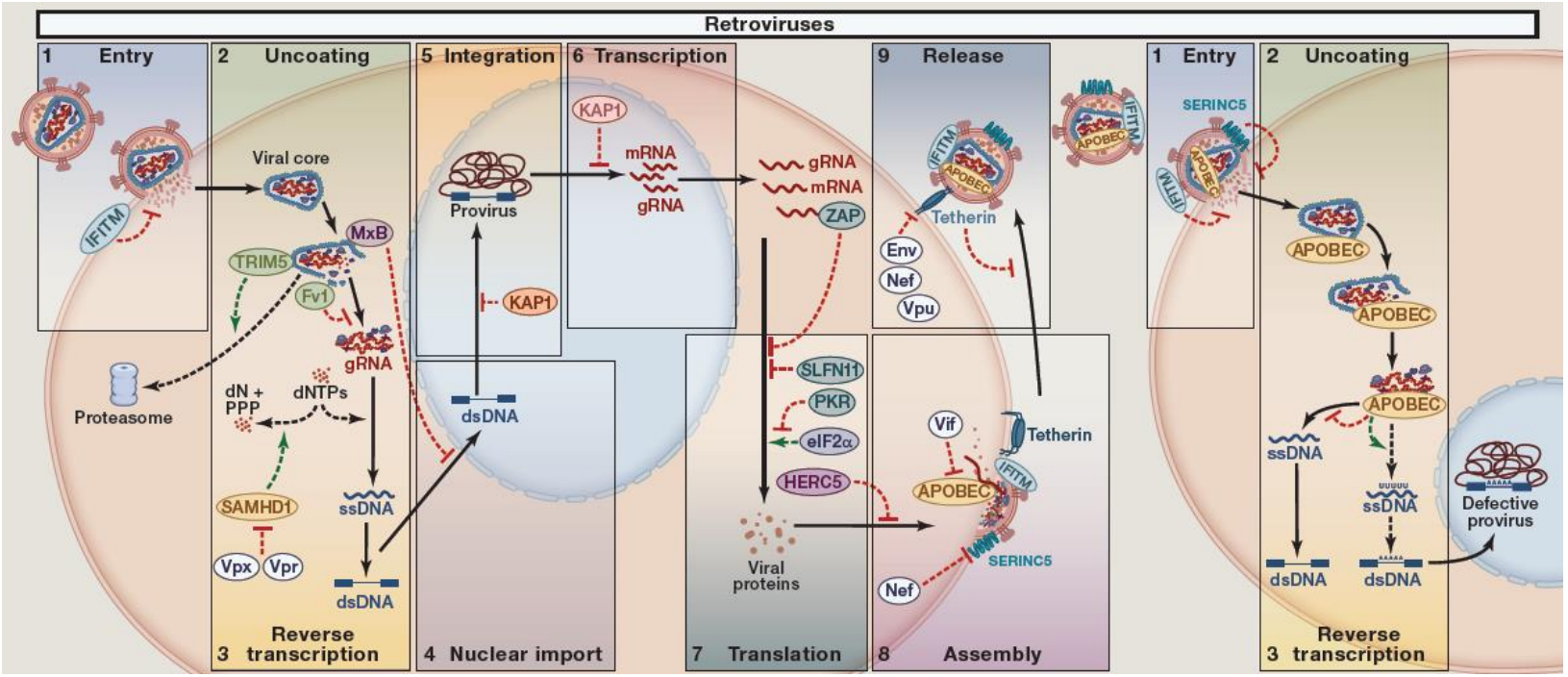

Figure 1.5. Intrinsic restriction factors at various stages of the retroviral replication cycle.

The interplay between HIV accessory proteins and intrinsic restriction factors as described in the adjacent sections. This image was reproduced under License: 4674921498531, and is Copyright © Springer Nature (258).

Viral infectivity factor (Vif)

Within the producer cell of certain cell lines, Vif was identified to be an important factor essential to increase the infectivity of viral particles, leading to a hypothesis that it was compensating for the absence of a necessary cellular factor that would contribute to a productive infection (259). After the discovery of A3G, it was identified that Vif was responsible for excluding this restriction factor from budding viral particles (260). This truly highlights the efficacy of APOBEC3 as restriction factors, as the accessory protein responsible for counteracting them received the title 'Viral infectivity factor'. The mechanism of exclusion from virions was determined to be based on an interaction between Vif and APOBEC3 that induces the degradation of the restriction factor (261). Though A3G is the most studied of the family, Vif has been recognized to potently restrict all biologically relevant APOBEC3 proteins (262). This interaction resulted in the Cul5-dependent ubiquitination of APOBEC3, targeting it for proteasomal degradation (263). Given the strong restriction by APOBEC3 observed in the absence of Vif, this interaction has been a target for inhibitor design, though there have been some surprises along the way (264). Since the formation of this ubiquitination ligase complex involves CBF-β, it was discovered that sequestering this protein also reduced transcription of APOBEC3 (265). Independently of these activities, Vif was shown to inhibit translation of APOBEC3 mRNA (266). It is clear that Vif has evolved a strong counteracting ability to reduce the inactivation potential of APOBEC3, which may be more difficult to therapeutically target than once thought.

Negative factor (Nef)

First identified as a negative factor for viral replication, Nef has never lost that nickname (267). Though a decade later, a role for positively influencing infectivity by means of viral fusion or entry was implicated (268). However, the mechanism behind this has only recently been uncovered as an activity directly thwarting the role of SERINC (269). It accomplishes this by directing the endocytosis of SERINC within the producer cell, preventing it from incorporating onto the surface of budding virions (270). This

process results in the lysosomal degradation of SERINC (271). Recognition of an intracellular loop of SERINC by Nef is crucial for its activity (272). This function is conserved across the species barrier, highlighting broad action of Nef (273). Nef seemingly offsets the TIM family of restriction factors; however it may do so indirectly through a destabilization of the protein based on an antagonism of SERINC (217). A new report suggests that Nef may even counteract additional, undiscovered restriction factors (274). This small protein has a complex and diverse role within the retroviral replication cycle of HIV that has often been overshadowed by its downregulation of other membrane proteins (i.e. T-cell receptor, MHC Class I, CD4 and tetherin).

Viral protein u (Vpu)

Several roles for viral protein u (Vpu) have been described. Firstly, it was identified in the presence of a factor that presumably inhibited viral production (275). It was later determined that this restriction factor tethered assembled viral particles to the surface of producer cells, earning the name tetherin (208). Vpu acts to downregulate the surface levels of tetherin, preventing its activity on budding virions (276). It was determined that the transmembrane domain of Vpu interacts with that of tetherin, resulting in the lysosomal degradation of the restriction factor (277). Alternatively, or additionally, Vpu accelerates degradation of tetherin through the proteasomal pathway (278). As if this were not enough, Vpu also reorganizes the placement of newly synthesized tetherin to avoid viral budding sites (279). However, this role of Vpu is not independently sufficient to improve viral replicative fitness *in vitro* (280). It is difficult to dissect this specific role of Vpu from the many other complex functions it undertakes within the producer cell.

Viral protein r (Vpr)

Viral protein r (Vpr), an HIV-1 specific protein, similarly recruits the ubiquitination ligase machinery to invoke the degradation of cellular factors that would otherwise restrict retroviral

replication (281). Surprisingly, APOBEC3 has been identified as a restriction factor targeted by Vpr for degradation in a similar fashion to that of Vif (282). Similarly, Vpr targets UNG2, a uracil DNA glycosylase, for degradation (283). It was recently uncovered that UNG2 acts to restrict retroviral replication by cleaving uracils, creating abasic sites and preventing the integration of a provirus (284). HIV proviral DNA is loaded with uracils due to the inability of the RT to distinguish dUTP from dTTP (285). Furthermore, an exonuclease (Exo1) that may target the replication intermediates of HIV-1 is targeted for degradation by Vpr (286). The transcriptional repressor, HLTF, was also found to be inhibited by Vpr-induced degradation at the producer cell level (287). Thus, while Vpr is well known for its ability to induce a cell cycle arrest, it is also a highly competent antagonist of several restriction mechanisms.

Viral protein x (Vpx)

HIV-2 does not have a Vpu, instead it encodes for viral protein x (Vpx). Likely arising through gene duplication, Vpx and Vpr proteins share some homology and functionality, an example of which is the recruitment of the same ubiquitination machinery (288). The restriction factor targeted in this case is SAMHD1, resulting in successful reverse transcription even in its presence (289). This targeting appears dependent upon the nuclear localization of SAMHD1 and Vpx (290). However, new evidence indicates a SAMHD1-independent role for Vpx in allowing reverse transcription to occur in resting CD4 T cells (291). Perhaps there are other restriction factors that Vpx can abrogate, though it has received less attention due to the reduced pathology of HIV-2.

MLV

Murine leukemia viruses are thought of as a representative, simple retrovirus. This is why it came as a surprise to identify the paradoxically complex accessory protein, glycosylated Gag, within the genome of MLV. The role of this protein within the life cycle of MLV is still being elucidated, however it is clearly an antagonist of multiple restriction factors. Upon comparison of this protein to some of the accessory genes within HIV, the selective pressures of restriction factors upon retroviral evolution become more obvious.

Glycosylated Gag (gGag or gPr80)

First identified as a type II membrane protein on the surface of infected cells, the role and origin of Glycosylated Gag (gGag or gPr80) remained unclear (292). Initially, it was hypothesized that gGag and Gag were synthesized from the same protein precursor (293). However, the translation of each product was shown to initiate at two independent sites (294). Combined, these works indicated that there was an additional, unidentified start site located upstream of MLV MA (295). Indeed, this region was identified to contain an alternative start site, a CUG codon, within MLV (296, 297). Translation of this sequence may also result in a glycosylated form of Gag-Pol due to the same pseudoknot RNA structure (298). Sequence comparisons showed that the leader region responsible for this was highly conserved among gammaretroviruses, suggestive of a selective advantage (299). Initially it was thought to be an enhancement of replication, as antibodies directed towards surface exposed gGag had a significant blocking effect (300). Along these lines, gGag was deemed responsible for the enhanced pathogenesis and spread of MLV *in vivo*, despite being a target of the immune response (301, 302). This was confirmed for several strains of MLV (303). Its role was further emphasized based on the reversion of mutant to gGag expressing viruses within immunocompetent mice (302). Pathogenesis induced by gGag was deemed related to its cell surface expression, as mutants with lower surface levels of gGag were more pathogenic (304). However, there were no observable enhancements on replication with gGag *in*

vitro when a mutant was constructed (296). This phenotype was confirmed as replication was not hindered but plaque morphology was less pronounced in gGag-deletion mutants (305). This implies that the leader sequence between the 5' LTR and the Gag coding sequence encodes for a biologically relevant accessory protein that shares a substantial homology with Gag.

Despite the obvious presence of a mounted immune response, the conservation of these sequences in a variety of gammaretroviruses suggests there must be a replication advantage (300, 306). The lack of any obvious phenotype of gGag *in vitro* had inspired further dissection into its role within the cell. It was first identified that while the N-terminal leader sequence is responsible for the localization and post-translational modifications, the specific glycosylation sites were identified to be within the Gag sequence (307). Nevertheless, this protein still has a remarkable resemblance to the native Gag polyprotein. It came as a surprise, however, that gGag is inefficiently processed into mature MA and CA, likely due to the presence of glycans or change in protein folding (298, 308). Though the large gGag polyprotein was identified to be proteolytically processed, presumably by a cellular protease (309). The main cleavage products were identified to be a membrane-associated N-terminal product of ~55kDa and a secreted C-terminal product of ~40kDa (72). Portis' group was the first to identify a unique ability of membrane bound gGag products to have either a type I or a type II orientation. Though originally undetectable in viral isolations, the membrane bound N-terminal fragment of gGag was found in both microvesicles and viral particles (310). It was speculated that gGag may be involved in viral budding or release, as mutant viruses formed tube-like viral particles on the surface of producer cells (311). This was associated with virion accumulation of cholesterol, likely by facilitating release through lipid rafts (312). Even with this knowledge, the main role of gGag remained an enigma.

Functional comparisons of gGag alongside Nef, an accessory protein of HIV, revealed a strong convergent evolution phenotype (313). While gGag can rescue a Nef-deficient HIV, Nef could not replace gGag in an MLV infection. This implies similar, but not completely overlapping purposes of the two

accessory proteins. Only the cytoplasmic domain of gGag was required to fulfill the Nef-like role in HIV replication, relying on a role in enhancing endocytosis (304, 314). It was later determined that this endocytic activity was targeting the reduction of SERINC from the membrane of producer cells (269, 270). SERINC is then targeted for lysosomal degradation, explaining the previously observed phenotype of increased gGag surface expression correlating with reduced pathogenesis (315). The SERINC protective phenotype was only necessary for certain Env proteins, indicating other possible evolutionary mechanisms to avoid restriction (316, 317). Altogether, this illustrates that the selective pressures exerted by SERINC have pushed two very distinct retroviruses to develop similar counteracting mechanisms. Whether this is related to the ability of these proteins to increase the cholesterol content of released viral particles remains to be determined.

Another functionality of gGag was found to be its specific protection from APOBEC3 activiy (224). Mice that have genetically inactivated mA3 allowed for the *in vivo* propagation of gGag-null viruses, similar to that of gGag wild type strain. The protection from mA3 may be uniquely developed due to the coevolution of virus and host, as human APOBEC3B (A3B) and A3G exhibit a strong restrictive phenotype of MLV in the presence of gGag (318). The mechanism behind protection of the RTC from APOBEC3 is related to an enhancement in core stability, which also protects the RTC from exogenous APOBEC3 within a target cell independently of its deaminase activity (136, 225, 238). Intriguingly, however, some strains of MLV are susceptible to the mutagenic potential of mA3, despite coding for a gGag (319). Though the overall mechanism for gGag protection is still not clear, as mA3 is detected within viral particles and does have an inhibitory effect on viral replication. While some of the functions of gGag are slowly being uncovered, much remains to be discovered, especially considering the Nef-complementation of gGag-deficient MLV. Whether this implies gGag is counteracting other restriction factors or promotes viral replicative fitness in another way remains to be determined. Investigations towards tetherin, another restriction factor, revealed that gGag had no impact on its restriction of MLV

(320). Thus, more efforts are required to decipher the mechanisms of action of gGag, especially considering its modification of the endosomal sorting pathways which has strong implications for the field of extracellular vesicles.

Extracellular Vesicles

Cellular Messengers

The definition of the term extracellular vesicle (EV) is all-encompassing, meaning any vesicle that is exterior to the cell. The field of EVs has certainly come a long way since the first reference to them as "platelet dust" (321). The International Society for Extracellular Vesicles has encouraged a strong collaborative effort among the experts in this field to establish firm guidelines for the characterization and classification of EVs (322). It is now understood that EVs come in various shapes and sizes (**Figure 1.6**), through multiple biogenesis pathways and have an array of functions. The smallest EV family member is secreted through a mechanism very similar to endocytosis, termed exocytosis (323). The similarity comes from their origin within multivesicular bodies (MVBs), resulting in the release of exosomes with sizes from 30-150nm in diameter. Microvesicles, on the other hand, range from 50-1000nm in diameter and bud directly from the surface of the cellular membrane. Even apoptotic bodies are classified as EVs. These can range from as small as exosomes to micrometers in diameter, the mechanisms behind their assembly and release are also tightly regulated (324). Each of these EVs incorporate both cytosolic and membrane components of their parental cell, with the potential to deliver this cargo over large distances (325). The synthesis and secretory processes of these vesicles involves the ESCRT-0, I, II and III (endosomal sorting complex required for transport) families (326, 327). Though this is not always the case, as ESCRT-independent assembly has been illustrated by tetraspanins (328). While the exact mechanisms and triggers behind the assembly and release of these EVs are not entirely clear, their physiological relevance as a communication network is undeniable.

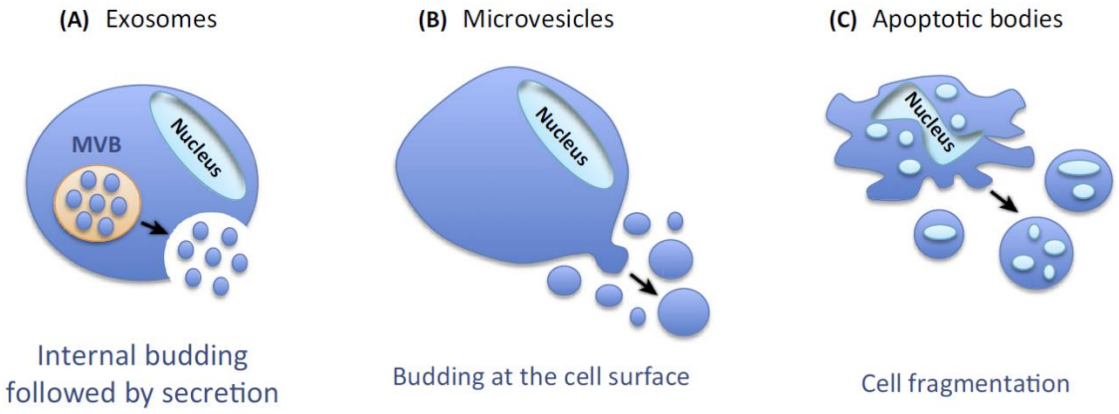

Figure 1.6. Subpopulations of extracellular vesicles.

Differences in budding and size of (A) exosomes, (B) microvesicles and (C) apoptotic bodies are represented in this cartoon. This image was reproduced under License: 4674941205962, and is Copyright © Elsevier (329).

EVs in the Context of Viral Infection

The release of EVs has been documented from all known cell types tested so far (330). Typically, the content of EVs contain coding and non-coding RNA, DNA and even proteins that may be functionally delivered to other cells (331). Furthermore, various stressors have been noted to modify the frequency and content of vesicular release (332). This is especially true for many viral species. An infected cell may release EVs that contain viral RNAs to activate nucleic acid sensors in the recipient cells, resulting in immune activation (333, 334). Moreover, EVs play a crucial role within the milieu of a viral infection. Indirectly, EVs may impair viral propagation by delivering restriction factors to neighbouring cells (335). Alternatively, direct impairment of infection has been seen through the physical interaction of an EV-associated receptor and viral Env, whereby the EV acts as a 'decoy' target cell (336). However, through millennia of coevolution, viruses have developed mechanisms to hijack EV biogenesis and release pathways. HIV Nef, for example, prevents CD4 from associating with EVs to improve viral infectivity (336). Nef has even been observed within EVs (337). Even non-enveloped viruses, such as hepatitis A and hepatitis E, have been identified to exist in a quasi-enveloped state, thereby expanding tropism, by egressing as an EV (338, 339). Retroviruses, such as MLV, HIV and HTLV, acquire an envelope through the release pathways of either exosomes or microvesicles, specifically by hijacking ESCRT proteins (116, 340, 341). Evidence has also implicated tetraspanins in the release of the aforementioned retroviruses (117, 342, 343). The striking similarities between biogenesis and egress of both EVs and viruses, especially retroviruses, have led some to wonder about the relationship between these two species (344). Nevertheless, it is clear that viral infection modifies the intracellular environment in such a way that results in a detectable change in the content of EVs.

Discriminating EVs from Viral Particles

Currently, an infection is characterized by the net effects of all EVs and virions within a given sample. However, as previously mentioned, EVs are heterogenous in nature. While some may impose a

proinflammatory response, others may directly spread viral infection. For this reason, both qualitative and quantitative analyses of EVs and viral particles is a topic of great interest within this field of research. By this measure, an ultimate goal represents the determination of the influence of either EVs or viral particles on an independent level. Crucially, this requires either physical or analytical separation of these biologically-similar entities. Ultracentrifugation through differential density gradients is a standard method to isolate pure preparations of virus, but even this cannot purely separate EVs due to their similar sizes and buoyant densities (345). However this method of virus purification can be quite labour-intensive, particularly if requiring a dialysis step to remove the chemical composition of the density gradient. More importantly, ultracentrifugation has the potential to damage viral particles, hence impacting any downstream analysis (346). A less detrimental alternative involves the immunomagnetic depletion of EVs from a viral sample (347). This method takes advantage of cellular CD45 expression, which is highly abundant on most EV species derived from hematopoietic cells but is not detected on HIV (348, 349). Although, some immunocapture data indicates that there may be low levels of virus associated CD45 (350). The caveat here being the virus must be produced from a CD45-expressing cell, limiting the experimental range. However, this method does result in a significant enrichment of viral particles based on a near-complete depletion of EVs. Even the opposite has been demonstrated when isolating exosomes from human plasma, in an effort to avoid contamination with HIV particles (351). Unfortunately, given that some EVs do not incorporate CD45 and a minor population of HIV does, this method cannot permit the full distinction viral functions apart from that of EVs. Even a novel chromatography-based purification method managed to significantly enrich, but not purify, retroviral particles (352). Therefore, there is no established method to date that can entirely purify EVs or virions from a heterogenous sample due to the overlapping characteristics in size, buoyant density and surface marker expression.

As an alternative to the difficult task of physical separation, one may endeavour to analytically separate EVs from virions. However, this may lead researchers to unconventional means of viral sample analyses. Typical analytical methods for the characterization of viral samples are based on protein or nucleic acid content, infectivity or microscopy (353). Aside from high resolution microscopy methods, conventional viral analyses are conducted in an indiscriminate fashion, whereby both EVs and virions are assessed simultaneously for a viral feature. Certain microscopic techniques, such as electron microscopy or super-resolution microscopy, may enable the discrimination of EVs from viral particles with a high degree of confidence, based on morphology and composition (354, 355). However, these procedures are laborious and involve significant sample manipulation. Fluorescently-triggered nanoparticle tracking analysis (NTA), which is conventionally used by the EV field, has recently been shown to effectively enumerate the levels of respiratory syncytial virus within laboratory and clinically relevant samples (356). This methodology is rapid and involves minimal sample manipulation, thereby limiting the risk of damaging the viral particles. While this method does use a viral antigen for particle quantification, the association of this antigen with EVs is not considered. Furthermore, NTA has been limited in its multiplexing and antigen quantification abilities. To address these limitations, an innovative adaptation to the field of virology utilizes a method known as flow virometry to analyze small particles by flow cytometry.

Flow Virometry

Flow virometry has been possible for decades, though originally with custom-built flow cytometers (357). This technique enables a rapid assessment of viral samples, allowing for quantification and characterization of virions at the single particle level. More recently, conventional and commercially-made flow cytometers have been determined to have the capability to detect and analyze viral particles (358). This is in large part due to the optimization in signal to noise ratio, allowing the visualization of smaller particles. However, many of these instruments are built with cells in mind. This

results in relatively large flow cells, microns in diameter, allowing for the clustering of viruses or other small particles. Consequently, the cytometer may perceive multiple virions, or a range of particles, as a single event. Therein lies one major complication of flow virometry, termed coincidence or swarming, which has been well-documented (359). Ideally, flow virometry should be conducted for the single particle analysis of individual events (**Figure 1.7**). Further discrepancies from conventional flow cytometry arise when considering the diameters of most viruses are smaller than the wavelengths of light being used to analyze them. This results in increased perpendicular scattering of light, also referred to as side scattering (SSC) (360). However, the precise nature of scattering on small particles is still being determined. A final major complication of flow virometry is the decreased antigenicity on a viral surface compared to that of a cell. Based on the circumference of a perfect sphere, simple mathematics dictates that for every 10-fold decrease in size (i.e. 10µm → 1µm → 100nm), there will be an associated 100-fold decrease in surface area. Though biological particles are more complex in size, this rough approximation demonstrates the principal of reduced antigenicity based on diameter alone. Thus, the use of flow cytometer to analyze viruses is indeed possible, but one must take care to address the underlying complications of such a technique.

Over a dozen independent groups have demonstrated virus particle analysis by flow virometry (358). The sensitivity of this technique has been demonstrated to be greater than ultra-sensitive enzyme linked immunosorbent assays (ELISA) and similar to that of a polymerase chain reaction (PCR), an amplification-based method (361). Such superior sensitivity is only achieved when there is confidence in discrimination between EVs and virions, which was realized via genetic engineering of a viral structural protein to contain a fluorescent reporter. One caveat here is the possibility of incorporation of this structural protein into EVs, which was not excluded as a possibility. Less manipulative approaches have been demonstrated whereby individual particles within viral supernatants have been labelled for the presence of viral antigens and nucleic acids (362, 363). Even the maturation of viruses has been

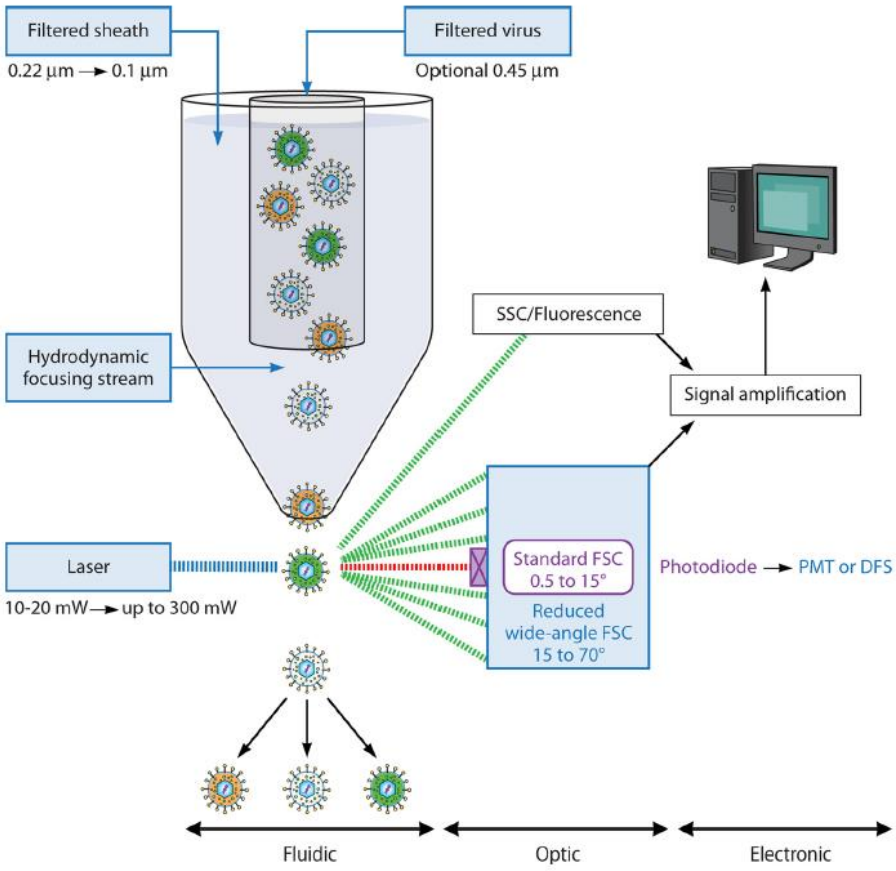

Figure 1.7. Flow virometry discrimination of viral particles.

A viral sample analyzed by a flow cytometer at the proper dilution will result in single particle interrogation. Filtration of a viral sample is ideal to ensure removal of cells and large debris. Sheath fluid must be filtered below the expected size of the viral sample. Hydrodynamic focusing reduces fluidic induces noise. Laser wavelength and power can be optimized for detection. FSC / SSC / fluorescence optimization and signal amplification can be done for improved event detection. If fluidics are capable, samples can be sorted based on differences in antigenicity (represented by colour differences). This image is reproduced from (358) with proper permissions (see Rights & Permissions section of thesis).

observed using flow virometry (364). However, at this point there has been little discrimination between EVs and virions using this technique. The ability of flow cytometry to multiplex, coupled with the wide assortment of dyes, aptamers and antibody labeling strategies that already exist for the analysis of cells, uniquely places this technique as a major analytical option to distinguish a virion from other membraned-vesicles. More importantly, the ability of flow cytometers to physically sort events for downstream applications has already been demonstrated as a possibility for viral samples (361, 365). The results of viral sorting research has revealed a surprising heterogeneity of infectivity profiles between viral populations (365). This indicates that upon the development of proper techniques to label viruses, flow virometry may enable the identification and characterization of subpopulations with viral samples, similar to what has already been achieved for cells. Furthermore, this may be the tool needed to physically separate and evaluate the individual roles of EVs compared to viruses.

Rationales and Hypotheses

Chapters 2 & 3

Retroviral evasion of host intrinsic restriction factors is a crucial phenomenon required for viral success. This is emphasized by HIV and the discovery of Vif in the circumvention of APOBEC3 (259, 260). The naming of Vif as viral infectivity factor exemplifies its necessity, as APOBEC3, most notably A3G, effectively terminates the propagation of HIV in a post-entry block mechanism. A significant amount of work has been and continues to be invested into deciphering and blocking the mechanisms behind the activity of Vif (366). Furthermore, the evolutionary rate of HIV has made the intervention with a Vif-targeting therapeutic blockade quite difficult (367). A different accessory protein of HIV, known as Nef, has demonstrated the capability of improving retroviral replication by directly targeting the degradation of SERINC, another restriction factor (269, 270). The complete mechanism behind Nef-directed targeting of SERINC is not yet known, though during the progression of the works presented in this thesis, it was determined that endocytosis and lysosomal degradation are directly involved (271). The development of therapeutics that push the efficacy or stability of restriction factors, such as APOBEC3 and SERINC, in the presence of retroviral antagonists represents a viable and clinically unexplored therapeutic option. To undertake this research, we propose MLV as a suitable model for small animal studies.

Similar selective pressures have led to the convergent evolution of MLV to develop its own accessory protein, gGag, which acts to circumvent both APOBEC3 and SERINC (224, 269, 270). The overall functions of this protein remains an enigma, despite decades of research; while its ability to counteract APOBEC3 is linked to viral core stability, how these two features are linked remains unclear (136, 225). This becomes even more perplexing when considering the limited levels of gGag, specifically N-terminal cleavage products, that are associated with virions (310). While gGag ultimately tries to evade APOBEC3, similar to that of Vif, the mechanism of action is distinct. In contrast, a recent report shows that gGag induces the endocytosis and subsequent lysosomal degradation of SERINC (315). This is

virtually identical to the mechanism observed for HIV-Nef (271). Thus, MLV infection represents a useful mouse model system for the dissection of the mechanisms behind restriction factors and the associated antagonism by retroviruses which may aid in the development of novel therapeutics targeting a mechanistically important cellular element or a conserved and essential viral feature.

As with most things in life, start with the simple and move towards more complex tasks. Given the reduced complexity of MLV, containing only one accessory protein, it represents a valuable model. We sought to uncover functional aspects of gGag that are required for its induced resistance to APOBEC3. There has already been an established connection that links gGag, enhanced capsid stability and this resistance (136, 225). Considering the main structural components of MLV are provided by the Gag region, **I hypothesized that it is the glycosylation of Gag that enhances the structural stability of the viral core.** This is supported by the evidence of reduced viral protease cleavage of gGag and the enhanced stability provided by unprocessed Gag (126, 298, 308). In **Chapter 2**, we confirm the necessity of gGag for resistance to APOBEC3 and observe, for the first time, that mutating the glycosylated residues to a structurally similar amino acid (N→Q) results in enhanced susceptibility of MLV to APOBEC3 (368). As a continuation of this work, in **Chapter 3** I aimed to determine the mechanism behind this increase in core stability, especially considering that previous groups were only able to identify N-terminal fragments of gGag within virions (310, 369) . Perhaps this is due to the only unique feature of gGag, distinguishing it from the Gag polypeptide, being localized to the N-terminus. However, by genetically tagging the C-terminus of gGag, we were able to identify the presence of full-length gGag oriented within the virion as a type I membrane protein. Further, I was unable to separate the phenomenon of viral core stability from that of resistance to APOBEC3. This leads me to a **slightly modified hypothesis: the structural components of gGag improve viral core stability by intricately coordinating each region of the viral core, from its transmembrane domain to the covalently-linked**

nucleocapsid region. The intricate nature of these interactions may impose a structurally based steric hinderance or blockade from APOBEC3 to access the reverse transcription complex.

Chapters 3, 4 & 5

The exploding field of EV research has highlighted the importance of EVs as messengers for intercellular communication. The cargo that is delivered by EVs is drastically altered during the state of infection, varying from observable pro-inflammatory to anti-inflammatory responses (344). However, it is difficult to discern the independent influence of EVs from that of viruses due to the inherent similarities between their biogenesis and egress. This is especially true for retroviruses, such as MLV (116, 327). These similarities have made pure separations of the two species nearly impossible, allowing for enrichments at best (345, 347, 351, 352). Retroviral enrichments have been analyzed by techniques that assume homogeneity in a given sample. The current gold standard for the discrimination of small particle subpopulations, such as EVs and viruses, are high-resolution microscopy-based techniques (354, 355). These techniques are time-consuming, labour-intensive, expensive, and most importantly, can involve manipulations that are harmful to the biological sample. A more promising method for both analytical and physical separation of EVs and viruses takes advantage of a currently existing tool, flow cytometry. Flow cytometry for the analysis of viruses, termed *flow virometry*, has been demonstrated in the analyses of a variety of viruses to date (358). However, most of these works have not effectively discriminated EVs from viral particles. As it requires minimal manipulation of the original sample, flow virometry is uniquely positioned to distinguish EVs from viruses at the analysis stage. This question must be addressed, especially considering the propensity of EVs to incorporate viral nucleic acids, proteins and even entire virions (344). From my work in **Chapter 3**, I identified that while gGag as a type I membrane protein was associating with MLV, the expected type II membrane protein gGag associated with EVs or VLPs (369). These VLPs were devoid of Env but contained significant amounts of Gag. This effectively demonstrated that even infection with MLV, a simple retrovirus, resulted in the production of

VLPs or EVs that contain viral proteins, revealing the complexities of such biological samples. Additional complications arise from virus-mediated incorporation of several host markers often used to identify EVs (117). The multiplexing capacity of flow virometry can be uniquely exploited to make these distinctions. Since the classifications of cellular subpopulations are based on multiple profiles, perhaps viruses and associated particles can be evaluated following the same principles. Thus, the field of virology will benefit immeasurably from the adaptation and optimization of flow virometry.

The optimization of flow virometry for the analysis of MLV in **Chapter 4** was facilitated through a collaboration with Dr. Vera Tang, manager of University of Ottawa's Flow Cytometry Core Facility at the Faculty of Medicine. I had previously assisted Dr. Tang with the demonstration of flow virometry on vaccinia (see Appendix 1), a substantially larger virus relative to MLV (370). In **Chapter 4**, I tested **the hypothesis that MLV Env was a discrimination marker that would specifically incorporate in virions with minor potential for EV association** (115). We expected minimal EV incorporation due to the tightly-controlled and specific association observed between MLV Gag and Env (93, 111).To accomplish this, I took advantage of our laboratory strain of MLV, which contains a GFP within the SU of the Env (371-373). Indeed, this is what we observed. Even transfections of MLV Env alone did not incorporate substantially into EVs. In **Chapter 4**, we did not address any key biological issues of MLV, but we did illustrate how to use a conventional flow cytometer for small particle flow cytometry, to analyze viruses and EVs. In **Chapter 5**, however, I exploited the features of flow virometry to uncover novel biological features of MLV (374). By using flow virometry to discriminate virions from EVs and enumerate them, I these data could be correlated with genomic quantification to calculate the vRNA genome packaging efficiency for MLV. **I hypothesized that this calculated value would represent an efficient genome incorporation, similar to that observed for HIV-1** (355). Unexpectedly, I discovered that the vast majority (80-85%) of MLV particles were lacking a genome pair. This has led me to now **hypothesize that MLV uses defective-interfering particles (DIPs) to act as immunological decoys and suppress viral**

pathology. The specific mechanisms behind MLV DIPs are not yet clear, but it is supported by the deployment of similar DIPs by other RNA viruses (375, 376).

Overall, the four data chapters of this thesis demonstrate the progressive deciphering of multiple facets of complexities within a 'simple' retrovirus. Fascinating examples of convergent evolution are observed between MLV and HIV, such as the protection from restriction factors, secretion of gGag into EVs and the production of DIPs. Improving our understanding of retroviral replication and immune response evasion will empower us against the ongoing battle with HIV and other retroviral threats.

Chapter 2: N-Linked Glycosylation Protects Gammaretroviruses Against Deamination by APOBEC3 Proteins

Preface

This chapter has been previously published as a research article:

Rosales Gerpe MC*, **Renner TM***, Belanger K, Lam C, Aydin H, Langlois MA. 2015. N-linked glycosylation protects gammaretroviruses against deamination by APOBEC3 proteins. J Virol 89:2342-57. https://doi.org/10.1128/JVI.03330-14.

*Co-First Authors.

Author Contributions:

M.C.R.G., T.M.R., K.B., H.A. and M.A.L. contributed to *in vitro* studies, cloning, data analysis and writing the manuscript. T.M.R. conducted *ex vivo* studies. C.L. performed most 3D-PCR analysis.

Abstract

Retroviruses are pathogens with rapid infection cycles that can be a source of disease, genome instability, and tumor development in their hosts. Host intrinsic restriction factors, such as APOBEC3 (A3) proteins, are constitutively expressed and dedicated to interfering with the replication cycle of retroviruses. To survive, propagate, and persist, retroviruses must counteract these restriction factors, often by way of virus genome-encoded accessory proteins. Glycosylated Gag, also called glycosylated Pr80 Gag (gPr80), is a gammaretrovirus genome-encoded protein that inhibits the antiretroviral activity of mouse A3 (mA3). Here we show that gPr80 exerts two distinct inhibitory effects on mA3: one that antagonizes deamination-independent restriction and another one that inhibits its deaminase activity. More specifically, we find that the number of N-glycosylated residues in gPr80 inversely correlates with the sensitivity of a gammaretrovirus to deamination by mouse A3 and also, surprisingly, by human A3G.

Finally, our work highlights that retroviruses which have successfully integrated into the mouse germ line generally express a gPr80 with fewer glycosylated sites than exogenous retroviruses. This observation supports the suggestion that modulation of A3 deamination intensity could be a desirable attribute for retroviruses to increase genetic diversification and avoid immune detection. Overall, we present here the first description of how gammaretroviruses employ posttranslational modification to antagonize and modulate the activity of a host genome-encoded retroviral restriction factor.

Importance

APOBEC3 proteins are host factors that have a major role in protecting humans and other mammals against retroviruses. These enzymes hinder their replication and intensely mutate their DNA, thereby inactivating viral progeny and the spread of infection. Here we describe a newly recognized way in which some retroviruses protect themselves against the mutator activity of APOBEC3 proteins. We show that gammaretroviruses expressing an accessory protein called glycosylated Gag, or gPr80, use the host's posttranslational machinery and, more specifically, N-linked glycosylation as a way to modulate their sensitivity to mutations by APOBEC3 proteins. By carefully controlling the amount of mutations caused by APOBEC3 proteins, gammaretroviruses can find a balance that helps them evolve and persist.

Introduction

Retroviruses are exceptional pathogens in that they permanently modify the genome of their host upon infection. Proviral integration can lead to deleterious insertions in the coding sequence of genes and thereby alters the sequence, stability, splicing, and function of host mRNAs. Additionally, because retroviruses encode an active promoter and enhancer sequences, they can also influence the expression of nearby host genes which can lead to diseases such as cancer (377). In response to this potential threat to their genome, vertebrates express several intrinsic antiretroviral restriction factors that are dedicated to the prevention of infection, replication, release and spread of retroviruses (378).

There are several retroviral restriction factors that operate in parallel in mammals, most notable are BST-2, TRIM5-α, SAMHD1, APOBEC3 (A3) proteins, as well as several other factors that are dependent on an interferon response for expression [reviewed by (379)]. To persist, retroviruses therefore need to concomitantly develop countermeasures to all these restrictions factors, often in the form of accessory proteins or by genetic substitutions at sites of interactions with restriction factors (377, 380, 381). HIV-1 and HIV-2 are amongst the most successful retroviruses in terms of avoiding restriction by the host; whereby BST-2 is defeated by expression of the viral accessory protein Vpu (208, 276), SAMHD1 by Vpx (289, 382), A3 (A3F, A3G, A3D and A3H) by Vif (383), and TRIM5α by the virus evolving target sequences that avoid its capsid being recognized by this restriction factor (384-387). HIV is not the only retrovirus that successfully counteracts the effects of restriction factors. Some murine leukemia viruses (MLVs) have also developed ways to avoid detection and restriction by host retroviral restriction factors (224, 225, 388, 389).

A3 proteins constitute a family of cytidine deaminases that convert deoxycytidines into deoxyuridines in single-stranded DNA (For a review see: (390)). These proteins have a major role in intrinsic defenses against foreign naked DNA, some DNA viruses, retroelements, but mostly against retroviruses. Humans and primates express seven A3 proteins (A3A, A3B, A3C, A3DE, A3F, A3G and A3H), with A3G being the most potent against retroviruses. Deamination occurs primarily on single-stranded minus-strand viral DNA during reverse transcription resulting in C-to-U transition mutations. Newly generated uracils then direct the incorporation of adenines on the plus-strand DNA, thereby generating G-to-A mutations. Intense deamination, or hypermutation, results in inactivating substitutions and premature stop codons in viral genes. A3 proteins can also, in some experimental conditions, inhibit retrovirus infection by multiple deamination-independent mechanisms (234, 240, 241, 244, 391-395).

Mice, in contrast to humans and primates, only express APOBEC3 (mA3) proteins from a single gene (260, 396). Although mA3 is able to potently restrict and hypermutate HIV and SIV in a Vif-independent manner *in vitro* (260, 397), it displays a variable, and often much weaker, ability to restrict murine retroviruses *in vivo* and *in vitro* (319, 398-400). This variability is likely due to mA3's prevailing inability to hypermutate most murine retroviruses and therefore does not genetically inactivate circulating viruses. The most striking example is the Moloney MLV (M-MLV) gammaretrovirus that is modestly restricted by mA3 in absence of detectable G-to-A hypermutation, despite efficiently packaging mA3 into virions (231, 233, 319, 401-403). However, M-MLV becomes much more sensitive to restriction by mA3 when expression of the glycosylated viral Pr80 Gag (gPr80) protein is suppressed (224, 225). This is reportedly caused by gPr80 blocking access of mA3 to the reverse transcription complex in viral cores (225).

The gPr80 protein of M-MLV appears as a multiband protein with an apparent molecular weight ranging between 80 and 100 kDa on SDS-PAGE (294, 404). This glycoprotein is expressed from an alternative in-frame CUG start codon 264 bases upstream of the primary AUG initiation codon of the structural polyprotein $Pr65^{gag}$, resulting in 88 additional amino acids at the N-terminus (297). Glycosylated Pr80 is then further processed by cellular proteases that cleave it into a 40 kDa amino terminal fragment (containing the gPr80 leader polypeptide, viral matrix (MA) and p12 proteins) and 55 kDa carboxy-terminal moiety (containing the viral capsid (CA) and nucleocapsid (NC)) (72, 405). Although the N-terminal 40 kDa moiety can associate with the cell membrane as a type II integral membrane protein, it also present in secreted viral particles (72, 297, 310). While the primary function of gPr80 has not been fully elucidated, its described roles include facilitating late-stage viral release from infected

cells, increasing viral core stability and integrity, and improving viral spreading and pathogenesis *in vivo* (225, 302, 311, 312, 402, 406).

AKV MLV is an endogenous murine gammaretrovirus that is highly similar in genomic sequence to M-MLV. However, AKV, in contrast to M-MLV, is sensitive to deamination by mA3 (319). In this study, we have mapped AKV's sensitivity to deamination and restriction by mA3 and hA3G to the *pr80* gene sequence of the virus. We have identified three putative *N*-linked glycosylation sites in gPr80 of M-MLV, but only two in that of AKV. Our biochemical and cell-based analyses show that the number of glycosylation sites in gPr80 inversely correlates with the level of resistance to deamination. Abolishing gPr80 expression also resulted in hypermutated virus, indicating that gPr80 and the *N*-linked glycans attached to it are together an integral part of the resistance mechanism. Additionally, we demonstrate that genetically modified mouse gammaretroviruses with fewer glycosylated sites in gPr80 are mutated by endogenous mA3 expressed in murine primary splenocytes. However, to our surprise, these mutated viruses remained infectious and capable of replication. These results highlight the important contribution of the host's post-translational modification machinery to helping gammaretroviruses modulate their sensitivity to deamination by mA3. This could constitute a novel strategy used by gammaretroviruses to increase their genetic diversity and avoid immune detection.

Materials and Methods

Mice. All breeding and manipulations performed on animals were in accordance with Ontario Animals for Research Act and were approved by the University of Ottawa Animal Ethics Committee, protocol #ME-133. A3-deficent (mA3 -/-; mA3 KO) mice were backcrossed twelve times to a C57BL/6 background. These mice have the A3 gene disrupted by the insertion of a neomycin selection cassette in exon 3

(407). C57BL/6 (mA3 WT) and mA3 KO mice were maintained in the barrier unit of the University of Ottawa Animal Care Facility.

Cells. Human Embryonic Kidney Epithelium cells (293T) and mouse embryonic fibroblasts (NIH 3T3) were cultured in in HyClone DMEM/High Glucose Medium (supplemented with 10% decomplemented Fetal Bovine Serum (FBS), 100U/mL penicillin and 100µg/mL streptomycin and propagated at 37°C in a 5% CO_2 incubator. Mouse splenocytes were prepared by homogenizing the spleens of neonatal mouse pups 3 to 5 days of age by enforced passage through a 70 µm nylon cell strainer as previously described (319).

Viruses and APOBEC expression vectors. The pMOV-eGFP expression vector encoding replicative M-MLV, the pAKV-NB-eGFP viral plasmid encoding replicative AKV MLV have been described before (319). Expression vectors for the Flag-tagged C57BL/6 allele of mouse APOBEC3 delta-exon 5 (referred throughput as mA3), Flag-tagged human APOBEC expression vectors (hA2 and hA3G), and their respective catalytic mutants (mA3 [E73A] and hA3G [E257A]) have been described before (319, 408). Hybrid viruses were generated by replacing DNA sequences in M-MLV by orthologous sequences from AKV (Fig. 3A). Viruses with point mutations in the *Pr80* gene sequence (for M-MLV: N113Q, N480Q, N505Q; for AKV: N113D, S507N) were made by using the QuickChange XL Site-directed Mutagenesis Kit (Agilent Technologies) according to the manufacturer's specifications. M-MLV [CTA] and AKV [CTA] viruses, which do not express gPr80, were generated by replacing the CTG alternative initiation codon in proviral plasmid DNA by CTA using site-directed mutagenesis.

Viral infections and spreading assays. These assays are graphically presented in Fig. 1.

In vitro (Fig. 1A): To produce replicative viruses, 3 x 10^5 293T cells were seeded in 6-well plates and grown for 24 h until they reached 50-60% confluence. Before transfection, the media was replaced. Co-transfections were done with 800ng of viral expression plasmid and 100ng of A3 expression plasmids, using GeneJuice transfection agent (Novagen) according to manufacturer's instructions. Virus-containing supernatant was harvested 48 h after transfection. Twenty-four hours prior to infection, 1 x 10^5 of NIH 3T3 target cells were seeded in 12-well plates and incubated for 24 h. At the time of the infection, NIH 3T3 cell media was replaced by fresh decomplemented media containing Polybrene (Sigma-Aldrich) at a concentration of 8µg/mL. Virus-containing supernatants were cleared by centrifugation and the concentration of viral p30 CA protein was evaluated by ELISA (QuickTiter™ ELISA Kit, Cell Biolabs Inc.). The amount of p30 CA protein yielding an MOI of 1 for virus produced in presence of A2 was calculated by infection titration. Similar amounts of p30 protein were then used for virus produced in presence of mA3, hA3G and their catalytic mutants. The cells were spin-infected at 800xg for 1h. Infected target cells were grown for 24-, 48- and 72 h before being harvested and split into two fractions: one for eGFP reporter gene expression using the Cyan ADP flow cytometer (Beckman Coulter), the other for mutation analysis by HyperHRM, 3D-PCR and direct DNA sequencing.

Ex vivo (Fig. 1B): Viruses harvested from stably infected NIH 3T3 cells were used as stock. One hour prior to infection, activated splenocytes were counted and seeded in activation media (319). Splenocytes were spin-infected at an MOI of 0.2. 24 h post-infection, infected cells were washed with 1X PBS pH 7.4, resuspended in complete RPMI with 10µg of LPS and incubated for 96 h for virus production. Virus-containing supernatants were passed through 0.45µm cartridge filters and viral titers (TU/mL) were determined on NIH 3T3 cells by limiting dilution using flow cytometry. The secondary infections

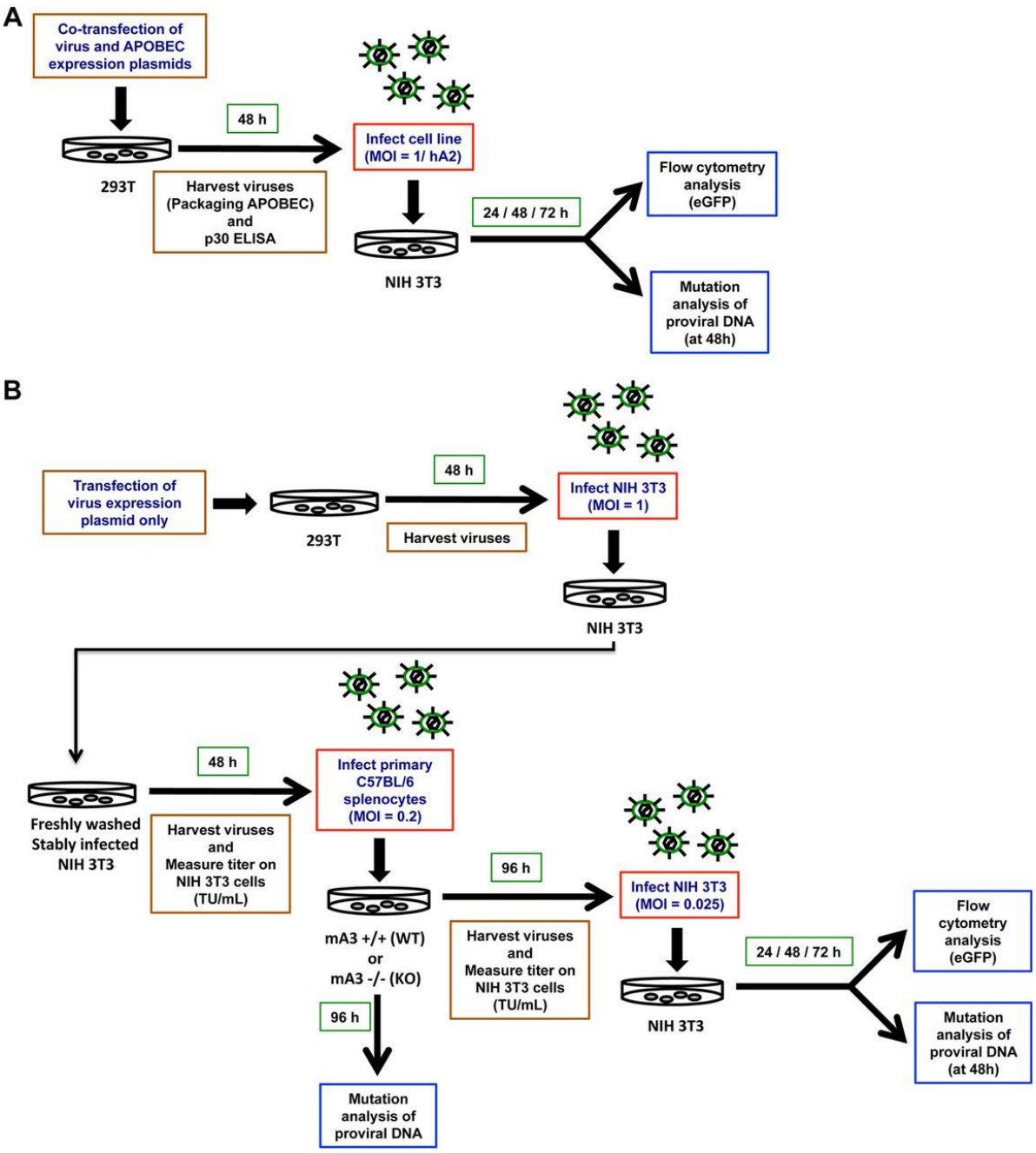

Figure 2.1. Flow chart of the infection assays.

(A) *In vitro* viral spreading assay. Viruses were produced by plasmid co-transfection in 293T cells and were harvested after 48h. NIH 3T3 cells were infected with a MOI of 1 in respect to control viruses produced in presence of hA2. Infection was measured at 24 h intervals for 72h. (B) *Ex vivo* viral spreading assay in primary murine splenocytes. Stably infected NIH 3T3 cells were first generated. Viruses released from these cells were then used to infect primary murine splenocytes. Splenocytes from wild type (WT) and mA3 -/- (KO) C57BL/6 mice were infected with a MOI of 0.2. Cells were washed 24 h after infection and viruses were harvested 96 h later and used to infect NIH 3T3 cells with a MOI of 0.025. Infection was monitored every 24 h for 72 h.

(viral spreading assays) were performed on NIH 3T3 cells, using an MOI of 0.025. Cells were analyzed by flow cytometry for eGFP expression at 24, 48 and 72 h post-infection. Genomic DNA was extracted from infected splenocytes 96 h post-wash, and from the NIH 3T3 cells at each time point.

APOBEC viral packaging assays. Virus-containing supernatants were filtered and then purified by ultracentrifugation through a sucrose cushion as previously described (392). Viral lysates were then processed for immunoblot analysis

Western blotting. Details on sample preparations can be found here (392). Blots were probed with anti-FLAG (Sigma-Aldrich), anti β-tubulin (Abcam) and anti-p30 (ATCC, clone R187). Detection of M-MLV-expressed gPr80 in was performed using an anti-$p30^{CA}$ antibody kindly provided by Dr. Hung Fan (University of California, Irvine). Detection of recombinant gPr80-V5 was performed using an anti-V5 polyclonal antibody (Sigma #V8137).

3D-PCR analysis. 3D-PCR was performed in a two-step protocol using PrimeSTAR high fidelity polymerase (Takara). A first-round PCR was performed to amplify a 717bp eGFP amplicon using primers GFP-717 FWD and GFP-717 REV (409). A second-round gradient PCR targeting a 279 bp nested fragment within the eGFP sequence was then performed using primers R279-FWD and GFP-REV. PCR cycles were: 94°C for 50s, followed by 30 cycles of a denaturation gradient from 91.1-88.0°C for 50s, annealing at 56°C for 30s, and an extension at 72°C for 1min, with a final extension of 72°C for 5min. Samples that amplified at the lowest denaturation temperature were column-purified, cloned using TA cloning (Promega) and sequenced (Nanuq Sequencing Facility at McGill University and Genome Quebec

Innovation Center). Deamination intensity graphs were generated by illustrating the number of amplicons that can be detected in a 7-well 3D-PCR gradient set. Confirmation of the presence of hypermutation in an A3G or mA3 context was done by DNA sequencing (Table 1). Our experimental conditions were optimized so that 3D-PCR performed on integrated proviral DNA of virus alone or virus produced in presence of catalytically inactive A3 proteins consistently yielded amplification only at the 2 highest denaturing temperatures of the gradient.

HyperHRM analysis. HyperHRM analyses were carried out as previously published (409). Briefly, proviral DNA was amplified from the gDNA of virus-infected cells using primers R648-FWD and GFP-REV to generate a 648bp amplicon. Amplicons derived from each infection condition were then cloned and colonies positive for an insert were diluted in 250µl of water, of which 8µl were used for HRM analysis in a 96-well plate format. To generate standard curves for mutation quantification purposes, bacterial clones containing defined numbers of G-to-A mutations were used. Amplification by qPCR was then carried out and immediately followed by a melting curve analysis in which DNA amplicons were gradually heated from 72°C to 95°C and fluorescence values were acquired at 0.025ºC intervals. Determination of the number of mutations in each clone was achieved by applying the algorithm previously described (409). Unmutated clones were excluded from the calculation of mutation frequency of Tables 1 and 2. DNA sequencing of randomly selected proviral clones was performed as quality control and to ensure that the results were not biased by clonal amplification of a unique sequence (data not shown).

Table 2.1. Mutation analysis of proviral DNA by direct sequencing

Virus	3D-PCR band number sequenced	Clones[a] analyzed	Clones[a] with G-to-A mutations	Total mutations[b]		Mutations in a 5'Y**C** context (%)
				G-to-A	Other	
M-MLV	2	5	1	1	1	100
M-MLV [N113Q]	3	6	6	31	2	71
M-MLV [N505Q]	3	5	5	15	1	75
M-MLV [N113Q/N505Q]	4	5	5	41	0	59
M-MLV [CTA]	4	5	4	26	2	69
Hybrid 1	2	5	1	1	3	100
Hybrid 2	3	5	5	9	4	67
Hybrid 3	3	5	4	12	2	75
AKV	3	5	5	30	0	67
AKV [N113D]	4	5	5	34	0	77
AKV [S507N]	2	8	3	3	2	67
AKV [CTA]	4	5	5	27	0	70
Spl.: M-MLV	3	10	7	7	2	29
Spl.: M-MLV [N113Q/N505Q]	4	8	8	59	3	98
Spl.: AKV	4	11	10	27	4	74
Spl.: AKV [S507N]	3	6	2	2	2	50
3T3: M-MLV	3	8	0	0	4	0
3T3: M-MLV [N113Q/N505Q]	4	7	6	18	3	78
3T3: AKV	4	25	23	62	9	84
3T3: AKV [S507N]	3	12	6	6	7	84

[a] The clones contain the first 279 bp of the eGFP reporter gene. Viruses were produced in the presence of transfected mA3 or endogenous mA3 in murine splenocytes. Clones displaying identical deamination profiles were excluded from the calculations. Spl., proviral sequences from infected wild-type C57BL/6 mouse splenocytes; 3T3, proviral sequences from NIH 3T3 cells infected with viruses released from splenocytes. [b] Mutations compiled on the coding strand of the proviral DNA.

Results

Murine gammaretroviruses display different sensitivities to restriction and deamination by APOBEC3. M-MLV and AKV are two murine gammaretroviruses with very high sequence identity, but with strikingly different sensitivities to restriction and deamination by mA3. Here we performed infection assays with the two viruses being produced in cells expressing hA3G, its catalytic inactive mutant (hA3G [E259Q]), mA3, and its catalytic mutant (mA3 [E73A]). Human APOBEC2 (hA2) was used as a negative control because it neither deaminates nor restricts these viruses (392). Viruses were produced by co-transfection in 293T cells, harvested and normalized for p30 content by ELISA (Fig. 1A). The cell expression and virion packaging efficiency of all APOBEC proteins was monitored and comparable (Fig. 2A). Target NIH 3T3 cells were then infected at an MOI of 1 in respect to the hA2 control, and infection was assessed by measuring eGFP reporter gene expression over 72 h (Fig. 2B). All wild type A3 proteins tested had an effect on the infection of both viruses at the 24 h time point at varying degrees. This is the result of the well-documented deamination-independent restriction that is especially prominent in tissue culture assays (Fig. 2B). After 48 h, and likely after a second cycle of viral infection, both viruses remained completely restricted by hA3G but proliferated when packaged with catalytic inactive hA3G [E259Q] and mA3 [E73A]. In contrast, mA3 delayed the ability of AKV to spread, as can be observed by a downward inflection in the growth curve (Fig. 2B) and a nearly 45% reduction in the level of infection compared to that achieved for M-MLV at 48 h (Fig. 2C).

We next looked at the intensity of cytidine deamination in integrated provirus DNA. Here we used 3D-PCR which is a method used to selectively amplify hypermutated DNA sequences based on the premise of reduced PCR amplicon melting temperatures as a consequence of A/T base enrichment due to the deamination cytosines into uracils (410). 3D-PCR, however, does not provide information on the

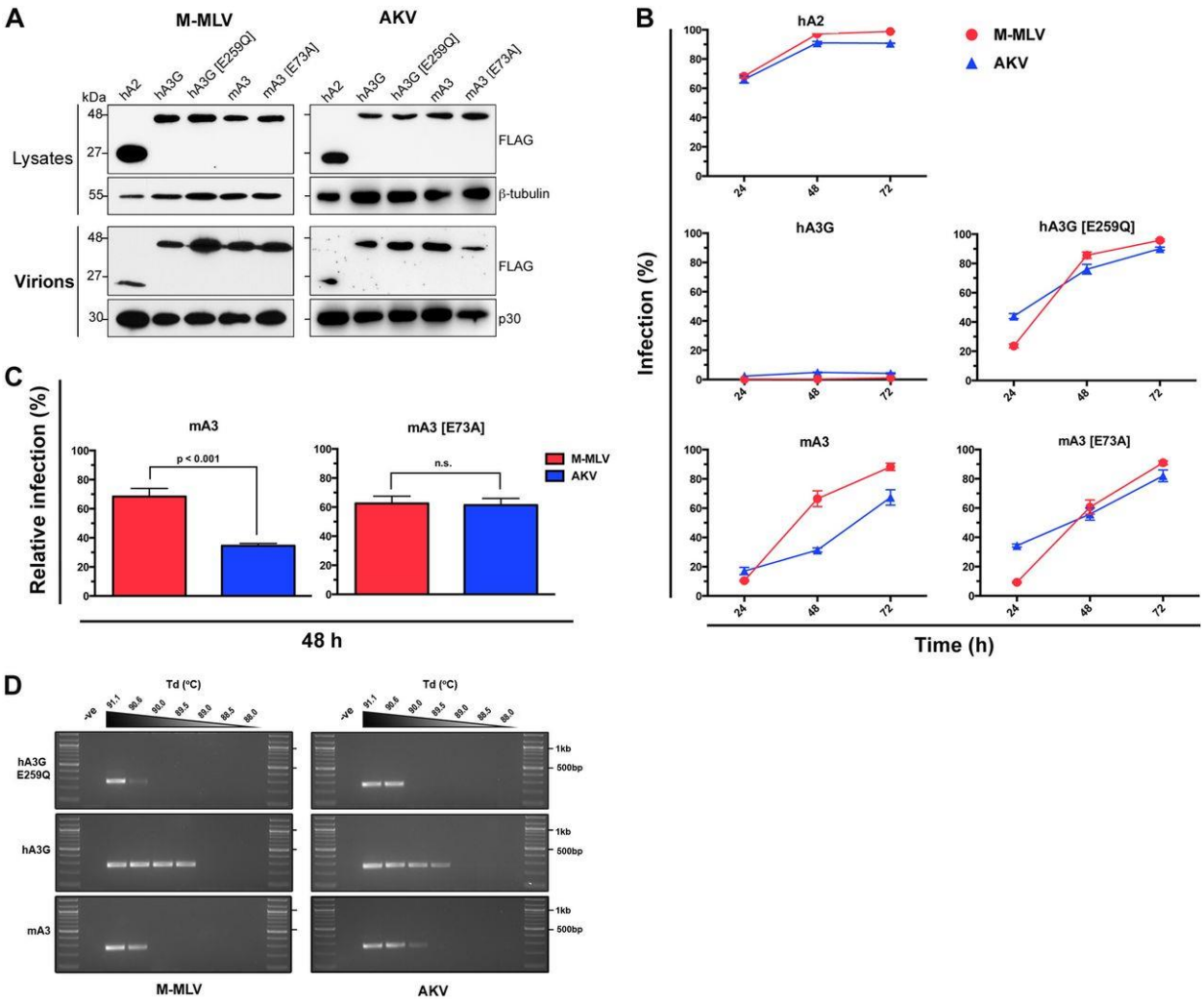

Figure 2.2. Sensitivity of M-MLV and AKV to deamination and restriction by A3 proteins.

(A) (Top) Expression of the various APOBEC proteins in lysates of cotransfected 293T cells used to produce M-MLV and AKV was analyzed; (bottom) virions harvested from the culture supernatant of 293T cells were analyzed for the efficiency of packaging of the various APOBEC proteins. (B) Analysis of the spread of M-MLV and AKV infection produced in the presence of APOBEC proteins, represented as the percentage of cells expressing the eGFP reporter at the various time points after infection. Infection results are from at least three independent transfections with triplicate infection values for each. Results are presented as the mean level of infection ± standard deviation. (C) Comparison of the relative infection of M-MLV and AKV produced in the presence of mA3 or mA3 (E73A) at 48 h postinfection. Values were normalized to those for infection with virus produced in the presence of hA2 at 48 h. Error bars represent standard deviations. Statistical significance was determined using a two-tailed unpaired Student t test; P values are indicated on the graph. n.s., not significant. (D) 3D-PCR analysis performed on genomic DNA extracted from infected NIH 3T3 cells from the 48-h time point for M-MLV and AKV. Representative gels from 3 independent assays are shown. Td, denaturing temperature; −ve, negative.

proportion of sequences mutated in a population. It is a method that makes a qualitative assessment of how intensely viral sequences are hypermutated. We optimized our assays so that unmutated DNA (virus alone) amplified only at the two highest melting temperatures of the gradient out of a possibility of seven temperatures selected (Fig. 2D). Positive amplification at lower melting temperatures is indicative of hypermutated proviral DNA sequences. In our conditions, the threshold for reliable mutation detection by 3D-PCR is 3 or more G-to-A/C-to-T mutations per 279bp sequence (409). For positive amplicons, presence of transition mutations in an A3 deamination context (5'-C**C** or 5'-T**C**) was confirmed by DNA sequencing (Table 1). 3D-PCR assays were repeated at least 3 times from independent infection assays, representative gels are presented. Our results show that hA3G deaminates both M-MLV and AKV at the same intensity, meaning that the most intensely mutated sequences have similar numbers of G-to-A mutations (Fig. 2D). Catalytic inactive A3G [E259Q] was used as a negative control and only displays amplification in the first two conditions, similarly to virus produced alone or with hA2 (data not shown). On the other hand, mA3 weakly hypermutated AKV as judged by the presence of amplification in the 3rd lane and did not at all hypermutate M-MLV.

Resistance to deamination maps to the gPr80 accessory protein. In order to identify the regions of AKV that are responsible for rendering the virus sensitive to deamination by mA3, we generated three hybrid viruses by progressively replacing the proviral DNA of M-MLV with that of AKV (Fig. 3A). We then performed an infection assay under the same conditions described above. We found that A3 protein encapsidation was similar for all hybrid viruses (data not shown). Viral infection assays showed that hybrid 1, containing an AKV segment spanning from the R region to the N terminus of Gag, spread similarly to wild-type M-MLV (Fig. 3B). Hybrids 2 and 3, however, displayed a delay in spreading at the 48-h time point, similar to that seen for AKV, with, respectively, 18% and 24% reductions in the levels

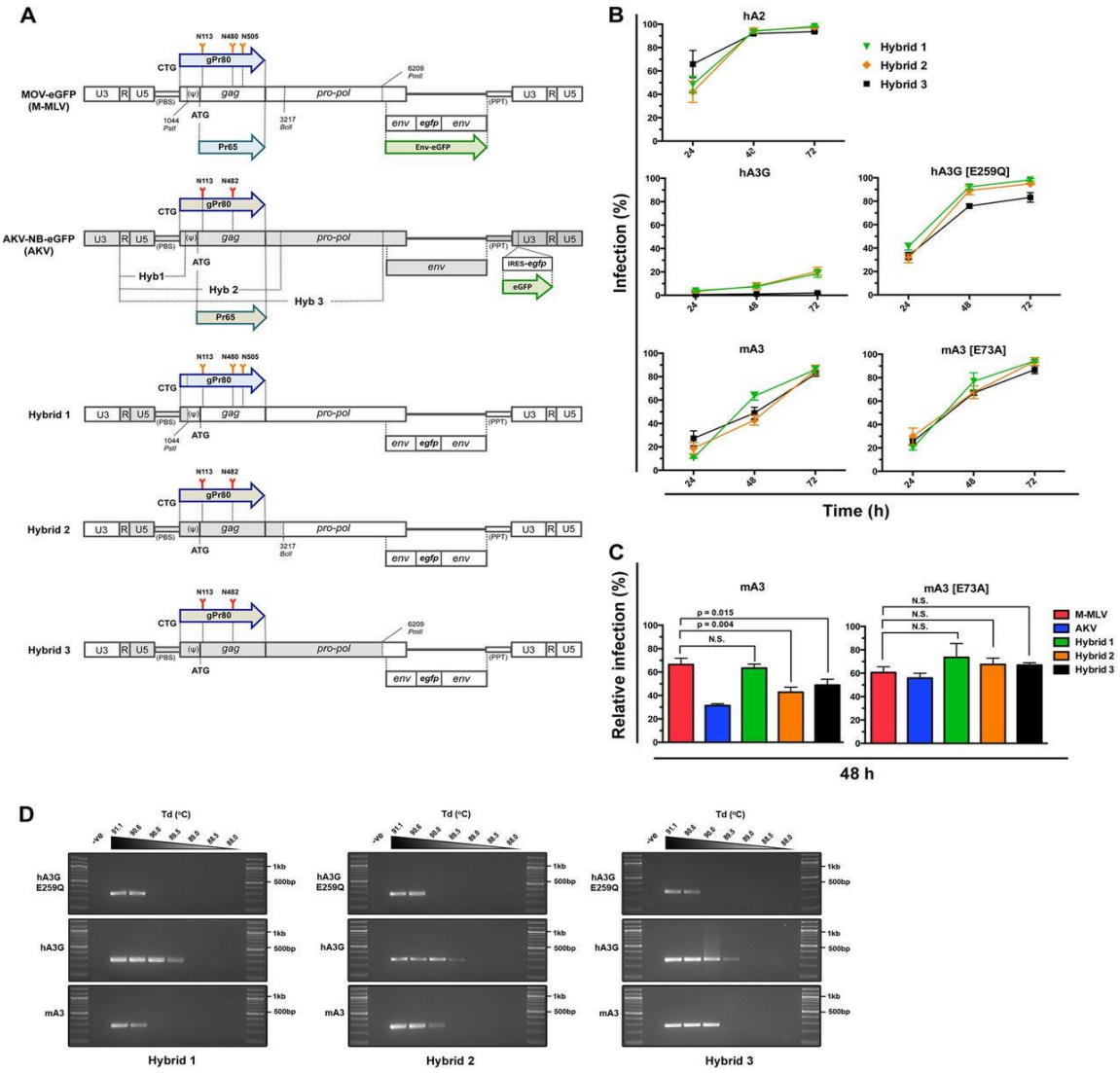

Figure 2.3. M-MLV-AKV hybrid viruses reveal that deamination-resistance maps to the gag gene.

(A) Schematic illustrations of the M-MLV, AKV, and hybrid proviruses. The segments used to construct the three hybrid viruses are indicated. Hybrid viruses are composed of M-MLV into which orthologous segments of AKV have been inserted. Hyb, hybrid; IRES, internal ribosome entry site; PBS, primer binding site; PPT, polypurine tract. (B) Analysis of spread of hybrid virus infection produced in the presence of the various A3 proteins. Infection results are from at least three independent transfections with triplicate infection values for each. Results are presented as the mean ± standard deviation. (C) Comparison of the level of infection with the hybrid viruses relative to that with M-MLV and AKV produced in the presence of mA3 or mA3 (E73A) at 48 h postinfection. Values were normalized individually to the value for infection with virus produced in the presence of hA2 at 48 h. Error bars represent standard deviations. Statistical significance was determined using a two-tailed unpaired Student t test; P values are indicated on the graph. N.S., not significant. (D) 3D-PCR analysis performed on genomic DNA extracted from infected NIH 3T3 cells from the 48-h time point. Representative gels from 3 independent assays are shown.

of infection relative to that for M-MLV being seen (Fig. 3C). Catalytically inactive mutants A3G (E259Q) and mA3 (E73A) did not have a significant effect on hybrid virus spread (Fig. 3B and 3C). 3D-PCR analysis performed on infected target cells revealed that hA3G hypermutated all three hybrids with the same intensity, while mA3 was able to hypermutate only hybrids 2 and 3 to levels similar to those for AKV (Fig. 3D).

The common DNA segment of hybrids 2 and 3 maps to the *gag* gene of AKV that includes sequences coding for both the gPr80 and Pr65 polyproteins. Because the spread curves and deamination intensities are similar between both hybrids, this led us to hypothesize that all determinants responsible for the contrasting phenotypes between M-MLV and AKV are located within this region. Two recent studies have highlighted the involvement of the gPr80 gag protein in resisting restriction by mA3 (224, 225). To distinguish if resistance to deamination was conferred by elements within the Pr65 or gPr80 polyproteins, we generated viral mutants, termed CTA mutants, that do not express gPr80 because their CTG initiation codon was replaced by a CTA trinucleotide (Fig. 4). Packaging of A3 proteins into these mutant viruses was similar to that for their WT counterparts (Fig. 4A). Restriction assays and growth curves of both viruses showed that they had similar profiles that closely resembled the profile for AKV (Fig. 4B and C). However, there was a small but noticeable decrease in infectivity of these mutants compared to that of the WT parental viruses. M-MLV and AKV produced with A2 infected 65 to 70% of the cell population after 24 h (Fig. 2B). With the CTA mutant viruses, this infection was reduced to 40% when the same amount of input virus (as measured by p30 ELISA) was used (Fig. 4B). Although CTA and CTG codons both code for leucine, the CTG codon in the viral RNA is located in the stem of one of the major stem-loops involved in packaging the viral RNA dimer (411). Hypermutation analysis of the M-MLV CTA and AKV CTA mutants revealed an increase in sensitivity to hypermutation by both mA3 and hA3G (Fig. 4D). This therefore allowed us to exclude the possibility of any potential roles for elements within Pr65 to be the cause for the resistance to deamination and to focus our attention on gPr80.

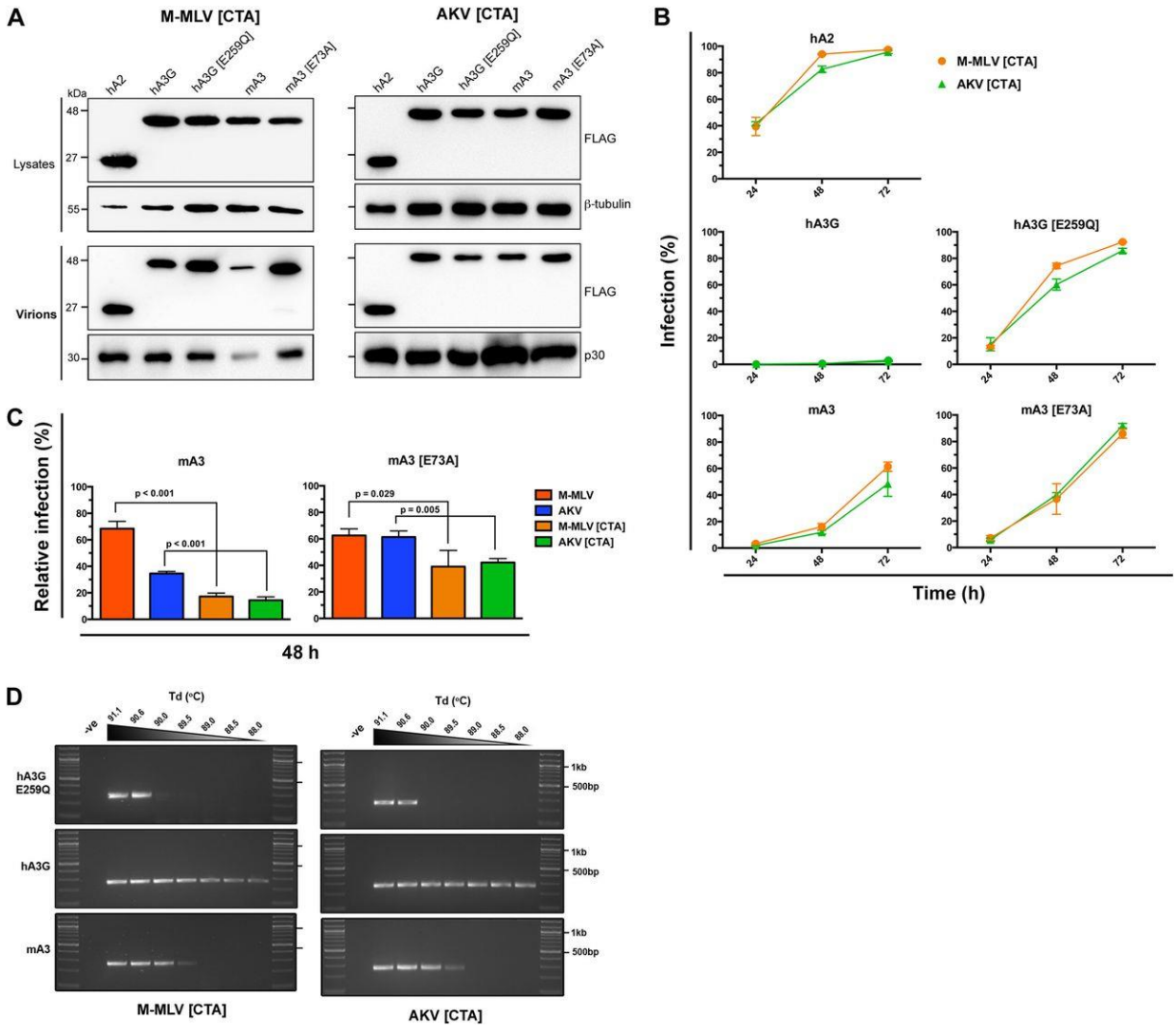

Figure 2.4. Analysis M-MLV and AKV mutants that do not express gPr80.

Analysis of M-MLV and AKV mutants that do not express gPr80. (A) (Top) Western blots showing the expression of the various APOBEC proteins in lysates of cotransfected 293T cells used to produce M-MLV (CTA) and AKV (CTA) mutant viruses are shown; (bottom) viruses (virions) harvested from the culture supernatant of 293T cells were analyzed for the efficiency of packaging of the various APOBEC proteins. (B) Analysis of the spread of infection of mutant viruses produced in the presence of the various A3 proteins. Infection results are from at least three independent transfections with triplicate infection values for each. Results are presented as the mean ± standard deviation. (C) Comparison of the level of infection with the CTA mutant viruses relative to that with M-MLV and AKV produced in the presence of mA3 or mA3 (E73A) at 48 h postinfection. Values were normalized individually to the values for infection with virus produced in the presence of hA2 at 48 h. Error bars represent standard deviations. Statistical significance was determined using a two-tailed unpaired Student t test; P values are indicated on the graph. (D) 3D-PCR analysis performed on genomic DNA extracted from infected NIH 3T3 cells from the 48-h time point for the various viruses. Representative gels from 3 independent assays are shown.

Three N-linked glycosylation sites in M-MLV gPr80 are required for complete resistance to deamination. Because the amino acid sequences of the gPr80 proteins of M-MLV and AKV are highly similar, we focused our attention on differences in the *N*-linked glycosylation patterns of the proteins (Fig. 3). We carried out an *in silico* analysis of the gPr80 proteins of both viruses using the NetNGlyc server to identify putative glycosylation sites within a Asn-Xaa-Ser/Thr, (Xaa $\neq$ Pro) sequon. We identified 3 possible glycosylation sites in M-MLV gPr80 (N113, N480 and N505), but only two in that of AKV (N113 and N482). N113 is located in the matrix (MA), while N480/N482 and N505 are located in the capsid (CA).

Using site-directed mutagenesis, we generated point mutants for each of the predicted glycosylated amino acids of gPr80 of M-MLV and AKV. We also introduced an additional N-linked glycosylated site at position S507 of AKV (AKV [S507N]), which is in a sequon favorable for glycosylation. The asparagine-to-aspartic acid substitutions chosen remove the glycosylated site, while they introduce a chemically conservative mutation. It should also be noted that changes in the gPr80 sequence downstream of amino acid 88 are also reflected in the Pr65 Gag protein. We also generated double and triple glycosylation mutants when appropriate. Western blot analyses of transfected cell extracts clearly show that the apparent molecular mass of gPr80 shifts according to the number of putative glycosylated sites mutated (Fig. 5A to C). Glycosidase treatment of the extracts reveals a gPr80 band lower than that of the gPr80 band of the M-MLV (N113Q/N505Q) double mutant, which indicates that amino acid N480 is also likely glycosylated, as predicted (Fig. 5A and B). The M-MLV (N113Q/N480Q/N505Q) triple glycosylation mutant demonstrated a band for gPr80 at the same height as that in the glycosidase-treated sample (Fig. 5C). Western blot analysis of AKV gPr80 showed that the S507N mutation increases the size of the band, suggesting that N-linked glycosylation at this site was indeed restored (Fig. 5B).

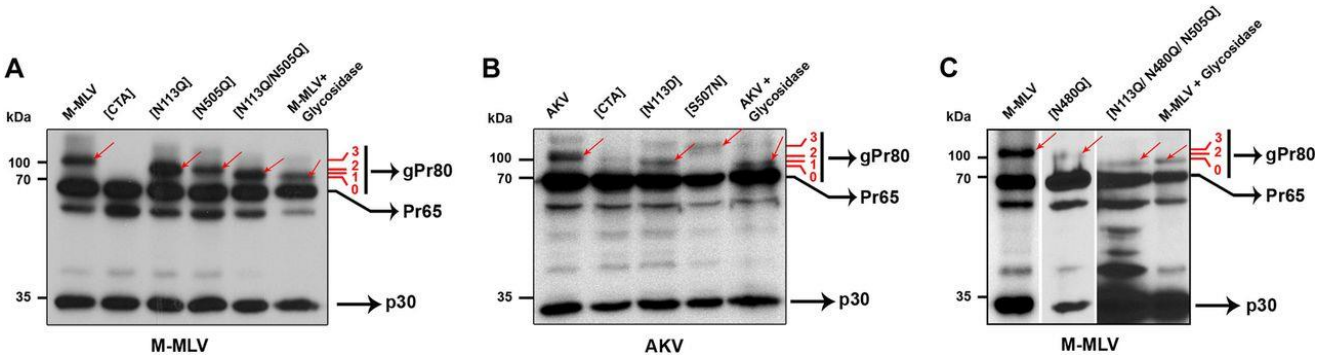

Figure 2.5. Identification of N-linked glycosylated sites in M-MLV and AKV.

(A - C) Western blot analysis of transfected cell extracts showing altered migration patterns caused by *N*-linked glycosylation. The last lane of each blot shows either M-MLV or AKV infected cell extracts treated with glycosidase. The gPr80 protein band is indicated for each virus by red arrows.

Restriction assays with the M-MLV single point mutants and the N113Q/N505Q double mutant clearly showed a delay in infection spread at 48 h with mA3 (Fig. 6A). The N113Q/N505Q double mutant was about twice as sensitive to mA3 restriction as the single point mutants (Fig. 6C). Mutant M-MLVs produced with mA3 (E73A) showed little or no difference in infectivity compared to that of the wild-type virus (Fig. 6C). Restoring glycosylation at position S507 of AKV increased the spreading kinetics to resemble that of mA3-resistant M-MLV (Fig. 6B); however, the N113D substitution did not render the virus more sensitive to mA3 restriction (Fig. 6D). Viral mutants M-MLV (N480Q) and AKV (N482D) displayed very poor infectivity (less than 2%), despite being efficiently released from the cells, as judged by p30 ELISA (data not shown). For this reason, these mutants were not analyzed further.

Although the sequential mutation of glycosylated residues in gPr80 had an overall modest effect on the sensitivity to restriction by mA3, a more pronounced impact on hypermutation could clearly be observed. Both mA3 and hA3G mutated the M-MLV and AKV mutants with an intensity higher than that for their WT counterparts (Fig. 6E and F). All mutants with N-to-Q point mutations of M-MLV gPr80 became more sensitive to deamination; this effect was slightly increased in the M-MLV (N113Q/N505Q) double mutant and the AKV (N113D) mutant. AKV (S507N), which had three glycosylated sites, became resistant to deamination (Fig. 6F).

To further characterize the intensity and frequency of deamination in proviral sequences, we performed mutation analyses on individual clones isolated from infected cells. We used HyperHRM, which is a high throughput method we developed to quantify the number of A3-induced mutations in a PCR amplicon (409). Confirming the 3D-PCR data, we found that there was an inverse correlation between the number of glycosylated residues in gPr80 and the proportion of hypermutated sequences in a specific virus (Fig. 7A, 7B and Table 2). Our data also show that the intensity of hypermutation increases when fewer glycosylated sites are present in either virus.

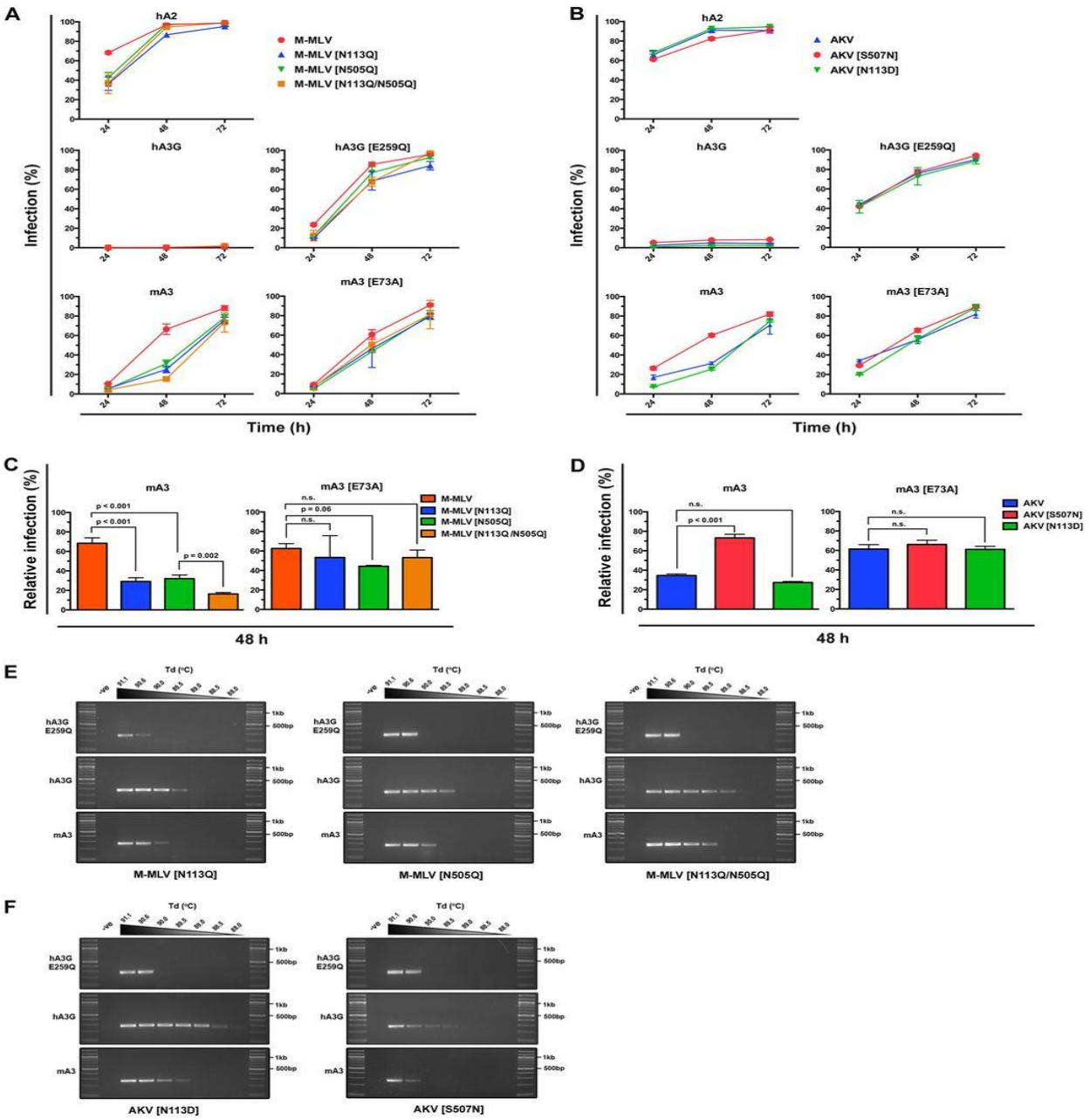

Figure 2.6. Intensity of gPr80 glycosylation correlates with sensitivity to deamination by mA3.

(A and B) Analysis of spread of infection of glycosylation mutants of M-MLV (A) and AKV (B) coproduced with various A3 proteins. (C and D) Comparison of the infection with the mutant viruses relative to that with M-MLV (C) and AKV (D) produced in the presence of mA3 or mA3 (E73A) at 48 h postinfection. Values were normalized individually to those for infection with virus produced in the presence of hA2 at 48 h. Error bars represent standard deviations. Statistical significance was determined using a two-tailed unpaired Student t test; P values are indicated on the graphs. n.s., not significant. (E and F) 3D-PCR analysis performed on genomic DNA extracted from infected NIH 3T3 cells from the 48-h time point for glycosylation mutants of M-MLV (E) and AKV (F).

gPr80 antagonizes both arms of mA3 restriction. Having identified M-MLV mutants that are sensitive to deamination, we next wanted to evaluate how gPr80 glycosylation affects deamination-independent restriction by mA3. Here we normalized the infection data at the 48-h time point to those for the hA2 control independently for each virus set: M-MLV (Fig. 7C) and AKV (Fig. 7D). We found that viruses were more restricted by catalytically inactive mA3 (E73A) when the gPr80 protein had fewer glycosylated sites or was not expressed altogether. The increased sensitivity to restriction of the CTA mutant viruses by mA3 (E73A) could reflect the protective effect of N480 glycosylation. Altogether, these results clearly show that N-linked glycosylation of gPr80 prevents restriction by deamination and also by deamination-independent mechanisms.

Endogenous mA3 inhibits MLV infection but is also a source of genetic diversification. Two reports have already established that the antiretroviral activity of mA3 is inhibited by gPr80 *in vivo* (224, 225). These studies were carried out by comparing the infectivity of deamination-resistant MLV strains with coisogenic strains unable to either express or produce a full-length gPr80 protein. Here we asked whether endogenous levels of mA3 are sufficient to hypermutate deamination-sensitive MLVs so as to affect viral fitness and replication of released viruses. We performed our experiments only with MLVs that expressed gPr80 in order to measure the direct contribution of *N*-linked glycosylation to the resistance.

We isolated splenocytes from wt (mA3 WT) or mA3-deficient (mA3 KO) C57BL/6 neonatal mice. The splenocytes were cultured, activated and then infected with a similar MOI with viruses that were produced in absence of mA3 in NIH 3T3 cells (Fig. 1B). The infectious titer of the viruses released by the splenocytes was assessed 96 h later as a measure of transducing units per mL of supernatant harvested

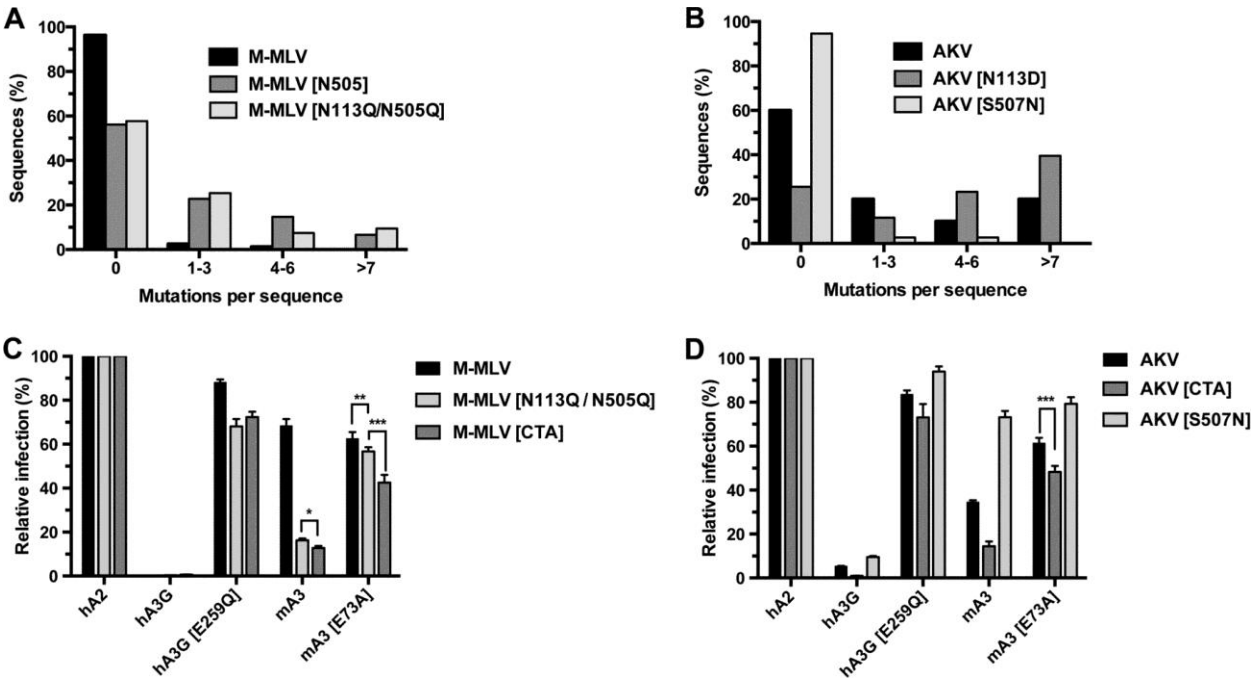

Figure 2.7. N-linked glycosylation inhibits deamination and deamination-independent restriction.

(A and B) Analysis of mutation intensities in proviral DNA by HyperHRM analysis. The histograms depict the proportion of total sequences containing the indicated number of mutations. The results of clone analysis are presented in Table 2. (C and D) Relative infection depicting the effect of gPr80 mutants on virus sensitivity to restriction at 48 h postinfection. Infection levels from experiments whose results are presented in Fig. 2B, 4B, and 6A and B were normalized to those for hA2 for each virus. Values presented are the means ± SEMs from three independent transfection experiments with triplicate infection samples. The Student unpaired t test was performed to assess statistical significance: *, P = 0.05; **, P = 0.19; ***, P = 0.02.

Table 2.2. HyperHRM analysis of the editing of M-MLV, AKV and glycosylation mutants by mA3

Virus	Clones analyzed	Number of mutated clones	Clones mutated (%)	Total number of mutations	Predicted G-to-A mutation frequency (mutations/kb)
M-MLV	80	3	4	9	0.17
M-MLV [N505Q]	66	29	44	117	2.74
M-MLV [N113Q/N505Q]	71	30	42	145	3.15
AKV	50	20	40	100	3.09
AKV [N113D]	43	32	74	232	8.33
AKV [S507N]	37	2	5	5	0.16

(Table 3). M-MLV was generally more efficient at replicating in these splenocytes than AKV. Differences in titers were also presented as relative infectivity to better illustrate that endogenous mA3 had a similarly potent effect at reducing the infectious titers of all viruses, including those resistant to deamination (Fig. 8A). This indicates that deamination by endogenous mA3 has little effect on viral restriction under these conditions.

To ensure that hypermutation of proviral DNA did occur in the WT splenocytes, 3D-PCR was carried out on proviral DNA from splenocytes at 96 h postinfection (Fig. 8B). Hypermutated viral sequences were detected only in WT splenocytes at various intensities for all viruses. Surprisingly, M-MLV and AKV (S507N) also showed evidence of hypermutation caused by mA3, but the intensity and frequency of the mutations were very low (Table 1). These data were also supported by HyperHRM analysis of individual clones, showing that they contained several transition mutations (Fig. 8C and Table 4).

To address whether the replicative fitness of MLVs sensitive to deamination was affected by being produced in splenocytes expressing mA3, we then used these viruses to infect NIH 3T3 cells with an MOI of 0.025. We monitored their spread in culture every 24 h for 72 h. These assays revealed that the pool of infectious viruses released from WT splenocytes did not exhibit a proliferation efficiency different from that of viruses released from mA3-KO cells (Fig. 8D). These results were confirmed by statistical analyses indicating that the slopes of the viral spreading curves were similar for viruses produced in WT or KO splenocytes (data not shown). We also analyzed proviral DNA sequences amplified from infected NIH 3T3 cells. We found by 3D-PCR clear evidence of hypermutation in viruses originating from WT splenocytes (Fig. 8E and Table 1). HyperHRM analysis revealed that the intensity and frequency of the transition mutations were, however, lower (Fig. 8F and Table 4). The mutation

Table 2.3. Titers of gammaretroviruses released from splenocytes

Virus	**Source**	**Virus Titer (TU/ mL) x10^5 ***
M-MLV		
	WT	0.047 ± 0.006
	KO	5.099 ± 1.964
M-MLV [N113Q/N505Q]		
	WT	0.037 ± 0.007
	KO	3.896 ± 1.740
AKV		
	WT	0.025 ± 0.005
	KO	1.796 ± 0.615
AKV [S507N]		
	WT	0.012 ± 0.002
	KO	0.302 ± 0.053

*TU: transducing units; WT: wild type C57BL/6 splenocytes; KO: mA3 -/- C57BL/6 splenocytes. Values represent the mean of triplicate infection values ± standard deviation; KO mice, n = 5; WT mice n = 6.

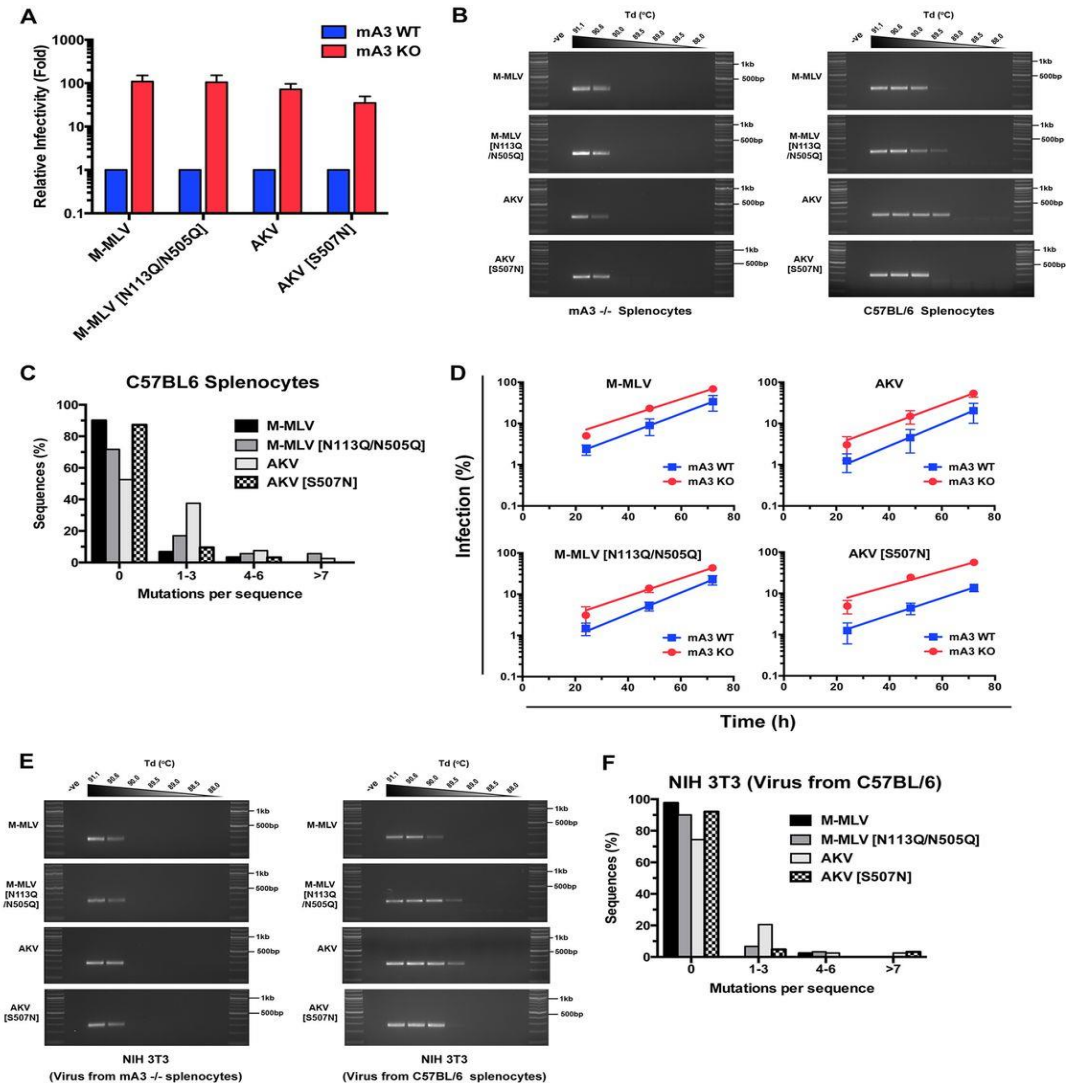

Figure 2.8. gPr80 glycosylation levels influence the intensity of deamination by endogenous mA3 expressed in mouse splenocytes.

(A) Relative infectivity of viruses released from infected splenocytes. The viral titers used to generate the figure are presented in Table 3. (B) 3D-PCR analysis performed on genomic DNA extracted from infected KO (left) or WT (right) C57BL/6 splenocytes. Representative gels from 3 independent assays are shown. (C) Analysis by HyperHRM of mutation intensities in proviral DNA isolated from infected C57BL/6 splenocytes. The histograms depict the proportion of total sequences containing the indicated number of mutations. The results of clone analysis are presented in Table 2. (D) Infection spread in NIH 3T3 cells. Cells were infected with an MOI of 0.2 with viruses released from the splenocytes for which the results are depicted in panel A. Infection was measured every 24 h for 72 h. The graphs represent nonlinear regression curves of the infection. Results are presented as the mean level of infection ± standard deviation. (E) 3D-PCR analysis performed on genomic DNA extracted from infected NIH 3T3 cells. Representative gels from 3 independent assays are shown. (F) Analysis by HyperHRM of mutation intensities in proviral DNA isolated from infected NIH 3T3 cells.

Table 2.4. HyperHRM analysis of the editing of M-MLV, AKV and glycosylation mutants by endogenous mA3 expressed in C57BL/6 splenocytes

Infected cells	Virus	Clones analyzed	Number of mutated clones	Clones mutated (%)	Total number of mutations	Predicted G-to-A mutation frequency (mutations/kb)
WT Splenocytes						
	M-MLV	81	12	15	38	0.73
	M-MLV [N113Q/N505Q]	53	15	28	59	1.72
	AKV	40	19	48	52	2.00
	AKV [S507N]	63	8	13	21	0.51
NIH 3T3						
	M-MLV	42	1	3	4	0.15
	M-MLV [N113Q/N505Q]	60	6	10	16	0.41
	AKV	39	10	26	30	1.19
	AKV [S507N]	63	5	8	21	0.51

HyperHRM was performed on gDNA from infected WT splenocytes 96 h after infection. NIH 3T3 cells were infected with viruses released from WT splenocytes. HyperHRM was performed 48 hours later.

frequency for AKV dropped from 2 mutations per kb in splenocytes to 1.19 mutations per kb in NIH 3T3 cells (Table 4). This indicates that more heavily mutated viruses were selected against and were not represented in NIH 3T3 cells but a significant proportion of sublethally mutated viruses still continued to replicate.

Discussion

The aim of this study was to identify what makes AKV different to M-MLV in respect to its sensitivity to deamination by mA3. Our results have clearly revealed that the number of *N*-linked glycosylation sites in the gammaretrovirus-specific gPr80 accessory protein inversely correlates with the intensity of mA3-induced deamination. This therefore supports the concept that gammaretroviruses employ the host's protein glycosylation machinery to protect themselves against innate restriction by mA3. Considering that the gPr80 protein of MLVs also reduces the potency of the mutator activity of human A3G, *N*-linked glycosylation may therefore be part of a broader strategy allowing gammaretroviruses to increase the success of zoonotic transmission between hosts of different species.

M-MLV is not the only murine retrovirus that is resistant to deamination by mA3. In fact, most mouse retroviruses, including the prevalent Friend MLV, which has the same number of putative gPr80 glycosylated sites as M-MLV, are resistant (Fig. 9A) (399). The xenotropic MLV-related virus (XMRV) is perhaps the only other currently known exception along with AKV of a murine retrovirus that is sensitive to deamination by mA3 (412). However, XMRV, contrary to AKV, is not an endogenous murine retrovirus with a long history of co-evolution with its host, but rather a recently emerged laboratory virus that was inadvertently created through provirus (PreXMRV-1 and PreXMRV-2) recombination during human xenograft passages in mice (413). What is further interesting about XMRV is that it has a deletion in the

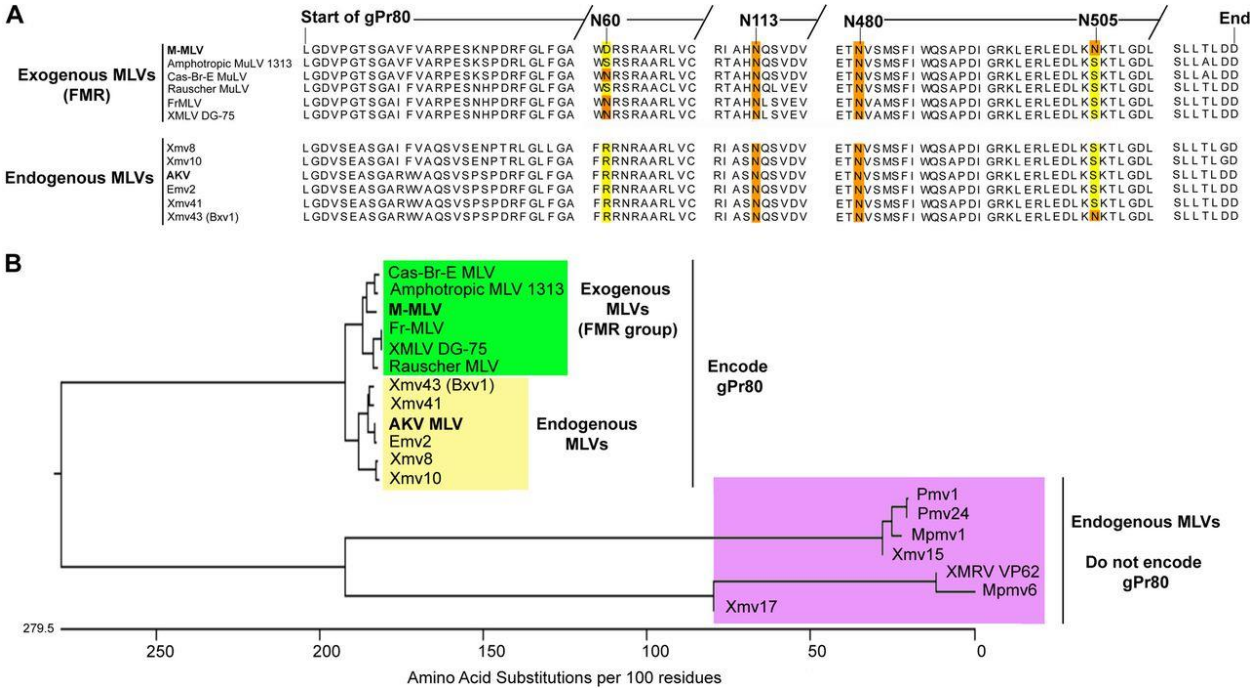

Figure 2.9. Phylogenetic analysis of the gPr80 amino acid sequence of various MLVs.

(A) Detailed alignment of MLVs able to produce gPr80. Residues at positions homologous to putative glycosylated sites for M-MLV are highlighted in orange. Amino acids different from asparagine at these positions are highlighted in yellow. N60 is a putative glycosylated site for several MLVs of the Friend-Moloney-Rauscher (FMR) group. (B) The amino acid sequences of exogenous and endogenous MLVs were aligned by use of the DNAStar Lasergene (version 8) MegAlign program (Clustal W method), and a phylogenetic tree was generated. Green shading, exogenous retroviruses belonging to the Friend-Moloney-Rauscher group; yellow shading, endogenous MLVs that produce a full-length gPr80; purple shading, endogenous MLVs unable to produce gPr80 because of deletions in the sequence. Endogenous MLV subgroups were xenotropic (Xmv), ecotropic (Emv), polytropic (Pmv), and modified polytropic (Mpmv). FrMLV and Fr-MLV, Friend MLV.

leader sequence of the *pr80* gene, as do some other murine ERVs, and therefore does not express gPr80 or any alternate form of a glyco-Gag-like protein (318). The mouse mammary tumor virus (MMTV), is a betaretrovirus that is restricted by mA3 but is resistant to deamination (400). Although MMTV does not encode a glycosylated Gag protein, it does encode a superantigen (SAg) with multiple *N*-linked glycosylated residues that could be packaged into virions and act as a functional surrogate to gPr80 (414). It would also be interesting to investigate whether *N*-linked glycosylation of virion-packaged proteins other than gPr80 can also inhibit A3 deaminase activity.

The exact role of the gPr80 protein of MLVs has long remained enigmatic. Early studies investigated various functional aspects of the gPr80 protein by comparing viral release, infectivity and virulence in presence or absence of the protein, or by exchanging *gag* gene segments between different MLV strains (231, 305, 312, 318, 406, 415). The general conclusion of these studies was that absence of a functional and full-length gPr80 decreases virus release and infectivity *in vitro*, but especially *in vivo*. However, recent studies have revealed new and important roles of this accessory protein in helping the virus evade innate immune defenses. Two studies have shown that gPr80 inhibits the antiviral activity of mA3 (224, 225). Stavrou *et al*. took these findings further by showing that gPr80 acts by preventing mA3 from accessing the reverse transcription complex in viral cores and also by hiding replication intermediates from cytosolic sensors (225). Our work here adds to current knowledge by showing that the *N*-linked glycans attached to gPr80 are in fact essential for its activity against host innate defences. MLVs that express few *N*-linked glycosylation sites in gPr80 are more susceptible of being hypermutated and restricted by mA3.

In contrast to hA3G that stringently restricts MLV infection and spread in human cells, mA3 does not inactivate mouse retroviruses with the same potency. All MLVs we tested, including those with fewer glycosylation sites in gPr80, that were produced in presence of mA3 spread to nearly all target cells 72 h after infection. Differences in the intensity of the deamination cannot alone explain this striking difference. In a previous study we reported that hA3G mutated AKV at an average rate of 8 mutations per kb of proviral DNA, here we have shown that AKV [N113D] is also mutated to that level by mA3 (Table 2) (319). It is therefore more likely that a factor other than deamination intensity, such as the consensus DNA sequence being deaminated, is the main explanation for the potency of viral restriction. While mA3 deaminates cytidines preferentially in a 5'T**C** context, hA3G prefers 5'C**C** (222, 319, 393). With the tryptophan codon being TGG (5'C**C**A as read on the minus strand DNA), hA3G is much better suited at generating all of the three termination codons than mA3. Mutations caused by mA3 therefore appear to have subtler and less deleterious effects on viral replicative fitness than hA3G-induced mutations that are almost always lethal for the virus.

An interesting result that emerged from the ex vivo assays is that infectious viruses with low levels of mutations have replicative fitness similar to that of nonmutated viruses (Fig. 8D). In a previous study, we showed how AKV released from wt splenocytes expressing endogenous mA3 were restricted when analyzed 48 hours after infection in NIH 3T3 cells (319). Here we took these results further by looking at the impact of mutations on virus spread over time. By normalizing input infectious viral titers, we compared the infection efficiency of a pool of mA3-mutated viruses to that of nonmutated viruses. Viruses that infected target NIH 3T3 cells had, as would be expected, fewer mutations than those recovered from the splenocytes, but nevertheless, a relatively large proportion (26% for AKV) had between 1 and 3 mutations per sequence analyzed (Fig. 8C and 8F). It therefore appears that viruses containing low levels of mutations can be as infectious as unmutated viruses under these experimental

conditions. In the context of a natural infection, such mutations could be beneficial and help the virus evade immune defenses.

These results now raise the question as to whether gammaretroviruses that are permissive to low levels of deamination, by way of less intensely glycosylated gPr80, have a greater success to infect and persist *in vivo*. In support to this concept, a prior study in which the authors performed a phylogenetic analysis of the nucleotide sequence of various MLV *pr80* genes revealed that clade A, B and C murine ERVs (xenotropic, polytropic and modified polytropic) are descendants of the same ancestral progenitor, while mA3-resistant viruses of the Friend-Moloney-Rauscher (FMR) group come from a different progenitor (318). If we now look instead at the amino acid sequence of their respective gPr80 proteins, we find that clade B and C endogenous retroviruses (containing AKV) cluster together and that their genomes generally encode a gPr80 with fewer putative glycosylated sites than the gPr80 proteins of the FMR group (Fig. 9A and 9B) The only exceptions are Rauscher MLV and Amphotropic MLV that only contain 2 putative glycosylation sites. However, it remains to be determined whether these viruses are sensitive or resistant to deamination by mA3, and also, whether they in fact only contain 2 glycosylation sites. Additionally, these two viruses have a serine at position 60, whereas AKV has an arginine, M-MLV has an aspartic acid, and the mA3-resistant Friend MLV has an asparagine in a perfect *N*-glycosylation sequon. It would therefore be interesting to investigate the impact of this variable residue on resistance to deamination, especially if Rauscher MLV and Amphotropic MLV were in fact shown to be resistant to deamination. Overall, these observations indicate that sensitivity to mA3 deamination may have given a subset of exogenous gammaretroviruses a selective advantage to become endogenized in the mouse germline. This concept that sublethal levels of A3-induced deamination could be a driving force behind retroviral/HIV evolution, drug-resistance and immune escape has been raised several times before (251, 416-420).

How the *N*-linked glycans of gPr80 prevent A3-induced deamination is still unknown. Although gPr80 is cleaved by cellular proteases, with its N-terminal extremity (containing N113) being packaged into virions (310), it is intriguing that the secreted C-terminal fragment containing putative glycosylated residues N480 and N505 also prevents deamination. It remains to be established whether gPr80 and mA3 interact. If mA3 were to facilitate the packaging of the full-length gPr80 protein or even that of each of its cleaved polypeptides, then a case could be made for gPr80 glycans acting collectively to physically block A3 proteins from accessing the viral cDNA substrate in the reverse transcription complex. Further studies are required to fully understand how *N*-linked glycans on gPr80 impede the deamination of gammaretroviruses by A3 proteins. Such efforts could potentially lead to the identification of a new class of A3 inhibitors.

Acknowledgements

We are grateful to Tara Read, and Kristin Kemmerich for technical and logistical support to the project, and Daniel Figeys and Rui Chen for advice with analyzing protein glycosylation. The authors also want to specially acknowledge Hung Fan and thank him for helpful discussions, comments on the manuscript and the anti-p30^{CA} antibody. M.-A.L. holds a Canada Research Chair in Molecular Virology and Intrinsic Immunity. This research was supported by a grant from the Canadian Institutes of Health Research #89774 and an Early Researcher Award from the Ontario Ministry of Research and Innovation to M.-A.L.

Chapter 3: Full-Length Glycosylated Gag of Murine Leukemia Virus Can Associate With The Viral Envelope as a Type I Integral Membrane Protein

Preface: This chapter has been previously published as a research article.

Renner TM, Belanger K, Lam C, Gerpe MCR, McBane JE, Langlois MA. 2018. Full-Length Glycosylated Gag of Murine Leukemia Virus Can Associate with the Viral Envelope as a Type I Integral Membrane Protein. J Virol 92. https://doi.org/10.1128/JVI.01530-17.

Author Contributions:

T.M.R. conducted Figures 1, 3, 4, 8 & 9. K.B. conducted Figures 2, 5 & 6. C.L & K.B contributed to Figure 7. C.L. performed all 3-D PCR analyses. M.C.R.G. & J.E.M. performed cloning. M.A.L. conceptualized the study. T.M.R., K.B. and M.A.L. took part in data analysis and writing the manuscript.

Abstract

The glycosylated Gag protein (gPr80) of murine leukemia viruses (MLVs) has been shown to exhibit multiple roles in facilitating retrovirus release, infection and resistance to host-encoded retroviral restriction factors such as APOBEC3, SERINC3 and SERINC5. One way gPr80 helps MLVs escape host innate immune restriction is by increasing capsid stability, a feature that protects viral replication intermediates from being detected by cytosolic DNA sensors. gPr80 also increases the resistance of MLVs against deamination and restriction by mouse APOBEC3 (mA3). How the gPr80 accessory protein, with its three *N*-linked glycosylation sites, contributes to these resistance mechanisms is still not fully understood. Here we have further characterized the function of gPr80 and, more specifically, revealed that the asparagines targeted for glycosylation in gPr80 also contribute to capsid stability through their parallel involvement in the Pr65 Gag structural polyprotein. In fact, we demonstrate that sensitivity to

deamination by mA3 and human A3 proteins is directly linked to capsid stability. We also show that full-length gPr80 is detected in purified viruses. However, our results suggest that gPr80 is inserted in the $N_{exo}C_{cyto}$ orientation of a type I integral membrane protein. Additionally, our experiments have revealed the existence of a large population of Env-deficient virus-like particles (VLPs) harbouring gPr80 inserted in the opposite ($N_{cyto}C_{exo}$) polarity which is typical of type II integral membrane proteins. Overall this study provides new insight into the complex nature of the MLV gPr80 accessory protein.

Importance

Viruses have evolved numerous strategies to infect, spread and persist in their host. Here we analyze the details of how the MLV-encoded glycosylated Gag (gPr80) protein protects the virus from being restricted by host innate immune defenses. gPr80 is a variant of the structural Pr65 Gag protein with an 88 amino acid extended leader sequence that directs the protein for translation and glycosylation in the endoplasmic reticulum. This study dissects the specific contributions of gPr80 glycans and capsid stability in helping the virus infect, spread and counteract the effects of the host intrinsic restriction factor APOBEC3. Overall this study provides further insight into the elusive role of the gPr80 protein.

Introduction

Infection, spread and persistence of retroviruses in an animal population is directly related to their ability to evolve under the selective pressures of host immune defenses. The success of HIV-1 as a pathogen is credited, amongst other strategies, to its accessory protein Vif that induces the proteasomal degradation of APOBEC3 (A3) proteins that are potent host-intrinsic retroviral restriction factors (Reviewed in (194, 421)). In contrast, murine gammaretroviruses, such as the Moloney murine leukemia virus (M-MLV), do not express a Vif-like protein, but rather a glycosylated version of their structural Gag

protein, termed glyco-Gag (gPr80), to defend against the deleterious effects of mouse A3 (mA3) (224, 225, 368).

gPr80 originates from the translation of the structural Gag polyprotein (Pr65) at an alternate (CUG) start codon upstream of the canonical AUG initiation codon, a process that adds 88 amino acids to the original sequence (Fig. 1A) (293, 294, 297, 404). This N-terminal leader segment of gPr80 encodes a signal peptide that directs the completion of polyprotein synthesis to the endoplasmic reticulum where it undergoes *N*-linked glycosylation. It also contains a signal/anchor site upstream of the junction of the leader and MA Gag domains that direct its insertion into the membrane (72, 422). The mature protein can be further proteolytically processed in the infected cell to yield a membrane-associated ~55 kDa N-terminal product, and a secreted ~40 kDa C-terminal product (72, 310). While the N-terminal protein segment associates with the cell membrane as a Type II integral membrane protein (422), it has also been detected in released retroviral particles, while the C-terminal fragment has not (310, 422). Three sites have been experimentally identified in the gPr80 protein of M-MLV that account for all detectable *N*-linked glycosylation: N113 located in the sequence of the viral matrix (MA), and N480 and N505 located in the capsid (CA) (Fig. 1A) (368).

Multiple functions have now been attributed to gPr80 that help the virus infect its host. Although expression of the protein has little effect on viral infection in most *in vitro* laboratory conditions (225, 296, 305), it enhances late step virus assembly and release through lipid rafts (311, 415), and is also involved in promoting virus replication, pathogenesis and neurovirulence *in vivo* (296, 302, 305, 311, 406, 415, 423), especially when mA3 is expressed (136, 224, 225, 368). First reported by Kolokithas *et al.*, these authors showed that gPr80 is required to support the replication of the neurovirulent CasFr^{KP} MLV *in vivo* when mA3 is expressed (224). Murine A3 is a cytidine deaminase that inhibits the infection

of most MLVs by interfering with the early stages of reverse transcription mainly through enzymatic-independent strategies (225, 319, 399, 400, 403, 424). In contrast, human A3 proteins acting on MLVs, and mA3 acting on retroviruses from other species than mice, primarily restrict and inactivate retroviruses through intense deamination of cytosines in single-stranded DNA replication intermediates produced during reverse transcription (260, 425). Generation of large numbers of C-to-T mutations in the targeted minus-strand proviral DNA is a process called hypermutation. While most MLVs are only modestly susceptible to mA3 restriction *in vitro* (233, 319, 403), some MLVs such as AKV are more sensitive to mA3 and this has been associated with fewer *N*-linked glycosylation sites present on the gPr80 protein of AKV (319, 368). We have previously shown, through site directed mutagenesis, that higher numbers of *N*-linked glycosylation sites on gPr80 appear to correlate with increased resistance to mA3 deamination and restriction *in vitro* and *ex vivo* in murine splenocytes (368).

Another important feature of gPr80 revealed in two studies by Stavrou *et al.,* showed that gPr80 increases MLV capsid stability (136, 225). Capsid integrity is important to create a shielded environment that protects viral replication intermediates from immune cytosolic DNA sensors that can induce an interferon response, and also from mA3 expressed in the cytosol of the recipient cells (136, 225). The importance of gPr80 in antagonizing mA3 was further showcased by demonstrating that gPr80-deficient viruses with a stop codon in the N-terminal leader peptide reverted back to gPr80-proficient viruses when passaged through mice expressing mA3, but not in mA3 knock-out mice (136, 225). These studies therefore suggest that one of gPr80's primary roles might in fact be to counteract the antiviral effects of mA3.

In light of a previous report by our group showing that the state of *N*-linked glycosylation was involved in modulating the sensitivity of MLVs to restriction and deamination of mA3 (368), here we further investigate the specific roles of gPr80 carbohydrates on capsid stability and resistance to editing by mouse and human A3 proteins. For our study we used a replicative competent M-MLV reporter virus that has a CTG to CTA mutation to abolish gPr80 translation initiation and M-MLV mutant viruses where the asparagines targeted for glycosylation have been individually converted to glutamine. We reveal that gPr80 contributes to increased capsid stability regardless of the presence of glycosylation, however these asparagines are also essential to maintain the structural integrity of the capsid. Furthermore, use of glycosylation inhibitors and cells unable to carry out complex *N*-linked glycosylation show that diminished capsid stability is required for mA3 to deaminate viral DNA. Finally, we also provide evidence that full-length gPr80 may provide structural support to virions as a Type I integral membrane protein, implying the glycosylated C-terminus of the protein may help improve their stability. Our study provides additional insight into the mechanisms by which the elusive gPr80 antagonizes host innate immune detection and restriction.

Materials and Methods

Cells

Human Embryonic Kidney Epithelium cells (293T), 293S GnTI- (ATCC, CRL-3022) and mouse embryonic fibroblasts (NIH 3T3) were cultured in DMEM/High Glucose Medium (Wisent) supplemented with 10% Fetal Bovine Serum (FBS) (Gibco), 100 U/mL penicillin and 100 µg/mL streptomycin (Multicell, Wisent Inc., Canada) and propagated at 37°C in a 5% CO_2 incubator. 293S GnTI- cells lack N-acetyl-glucosaminyltransferase I (GnTI) activity and therefore lack complex N-glycans.

Expression plasmids and viruses

The pMOV-eGFP expression vector encoding replicative M-MLV has been described before (319, 371). Expression vectors for the FLAG-tagged C57BL/6 allele of mouse APOBEC3 delta-exon5 (referred throughout as FLAG-mA3), human APOBEC2 (A2), human APOBEC3C (A3C), human APOBEC3F (A3F) and human APOBEC3G (A3G) have been described before (319, 408). The DNA coding sequences of human APOBEC3A (A3A), human APOBEC3B (A3B) and human APOBEC3H (A3H) were amplified from mRNA of human peripheral blood mononuclear cells (PBMCs). Products were then cloned downstream of a FLAG epitope tag in the pcDNA3.1 expression vector. The cDNA for Human APOBEC3D (A3D) was provided by the NIH AIDS Research and Reagents program in a pcDNA3.1 backbone (cat. no. 11433). A FLAG epitope tag was inserted upstream of the A3D coding sequence.

M-MLV [N480Q], M-MLV [N113Q/N505Q], M-MLV [N113Q/N480Q/N505Q] and M-MLV [CTA] were described in a previous report by our group (368). For cloning of recombinant gPr80 (wild type) and Pr80[N113Q/N480Q/N505Q], the cDNA sequence was amplified by PCR from their corresponding M-MLV expression vector. The forward primer contained a Kozak sequence and the ATG initiation codon instead of the non-conventional CTG initiation codon. The reverse primer contained the cDNA for the V5 epitope tag inserted before the stop codon at the 3' end of the coding sequence. The sequences of the primers were as follows: MoMLVPr80-EcoRI-ATG-FWD: 5'-ACAAGAATTCGCCACCATGGGAGACGTCC-3' and MoMLVpr80-V5-BamHI-REV: 5'-GTGTGGATCCCTACGTAGAATCGAGACCGAGGAGAGGGTTAGGGATAGGCTTACCGTCATCTAGGGTC-3'. The PCR amplicon was then directionally cloned using EcoRI and BamHI restriction sites into the pcDNA3.1 expression vector (Invitrogen). Constructs were sequenced for accuracy.

For assessing the virion incorporation of gPr80 in M-MLV[CTA], and distinguishing the N-terminal from the C-terminal fragments, a new construct was developed. As outlined in the primers below, a 3X FLAG tag was added just prior to the traditional ATG for the Pr65 protein, which was replaced with GGG. Briefly, the gPr80 leader sequence was amplified with a primer within the CMV promoter and cloned using the NheI site in the 5' MCS. This region already contained a Kozak sequence and ATG, as described above. The reverse primer bound just before the Pr65 start codon and added a SacII and AgeI site after the leader sequence. A 3X FLAG tag was developed by filling-in the two primers below. These primers had SacII and AgeI sites on the 5' and 3' end respectively. Finally the Pr65 was amplified using a forward primer with an AgeI site on the 5' end and a GGG instead of the ATG, while the reverse was virtually unchanged from the parental V5-tagged gPr80 vector. The leader sequence was cloned into a pcDNA3.1 backbone first, then the 3X FLAG tag was inserted using the SacII AgeI sites. The Pr65 was inserted into a separate pcDNA3.1 backbone and the leader sequence with the FLAG tag was inserted into the 5' of this vector using the NheI and AgeI sites. The primers are as follows: Leader sequence SacII AgeI REV: CATACCGGTCCGCGGATTTTCAGACAAATACAGAAACACAGTCAGAC; SacII 3X FLAG FWD: ATTCCGCGGGATTACAAGGACCATGACGGAGACTACAAAGATCACGACA; 3X FLAG AgeI REV: CATACCGGTGCCCTTGTCATCGTCGTCCTTGTAGTCGATGTCGTGATCT; AgeI Pr65 FWD: GGGACCGGTGGGGGCCAGACTGTTACCACTCCC; V5 SacII REV: CTAGGTACCCTACGTAGAATCGAGACCGAGGAGAGG. The vector sequence was confirmed by Sanger sequencing.

Western blotting and antibodies

Western blot analyses were conducted following procedures detailed in Gerpe *et al.* (368). Samples presented in Figures 8 and 9 were run on 4-12% Bis-Tris NuPAGE gels with MOPS-SDS running buffer (ThermoFisher). The following antibodies were used for this study: HRP-conjugated anti-FLAG (cat. no. A8592, Sigma), anti-eGFP (cat. no.632381, Clontech), HRP-conjugated anti-mouse IgG (cat. no.7076S, Cell Signaling), HRP-conjugated anti-rabbit IgG (cat. no. AB6721, Abcam), HRP-conjugated anti-rat IgG (cat. no. A5795, Sigma), polyclonal anti-V5 (cat. no. AB3792, EMD Millipore), monoclonal anti-V5 (cat. no. MA5-15253) and HRP-conjugated anti-β-tubulin (cat. No. AB21058, Abcam). The polyclonal anti-p30 antibody was kindly provided by Dr. Hung Fan (University of California, Irvine). The rat monoclonal anti-p30 R187 was purified from a B cell hybridoma (ATCC, CRL-1912).

Transfections, infections and p30 ELISA

Transfection and viral infectivity assays were performed as previously described (368). Briefly, 293T or 293S GnTI- cells were seeded at 3.0 x 10^5 cells per well in a 6-well plate or at 1.0 x 10^6 cells per 10 cm dish 24 h prior to transfection. Co-transfections in 6-well plates were performed with 800 ng of viral expression vectors and varying amounts (50 ng – 250 ng) of the A3-expression plasmids using GeneJuice transfection reagent (Novagen, EMD Millipore) according to the manufacturer's instructions. For work in 10 cm dishes, 10 μg of viral expression vectors with varying amounts of A3-expression plasmids were co-transfected using $CaCl_2$. Cells were then cultured for two days before viruses were harvested.

One day prior to infection, NIH 3T3 target cells were seeded at 1.0 x 10^5 cells per well in 12-well plates. At the time of infection, the medium was replaced with fresh medium containing Polybrene at a final concentration of 8 μg/mL and virus-containing supernatants from 293T producer cells were harvested,

cleared by centrifugation, and passed through 0.45 μm filters. Depending on the assays, target cells were infected with equal volumes of virus-containing supernatant, or the amount of p30 capsid proteins in each sample was determined by p30 ELISA (QuickTiter™ ELISA Kit, Cell Biolabs Inc.) and normalized viral supernatants were used to infect NIH 3T3 target cells by spinoculation. Forty-eight hours post-infection, the infected cells were partitioned for flow cytometry analysis of eGFP reporter gene expression and for gDNA extraction for subsequent mutation analysis.

To calculate the viral titer in transducing units (TU) / mL, equal volumes of virus-containing 293T cell supernatant was titrated on 1.0 x 10^5 NIH 3T3 cells per well in a 12-well plate. Twenty-four hours post-infection, these cells were analyzed by flow cytometry. Infections ranging from 2-30% were assumed to have one productive integration per cell, and used to calculated TU/mL with the following formula: TU / mL = # of infected cells / volume of viral supernatant.

Genome measurements

Viral genomes were extracted from supernatants using the QIAamp Viral RNA Mini Kit (Qiagen) following manufacturer's guidelines, with one exception. Just prior to washing, the dried silica column was incubated with 50μL containing 100U of DNase I (RNase free) with 1X reaction buffer (New England BioLabs). This was allowed to sit for 30 min at room temperature prior to washing the column to completely remove the transfected plasmid DNA. The RNA eluate was then reverse transcribed and analyzed by droplet digital PCR, using the QX200 system (BioRad), for the presence of the GFP coding sequence. The primers used for this analysis were R279-FWD and R279-REV, as previously described (409). Data was analyzed using QuantaSoft™ and extrapolated based on the dilutions used for the assay.

Viral core stability assay

Chronically infected NIH 3T3 cells, were seeded in 10 cm plates and were used to produce M-MLV, M-MLV [N480Q], M-MLV [N113Q/N505Q], M-MLV [N113Q/N480Q/N505Q] or M-MLV [CTA] over a period of 96h (368). Supernatants were then collected and filtered through 0.45 µm cartridge filters prior to treatment for 20 min at room temperature with 10% Triton 100-X to strip viral envelopes. Samples were then layered on top of a sucrose step gradient. The step gradient consisted of 5 ml of 20% (wt/vol) sucrose-PBS overlaid by 2 ml of 5% (wt/vol) sucrose-PBS containing 2% Triton X-100, or 0.2 % SDS. Gradients were centrifuged for 2 h at 100 000 x g in a 70 Ti rotor and viral cores were resuspended in 100 µl of RIPA lysis buffer (150mM NaCl, 1% NP-40, 0.2% sodium dodecyl sulfate (SDS), 1mM EDTA, 0.5% NA-Deoxycholate, 50mM Tris-HCL pH 8.0) supplemented with complete EDTA-free protease inhibitor cocktail (Roche) for 20 min on ice. The samples were then mixed with Laemmli loading buffer, boiled and analyzed by Western blot for the presence of envelope and p30 capsid proteins using anti-eGFP and monoclonal anti-p30 antibodies respectively. For glycosylation impact on stability, the same was done with chronically infected NIH 3T3 cells for M-MLV in the presence of tunicamycin (cat. no. T7765, Sigma), at a concentration of 0.2 µg/mL. However, in this experiment $3x10^6$ cells were seeded in 10cm dishes, incubated for 6 hours, washed 3 times with PBS and media was refreshed with the conditional presence of tunicamycin. This concentration was chosen to allow for virus production for approximately 36 hours, increased exposure or longer incubations had severe impacts on cellular viability. Alternatively, 293T or 293S GnTI- cells were seeded in 10 cm plates and were transfected with M-MLV, the supernatants were treated as above.

mA3 core packaging assay

M-MLV or mutant virus plasmids (10 µg) and 1 µg of mA3 expression plasmid were co-transfected in 293T cells. Three days after transfection, virus-containing supernatants were filtered through 0.45 µm cartridge filters and layered on top of a sucrose step gradient. The step gradient consisted of 5 ml of 20% (wt/vol) sucrose-PBS overlaid with 2 ml of 5% (wt/vol) sucrose-PBS with 0, 2, 5 or 10% Triton X-100. Gradients were centrifuged and processed as above.

A3-gPr80 interaction assay

293T cells in 10 cm dishes were co-transfected with 5 µg of FLAG-tagged A3G or mA3 and 20 µg of gPr80-V5 or Pr80[3Q]-V5 (Pr80[N113Q/N480Q/N505Q]-V5) and cultured for 72 h. Three days after transfection, complexes were purified using anti-FLAG conjugated agarose beads. Following incubation, bound complexes were spun down at 8,200 x g for 30 sec at 4 ºC, followed by four washes with 200 µL of the Wash Buffer 1 (50mM Tris-HCl (pH 8.0), 150mM NaCl, 1% Igepal CA-630, 0.5% sodium deoxycholate, 0.1% SDS). A last wash in 100 µL of Wash Buffer 2 (20 mM Tris-HCl (pH 7.4)) was then performed and the samples were resuspended in 40 µL of 5X Laemmli loading buffer. Protein-protein interactions were then determined by Western blot analysis using polyclonal anti-p30 and anti-FLAG antibodies.

Purification of FLAG-tagged A3 proteins

293T cells transfected with 1 µg of FLAG-tagged mA3 or A3G expression plasmids were lysed with M2 (Sigma) affinity gel lysis buffer for 30 min on ice. Following lysis, samples were cleared by centrifugation at 12,000 x g for 10 min at 4°C and mixed with 40 µl of anti-FLAG-conjugated agarose beads (cat. no. A2220, Sigma). Mixtures were rotated for 3h at 4°C followed by two washes with cold 1 X PBS prior to

the elution step. Elution was carried out by incubating the beads twice with 50 µl of 0.1 M glycine pH 3.5 for 5 min and eluates were collected in fresh tubes containing 3 µl of 1 M Tris-HCl pH 8.0. The protein concentration in immunoprecipitated samples was determined by Bradford assay (Sigma).

Purification of gPr80-V5 and Pr80[3Q]-V5

Two million 293T cells were seeded in a 10 cm dish and cultured in decomplemented media the day prior to transfecting 20µg of gPr80-V5-pcDNA or Pr80[3Q]-V5-pcDNA plasmids. The cells were harvested 96h later and washed four times with 1X PBS. The cells were then resuspended in 0.8 ml of M2 affinity gel lysis buffer containing 50mM Tris-HCl pH 7.4, 150mM NaCl, 1mM EDTA, and 1% Triton X-100. Lysates were then homogenized by enforced passage through a 19 gauge needle, and then rotated at 4°C for 30 min. Lysates were cleared by centrifugation at 12,000 x g for 10 min prior to adding anti-V5 conjugated agarose beads (Abcam, ab1229, Cambridge, UK). Stock anti-V5 beads were first spun down at 3,000 x g for 2 min to remove glycerol and washed with 1X TBS (50mM Tris-HCl, with 150mM NaCl, pH7.4). The anti-V5 beads (20 µl) were then added to the lysates and rotated overnight at 4°C. The samples were then spun down at 3,000 x g for 2 min. and washed with 1X TBS before proceeding to the elution step. Elution was carried out three times with 30 µL 0.1M triethylamine HCl pH 11.5 for 10 min. Samples containing the eluted proteins were spun after each 10 min. incubation at 3,000 x g for 2min. Eluates were pooled and added to a tube containing 6µL of 1M MOPS-HCl pH 3.0. Before loading on gel, 30µL of the sample was resuspended in 5X Laemmli buffer and boiled for 5min.

Oligo cleavage

Varying amounts of purified FLAG-A3 proteins with or without purified gPr80-V5 or Pr80[3Q]-V5 were incubated with 0.1 pmol/µl of a FAM-labeled oligonucleotide with TTC or CCC target sites in the presence of 50 µg/ml of RNase A in a final volume of 100 µl for 5 h at 37ºC followed by an incubation of 1 h at 37°C in the presence of 5 units of UDG. Both oligonucleotides used as substrates for mA3 and A3G have been previously described (424, 426). Reactions were terminated by the addition of 60 µl of formamide loading dye (95% deionized formamide, 0.025% bromophenol blue, 0.025% xylene cyanol FF, 5mM EDTA) containing 0.2M NaOH and heating at 95ºC for 20 min. Samples were then resolved on 15% TBE-urea polyacrylamide gels and visualized using a Typhoon Imaging system (GE Healthcare). Quantification analyses were performed using the ImageJ software.

3D-PCR analysis and DNA sequencing

This technique was conducted as detailed in Gerpe et al. (368). In brief, a first-round PCR was performed on 10 ng of genomic DNA from infected NIH 3T3 target cells in a two-step protocol using PrimeSTAR high fidelity polymerase (Takara) and primers eGFP-FWD; 5'-CGAGGAGCTGTTCACA-3' and eGFP-REV; 5'-CAGCTCGTCCATGCCGAGAGTGAT-3'. PCR cycles were 98°C for 1 min, followed by 32 cycles of denaturation at 98°C for 10 sec, annealing at 58°C for 5 seconds, and an extension at 72°C for 1 min and a final extension at 72°C for 2 min, 2 µL of a 1:1000 dilution of the first-round PCR products were used per reaction to perform a second-round gradient PCR using previously described primers (R279-FWD and R279-REV) (409). The PCR denaturation gradient ranged from 89.5°C to 86°C. Products were resolved on 2% agarose gels. Proviral DNA integrated into NIH 3T3 cells was isolated, amplified and cloned as described elsewhere (392). The region amplified corresponds to the 717 bp coding sequence of the eGFP reporter gene. Cloned DNA was sequenced.

Fate of Capsid Assay

NIH 3T3 producer cells produced virus as described earlier for 96 h. Supernatants were collected, 0.45µm filtered and centrifuged through a 20% sucrose cushion to clear free protein. Virus was resuspended in fresh complete media and levels of capsid were normalized by ELISA. This assay was performed similarly to previous groups (197, 225, 427-429), with some slight modifications. Briefly, 2.5 x 10^5 uninfected NIH 3T3 cells were seeded in 6-well plates one day prior to infection. One plate was dedicated to each of M-MLV, M-MLV[N113Q/N480Q], M-MLV[N113Q/N480Q/N505Q] and M-MLV[CTA]. Approximately 1x10^8 TU of M-MLV was used to infect each well in the presence of 8 µg/mL polybrene, equivalent levels of p30 was used for each virus. The plates were spinoculated at 1600 x g for 30 min in a pre-cooled centrifuge at 4°C. The cells were then incubated at 37°C in the presence of 5% CO_2 for 3 hours. Following incubation, the cells were washed 3 times with ice-cold PBS, followed by treatment with 1mL pronase (7 mg/mL) for 5 min at room temperature. The cells from each plate were pooled and then washed 3 times with ice-cold PBS by centrifugation. These pellets were lysed with 2.5mL hypotonic lysis buffer (10 mM Tris–HCl, pH 8.0; 10 mM KCl and 1 mM EDTA) supplemented with protease inhibitors and incubated on ice for 15 min. A Dounce homogenizer (7 mL) was used with the B pestle to continue lysis for 15 strokes. Cellular debris was cleared by centrifugation at 1600xg at 4°C. A 100µL aliquot from this cleared lysate was used for 'input' analysis by western blot. The remainder was diluted in cold PBS, centrifuged at 125,000 x g for 2 hours at 4°C through a 40% sucrose cushion in a 70Ti rotor. This pellet was then analyzed by western blot. For the pellet, signal was enhanced through the use of a sensitive detection reagent (cat. no. 34095, ThermoFisher).

Intact Virion Immunoprecipitations

For anti-V5 IPs, M-270 epoxy dynabeads (ThermoFisher) were covalently conjugated to a monoclonal (ThermoFisher) or polyclonal (Millipore) V5 antibody according to manufacturer's instructions. For anti-eGFP IPs, a µMACS GFP Isolation Kit (Miltenyi) was used according to manufacturer's instructions. 293T

cells were seeded and transfected as described previously in this section, and in accordance to the parameters outlined in Figure 9. The supernatants from these cells were filtered through a 0.45 µm syringe filter and ultracentrifuged through a 20% sucrose cushion prior to initiating the immunoprecipitation. Antibody conjugated beads were then incubated with virions for 3 hours at 4°C with constant rotation. The magnetic beads were then washed with 5mL of PBS before analyzing by SDS-PAGE. As with gels from Figure 8, these IPs were run on NuPAGE 4-12% gradient gels.

Sequencing

All the DNA sequencing in this study was performed at the McGill University, Génome Québec Innovation Centre, Montréal, Canada.

Results

gPr80-deficient MLV exhibits similar replicative fitness as the wild type virus.

We previously demonstrated that substitution of *N*-linked glycosylated amino acids (N→Q) of the gPr80 protein of gammaretroviruses increases the virus' sensitivity to deamination by virion-packaged mA3 and human A3G (368). While one glycosylation site maps to position N113 located in the viral matrix and the membrane associated segment of gPr80, the two other sites (N480 and N505) map to the viral capsid and are within the secreted segment of gPr80 (Fig. 1A). Additionally, it has also been reported that gPr80 expression contributes to capsid stability, thereby increasing protection of replication intermediates against cytosolic sensors and mA3 (136, 225). However, it is unclear how these glycans inhibit editing by A3 proteins or whether they also partake in increasing capsid structural integrity. We first examined the effect of *N*-linked glycans on various parameters linked to replicative fitness, notably particle release, infectious titer and spread. Our interest focused on a gPr80-deficient virus with the

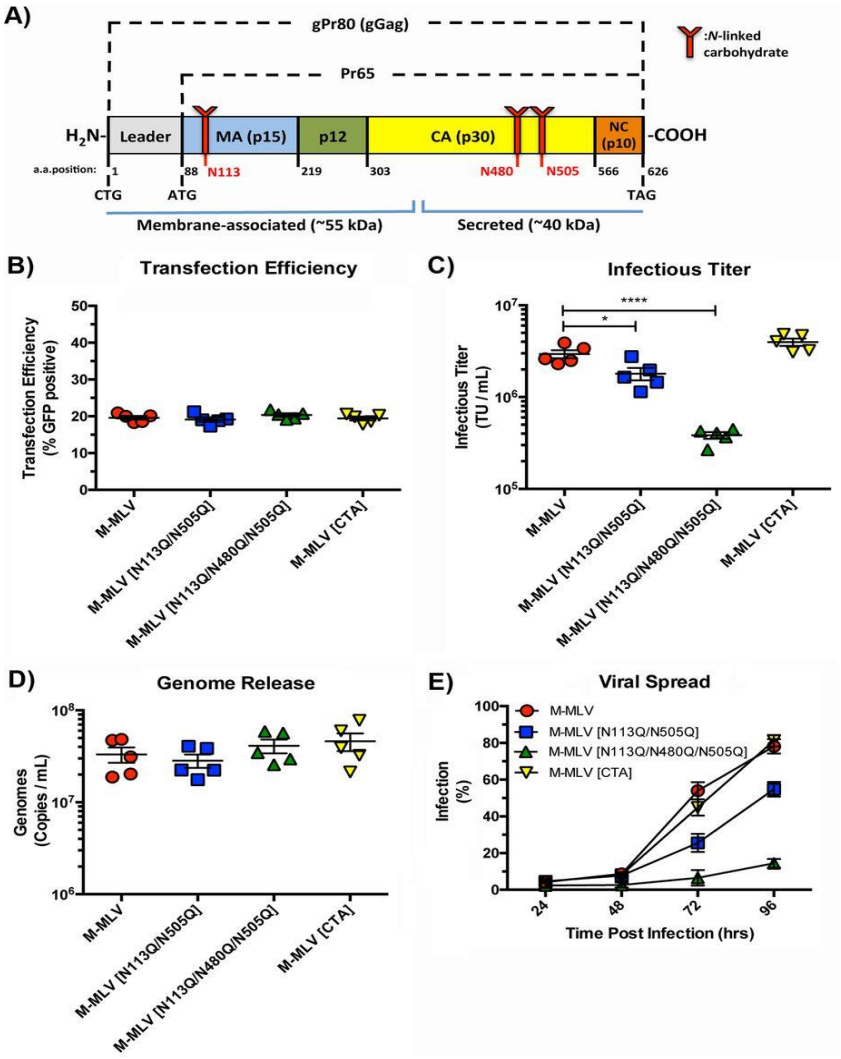

Figure 3.1. Replicative fitness of gPr80-deficient and mutant viruses.

(A) Schematic representation of the gPr80 and Pr65 proteins. The locations of the three N-linked glycosylation sites are indicated in red. The approximate regions encompassing the N-terminal membrane-associated domain and the C-terminal secreted domain are indicated with blue lines; the leader region contains the ER localization signal peptide. (B) Transfection efficiencies of virus expression constructs in transfected 293T cells. (C) Infectious titers of viruses released from transfected 293T cells. Viruses were harvested after 48 h and filtered through 0.45-µm filters. Equal volumes of the different viruses were then titrated on NIH 3T3 cells, and infection was measured by flow cytometry 24 h after infection. (D) Viral genomes released into the supernatants of the same transfected 293T cells as those described above were measured by digital droplet PCR (ddPCR). Samples were treated with DNase I prior to RNA extraction. (E) Replicative fitness of M-MLV and its glycosylation mutants. Input virus was normalized via the number of TU per milliliter. Infection was monitored by measuring EGFP expression at each time point following infection by flow cytometry. Data are the compilation of five independent transfection experiments done in triplicate. P values were calculated by Student's t test. *, $P \leq 0.05$; ****, $P \leq 0.0001$. P values for the data sets in panels B and D were not significant for comparisons to the M-MLV control (ns, $P > 0.05$).

gPr80 CTG (leucine) initiation codon substituted to a CTA (leucine) to prevent translation of gPr80, and also mutant M-MLV viruses containing a double (N113Q/N5050Q) or triple substitution (N113Q/N480Q/N505Q) to prevent glycosylation to different degrees (Fig. 1A). We have previously shown that virus with the N480Q mutation has severely compromised infectivity; this is why we chose to only use the triple mutant for simplicity and convenience (368). We first investigated how *N*-linked glycans affect viral genome release and infectious titer. Virus expression plasmids were transfected in 293T cells, and 48 h later, virus was harvested and passed through a 0.45 μm filter. Transfection efficiency was similar for all constructs, as measured by expression of the viral envelope-eGFP (Env-eGFP) fusion protein (Fig. 1B). Equal volumes of virus containing supernatant were used to infect NIH 3T3 cells to evaluate the viral titer (Fig. 1C). Titers of wild type M-MLV and the CTA mutant were nearly identical. A slightly reduced titer was observed for the double mutant, and the triple mutant had nearly a 10-fold lower titer. To ensure that differences in titer are not a reflection of compromised particle release, we measured viral genomes in the transfected cell supernatant, which confirmed that particle release was nearly identical (Fig. 1D). Finally we measured the replicative fitness of the viruses. NIH 3T3 cells were infected with equal TU, and viral replication was monitored for 96 h. The replicative fitness of M-MLV and M-MLV[CTA] were nearly identical, while both glycosylation mutants M-MLV[N113Q/N505Q] and M-MLV[N113Q/N480Q/N505Q] had reduced propagation efficiencies (Fig. 1E). The similar spread curves of M-MLV and M-MLV[CTA] are not surprising, as these data confirm previously published observations (313, 317). These results are also consistent with our previous report showing that an N-to-Q substitution at capsid residue 480 severely impairs infectivity of the viruses harboring that mutation (368).

Mutations at the sites of *N*-linked glycosylation reduce capsid stability.

We next investigated the effects of the asparagine mutations and absence of gPr80 protein expression on capsid stability. We first harvested virus-containing cell supernatants from infected cells and treated

them with 10% Triton X-100 to first remove the viral envelope. The naked capsids were then spun through a sucrose cushion containing either 2% Triton X-100 or 0.2% SDS and resolved further through a 20% sucrose cushion (Fig. 2A). These concentrations were shown in our preliminary optimization assays to be at the threshold for destabilizing naked wild type M-MLV capsids (data not shown). Virus pellets were then resuspended in RIPA lysis buffer and analyzed by Western blot using anti-eGFP to stain the viral envelope and monoclonal anti-p30 capsid antibodies. In agreement with previous findings (225), the capsid of the gPr80-deficient M-MLV [CTA] virus was completely dissolved by the detergents indicating less robust capsid stability than the wild type virus (Fig. 2B). We also observed reduced recovery of p30 with the glycosylation-null mutant M-MLV [N113Q/N480Q/N505Q] and the single point mutant, M-MLV [N480Q] (Fig. 2B). This assay does not show an important difference in capsid stability between the glycosylation mutant M-MLV [N113Q/N505Q] and the wild type virus.

gPr80 does not impact the level of mA3 incorporation in the virion

Our next question was whether mA3 was packaged similarly within the viral cores between all viruses tested or was excluded because of the gPr80 glycans. Previous studies have clearly shown that detergent-treated MLVs harbored mA3 proteins within the viral core (233, 403). To investigate this issue, we produced virus as detailed above but in presence of mA3. We then layered the supernatant containing enveloped virus directly onto sucrose cushions containing increasing concentrations of detergent (Fig. 2C). This approach exposes the virions to detergent only a short time, as it passes from the 5% sucrose to the 20% sucrose, gently and gradually stripping away the envelope, matrix and proteins located outside the viral capsid core as the detergent concentration increases. Four samples were analyzed individually, each with either 0%, 2%, 5% or 10% Triton X-100 in the 5% sucrose layer. Our results show that the capsid of M-MLV [CTA] was easily dissolved using the lowest concentration of detergent, while the capsids of the triple mutant and wild type viruses remained intact in all conditions

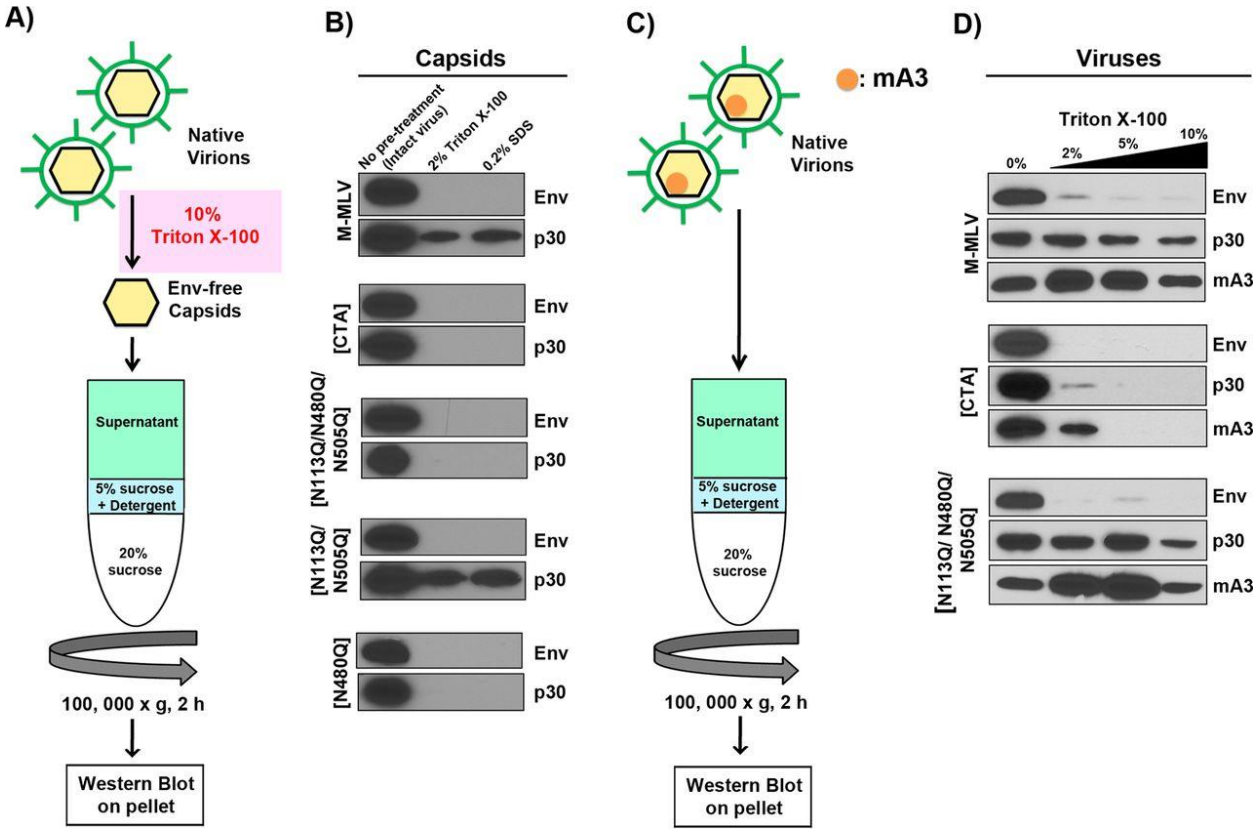

Figure 3.2. Glycosylation mutants have diminished capsid stability.

(A) Schematic representation of the procedure used for assessment of the stability of envelope-free viral cores in the presence of mild detergent. Native enveloped viruses were first treated with 10% Triton X-100 to strip the viral envelope. Envelope-free viral cores were then submitted to velocity sedimentation through a 5% sucrose step containing either 2% Triton X-100 or 0.2% SDS and then through a 20% sucrose step. (B) Western blots were carried out on intact core pellets by using monoclonal anti-p30 (R187) and anti-EGFP antibodies. EGFP was expressed as a fusion protein with the viral envelope glycoprotein (Env). (C) Schematic representation of the methodology used to assess packaging of mA3 inside viral cores. Native, enveloped virions were submitted to velocity sedimentation through a 5% sucrose step containing 0%, 2%, 5%, or 10% Triton X-100 and then through a 20% sucrose step. (D) Western blots were carried out on intact viral cores as described above; mA3 was detected using an anti-FLAG monoclonal antibody.

as judged by the relative abundance in the blots (Fig. 2D). These results highlight that the capsid of the gPr80-deficient virus is less stable than the virus with the triple viruses N-to-Q substitution. We can also conclude from this experiment that the levels of virion-packaged mA3 was comparable for all viruses, and that mA3 continued to be associated with p30 even when no viral envelope glycoprotein could be detected.

M-MLV asparagine mutants have compromised capsid stability

As an alternative approach to evaluate the structural integrity of the mutated viruses, we conducted a fate of capsid assay (197, 225, 427-429). M-MLV, MLV[N113Q/N505Q], M-MLV[N113Q/N480Q/N505Q], and M-MLV[CTA] viral preparations were normalized for p30 levels prior to infecting NIH 3T3 cells. Three hours post-infection, the cells were treated with pronase, washed, lysed, processed with a Dounce homogenizer and pelleted through 40% sucrose cushion to isolate intact capsid. An aliquot of the input samples pelleted through the dense sucrose was taken to normalize the pelleted fractions. As illustrated in Figure 3A and 3B, M-MLV, M-MLV[N113Q/N505Q], and M-MLV[CTA] all have similar levels of capsid that successfully entered the cell. However, the M-MLV[N113Q/N480Q/N505Q] mutant has approximately 20% less virus at this early stage of infection, implying there may be additional underlying defects with this virus. As expected, and in accordance with previous findings (225), M-MLV capsids are noticeably more stable than those of M-MLV[CTA] (Fig. 3C and 3D). In addition, both M-MLV[N113Q/N505Q] and M-MLV[N113Q/N480Q/N505Q] were less stable than wild type virus, approximately 40% and 60% less respectively (Fig. 3C and 3D). These data are directly reflective of our results with our previous assay in Figure 2B. This, taken together with the measure of viral fitness (Fig. 1), suggests that mutagenesis at key glycosylated residues of gPr80 impacts the structural integrity of Pr65 products, the matrix protein (N113), and capsid protein (N480/N505). However, the severely

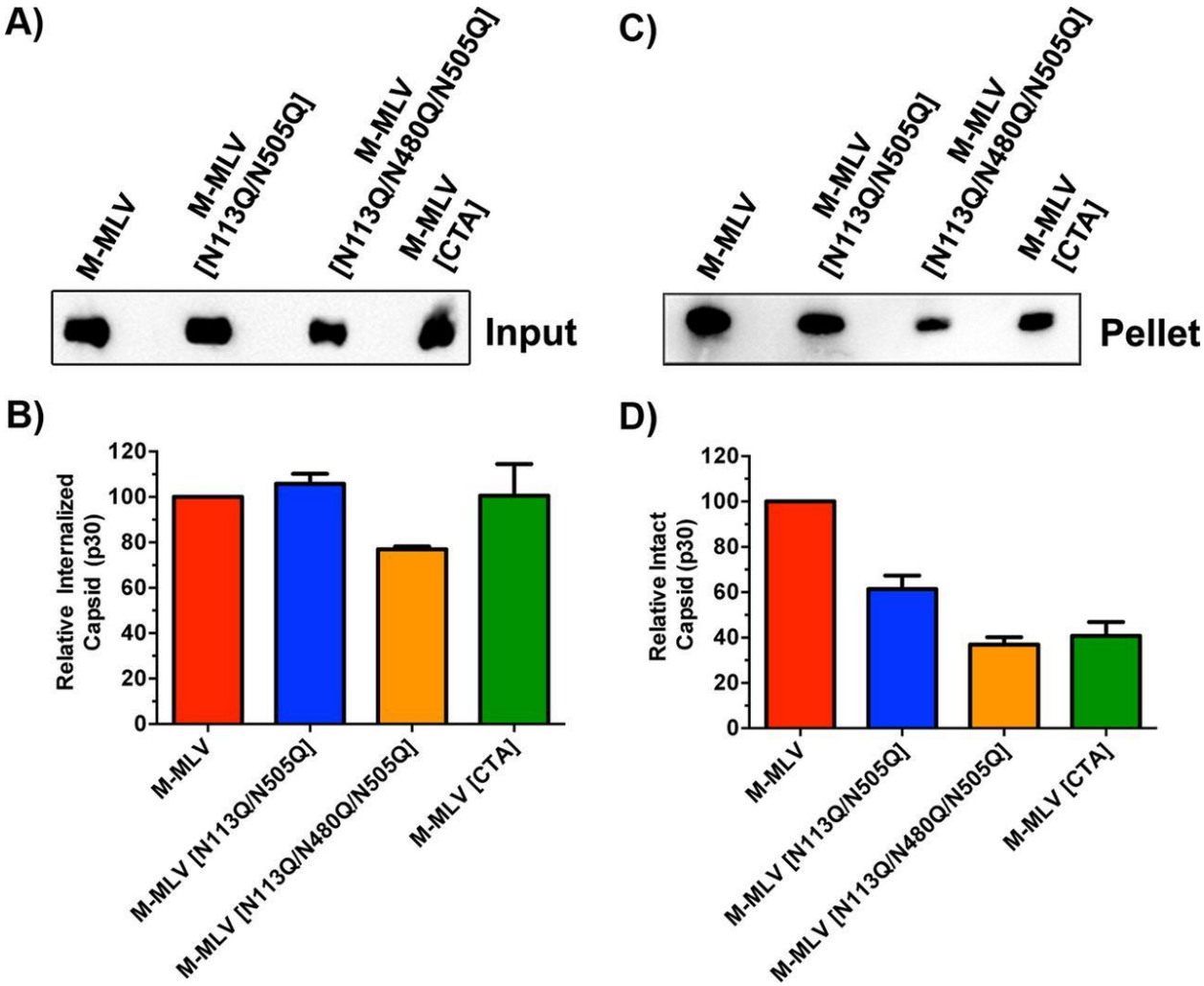

Figure 3.3. Intracellular fate-of-capsid assay.

(A) Western blot showing levels of CA p30 input protein. (B) Graphical representation of densitometry measurements for the samples from panel A. (C) Western blot revealing cytosol-derived capsids recovered following pelleting through a 40% sucrose cushion. (D) Graphical representation of densitometry measurements for the samples from panel C. Viruses from this assay were produced from NIH 3T3 cells chronically infected for 96 h, filtered through 0.45-µm filters, and further purified through a 20% sucrose cushion by ultracentrifugation. Capsid levels were normalized by p30 ELISA prior to infection.

reduced capsid stability of M-MLV[CTA] coupled with its unaltered replicative fitness suggests that these parameters are not related, at least for this virus.

M-MLV capsid stability and sensitivity to mA3 deamination are independent of *N*-linked glycosylation of gPr80.

A limitation in studying the glycosylation mutants is that both the gPr80 and the Pr65 polyproteins are impacted by alterations at the glycosylation residues. To further investigate the isolated impact of post-translational glycosylation we used two approaches. First, we employed the use of 293S GnTI- cells. Given that these cells do not have *N*-acetyl-glucosaminyltransferase I (GnTI) activity, and thus are unable to conduct complex *N*-linked glycosylation, they allowed us to uncouple the impact of diminished glycosylation complexity with gPr80 function. Surprisingly, loss of complex glycosylation was barely noticeable by SDS PAGE performed on gPr80 in cell lysates (Fig. 4A). M-MLV was produced and isolated from transfected 293S GnTI- and 293T cells and evaluated for p30 capsid stability as in Figure 2B. No difference was observed between these viruses (Fig. 4B). However, this does not exclude the possibility that simple glycans may still impair A3 activity. Infections were carried out with virus produced from both cell types and genomic DNA from the infected cells were analyzed by 3D-PCR for hypermutation. There was no important difference in terms of A3 restriction (Fig. 4C) or deamination intensity (Fig. 4D). This suggests that glycosylation complexity has no or little influence on the antagonistic effect of gPr80 on A3 function, at least in viruses with unaltered capsid stability.

The inhibitor tunicamycin was next used to evaluate the effect of completely preventing *N*-linked glycosylation. Figure 4E clearly shows that there is nearly a complete abolition of glycosylation on gPr80. Capsid stability was next evaluated on viruses produced from tunicamycin-treated infected NIH 3T3

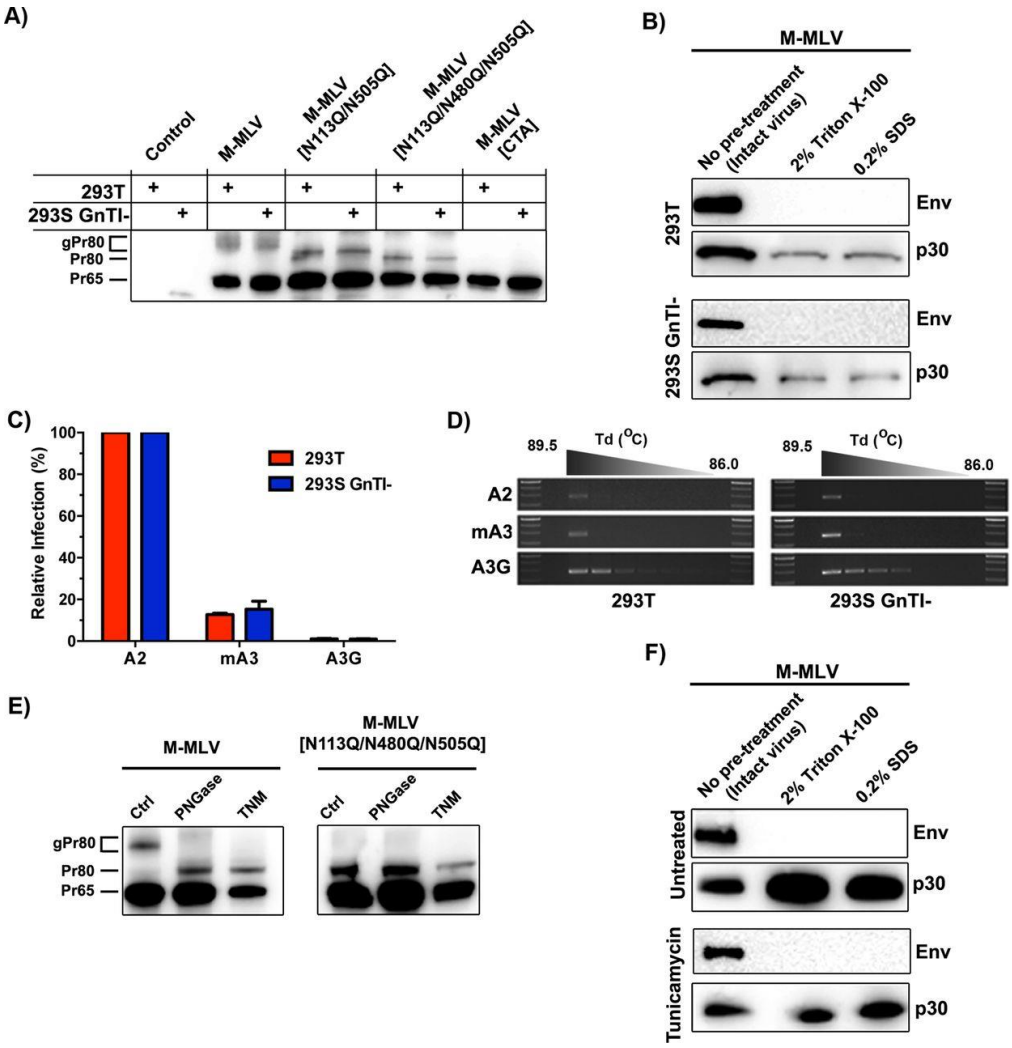

Figure 3.4. Influence of gPr80 glycosylation on capsid stability and resistance to mA3 deamination.

(A) Lysates from control (untransfected) or transfected 293T and 293S GnTI− cells were analyzed by SDS-PAGE. Protein expression was detected using the polyclonal anti-p30 antibody. (B) Viruses were processed as described in the legend to Fig. 2B. Western blots were carried out using monoclonal anti-p30 and anti-EGFP antibodies. EGFP was expressed as a fusion protein with the viral envelope glycoprotein (Env). (C) 293T and 293S GnTI− cells were cotransfected with M-MLV and APOBEC expression plasmids, and supernatants were harvested 48 h later. Infection in NIH 3T3 cells was measured by EGFP expression 48 h later. (D) Deamination intensity analysis by 3D-PCR. The analysis was performed on genomic DNAs extracted from the infected NIH 3T3 cells used for panel C. The results show a 279-bp product of the EGFP gene that was amplified using a decreasing denaturing temperature gradient (Td) from 89.5°C to 86.0°C. Larger numbers of bands indicate more intensely mutated products. (E) Western blot analysis of gPr80 expression in tunicamycin-treated cells. Untreated cells (left lanes) and PNGase F-treated lysates (middle lanes) were compared to tunicamycin-treated (TNM) cells (right lanes) for both M-MLV and M-MLV[N113Q/N480Q/N505Q]. (F) Capsid stability of viruses produced in tunicamycin-treated cells, determined as described for panel B.

cells. Once again, there was no apparent difference in capsid stability between the wild type and glycan-deficient viruses (Fig. 4F). This leads us to propose that the glycans alone are not responsible for capsid stability. Unfortunately, 293S GnTI- cells produce greatly diminished levels of virus, which were not conducive to carrying out quantitative fate of capsid assays. Furthermore, tunicamycin-treated cells yielded virus that was non-infectious, likely due to collateral effects on the viral envelope glycoprotein.

No detectable interaction between gPr80 and A3 proteins in the cytosol.

To gain further insight into how gPr80 antagonizes mA3 restriction and deamination, we next wanted to determine if the two proteins interact. It is well established that capsid inclusion of mA3 and human A3G into HIV-1 virions occurs through binding to the nucleocapsid (NC) region of the Gag polyprotein (226, 230, 430-433). Mouse A3 is also efficiently packaged into MLV particles (233, 319, 403), however, the 88 amino acid leader sequence of gPr80 does not appear to be involved, and the exact epitopes of NC to which mA3 binds have not yet been precisely mapped (224, 230). Here, we asked whether mA3 binds differently to gPr80 and the glycosylation-null Pr80[N113Q/N480Q/N505Q] protein, called henceforth Pr80[3Q] for simplicity. The gPr80 and Pr80[3Q] expression vectors have an ATG at the site of gPr80 protein translation instead of a CTG to increase protein translation efficiency. For our analysis, we prepared cytosolic lysates of 293T cells transfected with viral vectors (first 3 lanes), or with gPr80 and Pr80[3Q] expression vectors (last 2 lanes) (Fig. 5A). Western blot analyses show bands for Pr65, Pr80 and gPr80 can clearly be visualized where expected using our constructs.

Co-immunoprecipitation (Co-IP) analyses were next performed by capturing either FLAG-mA3 or FLAG-A3G from extracts of 293T cells co-transfected with gPr80 or Pr80[3Q]. The beads were recovered after overnight incubation and equal sample volumes were loaded on the gels for all Co-IP conditions. The

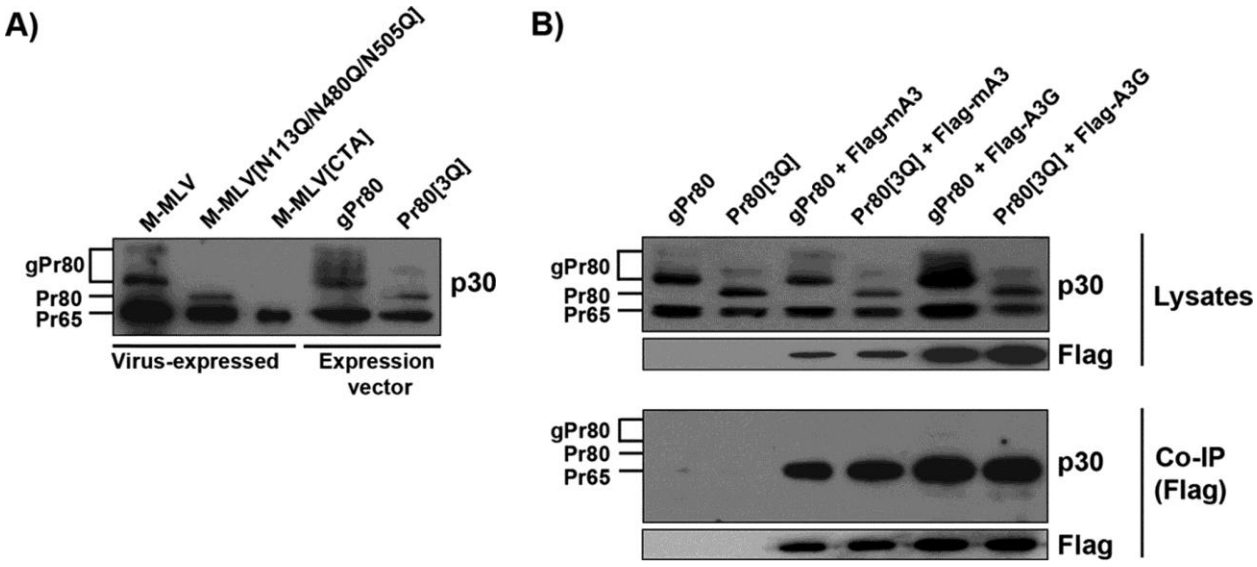

Figure 3.5. Binding of gPr80 to mA3 and A3G in the cytosol.

(A) Virus-expressed and plasmid-expressed gPr80 and Pr65 Gag proteins display similar profiles in transfected 293T cells. gPr80 and Pr80[3Q] were expressed from a CMV promoter. The gPr80 initiation codon was changed from CTG to ATG to improve expression. The Pr80[3Q] coding sequence was modified to replace the three glycosylated asparagines (N), at positions 113, 480, and 505, with glutamines (Q) (33). (B) Coimmunoprecipitation of FLAG-mA3 and FLAG-A3G with gPr80 and Pr80[3Q] in the soluble fraction of transfected 293T cell lysates. Protein interactions were revealed by Western blotting using anti-FLAG monoclonal and anti-p30 polyclonal antibodies.

blots were then stained with a p30 antibody. Our Co-IP results clearly show that mA3 and A3G only bind to Pr65 (Fig. 5B). Despite repeated attempts, we were unable to detect a signal for gPr80 or Pr80[3Q] in our experimental conditions. However, these results cannot exclude the possibility that our lysate conditions are not conducive to detecting an interaction between mA3 and Pr80. Additionally, mA3 interactions with gPr80 inside virions are at this stage unknown.

N-linked glycans do not inhibit A3 deaminase activity.

MLVs that express an unglycosylated Pr80 protein are more sensitive to hypermutation by mA3 (368). Although unlikely given the results of Figure 4, here we wanted to confirm through a different approach whether *N*-linked glycans or the gPr80 protein itself act as catalytic inhibitors of deamination. In order to address this issue, we purified FLAG-tagged mA3 and A3G, and V5-tagged gPr80 and Pr80[3Q] from transfected 293T cells. We then performed an oligodeoxynucleotide deamination assay using oligos containing a central 5'-CCC or 5'-TCC sequence for use in conjunction with A3G and mA3 respectively, as previously described (424, 426). The activity of both A3 proteins on their respective target oligo was first tested and showed cleavage efficiency as a function of the amount of input deaminase (Fig. 6A). The assay was then repeated using 800 ng of A3G and mA3 and by adding increasing amounts of purified gPr80 or Pr80[3Q]. We did not find any evidence that gPr80 acted as a catalytic inhibitor of A3 deaminase activity in our experimental conditions (Fig. 6B).

Capsid stability impacts susceptibility to deamination by all seven human A3 proteins.

In a previous report, we showed that absence of gPr80 or reduced glycosylation increases susceptibility to deamination by mA3 (368). Here we tested the sensitivity of M-MLV and M-MLV[N113Q/N505Q] to mA3 and to each of the seven human A3 proteins. M-MLV[N113Q/N505Q] with two of three possible

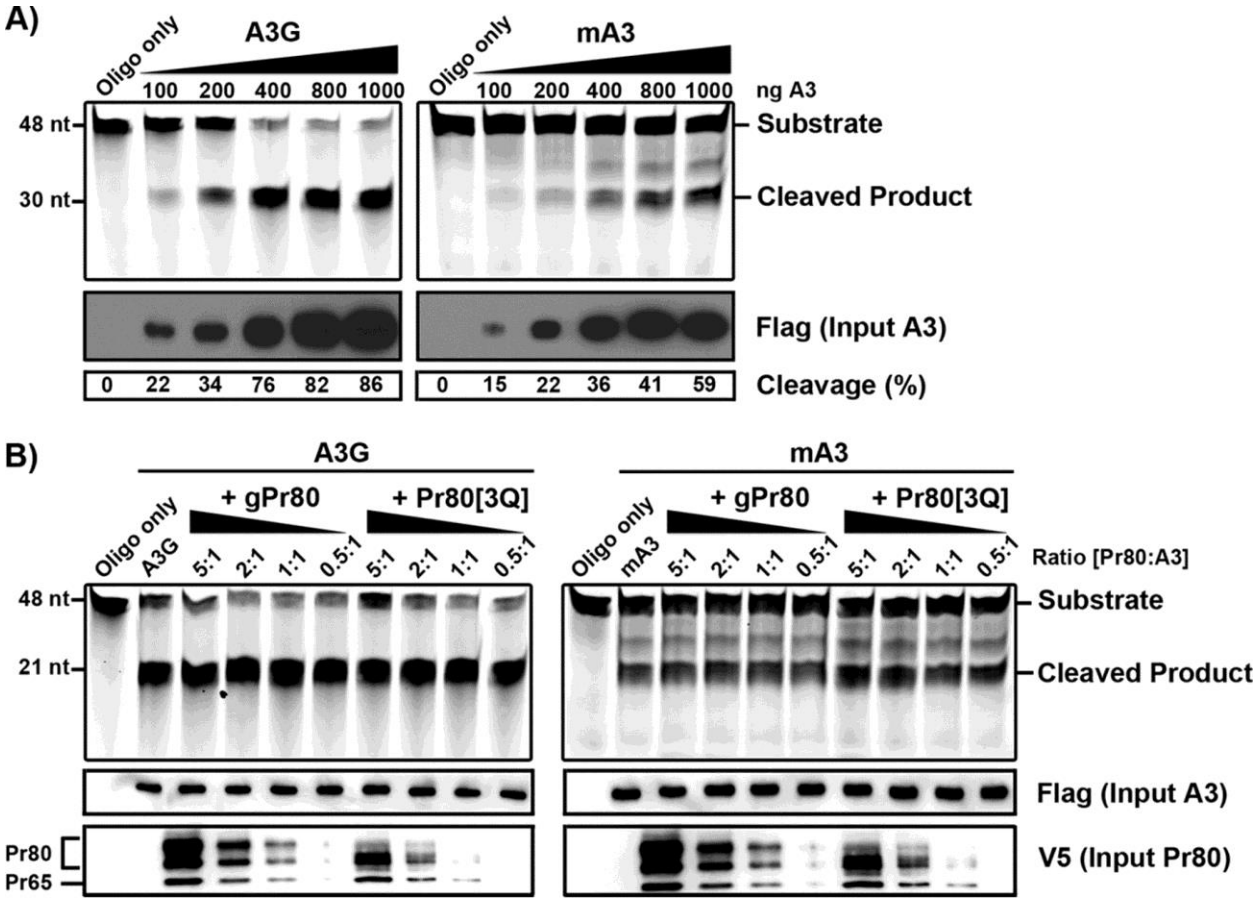

Figure 3.6. Oligonucleotide deamination assays.

(A) Oligonucleotide deamination was performed using purified mA3 and A3G. Lysates of 293T cells expressing FLAG-tagged mA3 or A3G were precipitated with anti-FLAG-conjugated agarose beads. Proteins were eluted from the beads and then used in oligonucleotide cleavage assays with 0.1 pmol/µl of FAM-labeled oligonucleotides containing TTC or CCC target sites. Deaminated oligonucleotides were treated with uracil DNA glycosylase (UDG), boiled, and resolved in an acrylamide gel. Input A3 protein and the efficiency of oligonucleotide cleavage are shown below the input gels. The percentage of cleaved oligonucleotide in each sample was determined using ImageJ software. (B) Oligonucleotide deamination assays in the presence of purified gPr80-V5 or Pr80[3Q]-V5 and 800 ng of mA3 or A3G were carried out as described for panel A. Molar ratios of gPr80/Pr80[3Q] to A3 are indicated above the gels. Input gPr80/Pr80[3Q] was assessed using a polyclonal anti-p30 antibody. The average cleavage efficiency was 84% for A3G and 46% for mA3 under all conditions in two independent experiments.

sites mutated was used because it displays only slightly reduced infectivity compared to the wild type virus, along with a minor reduction in capsid stability, as opposed to the triple mutant which has heavily compromised infectivity and capsid stability (Fig. 1E, 2B and 3) (368). Viruses were co-produced in 293T cells along with the various APOBEC proteins (Fig. 7A), harvested from the supernatant and normalized for p30 content by ELISA. Target NIH 3T3 cells were then infected at an MOI of 1 for the A2 co-transfection, while the others were infected with the corresponding amount of p30. Infection was assessed by measuring eGFP expression after 48 h (Fig. 7B). A3 proteins were expressed at comparable levels in all conditions (Fig. 7A).

Hypermutation analysis of integrated proviral sequences by 3D-PCR revealed an overall increase in mutation intensity with the M-MLV[N113Q/N505Q] mutant for all A3 proteins except for deaminase-inactive A2 (Fig. 7C). The increase in mutation intensity was most noticeable for A3A, A3G and mA3 in the double-mutant virus. DNA editing was confirmed by sequencing individual clones of amplified eGFP sequences from integrated proviruses (Fig. 7D). G-to-A mutation rates were calculated from 8 mutated clones and support the 3D-PCR data, whereby the most noticeable increases were seen with A3A, A3G and mA3 packaged into the MLV double mutant. Despite increases in mutation intensities, the effect on viral infection in single-round assays was relatively weak for mA3 and some other A3 proteins (Fig. 7B). Nevertheless, mutated viruses may be damaged in ways not detectable by this flow cytometry assay. Overall, these results imply that capsid stability has a primary role in influencing the susceptibility of M-MLV to A3-mediated deamination across multiple animal species.

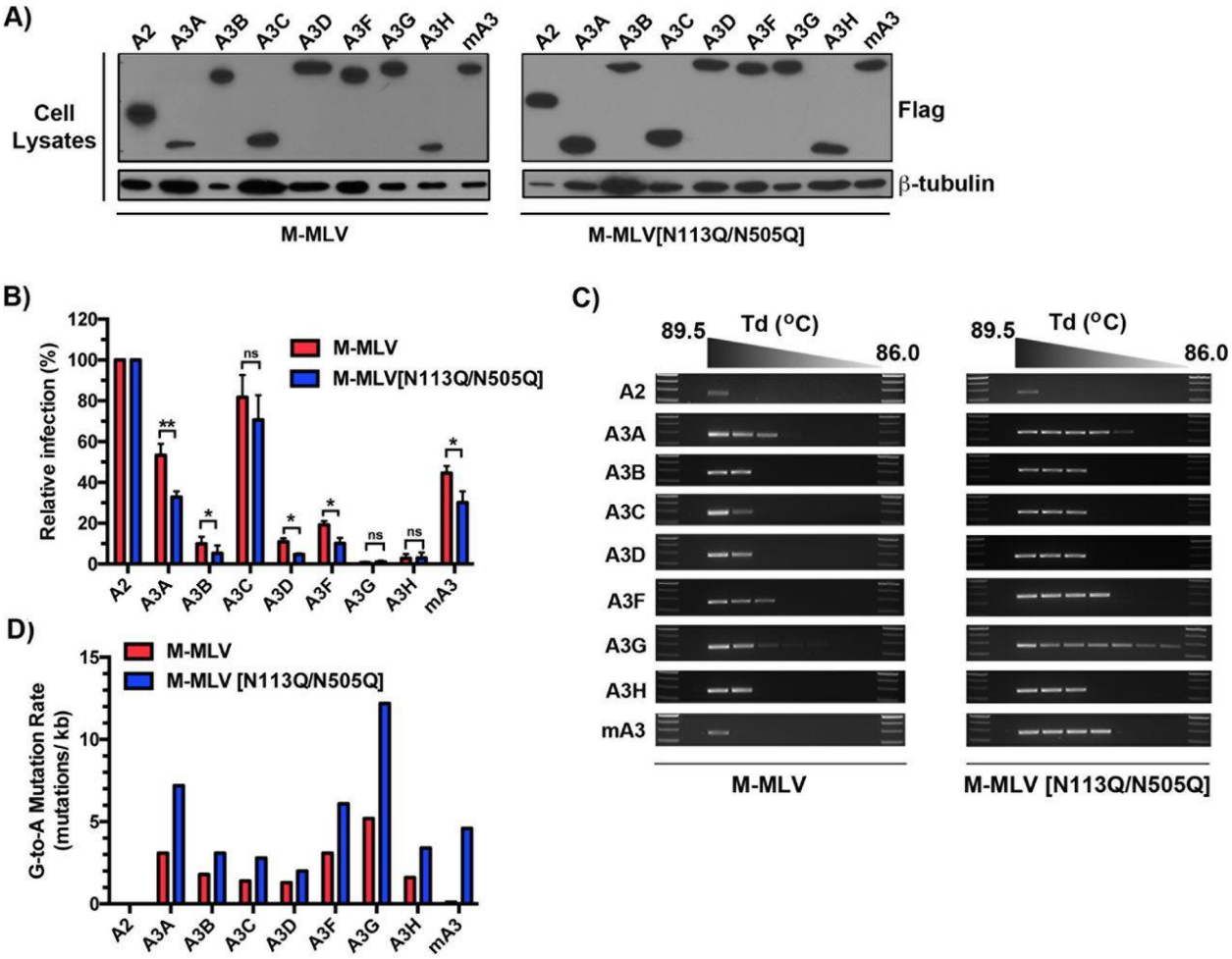

Figure 3.7. Impacts of glycosylation site mutations on deamination and restriction by all 7 members of the human A3 family.

(A) FLAG-tagged APOBEC expression plasmids were cotransfected with M-MLV or M-MLV[N113Q/N505Q] into 293T cells. Two days following transfection, cells were harvested and assessed for FLAG expression by Western blot analysis. The expression of β-tubulin was used as a loading control, and viral capsid protein expression was assessed using a monoclonal anti-p30 antibody. (B) NIH 3T3 cells were infected with p30-normalized amounts of the viruses produced for panel A. Infection was monitored as a function of EGFP reporter protein expression 48 h later by flow cytometry. Infection assays were performed for two independent transfections, with triplicate infection values for each. Results are presented as normalized mean infection values ± standard deviations (SD) relative to that for the A2 control. (C) Deamination intensity analysis by 3D-PCR. The analysis was performed on genomic DNAs extracted from infected NIH 3T3 cells at 48 h postinfection as described in the legend to Fig. 4D. (D) Genomic DNAs from infected target cells were amplified by PCR and cloned, and the EGFP gene was sequenced. Mutation rates reflect the averages for 8 independently mutated clones. P values were calculated by Student's t test. *, $P \leq 0.05$; **, $P \leq 0.01$; ns, $P > 0.05$.

Detection of gPr80 in the cell supernatant and virus preparations

Here we investigated how gPr80 glycosylated peptides interact with virions. It has been shown that the N-terminal cleavage product of gPr80 becomes associated with the cellular membrane and buds off with virions, while the C-terminus (containing mostly CA and NC) is secreted by the infected cell (72, 310). The N-terminal leader sequence alone with a functional ER signal and most of its transmembrane domain intact is insufficient the increase capsid stability (225). This implies that the C-terminus is likely responsible for capsid stability, either alone or in conjunction with the N-terminal peptide. However, according to these concepts, it is extremely challenging to explain how the glycosylated secreted C-terminal peptide has an effect on inhibiting deamination or increasing capsid stability if it is not actually present in viruses. Equally, it is unclear how the N-terminal peptide of gPr80 influences capsid stability, if it contains mostly the Leader, MA and p12 constituents, and is directed towards the luminal side of the viral envelope, as expected from Type II integral membrane protein (Fig. 1A). Here we generated a new gPr80 expression construct (gPr93FV) where we changed the Pr65 AUG initiation codon to GGG to prevent its translation by leaky scanning, and inserted a sequence coding for a 3X FLAG epitope tag immediately downstream of the leader sequence (Fig. 8A)(72). We also added a V5 epitope tag at the C-terminus of the protein. The apparent molecular weight of the unglycosylated form of the protein on our gels is 93 kDa.

The gPr93FV expression vector was transfected in the conditional presence of M-MLV[CTA] to complement the absence of virus-encoded gPr80. Cell lysates, supernatants and supernatants ultra-centrifuged through a sucrose cushion (Pellet) were analyzed by SDS-PAGE for gPr93 expression products using an anti-FLAG (Fig. 8B to 8D) or an anti-V5 antibody (Fig. 8E to 8G). Pr65 was only detected in cell lysates containing the viral vector (Fig. 8H). The mature p30 CA protein was detected in both the supernatants and in supernatant pellets, also only when the virus was present (Fig. 8I and 8J).

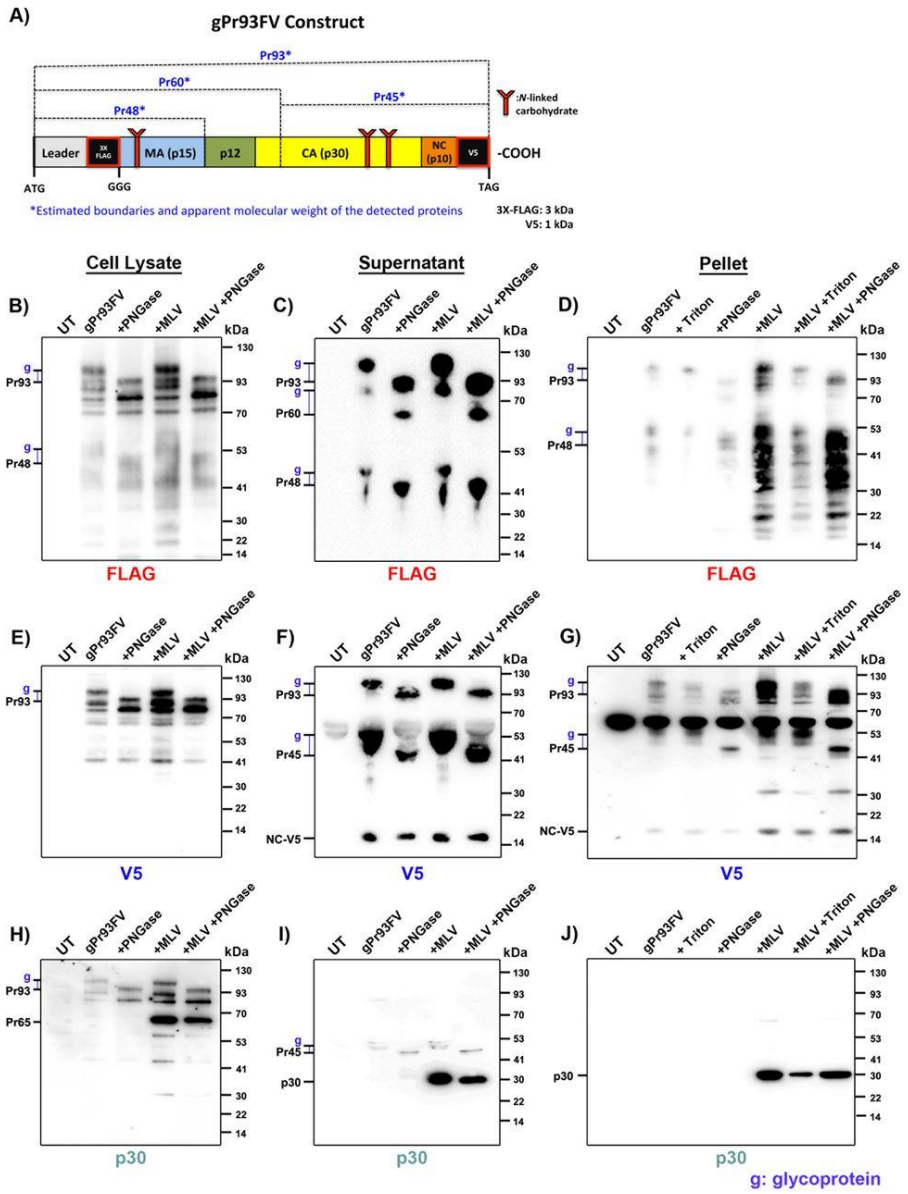

Figure 3.8. Association of gPr80-derived proteins with viral particles.

(A) Schematic representation of the dually tagged FLAG-V5-gPr80 protein (gPr93FV). The estimated positions of the detected peptides are indicated. Western blots were performed on cellular lysates of gPr93FV-transfected 293T cells (B, E, and H), 0.45-µm-filtered supernatants (C, F, and I), and pellets of supernatants ultracentrifuged through a 20% sucrose cushion (D, G, and J). Cotransfections with virus were performed with M-MLV[CTA] (+MLV). UT, untransfected. Samples prepared from cell lysates and supernatants were treated with PNGase F as indicated. Pellet samples were treated with 2% Triton X-100 for 30 min prior to ultracentrifugation as indicated. Tick marks to the left of each gel indicate glycoproteins of interest (g) along with their related unglycosylated forms used to estimate molecular masses. Samples were resolved by SDS-PAGE in triplicate and probed with anti-FLAG (B to D), anti-V5 (E to G), and monoclonal anti-p30 (H to J) antibodies. Data are representative of one experiment for at least three independent transfections.

The unglycosylated form of gPr93 appeared as a 93 kDa band in our gels (Pr93) due to the presence of the various tags. Detection of products in the supernatants and pellets when gPr93FV is transfected alone is indicative of virus-like particles (VLPs) and/or extracellular vesicles (EVs) packaging Pr93 or its cleavage products.

A number of glycosylated FLAG-labeled proteins were detected (indicated by a *g*), notably Pr93, Pr60 and Pr48, as evidenced by PNGase F treatment (Fig. 8A - 8D). Pr48 appears to be an N-terminal peptide that ends near or at the MA p15/ p12 junction. Pr60 appears to be the equivalent to the ~55kDa membrane-associated peptide of gPr80 (Fig. 1A) (72, 310). These three glycoproteins were clearly detectable in cell supernatants (Fig. 8C), but only Pr93 was clearly visible in virus pellets (Fig. 8D). Triton X-100 was used prior to pelleting the samples where indicated to dissolve EVs and strip the viral envelope. VLPs and virus cores are resistant to Triton X-100 treatment. This procedure ensures that the proteins detected are firmly associated with viral cores. Despite several attempts, multiple FLAG-containing cleavage products prevented clear identification of Pr60 and Pr48 in the virus pellets (Fig. 8D). Comparatively, there are much fewer detected bands containing the V5-tag in the pellets (Fig. 8G).

Full-length glycosylated Pr93 was also detected in cell lysates, supernatants and in pellets stained with anti-V5 (Fig. 8E to 8G). A large amount of this protein appears to be associated with the viral envelope (and to a much lesser extent, EVs and VLPs) in the pellets, as Triton treatment greatly diminishes, but does not abolish, the signal (Fig. 8G). An additional glycosylated protein of approximately 45kDa (Pr45) was also detected in supernatants and pellets only (Fig. 8F and 8G). We believe this protein to be equivalent to the ~40kDa secreted cleavage product of gPr80 that has also been previously reported (Fig. 1A) (72, 310). While Pr45 can easily be detected in all supernatants, only a very faint signal could be

detected in pellets, thereby indicating that most of this peptide is secreted in soluble form. However, in pelleted samples, the Pr45 peptide does appear to form detergent-resistant complexes, indicating that it may be cargo or a structural part of the capsid (Fig. 8G). Surprisingly, our p30 monoclonal antibody was extremely inefficient at detecting the full-length glycosylated Pr93 protein when the plasmid was transfected alone (Fig. 8H and 8J).

Glycosylated Gag has an unexpected orientation in the viral envelope

It was revealed in Figure 8D that full-length glycosylated Pr93 is detectable in pellets. Because viral pellets contain a mixture of virus, EVs and VLPs that co-purify by ultracentrifugation, here we sought to determine which Pr93 fragments are specifically virus-associated. To achieve this, we produced M-MLV[CTA] viruses in conditional presence of gPr93FV, as described in the previous section, purified them by velocity sedimentation through a sucrose cushion, and further isolated them with antibodies conjugated to magnetic beads directed against surface viral epitopes (V5 and eGFP). Full-length gPr80 has been previously characterized as a type II integral membrane protein, as such, our gPr93FV protein is expected to have its C-terminal V5 tag exposed to the external surface of the viral envelope (72). Additionally, our viruses have an envelope glycoprotein fused with eGFP (Env-eGFP) expressed on their surface (371). Recent work from our lab has revealed that the M-MLV envelope glycoprotein is nearly undetectable on EVs, and thereby constitutes a robust virus selection marker (373).

The V5 immunoprecipitation (IP) revealed many of the same V5-tagged proteins and fragments described in the pelleted fraction of the previous section (Fig. 9A to 9D). However, staining of V5-immunoprecipitated particles with anti-FLAG revealed almost exclusively full-length glycosylated Pr93 products (Fig. 9D). Unconjugated magnetic beads had no detectable binding to Pr93 (data not shown). In

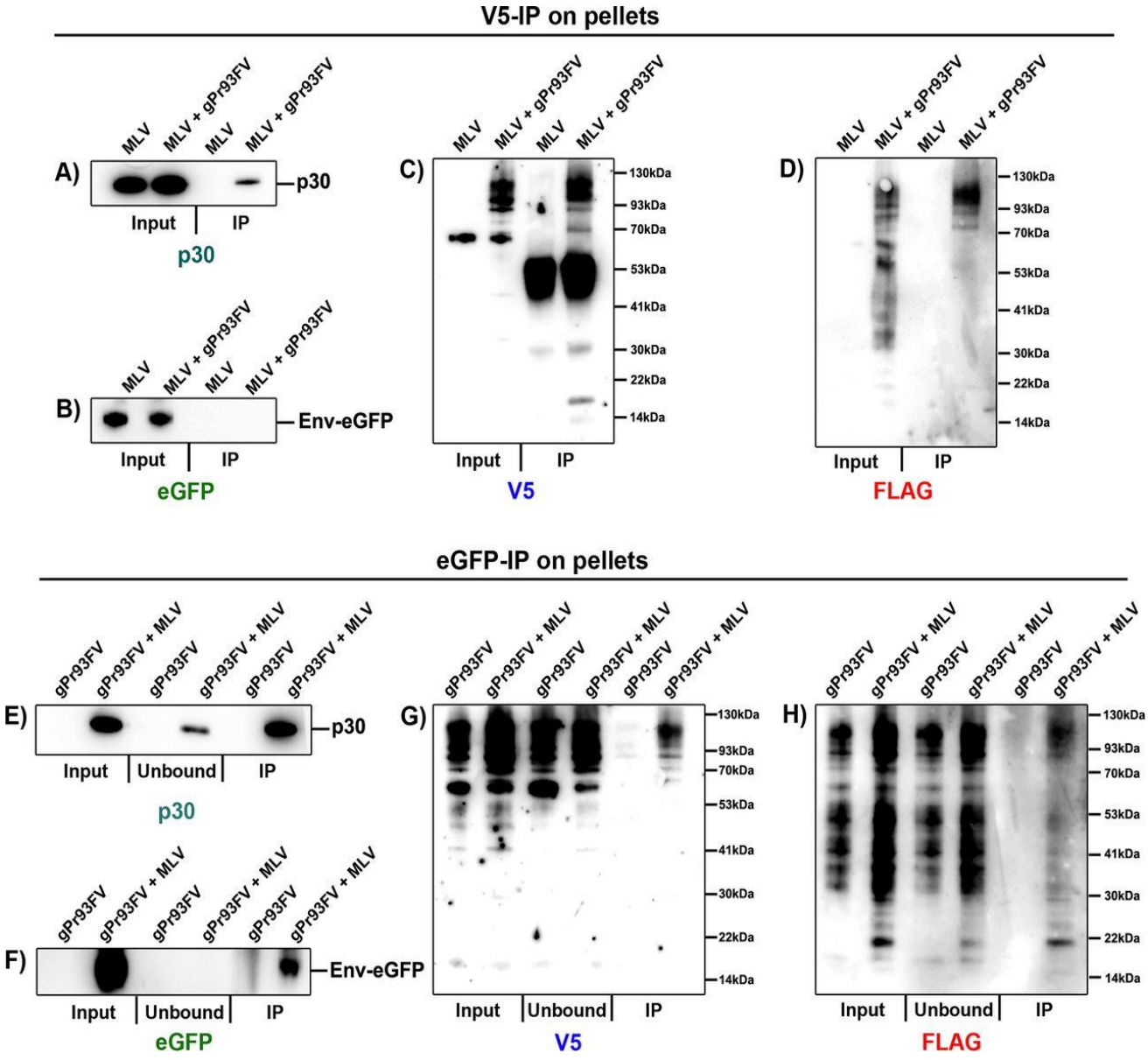

Figure 3.9. Glycosylated Gag adopts a type I integral membrane protein conformation in the envelope of viral particles.

293T cells were transfected similarly to those in Fig. 8. Supernatants were pelleted through a 20% sucrose cushion by velocity sedimentation and resuspended in PBS. (A to D) The viral preparations were immunoprecipitated by use of anti-V5-conjugated magnetic beads and washed with PBS. Input fractions (lysates) and anti-V5 IP purified particles were analyzed by SDS-PAGE and probed with p30 (A), EGFP (B), V5 (C), and FLAG (D) antibodies. (E to H) Viral preparations were also immunoprecipitated using anti-EGFP-conjugated magnetic beads. Input (lysates), flowthrough (unbound), and anti-GFP (IP)-purified enveloped particles were analyzed by SDS-PAGE and probed with p30 (E), EGFP (F), V5 (G), and FLAG (H) antibodies. Data are representative of one experiment for three independent transfections.

terms of viral constituents, p30 capsid was readily detectable, albeit at much lower levels than input (Fig. 9A). Most surprisingly, however, was that Env-eGFP levels were below the limit of detection of the assay in the immunoprecipitated samples (Fig. 9B). This implies that most particles that contain full-length glycosylated Pr93 with an antibody-accessible V5 tag are largely devoid of the viral envelope glycoprotein, and therefore constitute VLPs and not infectious virus.

In light of the data from the V5-IP isolation, we sought to analyze the population of particles that have an accessible Env-eGFP on their surface (Fig. 9E to 9H). Confirming the accessibility of envelope glycoprotein and the efficacy of this method, the eGFP blot reveals high levels of Env-eGFP in both input and IP fractions, but none in the unbound fraction (Fig. 9F). This is regardless of the length of the exposure (data not shown). In agreement with the V5-IP results, readily detectable p30 capsid protein was present in the unbound fraction of this isolation (Fig. 9E). Otherwise expectedly, abundant p30 capsid protein was detected in the IP fraction. On the search for Pr93, the FLAG blot revealed low levels of virus-associated full-length glycosylated Pr93 and a range of smaller FLAG-containing cleavage products (Fig. 9H). However, large amounts of full-length Pr93 and FLAG cleavage products remained in the eGFP-unbound fraction. Similarly, the V5 blot also showed low levels of full-length Pr93 associated with the virus and large amounts of it in the unbound fraction (Fig. 9G).

Given that that V5+ particles contained undetectable levels of Env-eGFP, and that full-length V5 and FLAG products are detected in Env-eGFP+ particles, the data suggest that glycosylated Pr93 is oriented as a Type I integral protein ($N_{exo}C_{cyto}$) in a large population of potentially infectious virus. The observation that glycosylated Gag can insert itself in the cellular membrane in a type I polarity was previously described by Fujiwara et al., but this study did not report that this phenomenon also occurred in egress

viruses (72). Finally, relatively large amounts of pelletable V5+ VLPs may also underline the discovery of a new mechanism whereby gPr80 induces the release of Env-deficient VLPs with exposed Gag sequences on their surface.

Discussion

Early research on gPr80 dates back to the mid 1970's when a glycosylated form of MLV gag was discovered at the surface of AKR lymphomas (292, 434). It was soon established that there were in fact two almost identical Gag proteins that were distinguishable only by the presence of glycosylation and by an additional short N-terminal leader sequence found on the glycosylated form (293, 294, 404). The first functional studies using gPr80-deficient viruses in cell culture systems were somewhat disappointing as the mutant viruses were replication competent with normal reverse transcriptase activity, and, most importantly, were nearly as infectious as their wild type counterparts (296, 305). However, these early infection assays were performed in NIH 3T3 and *Mus Dunni* cells, which are now known to express undetectable levels of the mA3 restriction factor. It is currently understood that one of the important roles of gPr80 is to antagonize restriction and deamination by mA3 (224, 225, 368). Looking back at early reports of infections assays in mice, it is clear that gPr80 has an important role in infection, spread and disease pathogenesis *in vivo* where mA3 is naturally expressed in cells targeted by murine retroviruses (302, 311, 423).

Several studies have clearly shown that mA3 restricts retroviruses *in vivo* and in primary mouse splenocytes (319, 399, 400). The strongest evidence that mA3 exerts selective pressure on retroviruses is the reversion of gPr80-deficient viruses to wild type in mA3-expressing mice but not mA3 knockout mice (225, 423). However, the impact of deamination by mA3 may not be as prominent as that of

human A3G, which restricts MLVs and HIV mainly through intense hypermutation (194, 421). Most murine retroviruses, like M-MLV, Friend MLV and MMTV, generally show no or very little signs of hypermutation; AKV MLV, on the other hand, shows clear but very modest levels of mA3-induced mutations (319, 399, 400). Nevertheless, even a mild increase in MLV susceptibility to deamination by mA3 would likely contribute to extinguishing the virus infection over time, as MLVs do not encode an A3 antagonist like HIV Vif. Although we found but a small decrease in infectivity as the mutation frequency increased by altering asparagine at position 113 and 505 in our assays (Fig. 7B), it is possible that the true effect of these mutations on viral replicative fitness may not have been observed in our experimental conditions. Single round infection assays, such as the ones used in this part of our study, are unable to reveal if overall virus replicative fitness and viral spreading are compromised by A3 mutations. Mutations in other parts of the virus could be deleterious, for example if critical residues of the catalytic centers of the integrase or reverse transcriptase genes were mutated. If this were the case, these *in vitro* assays would not immediately detect these perturbations.

In light of our previous observation that the number of *N*-linked glycans directly affects MLV sensitivity to mA3 deamination (368), we were curious to better understand the mechanism behind this phenomenon. It has now been ruled out that gPr80 negatively affects virion packaging or core localization of mA3 ((Fig. 2) and (224)). We also asked whether gPr80 or its sugars could interfere with the catalytic activity of mA3. We found no evidence that catalytic activity was affected, regardless of the mA3-to-gPr80 ratio in an oligo cleavage assay with purified proteins (Fig. 6). In fact, we found no evidence that mA3 and gPr80 naturally interact inside the cytosol (Fig. 5). mA3 is selectively packaged into MLV virions through an interaction with the MLV Gag protein. Lack of detectable protein interactions using the soluble fraction of cytosolic extracts may be indicative that gPr80 is maintained in an isolated cellular compartment up until the moment it reaches the cellular membrane when it is

recruited into assembling viral particles. In support of this, recent work has shown that gPr80 is produced in the rough endoplasmic reticulum and traffics through the Golgi apparatus to the cell surface (317). Given that neither the *N*-linked glycans nor the gPr80 protein itself affect the catalytic activity of mA3 in a test-tube assay, and that mutations at glycosylation sites on both the N-terminus and C-terminus of gPr80 influence deamination intensity (368), we proceeded to evaluate the role of capsid stability in more detail. Absence of gPr80 expression had an important impact on capsid stability, as did mutations at all three glycosylation residues (Figs. 2 and 3). Decreased capsid stability is the common feature of all MLVs displaying increased sensitivity to A3 deamination. What has not been fully resolved is the importance of *N*-linked glycosylation in preventing this mutator activity. Isolated disruption of glycosylation using inhibitors or GnTI-deficient cells appeared to have no impact on deamination intensity and/or capsid stability. If glycosylation does play a role in preventing A3 deamination in some manner, it does so in concert with decreased capsid stability.

Along these same lines, the improved capsid stability provided by gPr80 has been shown to prevent the premature decapsidation and cytosolic exposure of replication intermediates that could trigger innate immune responses (136, 225). Up until now, there was only evidence that the ~55 kDa N-terminus cleavage product of gPr80 could be detected in viral particles (224, 310). Furthermore, a previous study has shown that expression of the leader sequence of gPr80 alone did not rescue diminished capsid stability (225). The mystery as to how gPr80 increases capsid stability therefore remains. Our efforts to detect gPr80 peptides associated with viral particles have revealed several new pieces of information (Figs. 8 and 9). By expressing a dual tagged construct along with gPr80-deficient M-MLV, we were able using high affinity antibodies to detect interactions that have not been characterized before. We clearly showed that the full-length gPr80 (i.e. gPr93) and several of its C- and N-terminal domain peptides are associated with viruses, and more specifically with detergent-resistant viral cores. Additionally, full-

length gPr80 was also detected in cell supernatants and in pellets using antibodies against both V5 and FLAG epitope tags (Fig. 8). However, most of gPr80 appeared to be part of the envelope of viruses, VLPs and EVs, as the signal is greatly diminished upon detergent treatment. More in depth dissection of this issue using antibodies to capture external epitopes revealed that nearly all full-length gPr80 is present as a type I integral membrane protein in the envelope of infectious virus, and as a type II protein in Env-deficient VLPs (Fig. 9). However, this does not exclude the possibility that some infectious viruses harbor the previously observed ~55 kDa N-terminal peptide of gPr80 as a Type II membrane protein (72, 310). In fact, there is evidence that this fragment exists in our eGFP pull downs stained with anti-FLAG, however the abundance of FLAG-containing cleavage products makes it difficult to clearly resolve it (Fig. 9H). Importantly, however, a demonstration that complementation of the M-MLV [CTA] virus with gPr93FV restores capsid stability and deamination resistance will be essential to lend support to the physiological relevance of the observations made using the current laboratory system. Additionally, a formal demonstration that gPr80 also adopts such an unusual topology on the surface of the replicative wt virus is essential.

While the absence of the envelope glycoprotein on VLPs implies that these particles are non-infectious, it is entirely possible that they are still endocytosed, given the conserved YXXL motif present in the leader sequence of gPr80 (314). However, unlike Env-eGFP containing particles, they will not be able to escape the endosome. The presence of these VLPs stuck in endosomes could explain results observed in our fate of capsid assay. While normalizing to the same level of capsid input, gPr80-deficient M-MLV had noticeably less endocytosed intact capsid when compared to the WT virus (Fig. 3). Prior to this finding, the equal infectivity of these two viruses (Fig. 1C and 1E) was somewhat perplexing. Now it is clear, that an endocytosed intact virion, or VLP, may not be indicative of a productive infection when gPr80 is present. While this applies to our ecotropic MLV, it may vary with other amphotropic or xenotropic

strains (313, 317). This begs the question as to whether VLPs (and EVs) that express gPr80 as a Type II membrane protein influence adaptive and humoral immune responses in mice.

Given the very low levels of envelope glycoprotein on these VLPs, the role of gPr80 in antagonizing SERINC3 and SERINC5 incorporation into virions comes to mind. Recently, in a similar fashion to HIV-1 Nef, gPr80 has been shown to antagonize the effects of newly-identified restriction factors, known as SERINC3 and SERINC5, by preventing their incorporation into virions (215, 269, 270, 317). In fact, a Nef-deficient HIV-1 has its infectivity fully restored when complemented with gPr80 when SERINC3 or 5 is present (269, 270, 317). However, it is clear that the roles of gPr80 and Nef do not fully overlap, as Nef complementation does not rescue infectivity of gPr80-deficient MLV in some conditions (313). But given the Nef-like effect of gPr80 is mediated by its cytoplasmic N-terminal domain, dependent on the presence of the YXXL motif (314), and the type of viral envelop glycoprotein present (213, 317), it is tempting to speculate that VLPs may serve as decoys for the incorporation of SERINC proteins, sequestering them away from infectious virus. In all regards, further work should explore this new and intriguing avenue.

Overall our findings provide added insight into the mechanism behind gPr80 protection of MLV from host restriction. However, our understanding of gPr80 is not yet complete. *In vivo* or *ex vivo* evidence for gPr80 membrane orientation and VLP release must be confirmed. Additionally, if gPr80 is associated with EVs and VLPs alike, what are their impacts on host immune responses? Moreover, the relationships between Env, Nef, gPr80 and SERINC3 and 5 are still largely unresolved.

Acknowledgements

M.-A.L. holds a Canada Research Chair in Molecular Virology and Intrinsic Immunity. This research was supported by a grant from the Canadian Institutes of Health Research #89774 and an Early Researcher Award from the Ontario Ministry of Research and Innovation to M.-A.L. T.M.R. hold a QEII Graduate Scholarship of Ontario.

Chapter 4: Single-Particle Discrimination of Retroviruses from Extracellular Vesicles by Nanoscale Flow Cytometry

Preface: This chapter has been previously published as a research article.

Tang VA*, **Renner TM***, Fritzsche AK, Burger D, Langlois MA. 2017. Single-Particle Discrimination of Retroviruses from Extracellular Vesicles by Nanoscale Flow Cytometry. Sci Rep 7:17769.

https://doi.org/10.1038/s41598-017-18227-8

*Co-First Authors.

Author contributions:

V.A.T. and M.-A.L. designed the study. V.A.T., T.M.R., D.B. and A.F., carried out the experiments. V.A.T., T.M.R. and M.-A.L. wrote the manuscript.

ABSTRACT

Retroviruses and small EVs overlap in size, buoyant densities, refractive indices and share many cell-derived surface markers making them virtually indistinguishable by standard biochemical methods. This poses a significant challenge when purifying retroviruses for downstream analyses or for phenotypic characterization studies of markers on individual virions given that EVs are a major contaminant of retroviral preparations. Nanoscale flow cytometry (NFC), also called flow virometry, is an adaptation of flow cytometry technology for the analysis of individual nanoparticles such as extracellular vesicles (EVs) and retroviruses. In this study we systematically optimized NFC parameters for the detection of retroviral particles in the range of 115 - 130 nm, including viral production, sample labeling, laser power and voltage settings. By using the retroviral envelope glycoprotein as a selection marker, and evaluating a number of fluorescent dyes and labeling methods, we demonstrate that it is possible to confidently distinguish retroviruses from small EVs by NFC. Our findings make it now possible to individually

phenotype genetically modified retroviral particles that express a fluorescent envelope glycoprotein without removing EV contaminants from the sample.

Introduction

Retroviruses, such as the human immunodeficiency virus (HIV), are enveloped RNA viruses that range between 90 – 150 nm in diameter, depending on the species(435-437). When nascent virions egress from infected cells, they bear contents of the cytosol (e.g., proteins, mRNAs, miRNAs), as well as a portion of the cell membrane embedded with surface receptors to form the viral envelope(344, 438, 439). The phenotypic analysis of host-derived markers on the surface of individual viruses is of considerable interest, as it can provide information on the identity of the specific cell types that are infected in a host. However, a major hurdle in purifying retroviruses for single-particle characterization studies is the removal of EVs that are concomitantly released by the cells(345, 351, 440-442). EV is a broad term that describes all particles with a membrane bilayer released from cells; these can include exosomes, microvesicles, and apoptotic vesicles(325, 443-446). Small EVs, that are in the size range of retroviruses constitute a major contaminant of virus preparations as they are biochemically and biophysically similar to retroviruses in terms of their refractive indices, buoyant densities, and surface markers(344, 345, 447-449). Additionally, EVs can also package retroviral proteins and RNAs that further complicate discrimination(337, 450-453).

Nanoscale flow cytometry (NFC), also called flow virometry, is a new and powerful tool in the field of virology that enables the phenotypic analysis of the markers at the surface of individual virions(357, 361, 363, 365, 370, 442, 454-456). Virus populations can now be profiled and sorted in multi-parameter analyses, much in the same way as cells(361, 365, 370, 455, 457). However, NFC analysis with current instrumentation can be challenging due to the fact that these particles are at the limit of detection for flow cytometers. The research community is working towards the standardization of flow cytometer requirements, as well as acquisition settings and labeling procedures for NFC analysis, but there is yet to

be a consensus(458-460). To complicate matters, instruments of different make will have different optics, fluidics, electronics, detectors, and software. Even using the same instrument model, variations in sensitivity and resolution are common given that the instruments are operating at the threshold of their physical limits of detection. This can be much lower than the published manufacturer's specifications, but the onus falls on individual users to achieve this. Despite these caveats, several groups are currently using conventional flow cytometers originally designed for cells to analyze nanoparticles in the 90 - 150 nm size range(357, 361, 363, 365, 370, 442, 454-458, 460-464). Common instrument hardware additions for small particle detection include lasers with higher power and the use of photomultiplier tubes (PMTs) instead of photodiodes for forward scatter detection. Most commercial flow cytometers that claim small particle detection capabilities have a lower size limit in the 100 to 300 nm range based on detection of beads. However, there is currently no consensus in the field as to the minimum laser power required for the consistent detection and resolution of nanoparticles. While conventional flow cytometers clearly have the capacity to detect nanoparticles to varying degrees of sensitivity, standardization of instrument settings and sample acquisition procedures is necessary for cross-laboratory data validation and reproducibility.

Here we undertook a systematic approach to analyze viruses by NFC using a special order research product (SORP) BD LSR Fortessa flow cytometer. The model virus for our study is the Moloney murine leukemia virus (MLV), as it is a well-studied and characterized retrovirus that is non-infectious for humans. We identified the optimal settings for laser power and voltage to provide maximum particle enumeration and resolution, as well as sample dilutions and flow rates to minimize coincidence. We then compared data acquired using either fluorescence or side scattered light (SSC) as the threshold for detection. Finally, we compared various dyes and staining methods that can be used to discriminate MLVs from the EV contaminants.

Results

Analysis of single virions by NFC. For this study, we used the Moloney MLV expressing a chimeric envelope-eGFP surface glycoprotein (MLVeGFP). Moloney MLV is an enveloped virus that is nearly spherical with a mean diameter of 124 nm as measured by cryo-electron microscopy(436). It is estimated that there are approximately 100 envelope glycoprotein spikes per MLV virion, which is nearly an order of magnitude more than the 7-14 gp120 spikes found at the surface of HIV-1(465-467). We have shown previously that enveloped viruses can form aggregates when subject to centrifugation and repeat freeze thaw(370). For this reason, and to reduce other contaminants and purification artefacts, virus-containing supernatant from chronically infected NIH 3T3 cells cultured in 0.1µm filtered, serum and phenol red-free media was analyzed directly by NFC. We used a sample acquisition time of 60 seconds in all experiments of this study. The production of non-infectious particles was minimal with MLVeGFP, as there was a direct correlation between genome counts and infectious units (Fig. 1A). Similar high-efficiency viral genomic RNA (gRNA) packaging was previously reported for HIV-1(355).

To ensure that cellular debris is removed and that virus was present in single-particle suspensions, we used microfiltration (Fig. 1B). Virus-containing supernatants were passed through 0.45, 0.2 and 0.1 µm filters, diluted 100-fold in 0.1µm-filtered PBS, and analyzed by NFC. Filtration through a filter with a 0.45µm pore size removed approximately 10% of total eGFP+ particles, while filtering through a 0.2µm cartridge removed 30% of eGFP particles (Fig. 1B and 1C). Passing the sample through a 0.1µm filter removed nearly all eGFP particles, as expected, and displayed an overall residual particle profile similar to 0.45µm-filtered uninfected cell supernatant (Fig. 1B).

Because EVs can acquire viral proteins and nucleic acids when they are released from cells, we next sought to determine what proportion of all eGFP+ particles constitute virus. To measure the degree of MLV envelope-eGFP (Env-eGFP) incorporation into EVs, we cloned the coding sequence of Env-eGFP into

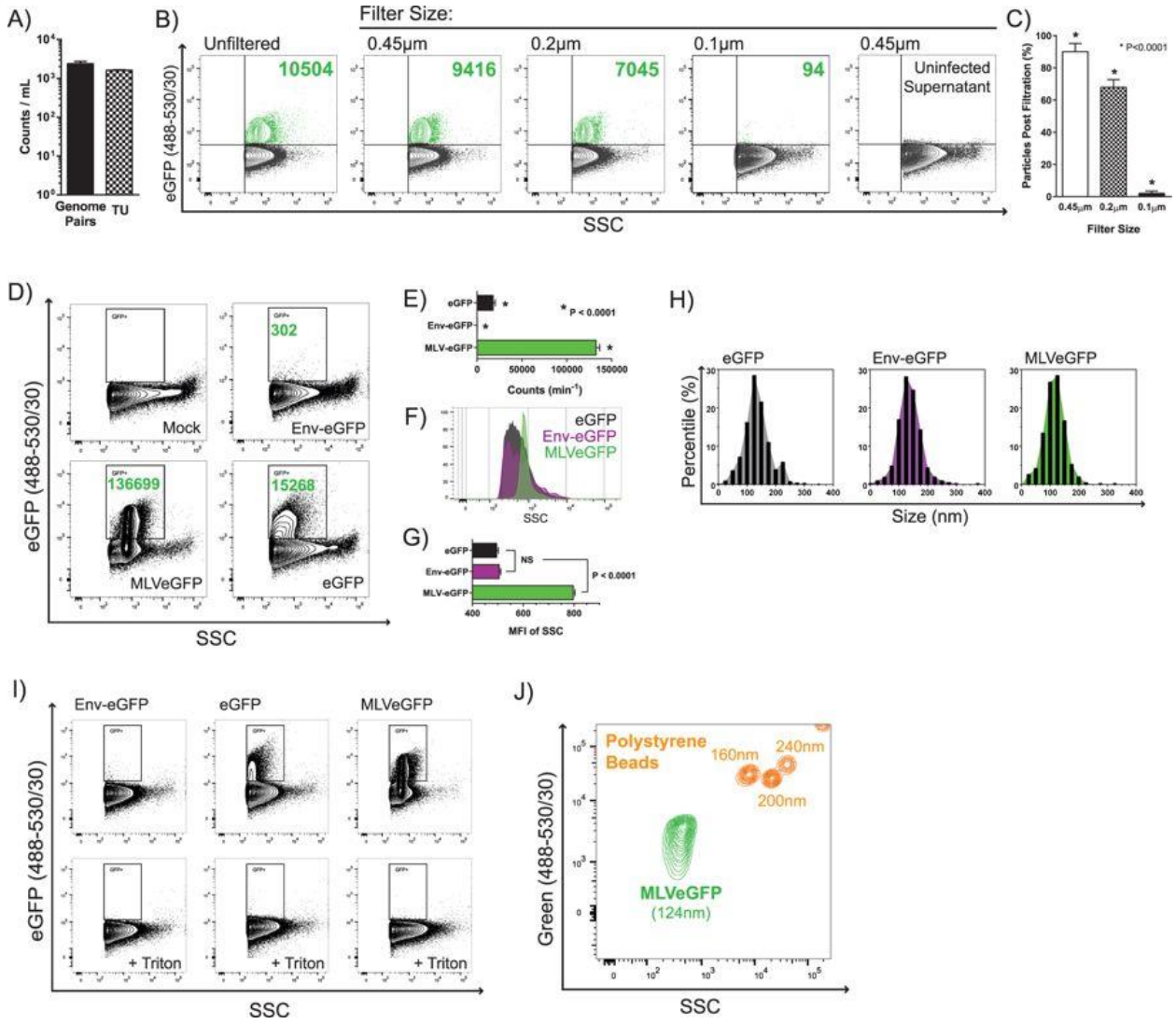
A)
Counts / mL
Genome Pairs
TU
B)
Filter Size:
Unfiltered
0.45µm
0.2µm
0.1µm
0.45µm
10504
9416
7045
94
Uninfected Supernatant
eGFP (488-530/30)
SSC
C)
* P<0.0001
Particles Post Filtration (%)
0.45µm
0.2µm
0.1µm
Filter Size
D)
Mock
Env-eGFP
MLVeGFP
eGFP
302
136699
15268
eGFP (488-530/30)
SSC
E)
eGFP
Env-eGFP
MLV-eGFP
* P < 0.0001
Counts (min⁻¹)
F)
eGFP
Env-eGFP
MLVeGFP
SSC
G)
eGFP
Env-eGFP
MLV-eGFP
NS
P < 0.0001
MFI of SSC
H)
eGFP
Env-eGFP
MLVeGFP
Percentile (%)
Size (nm)
I)
Env-eGFP
eGFP
MLVeGFP
+ Triton
eGFP (488-530/30)
SSC
J)
Polystyrene Beads
160nm
240nm
200nm
MLVeGFP
(124nm)
Green (488-530/30)
SSC

Figure 4.1. Analysis of MLVeGFP virions by NFC.

(A) MLVeGFP viral particles from chronically infected NIH 3T3 cell supernatants were filtered through 0.45 µm pore-sized PES cartridge filters and titered on NIH 3T3 cells for TU analysis. The same supernatant was analyzed by ddPCR for genome analysis. Both of these values were related back to the input volume of supernatant. (B) MLVeGFP from chronically infected NIH 3T3 cell supernatants were filtered through 0.45 µm, 0.2 µm and 0.1 µm pore-sized PES cartridge filters. eGFP+ particles are depicted in green and background noise and/or non-fluorescent particles in black. The number of eGFP+ events in the top right quadrant gate are indicated in green. (C) eGFP+ particle count post filtration as a percentage of the total eGFP+ particles in the unfiltered virus preparation. Statistical significance was calculated by 1-way ANOVA. (D) 293 T cells were transfected with expression plasmids for eGFP or Env-eGFP, or with the MLVeGFP expression plasmid. eGFP+ particles were analyzed by NFC as above. Transfection efficiency was approximately 75% in all conditions (data not shown). (E) eGFP+ particles from three independent transfections experiments as described in C, were tabulated. Average particle counts with standard deviation (S.D.) are presented. Statistical significance was calculated by 1-way ANOVA. (F) SSC intensity comparison of eGFP+ eGFP+ EVs and virus shows that MLVeGFP displays a more homogenous particle population that scatters light more intensely. (G) Quantification of SSC intensities (MFI) from three independent experiments with S.D., as described in F. P values were calculated by Student's t-test. (H) Representative size profiles of particles released from transfected 293 T cells expressing eGFP, Env-eGFP, and MLVeGFP. Samples were analyzed by nanoparticle tracking analysis (NTA). Results are displayed as the percentage of particles within 25 nm segments. (I) eGFP expression in EVs (eGFP and Env-eGFP) and MLVeGFP virus was abrogated by treatment with 0.05% Triton X-100. (J) Comparison of polystyrene green fluorescent beads and MLVeGFP on SSC vs. Fluorescence (Green 488–530/30).

an expression vector and transfected it into 293T cells. As a control for this experiment, MLVeGFP was produced by transfection as well. Transfection efficiencies for the eGFP and Env-eGFP plasmids were consistently between 45% and 55%, the transfection efficiency of the plasmid coding for MLVeGFP was around 8% - 10%. All samples were passed through a 0.45μm filter and diluted 100-fold in PBS prior to NFC analysis. Here we found that eGFP+ particles were 450-fold more abundant in the virus-containing cell supernatant than in supernatant containing EVs released from Env-eGFP transfected cells (Fig. 1D and 1E). Interestingly, when the cells were transfected with an expression plasmid coding only for eGFP, the number of eGFP+ particles was higher, representing 10% of the total eGFP+ count of the viral sample. These results indicate that by NFC analysis, Env-eGFP appears to be almost exclusively present in the culture supernatant when the virus is present. However, very low levels of particles clearly do express Env-eGFP when virus is absent. Particles released in cells transfected with eGFP or Env-eGFP displayed different side scatter (SSC) and fluorescence intensities than particles in the MLVeGFP containing supernatant (Fig. 1F and 1G). Viral particles had a higher SSC mean fluorescent intensity (MFI) and a more homogenous distribution, despite having a similar size distribution profile as measured by nanoparticle tracking analysis (NTA) (Fig. 1H).

To confirm that detected eGFP+ particles are indeed EVs and viruses, and not protein aggregates, all samples were subjected to treatment with Triton X-100 detergent, which is a effective way to dissolve EVs and strip the retroviral envelope leaving capsids intact (Fig. 1I)(354, 468). The eGFP fluorescent signal was lost in all samples. Therefore, the data presented in this figure support that most of the eGFP+ particles produced from MLVeGFP infected cells appear to be virus.

Finally, to emphasize the disparity of refractive indices and fluorescence between synthetic bead size standards and biological particles, we compared MLVeGFP with green fluorescent polystyrene bead populations that ranged from 160-240nm (Fig. 1J). Although MLVeGFP is only 40nm smaller in diameter than the 160nm beads, it displayed a SSC MFI that was approximately ten-fold lower. In comparison, the

difference in SSC intensity between the 160nm and 240nm bead populations was only about 3-fold. This comparison serves to demonstrate that a population of biological particles of similar size to a polystyrene bead population tends to display a much lower SSC MFI.

Impact of thresholding and sample dilution on electronic aborts and event counts. In order to have analyzed eGFP+ particles in the previous section, several NFC parameters had first needed to be optimized which include voltage, laser power, flow rates and sample dilutions. The following sections describe in detail how these settings were determined and also how they affect data acquisition.

Coincidence occurs when two or more particles are interrogated simultaneously(460-462, 469, 470). Flow cytometers are specifically designed to create a stream of single cells that are individually analyzed by the instrument. Because nanoparticles are much smaller than cells, it is more likely that several particles are coincidentally interrogated at the same time if the sample is too concentrated. Each event where the signal is above the designated threshold is registered as a voltage pulse with a height, width, and area parameter. The height is the intensity of the pulse, while the width is the time of flight of the particle during laser interrogation. Area is the integrated value under the voltage pulse, which represents the intensity of the signal over time as calculated using the height and width values. In BD FACSDiva, each pulse is assigned a windows extension, which is a specific measure of time at the beginning and end of each voltage pulse. If the windows extension of two events overlap, as in the case of coincident events, the signals will not be processed and will instead be aborted. This is what is called an electronic abort(471). Therefore, if a very concentrated sample is analyzed, a large number of electronic aborts will occur and data events will be discarded. This constitutes a major concern when analyzing nanoparticles by NFC.

Additionally, since the signal generated by biological nanoparticles is very dim (Fig. 1J), the threshold for detection is set at or near the lower limit. Low threshold values translate into reduced stringency of what is considered an event and this results in an increased likelihood of coincidence and background noise. Thresholding off of SSC will result in more particles analyzed by virtue of the fact that all particles, including any sample contaminants (i.e. PBS crystals, protein aggregates), will have size. On the other hand, a fluorescence threshold will generally be set at a slightly higher value to visualize only the fluorescently labeled particles of interest. This theoretically should result in fewer electronic aborts when comparing identical samples since there will be less total events processed. However, the compromise is losing information about total particles in the sample (i.e., very dim or unlabeled particles). Here we have systematically compared the effects of sample dilutions and flow rates on both SSC and fluorescence thresholding on total counts for our particles of interest.

Serial dilutions of a single sample of 0.45µm-filtered supernatant containing MLVeGFP produced from chronically infected NIH 3T3 cells was analyzed using the *low* sample flow rate setting. The undiluted sample was further analyzed on *medium* (med) and *high* settings to further exaggerate and emphasize the effects of coincidence and electronic aborts. The average virus titer in the undiluted filtered supernatant remained constant throughout replicate experiments at approximately $1.5 – 3 \times 10^6$ transducing units (TU)/mL. The samples were analyzed using fluorescence thresholding (Fig. 2A) or SSC thresholding (Fig. 2B), and the electronic abort rates were manually recorded. The optimal sample concentration and flow rate are where signal intensities stabilize and event rates linearly correlate with changes in sample concentration(460-462, 469, 470). Sample acquisition data was plotted to display

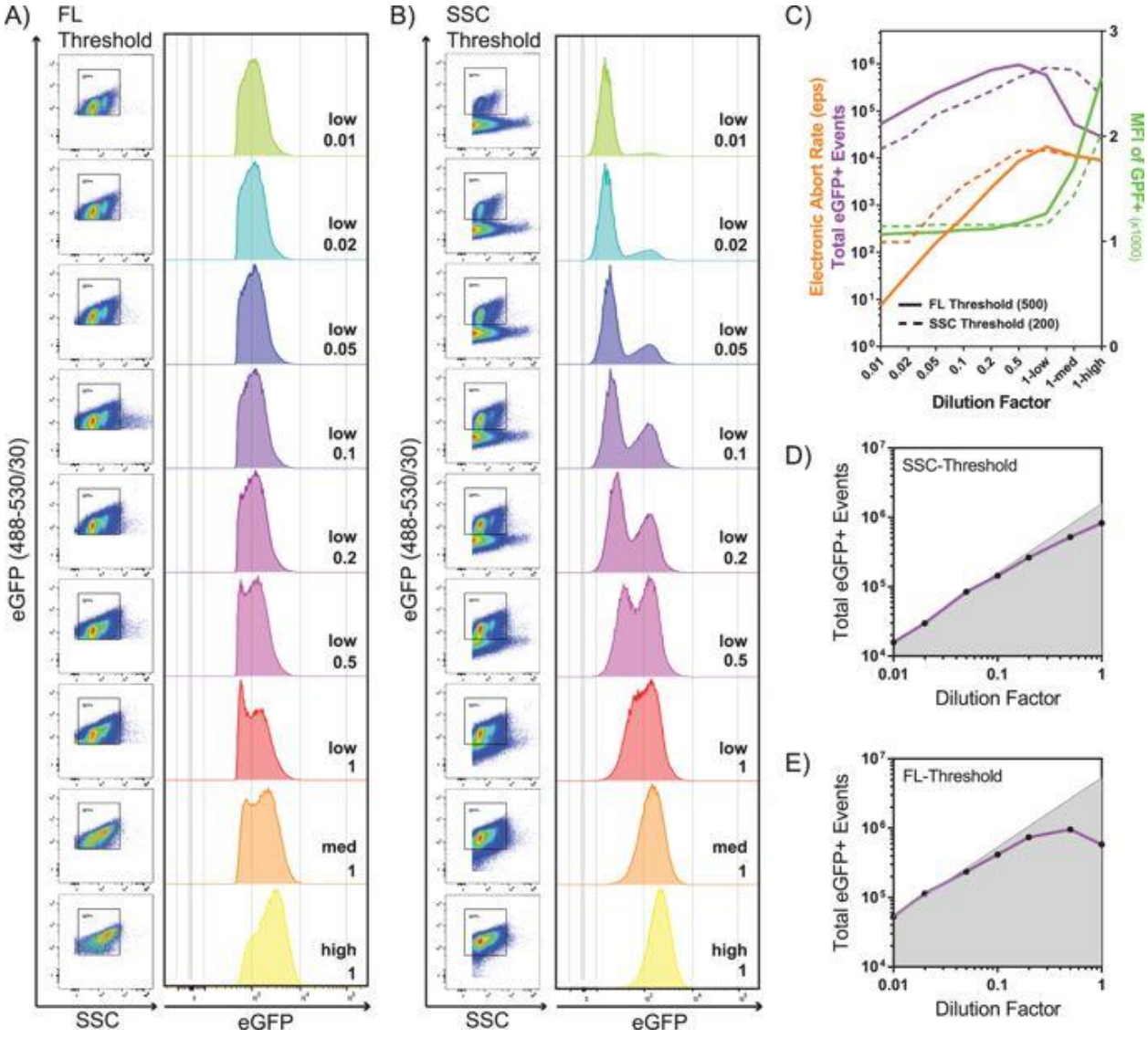

Figure 4.2. Effect of fluorescence and SSC thresholding on particle counts and electronic aborts. Effects of sample dilutions and flow rates on data acquisition.

(A) MLVeGFP was analysed with the event threshold set at a fluorescence intensity of 500 on green fluorescence channel (488–530/30) (FL-Threshold) and (B), SSC from the 488 nm laser at a fluorescence intensity of 200 (SSC-Threshold). Serial dilutions were performed on 0.45 µm-filtered cell supernatants: undiluted: 1; 1/2: 0.5; 1/5: 0.2; 1/10: 0.1; 1/20: 0.05; 1/50: 0.02; 1/100: 0.01. All diluted samples were analyzed with the sample flow rate set to low. Undiluted samples were analyzed with flow rates set to low, medium (med) and high. (C) Electronic aborts, Total eGFP events and median fluorescence intensity (MFI) of eGFP+ particles were plotted as function of the dilution factor and flow rate. SSC-threshold (dotted line) and FL-threshold (solid line). Total counts of eGFP+ particles were plotted for SSC-thresholding (D), and FL-thresholding (E), against a linear regression plot of predicted events (grey area) based on counts measured for the 1/100 dilution for each thresholding condition. Data is representative of two separate experiments.

electronic aborts, total events and median fluorescence intensity as a function of sample dilution and increasing flow rates for the undiluted sample (Fig. 2C). Total events acquired using SSC (Fig. 2D) and fluorescence (Fig. 2E) thresholding were separately plotted against a linear regression curve in order to emphasize the dilutions in the linear range. Linear regression of the predicted number of eGFP+ events (shaded area) was extrapolated using the eGFP+ counts from the most dilute sample for each thresholding condition. Our data shows that electronic aborts steeply rise as the samples become more concentrated. Consistent with coincidence, an increase in electronic aborts correlates with a rise in mean fluorescence intensity (MFI) of particles (Fig. 2C). Surprisingly, the increase in MFI is not seen until the undiluted sample is run at *medium* or *high* sample pressures. Total and eGFP particle counts are inversely proportional to the dilution factor of the sample when in the range of 0.01 to 0.05 (Fig. 2D and 2E). Contrary to what would be expected, particle counts appear to be slightly lower using SSC compared to fluorescence thresholding by a factor of 3. This is likely due to the higher rate of electronic aborts using SSC thresholding, even at a dilution of 0.01 (Fig. 2C). Taken together, the data shows that a stable MFI alone does not necessarily indicate that the sample is running at an optimum event rate. While there is a wide window of dilutions that provide constant MFI values, event count analysis provides a more accurate way of determining optimal flow rates and sample dilutions.

Effects of voltage and laser power settings on particle detection, resolution and electronic aborts. Here we systematically measured the effect of increasing voltage and laser power on our virus preparation (Fig. 3A). We began with the 488 nm laser at full power (300 mW) and increased the SSC voltages in increments of 50 V, and then gradually reduced laser power all the way while keeping eGFP MFI of our population of interest constant. In a subsequent acquisition set, we also increased green fluorescence (488-530/30) detector voltage in increments of 100V (while keeping the SSC MFI constant) to determine the range of settings at which eGFP+ particles are detected (Fig. 3B). Threshold was set on SSC off the 488 nm laser at the lowest value permitted by our acquisition software, which is 200 relative

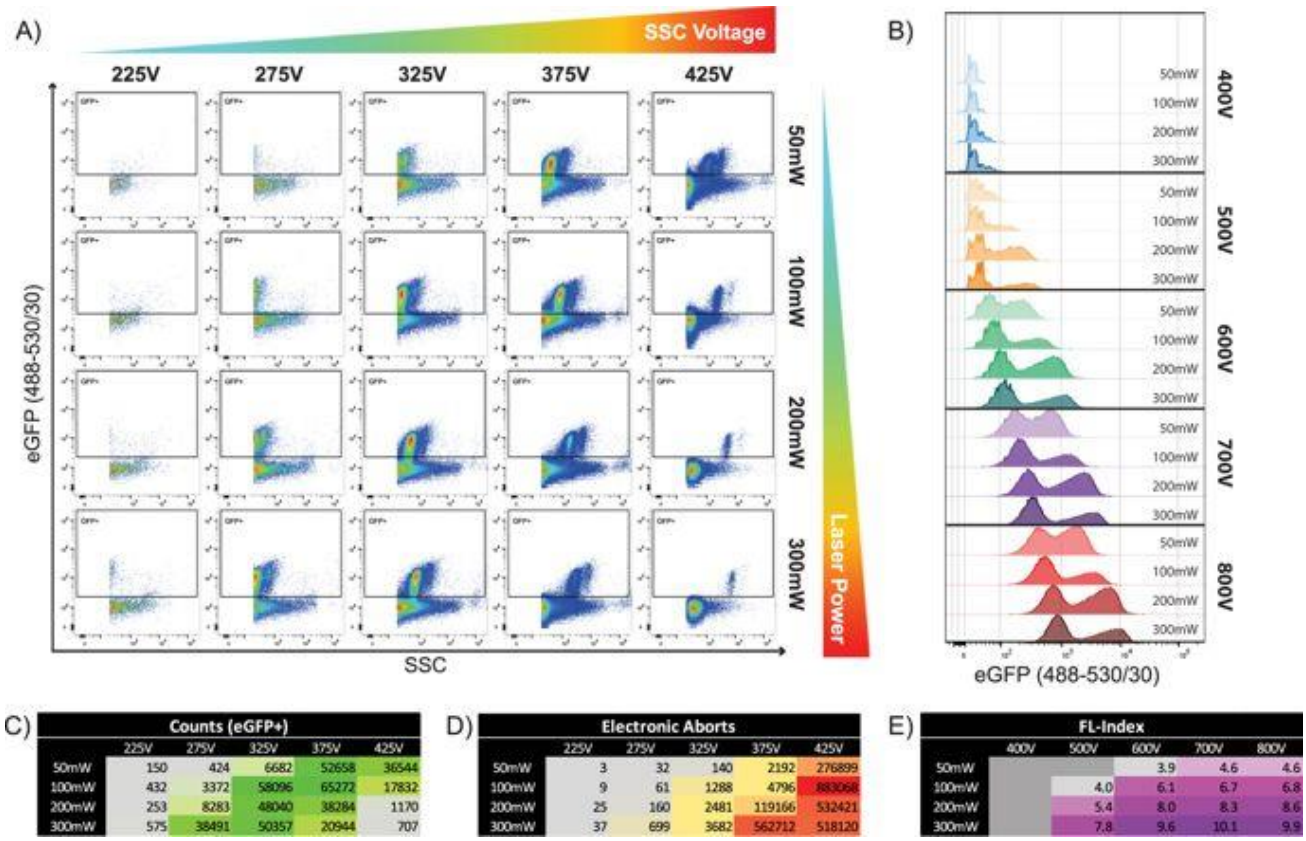

C) Counts (eGFP+)

	225V	275V	325V	375V	425V
50mW	150	424	6682	52658	36544
100mW	432	3372	58096	65272	17832
200mW	253	8283	48040	38284	1170
300mW	575	38491	50357	20944	707

D) Electronic Aborts

	225V	275V	325V	375V	425V
50mW	3	32	140	2192	276899
100mW	9	61	1288	4796	883068
200mW	25	160	2481	119166	532421
300mW	37	699	3682	562712	518120

E) FL-Index

	400V	500V	600V	700V	800V
50mW			3.9	4.6	4.6
100mW		4.0	6.1	6.7	6.8
200mW		5.4	8.0	8.3	8.6
300mW		7.8	9.6	10.1	9.9

Figure 4.3. Effects of laser power and PMT voltages on fluorescence and SSC.

MLVeGFP was analysed with systematic adjustments of voltage for detection of green fluorescence and SSC off the 488 nm laser. (A) Increments of 50 V were made on SSC off the 488 nm laser from 225 V to 425 V while maintaining a consistent MFI for the eGFP+ population on the green fluorescence channel (488nm-530/30), while simultaneously increasing laser power from 50 to 300 mW. Threshold was set at SSC fluorescence intensity 200. (B) The same voltage and laser power adjustments were made on the green fluorescence channel while maintaining constant the MFI in SSC of the eGFP+ population. (C) Tabulation of the number of eGFP+ events in gates set in A. (D) Tabulation of the number of electronic aborts generated during the acquisition of each condition described in A. (E) Fluorescence Index calculated for each condition portrayed in B. FL-index = (MFIeGFP+ − MFIeGFP−)/SDeGFP−. Data is representative of three separate experiments.

fluorescence intensity units. We chose to threshold off of SSC to include detection of all fluorescent and non-fluorescent events. Because acquisition is carried out on the same sample, changes will reflect the effects of the settings. When voltages were increased on SSC, the noise and event rate also increased to a certain limit (Fig. 3C), which correlated with increased electronic aborts (Fig. 3D). The increased electronic abort rate at higher SSC voltage settings resulted in a diminished number of total eGFP+ particles being acquired.

When comparing data collected for a given SSC voltage setting, increase in laser power resulted in an increase in the separation of the MFI of SSC signal intensities between the eGFP+ and eGFP- populations (Fig. 3A). This is most evident in the voltage range between 325 to 425 V for SSC, where the eGFP+ population is above threshold on SSC. Furthermore, peak particle counts was reached at a lower voltage as laser power increases (Fig. 3C). This tracked with electronic aborts, which were at their maximum when laser power and PMT voltages were at their highest settings (Fig. 3D).

When laser power and voltage on the green fluorescence channel were increased, it was evident that signal intensities of both the eGFP+ and eGFP- populations were also increased (Fig. 3B). To determine if the increase of laser power resulted in an increase in separation of the positive and negative populations in the green fluorescence channel, a fluorescence index (FL-index) value was calculated. This value is based on the difference in the MFI of the eGFP+ and eGFP- populations divided by the standard deviation of the eGFP- population (Fig. 3E). Samples where there was no clear resolution of an eGFP+ population were omitted (grey boxes). When comparing samples acquired at the same voltage, higher laser power provided improved resolution of the fluorescence signal (defined by the separation of the positive population from the negative) as represented by a higher FL-index value (Fig. 3E). These results clearly indicate that our virus can be detected over a wide range of voltage and laser power settings, however greater laser power more noticeably improves fluorescence and scatter resolution.

Discrimination of retroviruses from extracellular vesicles using fluorescent dyes. To date, several groups have demonstrated the ability to label EVs and viruses through the use of commercially available dyes(370, 454, 457, 460, 472). Dyes that target different cellular components, such as proteins, lipids and nucleic acids, have been proven effective to stain EVs and viruses in flow cytometry applications. However it has yet to be demonstrated that these methods can be used to discriminate between viruses and EVs.

To identify both virus and EV populations in our infected cell supernatants, we used fluorescent dyes that target cellular membrane components. Dyes were selected over the use of antibodies due to their ability to stain particles based on their biochemical constituents. Dyes are also not subject to some of the limitations of antibodies such as low surface antigen expression, epitope heterogeneity, and particle aggregation(370). There is currently a large number of commercially available dyes that target different molecules and cellular components. Using supernatants containing MLVeGFP, we first tested lipid dyes DiD, DiI, FM4-64, fluorescent sphingolipid (Ceramide-BODIPY TR) and fluorescent phospholipid (DHPE-Rhodamine). Several groups have published methods to directly label virus with dye(473-476), however these studies did not account for EV contamination in virus sample preparations. In our system, virus particles are distinguished from EVs by the surface expression of Env-eGFP. EVs are largely devoid of Env-eGFP on their surface (Fig. 1D), and therefore will only emit fluorescence at the wavelength of the dye.

For all the dyes tested, the direct sample staining approach discriminated virus from EVs by strongly labeling EVs while not detectably labeling virus (Fig. 4). Ceramide-BODIPY TR was the only dye that labeled the virus population at a low level, which was not completely resolved from background (Fig. 4E). Since excess dye was not washed away in this method, stained particles were detected in the PBS controls for DiI, DHPE-rhodamine and Ceramide-BODIPY TR, but not with DiD or FM4-64. This may

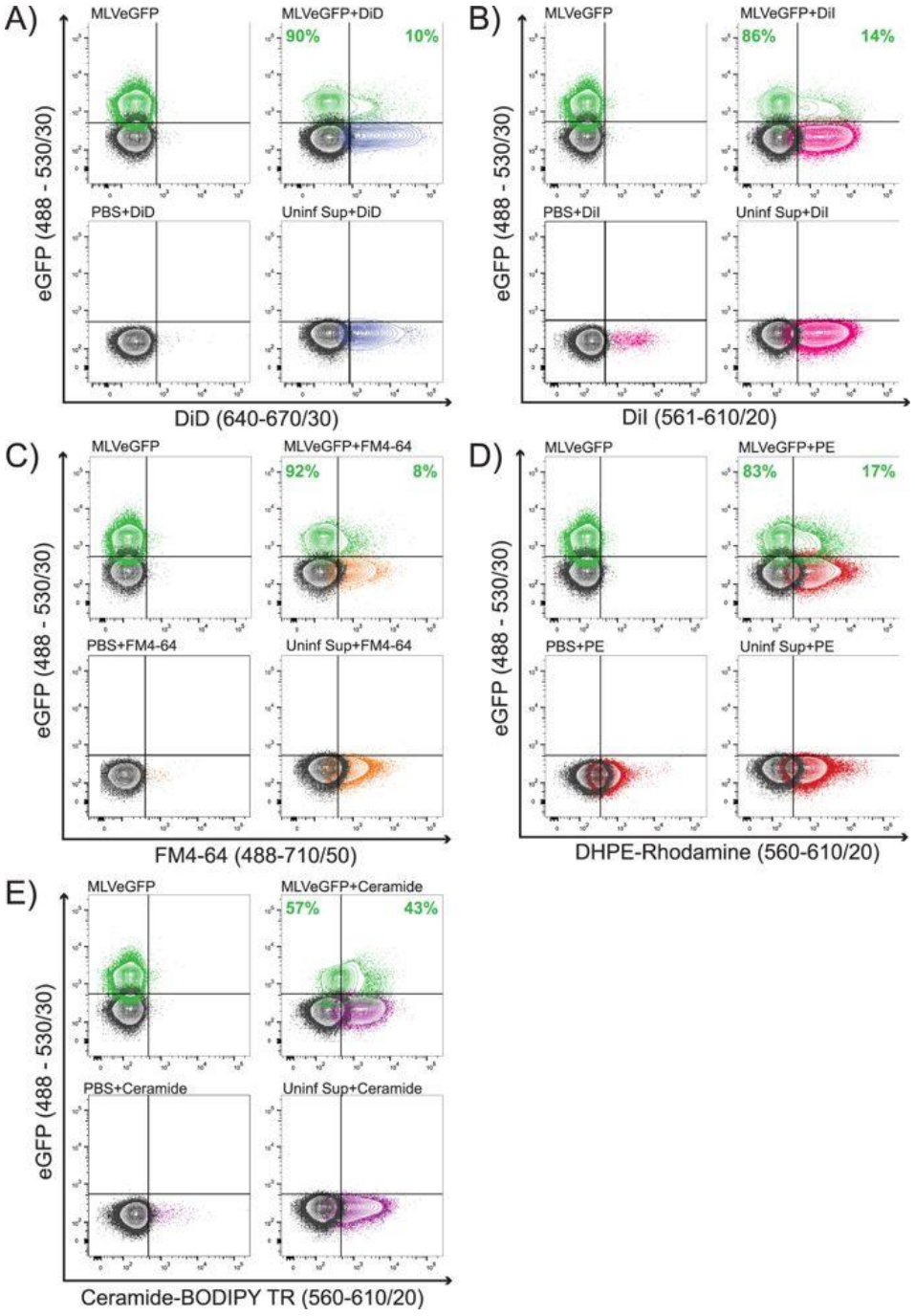

Figure 4.4. Direct staining of virus.

MLVeGFP viruses from chronically infected NIH 3T3 cell supernatants were labeled with (A) DiD, (B) DiI, (C) FM4–64, (D) Rhodamine-1,2-DihexadecanoylPhosphatidylethanolamine (DHPE-Rhodamine), and (E) Ceramide-BODIPY TR. Samples were then analyzed by NFC without purification. eGFP+ particles are depicted in green, background noise or non-fluorescent particles in black, dye-labeled particles in color (other than green). The distribution of total dye-labeled and unlabeled eGFP+ particles is indicated in green. Included in each panel: unstained virus (MLVeGFP), stained virus (MLVeGFP+ dye), dye alone (PBS + dye), and uninfected supernatant with dye that serves as an EV-only sample (Uninf Sup + dye).

reflect insoluble dye aggregates or micelle formation as evident with other lipophilic dyes(472). In this method of direct labeling, we show that the majority of viruses did not uptake dye, except for a small fraction of dual labeled particles that consistently represented between 8 – 17% of the virus population.

Our next approach was to stain virus-infected cells *in vitro* such that virus and EVs would egress directly from fluorescently labeled lipid membranes. To our knowledge, this method has been shown to label EVs, but has yet to be shown to label retroviruses. The same panel of dyes as above were tested. Staining on cells was confirmed by fluorescence confocal microscopy (Fig. 5A-5E, *right panels*). The population of MLVeGFP virions indirectly labeled with DiD, DiI and FM4-64 was nearly completely resolved from noise by each of these dyes (Fig. 5A, 5B, and 5C). However in this indirect staining method, virus as well as EV populations were labeled by the dyes, as seen with the EVs released from uninfected cells. DHPE-Rhodamine did not significantly label MLVeGFP (Fig. 5D), while Ceramide appeared to label similarly to the direct staining method, and again, was unable to resolve the virus population from the background (Fig. 5E).

Next we assessed if dye-labeled viruses remained infectious. This could be of use for downstream applications. DiI stained cells were excluded from this assessment, as it is chemically analogous to DiD. The effects of solvents were included as controls. The infectivity of viral supernatants produced in DiD and Ceramide labeled cells was abrogated, while DHPE-Rhodamine and FM4-64 labeled cells produced virus with significantly reduced infectivity (Fig. 5F). Although, virus infectivity may be compromised by the dyes, we also assessed whether treating the infected cells with the dyes affected viral particle release. Indeed, fewer viral particles were released with most of the dyes (Fig. 5G), however this did not account for the total loss of infectivity. To confirm that fluorescent particles were indeed viruses and EVs, samples were treated with 0.05% Triton X-100. The EV population was abolished by detergent treatment, as was eGFP fluorescence emitted by the virus (Fig. 5H).

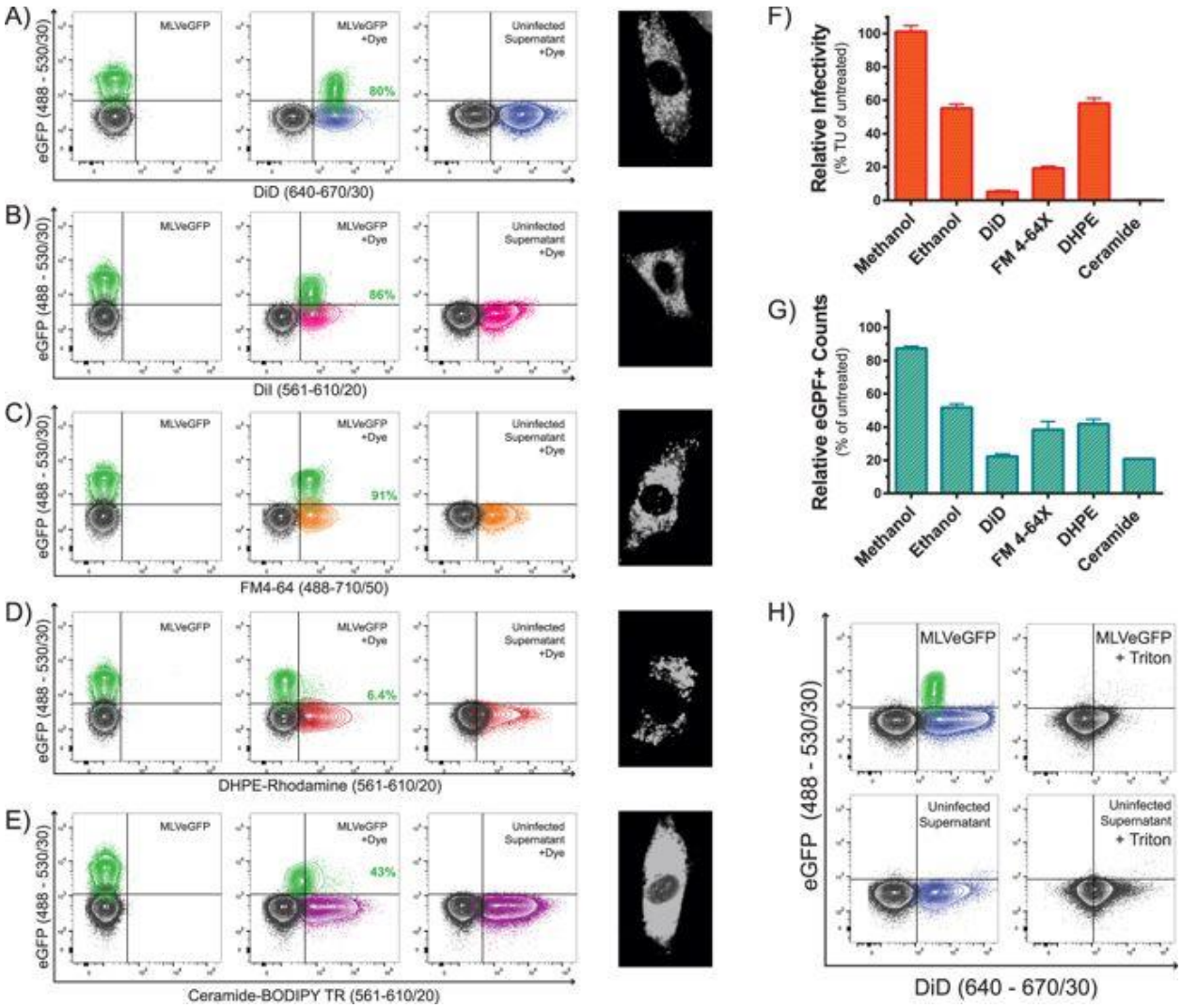

Figure 4.5. Indirect staining of virus.

Supernatants of chronically infected and uninfected cells labeled with (A) DiD, (B) DiI, (C) FM4-64, (D) DHPE-Rhodamine, and (E) Ceramide-BODIPY TR were analyzed by NFC. (F) Relative virus infectivity (transducing units (TU) per mL) and (G) counts of eGFP+ particles released from the supernatants of infected cells labeled with the different dyes. Infectivity and counts are presented as the percentage of total number of eGFP+ particles released from unstained virus-infected cells. Data depicts the mean with S.D. from three independent experiments. (H) Supernatants from DiD-stained infected and uninfected cells were treated with 0.05% Triton X-100.

Discriminating enveloped viruses from EVs by nucleic acid labeling. We next attempted to discriminate EVs from viruses based on their nucleic acid content. MLVeGFP, similarly to other retroviruses, packages two copies of its ~9Kb single-stranded RNA genome. In addition, retroviruses also package large amounts of cellular mRNAs, tRNAs and non-coding RNAs that represent approximately 50% of total RNA in the virion(148, 477). While EVs are known to also package nucleic acids, both DNA and RNA, the total amount of nucleic acids they package in comparison to retroviruses is unclear(446, 478, 479). SYBR Green is a dye that has a strong affinity for nucleic acids, with chemical variants that have been developed with higher affinities and quantum yields for RNA (SYBR II) or DNA (SYBR I). Nucleic acid dyes such as SYBR Green have been shown previously to label virus, however in those studies, it was unclear whether the dye-labeled virus samples were contaminated with EVs(363, 454, 457).

To attempt to discriminate EVs from viruses, MLVeGFP was first labeled with the lipid membrane dye DiD followed by SYBR II. The nucleic acid labeling procedure, as described previously(363, 454), requires fixation of the virus followed by staining at 80°C. This exposure to heat denatured eGFP on the surface of the MLVeGFP virus and it was no longer fluorescent (Fig. 6A), while fixation with 2% paraformaldehyde (PFA) alone had no significant impact on eGFP fluorescence (data not shown). MLVeGFP and uninfected cell supernatants were labeled alone with DiD (indirect) (Fig. 6B and 6C), or SYBR II (direct) (Fig. 6D and 6E), or dual labeled (Fig. 6F and 6G). When the DiD+ population in the MLVeGFP sample was compared with that of the uninfected supernatant control, the two populations exhibited different MFI peaks despite largely overlapping (Fig. 6C). The same was true for the SYBR II-positive and DiD/SYBR II double labeled populations (Fig. 6E and 6G). Vaccinia virus (VV) is an enveloped DNA virus with a much larger genome of 192 kbp(480). VV harboring close to 20 times more nucleic acid content was used as a positive control for nucleic acid staining. The combined use of SYBR I with DiI distinctly resolved three populations: DiI-SYBR+ (1), DiI+SYBR+ (2), and DiI+SYBR- (3) (Fig. 6H and 6I). This

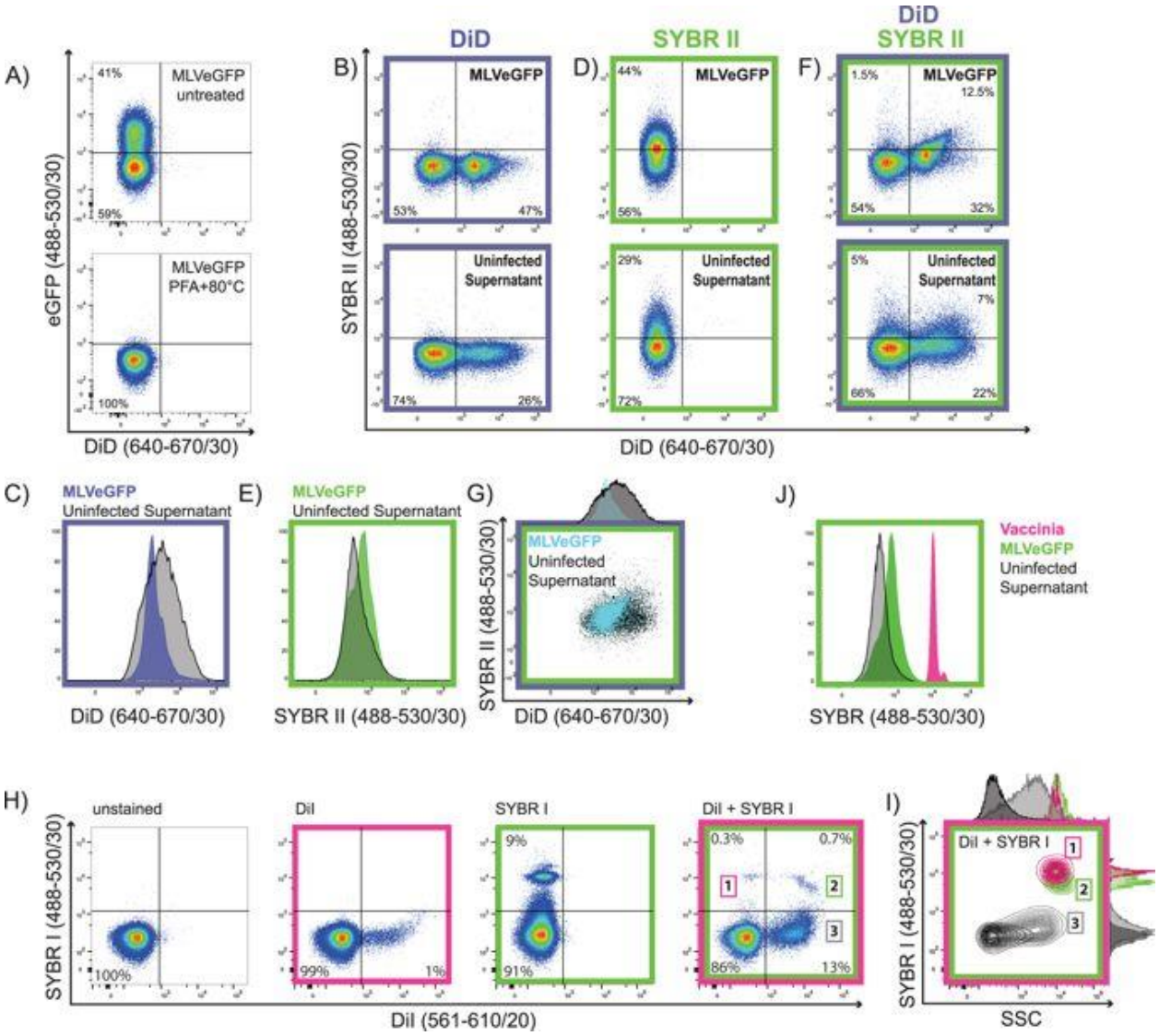

Figure 4.6. Discrimination of enveloped viruses from EVs by a combination of membrane and nucleic acid dyes.

(A) MLVeGFP was treated with 2% PFA at 80 °C to fix the virus and permeabilise the envelope and capsid, rendering the content of the particles amenable to staining by nucleic acid dyes. MLVeGFP infected and uninfected cells were stained with DiD, and then particles in the supernatant were analysed directly (B), or further stained with SYBR II following fixation and heat treatment (F). (D) Supernatants from infected and uninfected cells were stained with SYBR II only and analysed. Comparison of fluorescent intensities between supernatants from infected (coloured histograms) and uninfected cells (black histograms): (C) DiD stained cells, (E) SYBR II stained supernatants, (G) histogram and dotplot overlay of dual stained DiD/SYBR II nanoparticles from infected and uninfected cells. Nanoparticles from uninfected cells are depicted in black, and from infected cells in blue. (H) Direct labeling of VV with DiI or SYBRI alone, or in combination (fourth panel). (I) Relative sizes of nanoparticle populations 1 to 3, displayed as a comparison of SYBRI vs SSC. (J) Overlay of SYBR fluorescence intensity from stained MLVeGFP, VV and EV-containing cell supernatant.

was not completely surprising, as it is known that VV can be released as single-membrane and dual-membrane particles, and can also produce genome-deficient viral particles(481-483). When plotting VV alongside MLVeGFP and EVs, we can clearly discern differences in SYBR staining between these three populations (Fig. 6J). These data indicate that nucleic acid staining is an effective way to distinguish virus with a large genome but not retroviruses from EVs.

Discussion

Careful optimization of instrument settings is often underappreciated to obtain the best performance from a flow cytometer. In conventional flow cytometers, this optimization is standardized with beads as a reference material. In BD instruments like ours, this is achieved with the automated BD CS&T program and beads, however CS&T target values are optimized for cells. Therefore voltages and laser settings for the analysis of nanoscale particles need to be optimized manually with relevant reference materials, especially since the particles of interest are at the limit of detection of current instruments (90 - 200nm). In fact, there exists a large discrepancy in both fluorescence intensity and refractive index (RI) between most calibration beads and biological nanoparticles of interest(484-486). As such, we chose a fluorescently tagged virus as the standard, which allowed us to optimize our instrument settings on a biologically relevant particle. Alternatively, other groups have been successful at analyzing nanoparticles through conjugation with fluorescent beads(442). The obvious benefit of these bead conjugates are that they are easily detected on a wide range of flow cytometers, however their multivalent nature may also be a source of bias introduced during data acquisition. Antibody labeling of nanoparticles can in some circumstances induce aggregation(370). For this reason, we carried out our study on fluorescent viruses having undergone a minimal amount of manipulations that were limited to dye-loading, followed by filtration and dilution. As such, the limits of our method to discriminate between retroviruses and EVs are, for the moment, reserved for research applications where the use of a genetically engineered virus with a fluorescent envelope glycoprotein are possible, such as in cell lines or animal models.

There are advantages and disadvantages in selecting light scatter as the threshold parameter. On the one hand it allows for the detection of all non-fluorescent particles, but on the other hand, with our instrument and software, we see an increase in the overall abort rate. This increased abort rate resulted in a 3-fold reduction in the total eGFP+ events in comparison to fluorescence thresholding (Fig. 2D and 2E). The choice between SSC and FL for threshold is therefore application-dependant. In an experiment where the enumeration of a population of interest is required, samples should be collected using FL-thresholding; the caveat being that this population must be fluorescently labeled. On the other hand, if the goal of the study is to analyze different populations labeled with mutually exclusive fluorescent marker combinations, then SSC thresholding should be chosen to collect all relevant data, and better appreciate small differences in population relative sizes, clustering and distributions.

When analyzing MLVeGFP viruses that contain approximately 100 Env-eGFP molecules on their surface(467), we see the greatest gain in fluorescent particle resolution when the power of the 488nm laser increases from 100mW to 200mW (Fig. 3B and 3E). Nonetheless, for the detection of antigens at the surface of nanoparticles that are less abundant than Env-eGFP, like for example gp120 on the surface of HIV-1 virions(465, 467), the higher power laser will likely greatly improve signal resolution.

As mentioned earlier, retroviruses share many physical properties with EVs. Yet despite these similarities, MLVs, as a population, are distinct from EVs in that they are more homogeneous in light scattering properties (Fig. 1F). They are also more resistant to the uptake of membrane dyes when directly labeled (Fig. 4), and appear to contain slightly more nucleic acids than the EVs (Fig. 6E). These small differences are important in the context that EVs will contaminate even the purest of retrovirus preparations, as fractionation, filtration, and size exclusion techniques are not entirely effective(344). Furthermore, given that EVs are known to harbour viral proteins and nucleic acid fragments, and share numerous surface markers, it is most challenging to discriminate them using standard biochemical

approaches(344). If single-particle characterizations are carried out on viruses, it is therefore essential to develop methods to discriminate them from EVs.

In this work, we clearly demonstrate that a fluorescent tag on the retroviral envelope glycoprotein of MLV can serve as an excellent identifier. While providing specificity to detect viral particles, our MLVeGFP virus enabled us to evaluate the efficacy of various membrane dyes and staining methods. We found that retroviruses released in the cell supernatant were generally poorly amenable to staining with membrane dyes, in contrast to EVs (Fig. 4). This may be indicative of small, but significant biochemical differences in the membranous envelope of retroviruses and EVs. However, approximately 8 – 17% of viruses do appear to have been labeled by the dyes. This does not come as a complete surprise since it has been previously documented that a small fraction of MLVs are released through the endosomal pathway rather than budding at the cell surface and these viral particles might take up dye more efficiently than virus budding at the cell surface(120, 487). This would suggest that these dual-stained retroviruses share even greater biochemical similarities to small EVs, which are mostly comprised of exosomes(447). In comparison, the indirect staining method may label the viruses non-specifically through uptake of unbound dye present in the cytosol or indirectly through packaging of macromolecules stained by the dye (Fig. 5).

Fluorescent labelling of the virus with dyes had a severe impact on its infectivity (Fig. 5F and 5G). Even DHPE-Rhodamine, which stained very poorly, had a negative impact on infectivity. Our data indicate that membrane dyes are imposing a defect at egress in the producer cells or are directly affecting the infected cell metabolism (Fig 5G). It is clear that these staining methods are not suitable for some downstream applications that require infectious virus, and caution should be taken when analyzing viral fitness using chemically stained particles. Similarly, the same caution should be taken when using these dyes with EVs for functional studies.

In a further attempt to differentiate retroviruses and EVs, we investigated if nucleic acid packaging could be a discriminating factor. Though MLVeGFP was unable to be clearly resolved from EVs by dual lipid and nucleic acid staining, it did show superior particle homogeneity and slightly more fluorescence (Fig. 6C, 6F and 6G). In contrast, VV which has a much larger physical size (250x270x360nm)(488) and genome than MLVs is clearly resolved by using a fluorescent nucleic acid dye and SSC (Fig. 6I and 6J).

With technical advancements in flow cytometry it is now possible to visualize nanoparticles in the 90 – 120 nm size range using NFC. This innovation opens a wide array of new possibilities that result from single particle analysis of viruses and EVs that include the individual profiling of surface antigens, sorting of particles with distinct markers, and even the precise enumeration of particles displaying certain fluorescence or light scattering characteristics. NFC has the potential to bring new understanding to the fields of virology and EV research, as it provides a tool to answer questions that were not previously possible to address.

Methods

The datasets generated during and/or analysed during the current study are available from the corresponding author on reasonable request.

Flow cytometer features and specifications. SORP BD LSRFortessa for small particle detection with a PMT for forward scatter detection. Specifications for laser wavelengths and power are as follows: 405 nm – 50 mW, 488 nm – 300 mW, 561 nm – 50 mW, and 640 nm – 40 mW. Acquisition was done with BD FACSDiva version 8.0.1. BD Coherent Connection software was used for laser power adjustments. Samples, unless otherwise indicated, were acquired on the *low* sample pressure setting (at 5 turns on the fine adjustment knob), which equated to a measured flow rate of 20 µl/min. This instrument is run with a BD FACSFlow Supply System (FFSS) for day to day acquisition of cells, however for small particle detection, a dedicated steel sheath tank with a 0.1µm inline filter was used along with a separate waste

tank. This was done because we found the FFSS contributed to excess fluctuations in instrument background noise. Surfactant-free, ultra-filtered, low particle count sheath fluid was used for acquisition (Clearflow Sheath Fluid – Leinco). CS&T was run using the dedicated tank to obtain appropriate laser delays for use with the tank, since there is a difference in pressure between the FFSS and the steel tank. Instrument cleaning procedure prior to acquisition: 10mins distilled water, 30 min FACSClean (BD Biosciences), 10min distilled water, 60 min 10% Decon™ Contrad™ 70 Liquid Detergent (Thermo Fisher Scientific), and 10 min distilled water.

Fluorescence Index calculation. The fluorescence index was calculated as the difference of the median fluorescence intensity of the positive and negative population divided by the standard of deviation of the negative population. Fluorescence index = (MFIpos – MFIneg)/SDneg.

Data acquisition and analysis. Flow cytometry data was displayed in height for all figures. For small particle analysis, height is the preferred parameter over area. Area is the integrated value of an electronic pulse based on the height and width (time of flight). However, since the particles of interest are very small, the width or time of flight measurements become less precise. This leaves height as the intensity of the signal as the most accurate parameter for analysis of submicron-sized particles.

In our instrument platform, side-scatter was chosen over forward-scattered light detection for the approximation of particle sizes. As approximated by Mie Scatter Theory, the angle of light scatter from a particle in the 100-200 nm size range is such that more light is captured at the side-scatter angle rather than forward, whereas with a cell-sized particle (10µm) the opposite is true(469, 489). We found that despite having a PMT for FSC detection, resolution in SSC was still superior for our particles of interest. Flow cytometry data was analysed using Flowjo VX (FLOWJO, LLC). GraphPad Prism v6 was used for the generation of graphs (GraphPad Software).

Fluorescent polystyrene beads. Megamix-Plus SSC fluorescently labeled beads (Biocytex, Marseille, France #7803) with 160nm, 200nm, 240nm, and 500nm size populations was used. The 500nm bead population was off scale when run at settings optimized for MLVeGFP resolution.

Cells, Plasmids and Viruses

Cell Culture: Human embryonic kidney (HEK) 293T and mouse embryonic fibroblast NIH 3T3 cells were cultured in DMEM High Glucose Medium (Wisent, St Bruno, Canada), supplemented with 10% Fetal Bovine Serum (FBS, Gibco by Thermo Fischer Scientific, Waltham, MA), 100 U/mL penicillin and 100 µg/mL streptomycin (Wisent, St Bruno, Canada). This media will be referred to as complete media. Propagation was continued at 37°C in a 5% CO_2 incubator.

MLVeGFP: Replicative Moloney-MLV, referred to as MLVeGFP throughout this study, was produced from the pMOV-eGFP expression plasmid(319, 371, 372). The eGFP reporter is inserted in frame within the proline-rich region of the viral envelope glycoprotein, is expressed on the exterior surface of the virus, and does not alter infectivity nor ecotropic receptor specificity(372).

Production of MLVeGFP from chronically infected cells. Aside from MLVeGFP used in Fig.1D – 1H that was produced by plasmid transfection in 293T cells, MLVeGFP virions were otherwise produced from chronically infected NIH 3T3 cells. For the generation of chronically infected cells, NIH 3T3 cells were infected with MLVeGFP at a very high multiplicity of infection (MOI). In short, 10mL of MLVeGFP-containing cell supernatant was produced by transfection of 293T cells in a 10cm dish for 72h. The supernatant was cleared through a 0.45µm filter and was ultra-centrifuged at 100,000xg for 3h in a 70Ti rotor at 4°C. The entire viral pellet was resuspended in DMEM and used to infect NIH 3T3 cells seeded at 500 000 cells /well in a 6-well dish. For virus production, uninfected control cells or chronically infected NIH 3T3 cells were seeded at a density of 5 x 10^5 cells/well in 6-well plates in complete media. After 18h, cells were washed three times with 0.1µm filtered PBS and incubated in 1.5 ml of 0.1µm filtered, serum-

, antibiotic- and phenol red-free DMEM for 3h. Unless otherwise stated, the cell supernatant was passed through a 0.45µm acrodisc syringe filter with SuPor (PES) membrane (Pall Corporation, Port Washington, NY, cat. #PN4614) and diluted 100-fold in 0.1µm ultrafiltered PBS before NFC analysis.

Production of MLVeGFP by transfection. The plasmid eGFP-C3 (Clontech, Mountain View, CA) was used for cytoplasmic eGFP expression. For the construction of an Env-eGFP expression plasmid, the Env-eGFP gene of pMOV-eGFP was amplified by PCR using the following primers: 5'-GCTAGCGCCGCCACCATGGCGCGTTCAACGCTCTCAAAACC-3' (forward) and 5'-CTCGAGCTATGGCTCGTACTCTATAGGCTTCAGCTGGTG-3' (reverse). The amplification product was then inserted between the NheI and XhoI restriction sites of the expression vector pcDNA 3.1 (-) downstream of the CMV promoter.

For virus or EV production, 293T cells were transfected with pMOV-eGFP, pEnv-eGFP or peGFP-C3. 24h before transfection, 293T cells were seeded at a density of 1.25 x 10^5 cells/well in a 24-well plate in complete DMEM media. For each well, a total of 500 ng of DNA was transfected using GeneJuice (Novagen, EMD Millipore, Billerica, MA) according to manufacturer's instructions. After 36h, the cells were washed with PBS and media was changed to 0.1µm-filtered, serum and phenol red-free DMEM (Wisent), to allow for virus or EV production with minimal contaminants. After 3h, the cell supernatant was harvested and cleared through a 0.45µm acrodisc syringe filter with SuPor (PES) membrane (Pall Corporation) unless otherwise specified. For analysis of the effects of microfiltration on viral sample, supernatants were filtered through 0.1µm (cat. #PN4612), 0.2µm (cat. #PN4612) or 0.45µm filters (Pall Corporation). Samples produced from transfections were diluted 1:10 in 0.1µm-filered PBS prior to analysis by NFC.

Virus titer calculations. To calculate of the viral titer in transducing units (TU) / mL, known volumes of 0.45µm-filtered viral supernatant was titrated on 1.0 x 10^5 NIH 3T3 cells per well in a 12-well plate.

Twenty-four hours post-infection, these cells were analyzed by flow cytometry. Infections ranging from 2-30% were assumed to have one productive integration per cell, and used to calculate TU/mL with the following formula: TU / mL = # of infected cells / volume of viral supernatant.

Viral genome quantifications by ddPCR. Viral RNA genomes were isolated from infected cell supernatants using the QIAamp Viral RNA Mini Kit (Qiagen) following manufacturer's guidelines. The RNA eluate was then reverse transcribed using the Advanced cDNA Synthesis Kit (Wisent) and analyzed by droplet digital PCR, using the QX200 system (BioRad), for the presence of the eGFP coding sequence. The primers used for this analysis were R279-FWD and R279-REV, as previously described by our group(409). Data was analyzed using QuantaSoft™ and extrapolated based on the dilutions used for the assay.

Vaccinia virus stock preparation. VVDD-mCherry stocks were obtained from John C. Bell. Briefly, virus stocks were produced by infecting HeLa cells at a low MOI (0.01). Infected cells were lysed by repeat freeze-thaw cycles (-80°C/37°C), cell debris was removed by centrifugation, and virus was clarified through a sucrose cushion at 20,700 x g with a JS-13.1 rotor for 80 min at 4°C (370, 490, 491).

Nanoparticle tracking analysis and zeta potential measurement. Nanoparticle tracking analysis (NTA) was carried out using the ZetaView PMX110 Multiple Parameter Particle Tracking Analyzer (Particle Metrix, Meerbusch, Germany) in size mode using ZetaView software version 8.02.28. Samples were diluted in PBS to ~10^7 particles/ml. The system was calibrated using 105 and 500 nm polystyrene beads and then videos were recorded and analyzed at all 11 camera positions with a 2 second video length, a camera frame rate of 30 fps and a temperature of 21˚ C. Analysis was performed using Particle Explorer version 1.6.9 (Particle Metrix). Analysis parameters were: segmentation-fixed, centroid estimation-blob, drift compensation-auto, log detection threshold-0.0175, max particle size-1000, min particle size-6.0, segment threshold-18. Results are displayed as the percentage of particles within 25

nm segments and as mean particle size. Zeta potential was measured using the ZetaView PMX 110 Multiple Parameter Particle Tracking Analyzer (Particle Metrix) in zeta potential mode as described previously (492). All measurements were performed at 21°C using samples diluted in 0.1x phosphate buffered saline (diluted in double-distilled H_2O to ensure conductivity of approximately 500 µS/cm. Uninfected supernatants were diluted 1:10 and MLVeGFP was diluted 1:100 to achieve equivalent particle concentrations. Data were analysed using ZetaView software (version 8.02.28). Instrument settings were as follows, sensitivity: 85, frame rate: 30 frames per second, shutter speed: 100. Post-acquisition parameters were set to a minimum brightness of 20, a maximum size of 200 pixels, and a minimum size of 5 pixels. Temperature, conductivity, electrical field, drift, and pH of the diluent were consistent for all samples. The zeta potential of particles released in the supernatent of non-infected cells was -23.2 $\pm$ 2.5 mV, and -33.6 $\pm$ 2.6 mV for particles in the infected cell supernatant.

Lipophilic membrane dyes and nucleic acid labeling

Direct labeling with lipid dyes: Dyes were added directly to undiluted control or MLVeGFP containing supernatant at optimized concentrations indicated below. The dye-labeled control or viral supernatants were diluted 1:10 and 1:100 in 0.1µm filtered PBS, respectively. These were then filtered with a 0.45µm pore-size syringe filter prior to acquisition on the cytometer. DiD and DiI solutions were used at 10µM, while DHPE-Rhodamine, FM 4-64X and BODIPY TR Ceramide were used at 10µg/mL (all Thermo Fisher Scientific).

Indirect labeling with lipid dyes: Uninfected and infected NIH 3T3 cells were cultured overnight with dye. The following day, cells were washed 3 times with 0.1µm-filtered PBS to remove excess dye. Following washing, the cells were placed back in the 37°C incubator with 0.1µm filtered, serum and phenol red-free media. After 3h, supernatant was collected, 0.45µm-filtered (unless otherwise indicated), and analyzed by NFC. As before, control or viral supernatants were diluted 1:10 and 1:100 in

0.1µm filtered-PBS, respectively. DiD and DiI solutions were used at 25µM, DHPE-Rhodamine and FM 4-64X were used at 25µg/mL, and BODIPY TR Ceramide was used at 12.5µg/mL. DiD and DiI were dissolved in ethanol, while DHPE-Rhodamine, FM 4-64X and BODIPY TR Ceramide were dissolved in methanol. Titrations were performed for both the direct and indirect labeling methods and optimal concentrations were chosen (data not shown).

Nucleic acid labeling. The protocol for nucleic acid labeling with SYBR Green was adapted from Brussard *et al.* (363, 454). Briefly, supernatants were fixed in 2% methanol-free paraformaldeyde (PFA) solution (Thermo Fisher Scientific, cat. #28906). Virus samples were stained with 1x SYBR Green I (DNA) or SYBR Green II (RNA) at 80°C for 10 minutes. For dual labeling of MLVeGFP, lipophilic dye was loaded onto the virus by indirect labeling prior to nucleic acid staining. For dual labeling of VV, virus particles were labeled using the direct method post SYBR Green I staining. Samples were diluted and 0.45µm-filtered after staining for analysis by NFC.

Fluorescence Microscopy. Uninfected NIH3T3 cells were labeled as described above for the indirect staining method, but scaled down to fit 35 mm dishes (Ibidi, Fitchburg, WI). The Zeiss LSM 880 was used for live imaging confocal microscopy, ImageJ (1.8.0) was used to generate the images.

Acknowledgements

The authors would especially like to thank members of the BD Biosciences technical support team, Emily Chomyshyn and Steven Collister, for valuable assistance throughout this study. M.-A.L. holds a Canada Research Chair in Molecular Virology and Intrinsic Immunity. T.M.R. holds a Queen Elizabeth II graduate scholarship in science and technology (QEII- GSST). This work was supported by a research and development grant from the University of Ottawa Faculty of Medicine to the FCV Core Facility, and a Discovery Grant by the Natural Sciences and Engineering Research Council of Canada (NSERC) to M.-A.L.

Chapter 5: Intact Viral Particle Counts Measured by Flow Virometry Provides Insight into the Infectivity and Genome Packaging Efficiency of the Moloney Murine Leukemia Virus

Preface: This chapter has been submitted for publication as a research article to the Journal of Virology.

Tyler Milston Renner, Vera A. Tang, Dylan Burger & Marc-André Langlois

Author Contributions:

T.M.R. performed nearly all experiments, wrote the manuscript, analyzed the data and designed the study. V.A.T. assisted with flow virometry set up and provided support. D.B. performed NTA experiments. M.A.L. conceptualized, designed, and cooperated in manuscript writing and data analysis.

ABSTRACT

Murine leukemia viruses (MLVs) have long been used as a research model to further our understanding of retroviruses. These simple gammaretroviruses have been studied extensively in various facets of science for nearly half a century, yet we have surprisingly little quantitative information about some of the basic features of these viral particles. These include parameters such as the genome packaging efficiency and the number of particles required for a productive infection. The reason for this knowledge gap relies primarily on the technical challenge of accurately measuring intact viral particles from infected cell supernatants. Virus infected cells are well known to release soluble viral proteins, defective viruses and extracellular vesicles (EVs) harboring viral proteins that may mimic viruses, all of which can skew virus titer quantifications. Flow virometry, also known as nanoscale flow cytometry or simply small particle flow cytometry, is an emerging analytical method enabling high throughput single-virus phenotypic characterizations. By utilizing the viral envelope glycoprotein (Env) and monodisperse light scattering

characteristics as discerning parameters of intact virus particles, here we analyzed the basic properties of Moloney MLV (M-MLV). We show that less than 24% of total p30 capsid protein measured in infected cell supernatants is associated with intact viruses. We calculate that about one in five M-MLV particles contain a viral RNA genome pair and that individual intact particle infectivity is about 0.4%. These findings provide new insights into the characteristics of an extensively studied prototypical retrovirus, while highlighting the benefits of flow virometry for the field of virology.

IMPORTANCE

Gammaretroviruses, or more specifically murine leukemia viruses (MLVs), have been a longstanding model for studying retroviruses. Although being extensively analysed and dissected for decades, several facets of MLV biology are still poorly understood. One of the primary challenges has been enumerating total intact virus particles in a sample. While several analytical methods can precisely measure virus protein amounts, MLVs are known to induce the secretion of soluble and vesicle-associated viral proteins that can skew these measurements. With recent technological advances in flow cytometry, it is now possible to analyze viruses down to 90nm in diameter with an approach called flow virometry. The technique has the added benefit of being able to discriminate viruses from extracellular vesicles and free viral proteins in order to confidently provide an intact viral particle count. Here we used flow virometry to provide new insights into the basic characteristics of Moloney MLV.

INTRODUCTION

Murine leukemia viruses (MLVs) were first discovered as a result of their oncogenic effects over half a century ago (18, 21, 22). Shortly thereafter, it was revealed that infections of germline cells led to the heritable and ubiquitous nature of endogenous retroviruses (ERVs) (34, 35). In this regard, ERVs account for 8-10% of the mouse genome (493). Typically most mouse ERVs were found to be closely related to gammaretroviruses resembling MLV (493). The broad popularity of MLV as a model retrovirus began with its critical role in David Baltimore's research that led to the shared discovery of the reverse transcriptase

with Howard Temin who was focusing on another retrovirus, Rous sarcoma virus (38, 494). The role of MLV as a prototypical retrovirus has been escalated by its genomic simplicity, originally thought to encode only the bare necessities for retroviral replication and infection: Gag, Pol and Env (63). Dissection of the function of these three proteins and of the retroviral replication cycle of MLV has been invaluable for the field of retrovirology (157, 495).

Much of the knowledge acquired by studying MLV family members has been relatable to more complex retroviruses, as well as those with more direct relevance to humans, such as the human immunodeficiency virus (HIV) and the human T-cell lymphotropic virus (HTLV). These findings include the process of reverse transcription, integration, viral genomic RNA dimerization, and selective viral RNA packaging (Reviewed in (496-498)). An enhanced understanding of retroviruses has also created the opportunity of using MLV as a gene therapy vector in the laboratory, given its well-documented genome and versatility in stable gene delivery. In the clinic, however, HIV-based lentiviral vectors have become more favorable candidates for gene therapy in humans due to their reduced oncogenic potential compared to MLV vectors (499). Despite a wide array of data revolving around MLV and other retroviruses, there remains important knowledge gaps in the field. These include quantitative assessments of the physical viral titer, the viral genome packaging efficiencies and the number of particles required for a productive infection. These issues can easily be addressed if a method could rapidly discriminate and enumerate intact viral particles.

Generally, methods that quantify physical viral titers target individual viral components (i.e. nucleic acids or proteins) within a homogenized virus sample. While being invaluable tools, these types of approaches do not provide direct information on individual virus particles. Secreted proteins, degraded virions and extracellular vesicles (EVs) represent sources of impurities within a viral sample. EVs are an important confounding factor, given their propensity to incorporate viral protein and genomic content in a similar fashion as viruses (344, 500, 501). The concern of EV contamination in this regard is further emphasized when considering the significant overlap between EV and virus biogenesis (337, 451, 502). This is especially true for retroviruses, which have evolved to assemble and egress using largely shared synthesis

and secretory pathways as EVs (116, 120, 340). In fact, our group and others have highlighted the incorporation of MLV proteins into EVs (310, 369). It is therefore clear that in order to effectively quantify viral samples, a robust discrimination between EVs and intact viral particles must be achieved.

In this report we demonstrate that small particle flow cytometry performed on viruses, an approach called flow virometry (FVM), can be used as a rapid, high throughput and effective method to quantify intact viral particles released by an infected cell. To validate this approach, we employed the use of a model retrovirus, the Moloney murine leukemia virus (M-MLV). The laboratory strain used here has been modified to contain a superfolder green fluorescent protein (sfGFP) within the proline rich region of the viral envelope glycoprotein (Env). We confirm our previously published results that MLV Env is an effective discrimination marker to distinguish virus from EVs based on fluorescence intensity and side scattered (SSC) light profiles by FVM (369, 373). We then compared virion titer quantifications by FVM to other common analytical techniques and demonstrate the importance of discriminating intact virions from EVs and from free viral proteins. Finally, to further highlight the value of FVM, we correlated intact MLV particle counts to the infection rate and to the absolute amount of viral genomic RNA (gRNA). These parameters then enabled us to calculate the infectivity of M-MLV and its genome packaging efficiency, which to this point was unknown.

MATERIALS AND METHODS

Cells

Human embryonic kidney epithelium cells (293T) and mouse embryonic fibroblasts (NIH 3T3), were cultured in DMEM high glucose medium (Wisent) that has been supplemented with 10% Fetal Bovine Serum (FBS) (Corning), 100U/mL penicillin and 100µg/mL streptomycin (Wisent) and propagated in an incubator at 37°C with 5% CO_2.

Plasmids and Viruses

The plasmid encoding M-MLV-sfGFP was generated through restriction-free cloning to replace the eGFP in the M-MLV vector which has been described by our group previously (368, 369). FWD Primer: 5'-TTCAGTCACCAAACCACCCAGTGGGAGCAAGGGCGAGGAACTGTTCACC-3', REV Primer: 5'-CGGTACGTACGCACCGGTGGACTTGTACAGCTTGTACAGCTCGTCCATGCCGTGGG-3'. This plasmid originated from the pMOV-eGFP vector, which has been described before (371, 372). To create MLV-DsfGFP, an R96C mutation was created within sfGFP. FWD Primer: 5'-GCTACGTGCAGGAATGCACCATCAGCTTCAAGGACGACGGC-'3; REV Primer: 5'-CTTGAAGCTGATGGTGCATTCCTGCACGTAGCCCTCGGGC-'3. For M-MLV-V5, which was created in this study, restriction-free cloning was conducted to insert the V5 tag within the proline-rich region of MLV Env. FWD Primer: 5'-GTGGGGGTATACGCGTGGGCAAGCCGATTCCCAATCCTCTGCTTGGCCTCGATTCAACTACGCGTGGG GCGATCGCGCCCGGG-'3 and REV Primer: 5'-CCGAAGAGCAAAATCATTAGGAGTACAATGAGGGGTCCC-'3.

Generation of MLV-sfGFP producer clones and virus production

The principal virus used throughout this study is M-MLV with sfGFP inserted in the proline-rich region of Env creating a fusion protein (Env-sfGFP) with sfGFP being exposed on the surface of the virus (368, 369, 372, 373, 503). We call this virus MLV-sfGFP throughout our study for simplicity. Virus was produced from chronically infected NIH 3T3 cells as previously described (368, 369, 373). However, in order to monitor possible heterogeneity between individual virus particles, these chronically infected cells were single-cell sorted based on sfGFP expression and expanded. For this investigation, virus released from ten different monoclonal expansions of chronically infected cells were randomly selected and scrutinized.

To produce virus, chronically infected NIH 3T3 cell clones were seeded at a density of $2x10^5$ cells per well in a 6-well plate. Exactly 2mL of media was provided for the incubation period of 72hrs. Supernatants were collected, cleared of cellular debris and passed through a 450 nm cartridge filter for downstream analysis.

Infected producer cell clones were analyzed by flow cytometry or SDS-PAGE to measure relative protein levels. For SDS-PAGE analysis, the following antibodies were used: R187 anti-p30 (CRL-1912; ATCC), anti-EGFP (JL-8; Clontech), HRP-conjugated anti-rat IgG (Sigma), HRP-conjugated anti-mouse IgG (Cell Signaling) and HRP-conjugated anti-β-Tubulin (Abcam). For transducing unit (TU) calculations, cells were infected at several multiplicities of infection (MOI) using spinoculation and polybrene as previously described (369). Flow cytometry analysis was conducted at 24hrs post-infection to mitigate the impact of viral spreading for a more accurate measurement of TU/mL in the initial stock. TUs were calculated using the following equation:

Transducing Units / mL = number of infected cells (#) / volume of viral supernatant (mL)

Generation of stably transduced sfGFP and Env-GFP expressing cells

To generate NIH 3T3 stably expressing sfGFP and Env-GFP, we used the M-MLV-based pMXs-Puro retroviral system (Cell BioLabs) to transduce the cells. The coding sequence of sfGFP or Env-GFP was inserted in the multiple cloning site of pMX-Puro. Virus particles were produced by co-transfection of the packaging plasmid pOGP (Gag-Pol) and pMDG (VSV-G), as described previously (504). Transfection of 293T cells were conducted with polyethylenimine (PEI) as described (505). Briefly, $5x10^5$ cells were seeded 24 hrs prior to transfection. A total of 2μg of plasmid DNA was transfected at a ratio of 1:0.7:0.3 (pMXs-Puro:pOGP:pMDG). Cells were incubated to produce virus for 72hrs before the supernatant was collected and cleared of cellular debris by centrifugation and microfiltration. NIH 3T3 cells were infected as described earlier. After 72hrs of expansion, the bulk of the fluorescent sfGFP- and Env-GFP-expressing infected cells were sorted by flow cytometry. These were then expanded and used as controls for this work.

Gag and Env Quantifications by ELISA

Commercially available ELISA kits were purchased from Cell BioLabs to analyze the levels of p30 (MuLV Core Antigen ELISA Kit; VPK-156) and Env-GFP (GFP ELISA kit; AKR-121). Manufacturer's instructions were closely followed. These kits provided a reliable concentration of protein content by mass

for p30 and GFP. The molar mass of p30 (**Table 1**) was used to determine moles of p30 in each sample. For theoretical viral particle titer calculations, an average of 2187 p30 molecules were assumed to constitute a single MLV virion (101). The molar mass of the GFP standard within AKR-121, which contains a His-Tag, was considered to determine moles of GFP, and therefore Env-sfGFP, within each sample. Similarly, to infer the viral particle titer, an average of 300 Env-sfGFP molecules were assumed to be expressed on the surface of a single virion (115).

Viral Genome Quantification

The QIAamp viral RNA mini kit (Qiagen) was used to isolate RNA from viral supernatants according to manufacturer's instructions, with the slight modification that an RNA standard (VetMAX) was added to the lysis buffer prior to initial lysis. RNA was eluted in nuclease free water and reverse transcribed using QScript with RNaseH activity. RNaseH was kept to avoid synthesis of multiple copies of cDNA per RNA molecule. The cDNA was diluted and analyzed by droplet digital PCR (ddPCR) of packaging signal (Psi) and Env-sfGFP sequence targets within each sample. Psi FWD: 5'-TGGGGGCTCGTCCGGGAT-3'; Psi REV: 5'-CCGGGTGTTCCGAACTCGTCAGTTC-3'; Psi Probe: 5'-ACCCCTGCCCAGGGACCACCGACCCACC-3'; Env-sfGFP FWD: 5'-CCGACAAGCAGAAGAACGGC-3'; Env-sfGFP REV: 5'-CTTGTACAGCTCGTCCATGCCG-3'; Env-sfGFP Probe: 5'-CCCCGTGCTGCTGCCCRACAACCACTACC-3'. Additionally, the RNA standard was monitored in each column to evaluate the extraction efficiency for each individual sample. A primers / probe mixture was provided and used according to the manufacturer's instructions (VetMAX). Data was analyzed using QuantaSoft™ and extrapolated based on the determined extraction efficiency and dilutions used for the assay.

Nanoparticle Tracking Analysis

Nanoparticle tracking analysis (NTA) was carried out using the ZetaView PMX110 Multiple Parameter Particle Tracking Analyzer (Particle Metrix) in size mode using ZetaView software version 8.02.28. Samples were diluted in PBS to ~10^7 particles/mL. The system was calibrated using 105 and 500 nm

Table 5.1: Reported p30 capsid and Env content within an MLV particle.

Viral Protein	Molecular Mass (kDa)	Proteins per virus particle
Capsid (p30)	30.61*	1100 – 1800 (436) 1860 – 2514 (101)
Envelope glycoprotein (Env)	73.30*	60 – 210 (506) 240 – 360 (115) ~300 (467)

*Molecular mass without post-translational modifications.

polystyrene beads and then videos were recorded and analyzed at all 11 camera positions with a 2 second video length, a camera frame rate of 30 fps, a shutter of 70 and a temperature of 21°C.

Flow Virometry analysis

A detailed description of the instrument settings and the MLV particles used in this study by FVM was published recently and uploaded to the BioRxiv preprint server (503). FVM was conducted using a Beckman Coulter CytoFLEX S using 405nm SSC-H as a threshold parameter (threshold typically at 1500 a.u.). All virus samples were passed through 0.45μm cartridge filters, unless otherwise stated, and analyzed without additional concentration or enrichment. Antibody staining was carried out with an aliquot of virus using PE-conjugated anti-GFP (FM264G; BioLegend) at a final concentration of 0.2μg/mL, this was then diluted for analysis. Optimal antibody concentrations for staining were previously established (373, 503). PE-conjugated polyclonal anti-V5 (Abcam; ab72480) was used at a concentration of 0.8μg/mL. Non-viral supernatants are analyzed at a 1 in 250 dilution, while viral supernatants are diluted 1 in 1000 using 100nm filtered PBS. Samples were acquired for 1min on the slow flow setting for a total of 10μL of each diluted sample. Concentrations are then extrapolated based on dilution factors.

RESULTS

Generation of ten unique virus producer cell clones. When retroviruses infect a cell population, a large proportion of cells will harbor proviruses integrated in unique positions in their genome (179, 180). Furthermore, transduced cells may harbor one or several integrated proviral genomes. These factors may affect both host and viral gene expression and result in cell-to-cell variabilities in regards to virus gene expression, virus production, efficiency, and virus infectivity. For this study, we used M-MLV that expresses sfGFP on its surface as a fusion protein with Env (MLV-sfGFP). MLV-sfGFP viral particles were used to infect NIH 3T3 cells and then infected fluorescent cells were isolated by single-cell sorting by flow cytometry. Ten fluorescent virus-producing cell clones (C1 to C10) were then randomly selected, expanded, and used throughout this study. Virus-containing supernatants from these clonal cell populations were directly used in our experiments without further enrichment and constitute the viral clone stocks.

Assessment of the MLV particle titer by ELISA. ELISAs were conducted to measure the amount two viral protein constituents: the viral capsid (p30) protein and Env in each of the viral clone stocks. ELISA is routinely used in the field to normalize virus input. Through the use of commercially available p30 and GFP ELISA kits, we found that each of the ten MLV-sfGFP clones displayed levels of p30 and Env within less than an order of magnitude of each other (**Fig. 1A**). With knowledge of the molar mass for these proteins, a concentration of molecules can be calculated (**Fig. 1B**). Guided by published literature values for the number of p30 and Env molecules in a single MLV virion (**Table 1**), ranges of inferred viral particle concentrations within these stocks were estimated (**Fig. 1C**). For our calculations, we used 2187 p30 molecules and 300 Env molecules per virion, which both constitute the median of published reported values (**Table 1**) (101, 115). If all p30 and Env molecules measured by ELISA were virus-associated, the average virus titer would be $2.55\pm0.06 \times 10^{10}$ particles/mL based on p30, or $2.53\pm0.10 \times 10^{10}$ particles/mL based on Env. However, this is likely to be an overestimate due to the presence of soluble or EV-associated viral proteins. The ratio of p30-to-Env is also constant among all ten clones tested averaging at 7.4 ± 0.8, except for one outlier at 5.4 ± 0.3(**Fig. 1D**).

Viral RNA genome content. As an alternative to protein content, measuring viral genomic content is another typical approach to estimate quantities of virus. MLV has been well-defined to specifically package zero or two copies of its viral RNA genome (gRNA), with no specific affinity for monomeric viral gRNA (77, 78, 127, 507). Here, we sought to determine the relative abundance of viral gRNA in each viral clone stock by amplifying two different regions of the viral genome: the packaging signal (Psi) and Env. Viral gRNA was isolated from an aliquot of each stock using a commercially available silica-based extraction column with carrier RNA to increase recovery. To account for possible nucleic acid loss during the purification process, a set amount of a commercial RNA standard was spiked into the lysis buffer before each extraction. The purified nucleic acid was then reverse transcribed into a cDNA that was then used as a template for probe-based droplet digital PCR (ddPCR) to determine the absolute copy number of viral gRNAs.

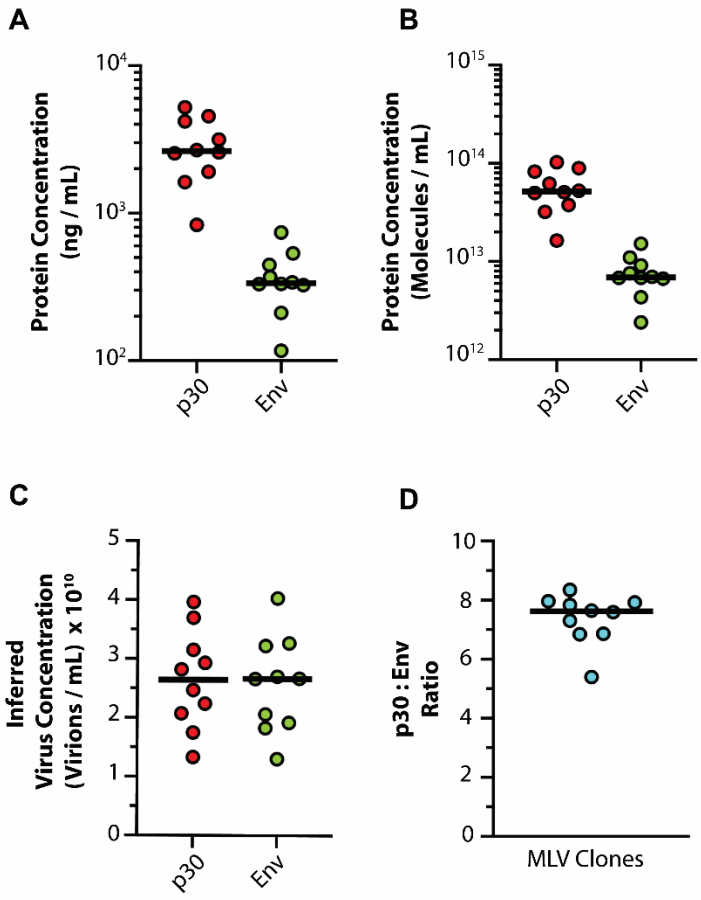

Figure 5.1. Viral titer measurement by ELISA.

(A) Protein content in viral supernatants was assessed using commercially available ELISA to quantify both p30 and Env (GFP) levels. (B) The concentration in (A) was converted to protein molecules using corresponding molecular masses (Table 1). (C) Number of protein molecules in (B) were converted to an inferred virus titer based on the stoichiometry outlined in Table 1. An average of 2187 p30 molecules and 300 Env molecules per virion is assumed based on the published literature. (D) The ratio of p30: Env protein molecules is illustrated for each viral stock.

While total isolation efficiency was monitored using the internally spiked RNA standard, the efficiency of each individual step was also monitored. Free RNA spiked into culture supernatants was rapidly degraded, while monitoring the isolation efficiency was made possible by spiking the RNA standard directly into the viral lysis buffer where RNase activity has been inactivated (**Fig. 2A**). In our system, we determined the RNA extraction efficiency to be approximately 50%, while reverse transcription (RT) maintained an efficiency of over 70%. Tracking the spiked RNA standard allowed us to determine the total procedural efficiency of viral cDNA synthesis for each independent sample, which averaged to be around 33% **(Fig. 2A)**. Through this determination of total isolation efficiency, the absolute number of viral gRNA copies was calculated for both Psi and Env amplicons (**Fig. 2B**). Similar to the ELISA results, the level of viral gRNA in each stock was quite consistent between each of the ten clones tested with on average 2.19 ± 0.22 x 10^9 genomes/mL.

MLV infectious titer. Not all viruses released from a transduced cell are infectious. Some viruses are devoid of genomes, others may harbor inactivating mutations or may be defective. Furthermore, given that the supernatant of infected cells contains soluble viral proteins, degraded virions, virus-like particles (VLPs) and EVs containing viral components, determining the true viral titer can be very challenging. As such, the infectious titer is often used for practical and functional reasons. Here, NIH 3T3 cells were infected with each of the viral clones and monitored for GFP fluorescence 24 hours post-infection by flow cytometry. By knowing the number of target cells infected and the volume of supernatant used, it is simple to determine the overall concentration of infectious or transducing units (TU) in the sample. Our data shows that the ten clones exhibited an average infectious titer of 2.18 ± 0.20 x10^7 TU/mL (**Fig. 2C**).

Characterization of sfGFP, Env-GFP and MLV-sfGFP producer cells and their supernatants. The accuracy of the various viral quantification methods is in large part limited by the ability to enumerate intact viral particles. Importantly, given the 'bulk' nature of these analytical methods, it is extremely challenging to discern the influence of soluble or EV-associated viral constituents. As a result, little robust information is currently available, for instance, about the genome packaging efficiency

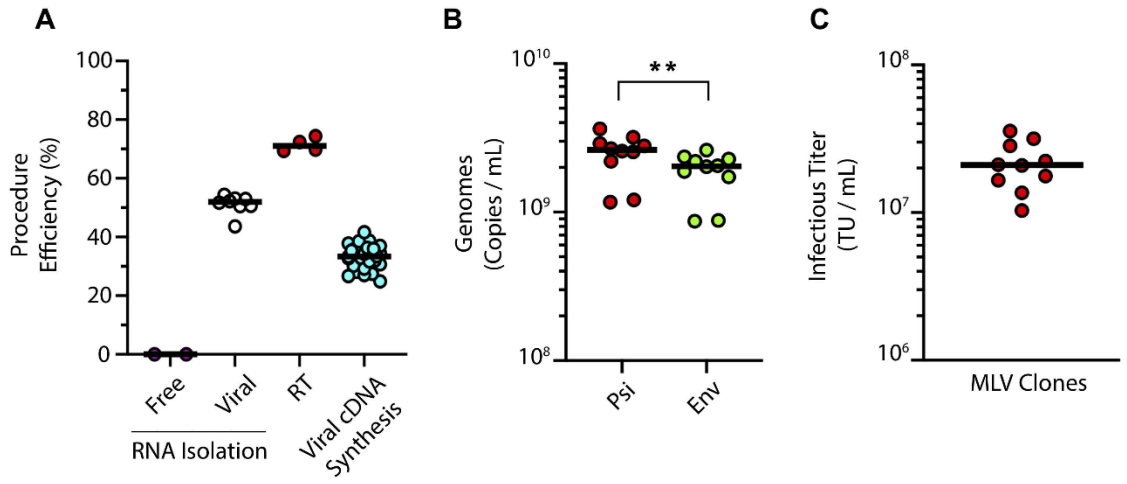

Figure 5.2. Measurement of viral gRNA and of the infectious titer.

(A) Efficiency of RNA column extraction and reverse transcription was monitored using an RNA standard. (B) Using the efficiency from (A), the absolute number of viral genomes was determined using a ddPCR strategy targeting the packaging signal (Psi) or Env. (C) Transducing units (TU) were measured for each viral stock clone. Virus was analyzed from 10 independent cell clones producing MLV-sfGFP. Each data point is representative of 2 independent experiments. P values were calculated by paired Student's t test. **, $P \leq 0.01$.

of M-MLV or the actual infectivity of released particles. This is because such calculations require an exact enumeration of intact viral particles in a sample (i.e. the physical titer). However, we have shown in a recent publication that Env expressed on the surface of M-MLV produced by cell transfection is a robust discrimination marker that can distinguish intact MLVs from EVs by FVM (373).

Here we wanted to determine if this discrimination between EVs and viruses holds true if Env is expressed by a retroviral vector in transduced cells, in contrast to episomal plasmid-expressed Env as we previously reported (373). To investigate this issue, we cloned sfGFP or the Env-GFP fusion protein into a retroviral vector to stably transduce NIH 3T3 cells. Infected fluorescent cells were then sorted to purity by flow cytometry. For sfGFP, we established cell populations expressing low and high levels of fluorescence by cell sorting. Cells labeled as control in the figures represent untransduced NIH 3T3 cells.

Transduced cells and their supernatants were analyzed by SDS-PAGE and blotted for GFP, β-tubulin and p30. As expected, transduced cells showed the appropriate sizes for GFP (~27kDa), unprocessed Env-GFP (~115kDa; gPr85-GFP) and the furin-cleaved surface (SU) moiety of Env-GFP that contains the fluorescent reporter protein (~100kDa; gp70-GFP) (**Fig. 3A**). The Env-GFP transduced cells also displayed an additional band of unknown nature (~60kDa). Expression of p30 was not detectable in either the cell lysates or in the supernatants, as would be expected (data not shown). Importantly, we did not detect GFP expression by Western blot analysis in the supernatants of transduced sfGFP or Env-GFP cells, not even when the supernatants were concentrated by ultracentrifugation (data not shown), which is not completely unexpected (361).

We then analysed each of the ten MLV-sfGFP producing cell clones and their supernatants by Western blot analysis (**Fig. 3B and 3C**). Our results show that the cell lysates of all ten clones also exhibit unprocessed and processed Env-GFP of the same size as the Env-GFP control, and p30 capsid protein in similar proportions to their respective Env-GFP (**Fig. 3B**). Similarly, supernatants from the various clones all had detectable levels of Env-GFP (SU) and proportional levels of their respective p30 (**Fig. 3C**). Despite differences in virus protein expression, egress viruses from all ten cell clones nearly completely resolved

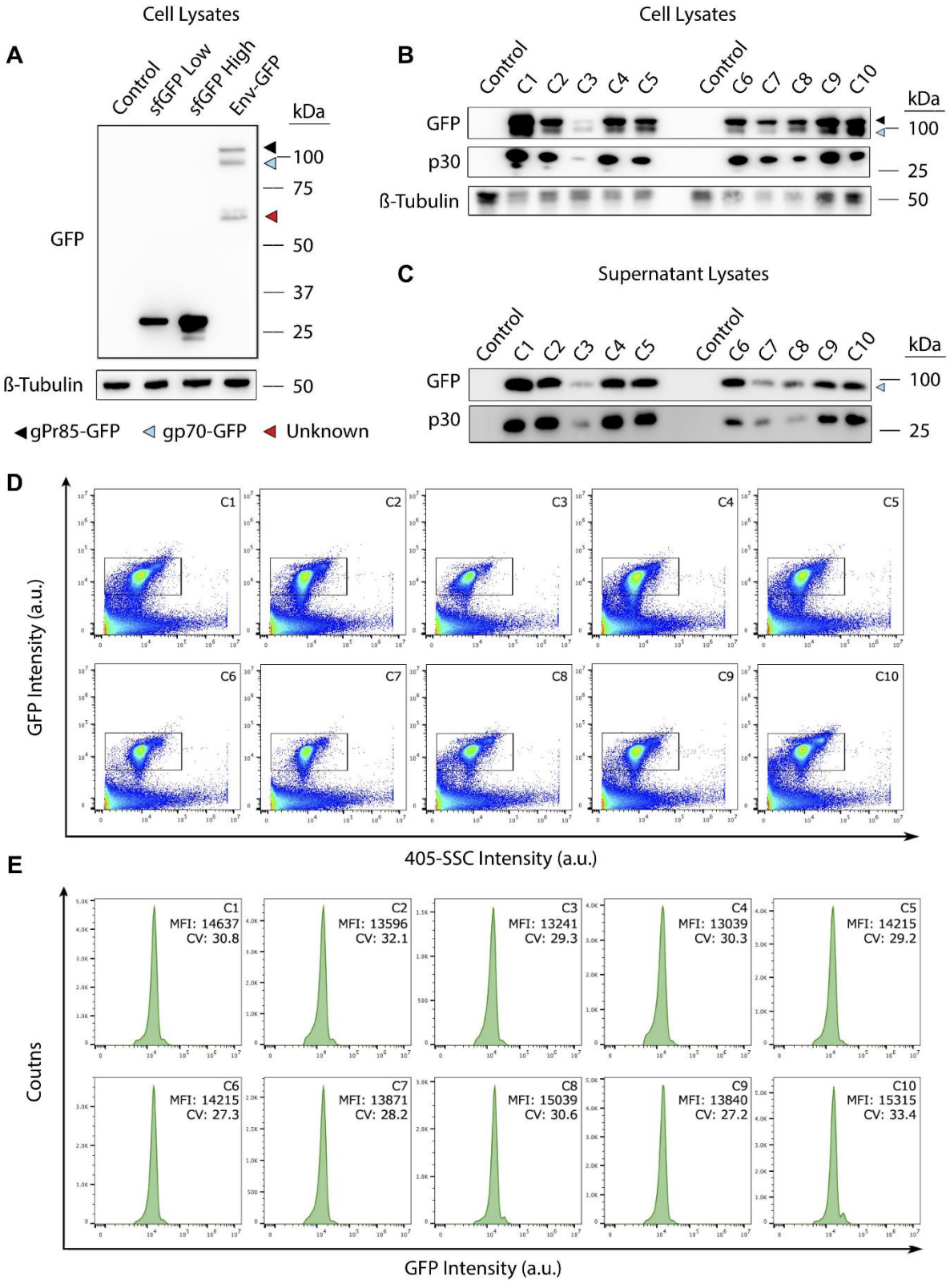
A
Cell Lysates
Control
sfGFP Low
sfGFP High
Env-GFP
kDa
100
75
50
37
25
GFP
ß-Tubulin
50
◀gPr85-GFP
◁ gp70-GFP
◀ Unknown
B
Cell Lysates
Control
C1
C2
C3
C4
C5
Control
C6
C7
C8
C9
C10
kDa
GFP
p30
ß-Tubulin
100
25
50
C
Supernatant Lysates
Control
C1
C2
C3
C4
C5
Control
C6
C7
C8
C9
C10
kDa
GFP
p30
100
25
D
C1
C2
C3
C4
C5
C6
C7
C8
C9
C10
GFP Intensity (a.u.)
405-SSC Intensity (a.u.)
E
C1
MFI: 14637
CV: 30.8
C2
MFI: 13596
CV: 32.1
C3
MFI: 13241
CV: 29.3
C4
MFI: 13039
CV: 30.3
C5
MFI: 14215
CV: 29.2
C6
MFI: 14215
CV: 27.3
C7
MFI: 13871
CV: 28.2
C8
MFI: 15039
CV: 30.6
C9
MFI: 13840
CV: 27.2
C10
MFI: 15315
CV: 33.4
Coutns
GFP Intensity (a.u.)

Figure 5.3. Comparative uptake of sfGFP and Env-GFP by MLV and EVs.

SDS-PAGE analysis of (A) sorted NIH 3T3 cells transduced with a retroviral vector expressing sfGFP or Env-GFP or (B) ten infected cell clones producing replicative MLV-sfGFP. (C) Viral supernatants from the cell clones were analyzed by SDS-PAGE and probed for p30and Env-GFP content. C1-C10depicts a unique chronically infected MLV-sfGFP cell clone isolated by single-cell sorting. (D) Supernatants from each of the ten clonal producer cells were analyzed by FVM. The gated region highlights GFP-positive particles. Each dot plot is representative of two independent experiments. (E) Histograms illustrating the GFP fluorescence intensity profiles from each of the ten clones analyzed in (D).

from instrument noise and non-fluorescent particles in the sample by FVM (**Fig. 3D**), and all viruses exhibited a highly homogenous fluorescent intensity (**Fig. 3E**).

Discrimination of MLV-sfGFP from EVs by FVM. The supernatants from MLV-sfGFP infected cell clones and from the sfGFP and Env-GFP transduced cells were directedly analyzed by FVM without further enrichment as previously described (373, 503). To minimize particle coincidence during sample acquisition, MLV-sfGFP samples were diluted 4-fold more than samples from sfGFP and Env-GFP transduced cells (**Fig. 4A**). Low frequency and dispersed fluorescent events were detected in supernatants from the sfGFP cells that corelate with their respective level of cytosolic sfGFP expression (**Fig. 4A and 4B**). These events likely correspond to EVs that incorporate cytosolic sfGFP as cargo. Env-GFP expressing cells also display low frequency fluorescent events with heterogenous SSC patterns. These are likely EVs with Env-GFP on their surface (369). In contrast, MLV-sfGFP infected cell clones release large numbers of highly monodisperse particles that are roughly 100-fold more abundant and 2-fold brighter than Env-GFP particles released from producer cells (**Fig. 4B and C**).

Viral incorporation of Env is highly consistent. Several studies have investigated MLV assembly and Env incorporation into the viral envelope (93, 508). Since the number of virion-associated Env molecules may affect virus infectivity, evaluating Env levels on individual virions is of significant interest in virology. However, until now, Env expression has primarily been calculated based on total protein content in virus lysates (509). Given that the fluorescence intensity of each virus is directly proportional to Env-GFP expression on its surface, it is now possible to measure relative levels of Env expression on individual viruses by FVM.

FVM analysis shows that the fluorescence intensity of the viruses is not directly related to Env expression levels in the infected cells (**Fig. 4C and 4D**). Also, MLV-sfGFP viruses acquire higher and much more homogenous densities of Env-GFP on their surface compared to EVs (**Fig. 4C**). This is exemplified by two MLV-sfGFP infected clones, each with a lower or higher relative fluorescence levels than the average in

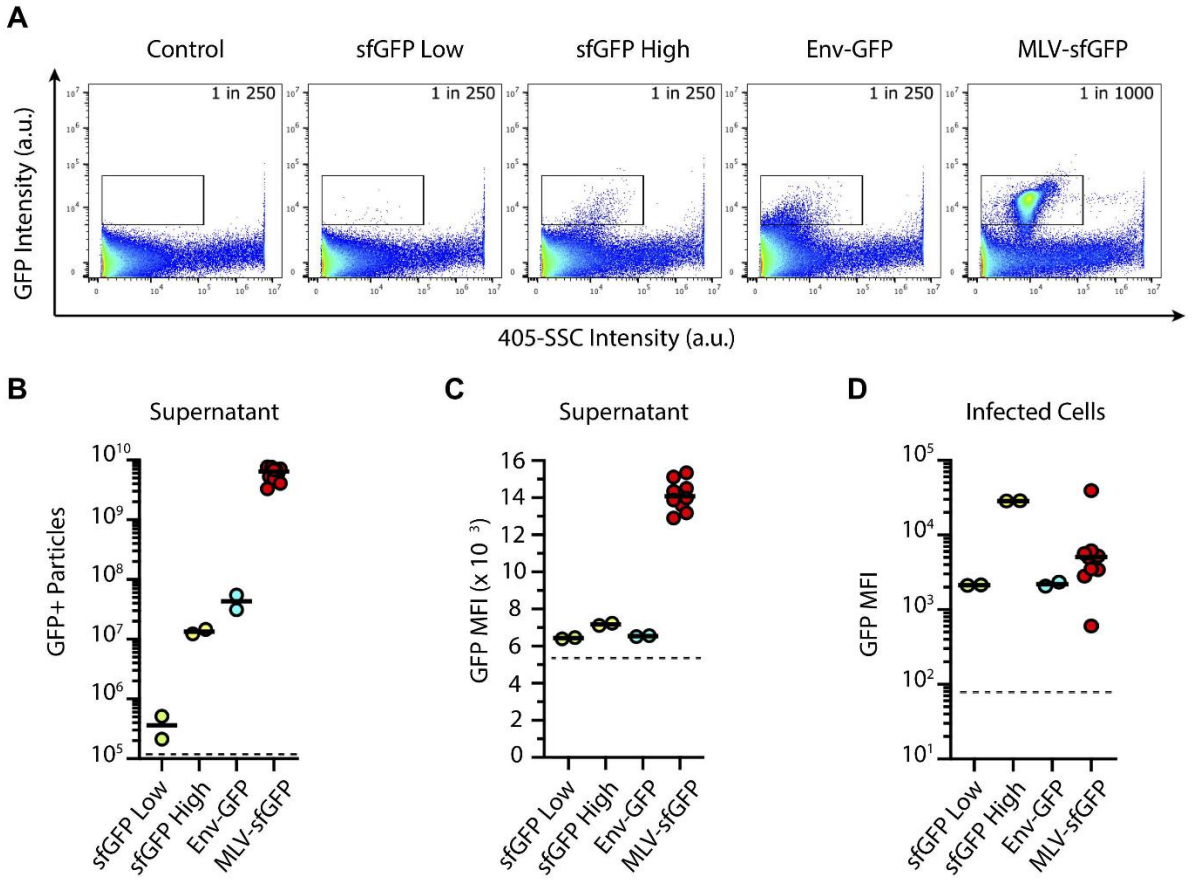

Figure 5.4. Enumeration and analysis of MLV and EV particles by FVM.

(A) Supernatants produced from uninfected NIH 3T3 cells (Control), sorted sfGFP and Env-GFP transduced cells, and MLV-sfGFP producer clone 6 were analyzed by FVM. The gated region highlights GFP-positive particles. The particles gated in (A) were analyzed for (B) number of GFP+ particles, and (C) GFP mean fluorescence intensity (MFI). (D) The producer cells from (A) were analyzed by flow cytometry for differences in GFP MFI. Dashed line indicates background levels established with the control sample. Virus was analyzed from 10 independent clones producing MLV-sfGFP; each data point is representative of two independent experiments.

the group (**Fig. 4D**), whereas all viral stocks display very similar Env-sfGFP incorporation levels (**Fig. 4C**). These data clearly highlight the tightly regulated nature of Env incorporation onto these viruses.

Intact particle enumeration by FVM can be achieved by antibody staining. Using FVM to characterize viruses may have limited use when virions do not exhibit intrinsic fluorescence such as MLV-sfGFP. Here we attempted to stain fluorescent and non-fluorescent viruses using a PE-conjugated anti-GFP antibody to compare intact particle counts. We generated a non-fluorescent MLV-sfGFP by mutating a single amino acid within the sfGFP sequence (MLV-DsfGFP). The mutated MLV exhibits no detectable GFP fluorescence but is clearly discernable by 405-SSC (**Fig. 5A**). Using a PE-anti-GFP antibody, we stained virus stocks of MLV-sfGFP and MLV-DsfGFP prior to direct FVM analysis (**Fig. 5B**). Appropriate concentrations of the antibody were previously established (503). Stained MLV-sfGFP and MLV-DsfGFP viruses displayed similar profiles of scattered light and fluorescence intensity. Our results show that not only does this display the potential of FVM for characterizing surface antigens on viral particles, but it enables an equally accurate way of enumerating non-fluorescent virions (**Fig. 5C**).

Intact viral particle counts reveal a large abundance of free viral protein and non-infectious virions. A valuable feature of FVM is its ability to provide an intact viral particle count, provided EVs are discernible. Here we aimed to correlate intact viral particle counts to viral gRNA and virus infectivity. We then used this information to compare the overall accuracy of FVM in parallel to some of the various other analytical methods used to measure virus titers.

The same ten viral stocks were quantified in parallel by FVM and nanoparticle tracking analysis (NTA) (**Fig. 6A**). The data was then directly compared to the other bulk analytical methods used in this study. While NTA did reveal a slightly higher particle count, the results were not statistically different to FVM (**Fig. 6B**). This highlights that the main particles in these viral stocks, from these specific producer cells, are indeed viral particles. ELISA analysis consistently overestimated the viral particle concentration, while

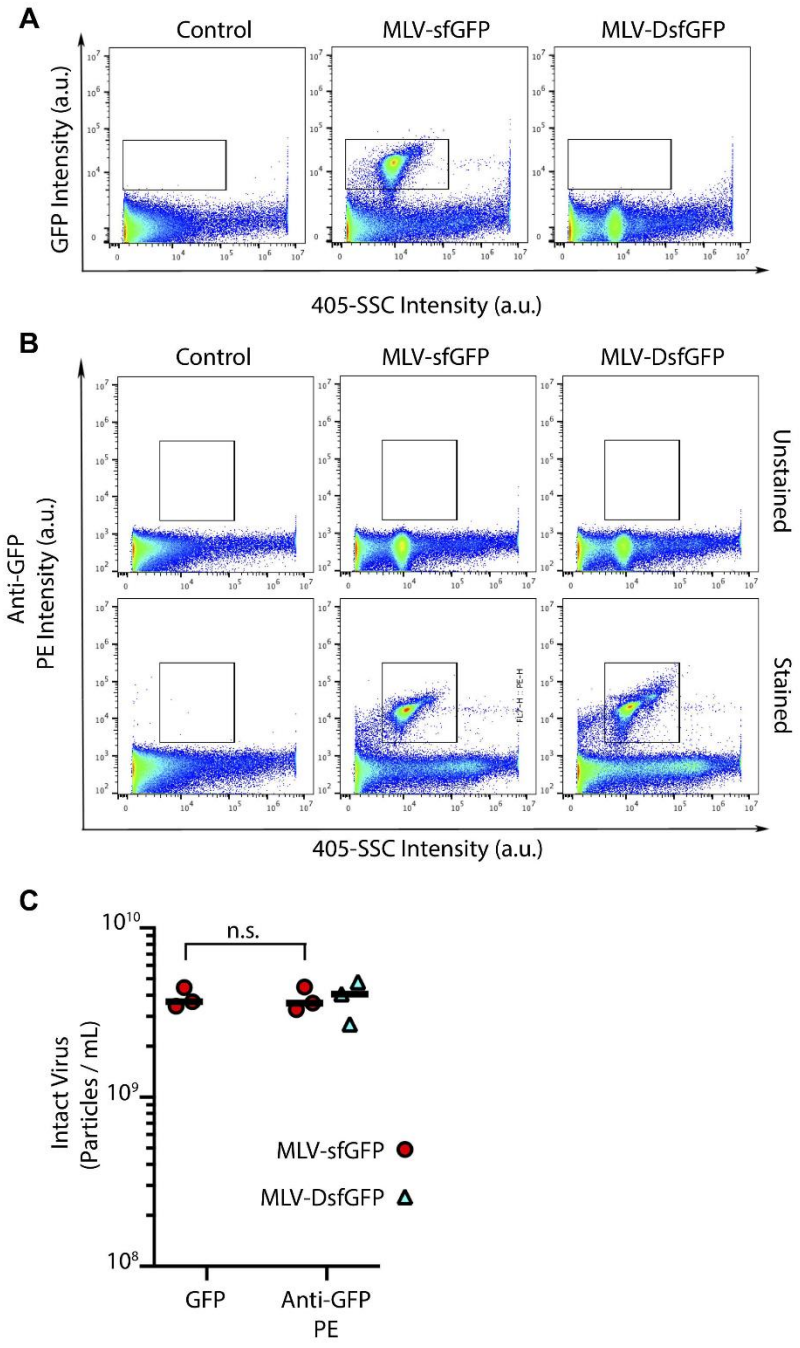

Figure 5.5. Viral particle quantification using antibody staining.

(A) FVM analysis comparing fluorescent (MLV-sfGFP, clone 6) to non-fluorescent (MLV-DsfGFP) virus. (B) Both viral supernatants were labelled with a fluorescent phycoerythrin (PE) antibody targeting an exposed epitope on GFP. (C) Quantification of virus stocks from three independent experiments are shown. P values were calculated by Student's t test. n.s.: not statistically significant, $P > 0.05$.

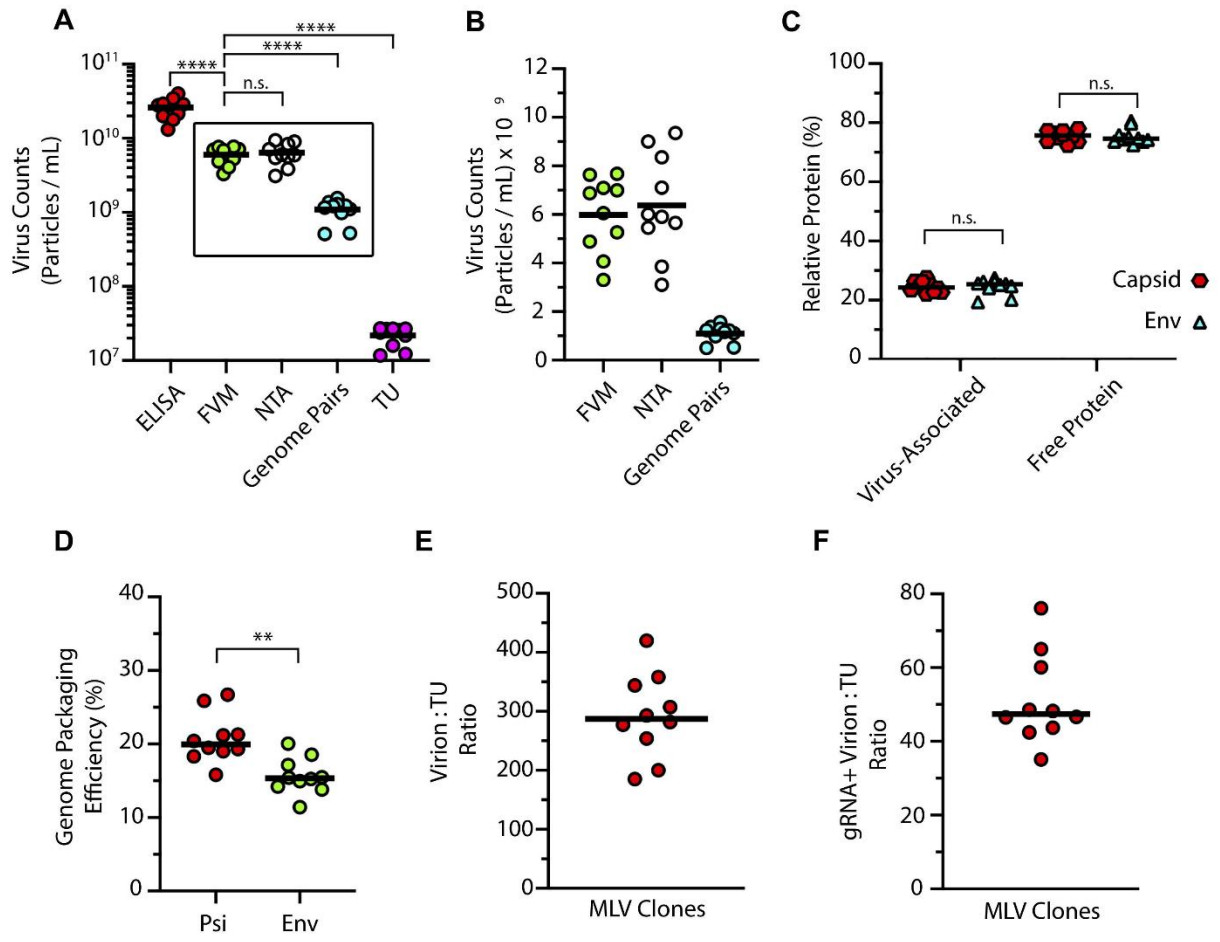

Figure 5.6. MLV particle infectivity and viral gRNA packaging efficiency determined by FVM.

(A) All ten MLV-sfGFP stocks were quantified by FVM and nanoparticle tracking analysis (NTA). Absolute viral counts obtained from each method is compared. Virus counts for ELISA reflect the total number of viruses obtained if all the p30 was associated with intact virus particles. (B) Zoomed in view from (A) to compare results obtained from FVM, NTA and Genome Pairs analysis. (C) Relationship of virus-associated compared to free viral protein (capsid p30 or Env) is shown using the information from (A), Figure 1B and Table 1. (D) Viral gRNA packaging efficiency calculated from information in (A) and Figure 2B. (E) Number of virions required for a productive infection using information from (A) and Figure 2C. (F) Number of viral gRNA-containing virions required for a productive infection. Each data point is representative of two independent experiments. P values were calculated by paired Student's t test. **, $P \leq 0.01$; ****, $P \leq 0.00001$; ns, $P > 0.05$.

viral genomic and TU analyses reported much lower values. With this in mind, the physical viral particle counts obtained from the FVM analysis were used to establish their relationship to viral constituents (e.g. protein and viral gRNA). With considerations given to published levels of p30 and Env expected in individual MLV particles (**Table 1**), the ELISA data indicates that each viral stock contains a surprisingly large amount of protein, over 76%, that is not associated with intact viral particles (**Fig. 6C** and **Table 2**).

Similarly, considering the necessity for the pairing of viral RNA genomes for efficient packaging into the capsid, the absolute genome count can be used to determine the packaging efficiency (77, 78, 127, 507). We illustrate that there is between a 16-21% (18% average) viral gRNA packaging efficiency for M-MLV, depending on whether the packaging signal (Psi) or Env sequences are used as targets for the amplification (**Fig. 6D and Table 2**).

Assessment of intact particle counts by FVM can also be related to TU values to determine the number of virions required for a single productive infection. The individual virion infectivity seems surprisingly low, with roughly 200-400 particles required for a single productive infection of NIH 3T3 cells (**Fig. 6E and Table 2**). By using the average packaging efficiency of both Psi and Env, we determined that approximately 50 genome-containing viral particles are required to productively infect a single NIH 3T3 cell (**Fig. 6F and Table 2**).

sfGFP insertion into Env does not alter virion stability. An interesting finding from **Fig. 6C** was the revelation of a large amount of soluble viral protein in infected cell supernatants. To determine if the insertion of sfGFP within Env influences virion stability, we sought to compare soluble and virus-associated p30 ratios of MLV-sfGFP to that of native M-MLV (referred to as WT) and to MLV-V5. This latter virus has a minimally modified Env containing a 14 amino-acid V5 epitope tag insertion in place of sfGFP (238 amino acids). Additionally, an important difference to note is that unlike MLV-V5 and MLV-sfGFP producer cells that are clones generated through single-cell sorting, the cells producing native WT MLV are a heterogenous and unsorted population of infected NIH 3T3 cells.

Table 5.2: Moloney MLV infectivity, virus-associated p30/Env, and viral gRNA packaging efficiency.

Virus-Associated p30 (%)	Virus-Associated Env (%)	Viral gRNA packaging efficiency[1] (%)	Overall Virus Infectivity[2] (%)	Infectivity of genome-containing viruses[3] (%)
23.8 ± 2.2	23.9 ± 3.8	18.2 ± 1.1	0.37 ± 0.03	1.98 ± 0.13

*Per individual virion as determined by FVM, ELISA and ddPCR. Results are displayed as an average ± standard error of viral stocks analyzed in duplicate from ten unique MLV clones. Pairwise analysis was conducted for each viral stock

[1] Proportion of intact virus particles containing two copies of the viral genome. Based on the literature, we assume a retrovirus has either 0 or 2 copies of the viral genomic RNA (77, 78, 127, 355, 507). The value represents the combined average packaging efficiency of the Psi and Env amplicons.

[2] Proportion of intact viral particles that generate a single transducing unit (TU) in NIH 3T3 cells.

[3]Proportion of genome-containing intact viral particles that generate a single transducing unit (TU) in NIH 3T3 cells.

Due to the lack of a commercially available fluorophore-conjugated MLV Env antibody, we were unable to directly stain WT MLV. Despite this shortcoming, enumeration of unmodified and unlabeled virus is still possible due to its distinct and uniform SSC characteristics by FVM (**Fig.7A**). Staining of surface epitopes within Env was conducted for both sfGFP and V5 (**Fig. 7B**). We then calculated as before inferred particles counts by p30 ELISA (**Fig. 7C**), and intact particle counts for both SSC analysis and epitope tag staining (**Fig. 7D**). The WT virus displayed more than 4-fold less p30 content compared to the clones (**Fig. 7C**), and as a result there were fewer intact viruses in the same proportion by SSC analysis (**Fig. 7D**). When comparing virus-associated to free p30 in infected cell supernatants, we notice that the WT virus has more virus-associated p30 (28%) than MLV-sfGFP (17%) and MLV-V5 (18%) (**Fig. 7E**). Overall, all three types of virus produce a large amount of p30 that is not associated with intact virus particles, while sfGFP and V5 insertions in MLV Env do not appear to exert a major impact on virus particle stability.

DISCUSSION

Most analytical techniques in virology are incapable of differentiating intact virus form free soluble or EV-associated viral components in a sample. It is now well established that EVs associate with viral proteins and nucleic acids in a variety of systems (337, 344, 369, 451, 500-502). These phenomena emphasize the importance of developing techniques to separate EVs from viral particles, either physically or analytically. One such method to achieve this, as demonstrated here, is the use of FVM. We and others have shown the capabilities of FVM to detect and enumerate viral particles (361, 364, 370, 373, 442, 510-513). In this work we took the technology further to quantify intact M-MLV particles and learn more about the biology of this important virus for the field of virology.

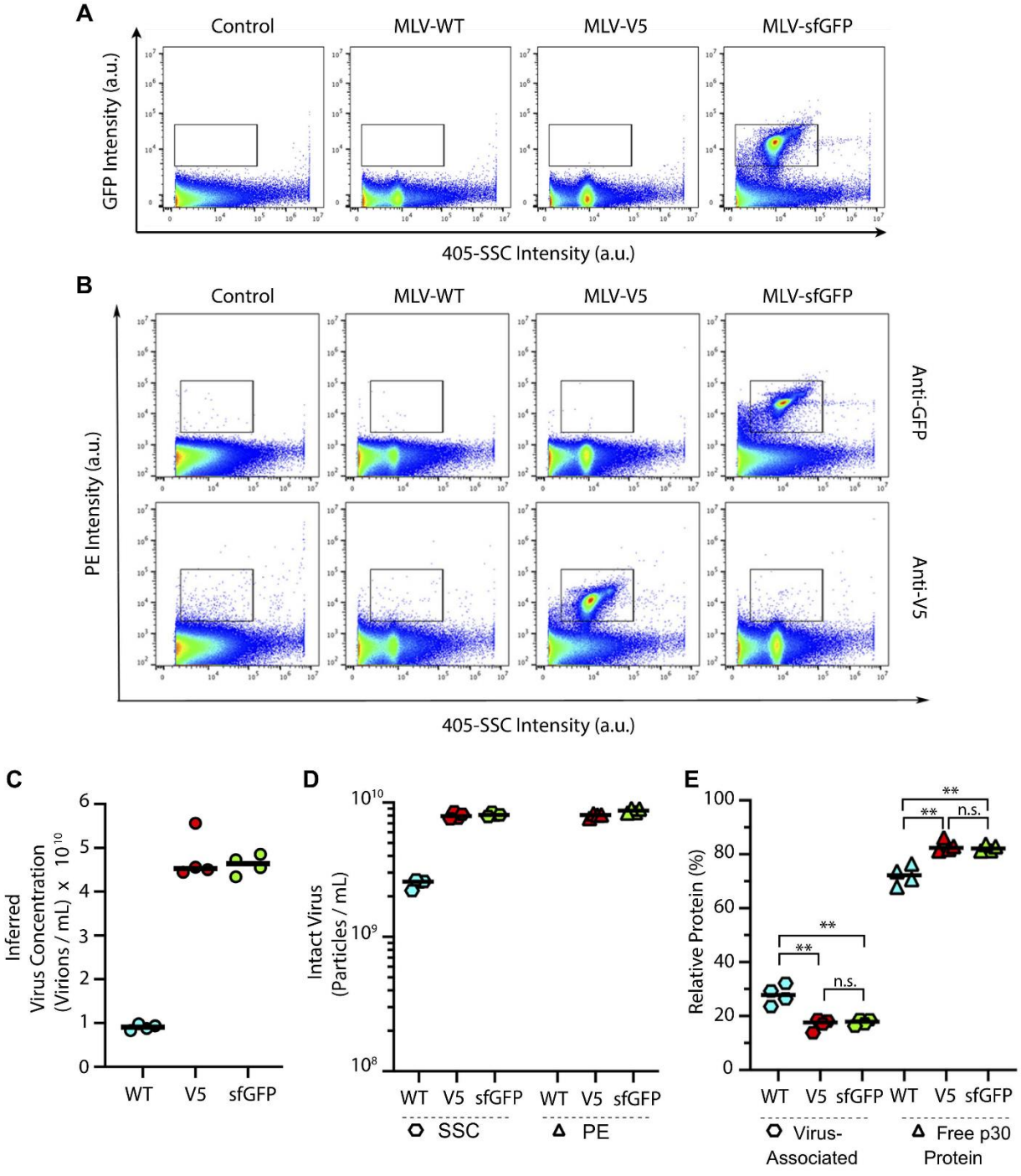
A
Control
MLV-WT
MLV-V5
MLV-sfGFP
GFP Intensity (a.u.)
405-SSC Intensity (a.u.)
B
Control
MLV-WT
MLV-V5
MLV-sfGFP
Anti-GFP
Anti-V5
PE Intensity (a.u.)
405-SSC Intensity (a.u.)
C
Inferred Virus Concentration (Virions / mL) x 10^10
WT
V5
sfGFP
D
Intact Virus (Particles / mL)
WT V5 sfGFP WT V5 sfGFP
SSC
PE
E
Relative Protein (%)
**
**
n.s.
**
**
n.s.
WT V5 sfGFP WT V5 sfGFP
Virus-Associated
Free p30 Protein

Figure 5.7. Impact of Env insertions on MLV stability.

(A) FVM analysis of fluorescent MLV-sfGFP and non-fluorescent MLV-WT and MLV-V5 viruses. (B) Viral supernatants were labelled with an antibody targeting an exposed epitope on Env (Top:anti-GFP PE; Bottom:anti-V5 PE). (C) Viral protein concentration as determined by ELISA was converted to an inferred virus titer based on the stoichiometry outlined in Table 1, as in Figure 1. (D) Physical titer quantification of virus stocks based on SSC analysis and PE staining. (E) Relationship between virus-associated and free capsid p30 protein based on data from panels C and D. The data represents four technical replicates from one experiment. **, $P \leq 0.01$; n.s., $P > 0.05$.

Importantly, this work was conducted with ten clonal expansions of single-cell sorted, chronically infected NIH 3T3 cells to capture possible diversity between individual virus particles. Furthermore, demonstrating that MLV can be distinguished from other cell-derived particles was critical. Env-GFP transduced cells were key to demonstrate that the relative frequency of Env accumulation on EVs is only about 1% when compared to MLV. However, one must keep in mind that the diversity, abundance and composition of EVs are likely to vary under different infection conditions or even in other cell types. Furthermore, it is clear that MLV incorporates a consistent amount of Env in each viral particle, more than twice that occurring in EVs. Cytosolic or Env-fused GFP expressed at similar or even at higher levels in cells than MLV-sfGFP do not produce EVs with the fluorescence intensity seen on the virus particles. Combined with our previously reported virus microfiltration and NTA data (373), we are very confident that the population visualized by FVM is in very large majority intact MLV.

Given that flow cytometer used in this work is set to threshold from SSC, only particles of a given size and light scattering properties will trigger a perceived and recorded event. While there is understandably some smaller EVs and various other types of particles that are below our limit of detection, free proteins or small aggregates will also go undetected. This is an important advantage of FVM because physical removal of these particles or even staining antibodies from samples becomes unnecessary. Additionally, MLV is confidently identified by both its surface expression of Env and its typical monodisperse SSC profile, which is granted by the highly controlled structural composition of the virus. These specific features thus greatly facilitate virus particle gating confidence in FVM applications. Even among the ten MLV-sfGFP producer cell clones analyzed, there is a disparity in Env expression of nearly 100-fold. Yet, this does not translate into a discernable variation in Env accumulation on individual virions, highlighting the tightly regulated incorporation of Env into MLV (**Figs. 3E and 4D**). Through a direct comparison of viral particle counts by FVM and protein levels measured by ELISA, we identified that there is an abundance of free viral protein in the chronically infected cell supernatants.

We then addressed valid concerns that the sfGFP sequence inserted in Env could be altering the stability of MLV. By using a WT virus and a virus with a short V5 epitope tag, we confirmed that this observation is indeed a general feature of MLV (Fig. 7). Other groups have also investigated the effects of insertions in MLV Env and Gag, and did not find those specific modifications to significantly alter particle structure or infectivity (120, 130, 514). However, we did observe that cells chronically infected with the WT virus produced fewer viruses and these displayed slightly more virus-associated p30 in their supernatants. It should be noted that the method we used to generate the cells chronically infected with the WT virus is slightly different to the way we produced the infected clones. Given that there is no direct way to monitor the infection by the WT virus in live cells due to the absence of a reporter or a commercial fluorescent Env antibody, we infected NIH 3T3 cells at a lower MOI than what was used with the clones and allowed the infection to blindly spread over 6 weeks. The infected cell population that resulted was used for the experiment presented in Figure 7. As such, there is a possibility that not all cells were in fact infected, or maybe the transcription of the virus in some cells was silenced. But, more likely, fewer cells were multiply infected which could easily explain the lower levels of virus produced overall.

Furthermore, given that the ratio of p30:Env is remains relatively constant in the supernatant of all viral clones (**Fig. 1C**), we posit that the vast majority of this free protein source is composed of degraded virions, as opposed to secreted soluble viral proteins. MLV has a relatively short half-life of 4.5hrs at 37°C, in contrast to >200hrs at 4°C (129). To obtain sufficient amoutns of virus for all the different types of analyses in this study, we harvested virus after 72hrs. This may have led to the accumulation of protein from degraded virions.

By relating the genome pair analysis with intact MLV particle enumeration, we calculated a viral genome packaging efficiency of between 16-21%, depending on the amplicon (Psi or Env). Viral genomes released by damaged particles are likely a minor source of experimental bias given that free RNA was entirely and rapidly degraded in our system. But yet again, viral genomic RNA is coated by nucleoproteins and ruptured

capsids may still offer some level of protection against nucleases. If this were the case, the true genome packaging efficiency of MLV would be lower than what we have calculated. EVs could also be potentially packaging viral RNAs, but we clearly demonstrated that there is minimal presence of EVs in our samples (**Figs. 4 and 6**). A small difference of 5% in packaging efficiency is seen when considering Psi (20%) and Env (15%) sequences. Possible explanations include: 1) amplification efficiency of the Psi sequence is slightly better than that of Env; or 2) a minor Psi+ and Env- splicing variant of the viral gRNA is recruited into virions. Although co-packaging of full-length viral gRNA and a subgenomic RNA has been reported, both these RNAs contain Psi and Env sequences and would unlikely contribute to the discrepancy in packaging efficiency (515). Regardless of the small 5% difference, both Psi or Env amplicons indicate that a large proportion of virions are lacking a RNA genome pair.

The low gRNA packaging efficiency that we have measured for MLV is in sharp contrast with the ~95% packaging efficiency observed for HIV-1 gRNA (355). However, it must be noted that the study referenced above was carried out with HIV-1 containing a heavily modified retroviral genome with several gene deletions and the insertion of 18-24 stem-loops that bind to a bacteriophage viral coat protein-fluorophore chimera. This system was used because it has the distinct benefit of single-copy resolution and direct visualization of genomic RNA within a virion. In perspective, our present study uses a minimally modified MLV genome that enabled us to correlate viral gRNA to intact particle counts by FVM to provide a quantitation of genome packaging efficiency. As a next step, analysis of HIV-1 genome packaging efficiency by FVM would be an interesting way to confirm previously published results.

A point of major intrigue that was revealed by this study is why does MLV have such poor gRNA packaging efficiency and produces such a large abundance of virus-like particles (VLPs)? Our group has also previously made similar observations concerning VLPs when studying the MLV glycosylated Gag accessory protein (369). One possibility is that MLV uses genome-deficient virions, degraded virions and EVs expressing viral proteins as decoys to overwhelm humoral immune responses. Or perhaps it is the opposite. Maybe these VLPs act in a similar fashion as defective-interfering particles (DIPs) that have been

recognized for a variety of other viruses to attenuate pathogenicity by stimulating viral neutralization and antiviral immune responses for the benefit of host survival (516-520). Either of these concepts could be contributing factors to the low pathogenicity of MLV *in vivo*.

Measuring viral titers has always been a primary requirement, a time-consuming chore and a challenge in virology. For practical reasons, it is the infectious titer that is usually measured, which corresponds to the infectious component of the total viral population in a sample. However, it has now become clear that the physical titer of the virus population is an equally valuable parameter. Non-infectious viral particles, especially in living animal model studies, can stimulate immune reactions to eliminate the virus (i.e. vaccines), divert them away from the infectious viruses (i.e., immunological decoys), or even attenuate virus pathogenicity for the benefit of the host and pathogen (i.e., DIPs). This is why classical titer measurements such as the MOI or the Tissue Infectious Dose 50 (TCID50), that correlates infectious titers to cytopathic effects, only describe part of the features of a given virus stock. Intact particle counts by FVM therefore offers a quick and simple way to measure the overall physical titer which can then be more accurately correlated to infectivity and cytopathic effects.

Precise enumeration of intact viral particles has also enabled us to calculate the number of particles required for a single productive infection. This varied between 200-400 particles for our ten clones, resulting in about 0.37% infectivity on average (**Table 2**). Albeit seemingly low, these values do fall in line with the reported ranges for retroviral particles per infectious unit (P/IU) observed in various other systems (521). This being said, we should emphasize that our experiments were carried out in controlled and optimized conditions, with the use of the polycation polybrene and spinoculation to enhance infections. Regardless of these technical efforts and because of mobility limitations of free virus in a liquid suspension that are governed by Brownian motion, there is a distinct possibility that some of the viruses in our assays still did not come into contact with a potential target cell (522). This scenario would result in an underestimation of the actual number of infectious units in our samples. Thus, measurements of infectivity will vary

considerably depending on the cells used and the experimental conditions. In sum, FVM now provides a new and easy way of monitoring the infectious titer under different experimental conditions. Importantly, we also demonstrated that intrinsically fluorescent viruses are not essential for use in FVM. Native viruses can be enumerated SSC analysis, but preferably, for more accurate results, should be stained using a fluorophore-conjugated commercial antibody (for inter-laboratory consistency) targeting highly expressed epitopes on the surface of the virus.

Further development of FVM and much needed improvements to the fluorescence detection sensitivity of flow cytometers will likely enable the scientific community to address new and unanswered questions about individual virus heterogeneity inside a virus population, in the same way as it is routinely done for cells using standard flow cytometry. As illustrated in this work, FVM can provide rapid and high throughput information about physical and infectious virus titers, packaging efficiency, presence of defective or interfering particles, and surface antigenic uptake. The minimal sample processing and time required to obtain results may even make this technique suitable for clinical diagnostics, especially given its higher sensitivity when compared to other common diagnostic methods (361).

ACKNOWLEDGEMENTS

T.M.R. holds a Queen Elizabeth II Graduate Scholarship in Science and Technology (QEII- GSST). V.A.T. is an International Society for Advancement of Cytometry (ISAC) Shared Resource Lab Emerging Leader. M.-A.L. holds a Canada Research Chair in Molecular Virology and Intrinsic Immunity. This work was supported by a research and development grant from the University of Ottawa Faculty of Medicine to the FCV Core Facility, and by a Discovery Grant and an Idea to Innovation (I2I) Grant by the Natural Sciences and Engineering Research Council of Canada (NSERC) to M.-A.L.

CONFLICTS OF INTERESTS

M.-A.L. is the CEO, and V.A.T. is the CSO of *ViroFlow Technologies*.

Chapter 6: General Discussion and Concluding Remarks

In this thesis research, I contributed to the deciphering of numerous functions of the enigmatic Glycosylated Gag (gGag) accessory protein of the Moloney strain of murine leukemia virus (MLV). This has implications for its role with regards to *in vivo* pathogenesis, as well as a restriction factor antagonist. Furthermore, using MLV as a model, I developed flow virometry as an innovative new tool within the repertoire of services offered by the Flow Cytometry and Virometry Core Facility at the University of Ottawa. With this tool, I evaluated numerous aspects of MLV and uncovered biologically relevant quantitative data that is independent of gGag expression. Altogether, the novelty of the discoveries presented within this thesis research highlights that there are ongoing discoveries to be made to elucidate further intricacies of retroviral infection, both simple and complex.

In **Chapters 2 and 3**, I investigated the role of post-translational modifications, more specifically N-linked glycosylation, on the functionality of gGag with regards to its antagonism of APOBEC3. These studies used a gGag-deficient virus with a mutated alternative start codon (CUG → CUA), as an APOBEC3-susceptible control. This is notably different than conventionally used barriers of translation, which may invoke a premature stop codon. In fact, some gGag-deficient MLV strains (i.e. Ab-X-MLV) contain a premature stop codon located five amino acids upstream of the initiation site for MLV Gag (305). Unfortunately, the precise positioning of the premature stop codon is rather complicated. It is located immediately downstream of the predicted transmembrane domain, but upstream of the Gag region. Thus, there is a high degree of likelihood that this protein is expressed and may function similarly to the native type II membrane protein, as they both have an identical cytoplasmic tail. This is supported by evidence that the leader sequence of gGag is a functional protein independent of the Gag region (314, 415). By removal of the alternative start codon, the complicated effects of a truncated gGag are ablated in this model. Additionally, to remove N-linked glycosylation, the targeted residues were

mutated to a structurally similar amino acid (N→Q). Alternatively, to observe the effects of an additional glycosylation on AKV, another MLV strain, the opposing contextual mutation was made (S→N). An important caveat to this approach, is that these mutations also impact Gag, the essential structural component of MLV. Through the use of these different mutants, the role of gGag within the context of circumventing APOBEC3-mediated mutagenesis was clarified. The most novel aspect uncovered in **Chapter 2** was the gradient of susceptibility that was dependent upon the level of glycosylation of gGag. In simpler terms, this is the order of viruses from highest to lowest levels of observable deamination and restriction in the presence of mA3: gGag-deficient > 1 glycan > 2 glycans > 3 glycans, where 3 glycans is the native state of gGag within Moloney MLV. This result remained true even with endogenous levels of murine APOBEC3 (mA3) in an *ex vivo* setting. Albeit the levels of mutations that occurred within the genome of AKV, an ERV with 2 glycans on gGag, in the presence of mA3 was significant, they did not lethally impact the viral replicative fitness. This data implies that some viruses may have evolved to allow for minor APOBEC3-induced mutagenesis to advance their rate of evolution. Indeed, there is a plethora of evidence to support an evolutionary advantage with regards to APOBEC3-mediated mutagenesis pushing for drug resistant and immune-escape HIV-1 variants (249, 255). This is especially true when considering the context of mutations preferred by mA3, as this APOBEC3 rarely induces stop codons (246, 523). Aside from the evolutionary implications, the findings herein were the first implication that the C-terminal region of gGag was involved in the retroviral resistance to APOBEC3.

In **Chapter 3**, I aimed to decipher the mechanism behind the observed protection phenotype from gGag and the glycosylations (369). Given the role of gGag that had already been established with viral core stability and the associated protective phenotype with APOBEC3, I evaluated the core stability of our gGag mutant and that of the glycosylation mutants (136, 225). With combined *in vitro* and intracellular core stability assessments, it was determined that increasing the number of glycans on gGag was linked with an increase in core stability. This finding has a remarkable correlation with the

aforementioned susceptibility to mA3 restriction. However, mutations that occur within the capsid domain of Gag may impose a reduced core stability by disrupting multimerization (97, 99). This often imposes a defect on replicative fitness, as we observed with both AKV and Moloney strains when mutating the residue equivalent to N480 on Moloney. With this in mind, I intended to distinguish between the effects of mutating amino acid residues and the direct glycosylation. To accomplish this, tunicamycin was used to completely block N-linked glycosylation during synthesis of the native gGag. This virus is produced with gGag that is devoid of glycans, but still maintains the original amino acid sequence. Interestingly, I did not observe any differences in viral core stability via an *in vitro* assessment using detergents. This implies that gGag, and not the glycans, provide a structural stability to the retrovirus. Given the conservation of these sites and their requirement for core stability, along with the recognized phenomenon of gGag-exposure of Gag antigens on the surface of infected cells, these may imply that the glycosylation sites were an adaptation to selective pressures. Since the glycosylated residues, especially N480 in Moloney MLV, is required for core stability, it suggests that the surrounding residues were selected to contain the recognized context for N-linked glycosylation. By exposing a glycosylated protein, it will protect these conserved residues from immune recognition – much in the same fashion of envelope glycoproteins (524). Overall, this work exemplified the role of viral core stability, and not exclusively gGag, in resisting the effects of APOBEC3. Even in the presence of gGag, but with mutated Gag (i.e. N→Q), this work revealed an increasing susceptibility to APOBEC3, both of mouse and human origins, that directly correlated with core stability. The observation itself may shed light on the protective means of other retroviruses, such as mouse mammary tumour virus, that have limited restriction by mA3 – despite no recognized viral antagonists, as of yet.

Up until this point, an important question remained unanswered: how does gGag influence capsid stability? To address this question, I had to determine which forms of gGag are present within a virion compared to EVs. Thus, bringing together all aspects of this dissertation, EVs and viral particles

had to be separated. As discussed in more detail later, in **Chapters 4 & 5** I determined that EVs incorporated minimal amounts of the MLV Env. This enabled an immunomagnetic capture of virions based on significant levels of Env. By targeting Env, I revealed a virtually complete capture of all Env-containing entities within the viral supernatants. Intriguingly, I discovered a co-association of full-length gGag with virions. Furthermore, given the traditionally observed type II membrane orientation of gGag, I attempted to immunocapture the viral particles based on the presence of the exposed C-terminal region of gGag. Virions, in the traditional sense, were not captured with this method. All particles containing the gGag type II membrane protein were devoid of Env, containing only a fraction of the total structural proteins. Altogether, these findings indicated that EV-associated gGag was in the traditional type II membrane protein orientation, exposing the C-terminus, whereas virion-associated gGag was in the orientation of a type I membrane protein, inserting the structural Gag region into the virion core (**Figure 6.1**). The original finding of gGag on EVs correlated with the presence of viral structural proteins in the same fraction (310). Furthermore, the identification of gGag as both type I and type II membrane proteins has been observed before *in vivo* (72). Additionally, the functionality of gGag in terms of SERINC antagonism is entirely conserved within the region upstream of the Gag domain (304, 314). This implies there must be some replicative benefit to attaching the Gag structural polyprotein to the small transmembrane domain encoded by the leader sequence. A few studies have indirectly addressed this question already, by assessing the role of gGag in mA3-deficient mice (224, 225, 238). These works were conducted using a gGag-deficient MLV with a premature stop codon immediately upstream of the initiation codon of Gag, potentially retaining the SERINC antagonism activity of that domain. Even still, these works directly linked the gGag-deficient viruses reduced core stability with a susceptibility to mA3, implying either a total loss of function for gGag or a specific function of the Gag region. I hypothesize the latter, that the ability of gGag to improve the structural stability of a viral core would come from its resistance to cleavage by the viral protease, which has been observed *in vitro* (298, 308). This is

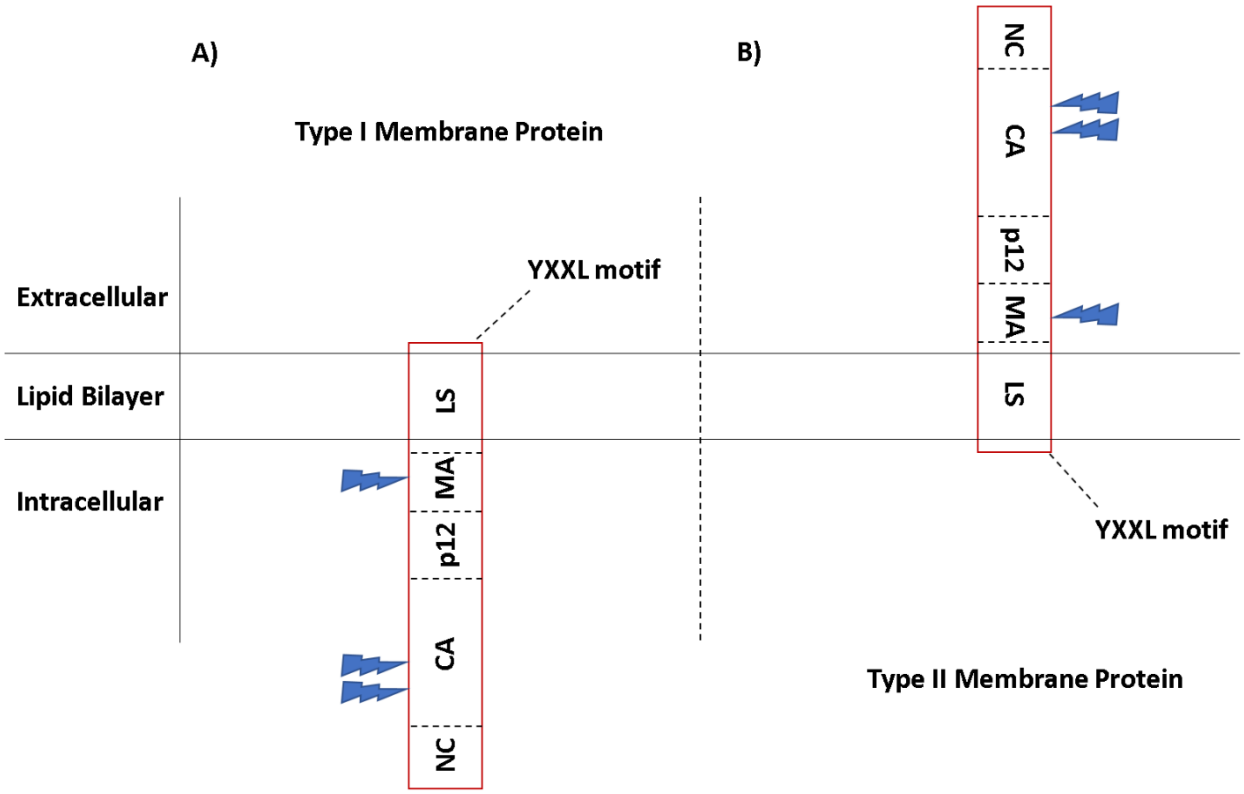

Figure 6.1. Membrane orientations of gGag.

Within Chapter 3, it was observed that full-length gGag as a type I transmembrane protein (A) can associate virtually exclusively with virions, whereas the type II transmembrane protein (B) associated virtually exclusively with VLPs or EVs containing significant levels of Gag. Presumably only the type II membrane protein can act to modulate the endocytic system due to the internalized YXXL motif. Blue lightning bolts represent glycosylation sites on Moloney MLV gGag.

supported by the fact that immature virions have enhanced mechanical stability, likely due to the covalent linkages between all domains (126). Altogether, this indicates that the orientation of gGag on virions, and specifically its structural Gag region, is the determining factor for viral core stability and therefore APOBEC3-resistance. The exact mechanism of protection has yet to be determined, but it may involve the steric hinderance of APOBEC3, preventing its access to the reverse transcription complex.

Unexpectedly, this thesis research has also revealed insights into some of the Nef-like effects of gGag. Details into the functional overlap between gGag and Nef has recently been documented (271, 315). Overall, it has been shown that Nef and gGag both support the endocytosis and lysosomal degradation of another potent restriction factor, SERINC. Through its manipulation and dysregulation of the cellular endosomal system, it was also reported that Nef is associated with exosomes (337). It was therefore not surprising to find that gGag associates with EVs, likely exosomes, with gGag in the traditional type II membrane protein orientation (**Figure 6.1**). In this orientation, the cytosolic tail of gGag is implicated to be essential for its control over the endosomal sorting pathway. This may allow for the exosomal delivery of gGag into potential target cells, allowing for viral priming prior to infection. In fact, the delivery of exosomal Nef has been noted to significantly alter the lipid raft metabolism of target cells (525). Furthermore, the Nef-like effects of gGag extend to its modulation of lipid rafts (312). Thus, like Nef, gGag may exacerbate the presence of lipid rafts on bystander cells, which upregulates TLR4 and pro-inflammatory signaling. Additional evidence suggests that MLV Env has evolved to directly interact and activate TLR4, leading to B cell activation *in vivo* (526, 527). Thus, MLV uses gGag and Env to independently induce a state of activation within the immune cells of an infected host. This demonstrates the delicate balancing act of a retroviral infection, as immune induction directly increases the pool of target cells due to the mitotic requirement of MLV, while at the same time increasing risk of neutralization (139).

More surprisingly, however, was the association of MLV structural proteins within these gGag-exposing EVs. Considering the association of MLV Gag with the viral genome and Env may occur within the endosomal system, some intersections can be expected (108). The findings portrayed in this thesis indicate that gGag associates with Gag by means of EVs but prevents the incorporation of Env. This is a unique finding, yet both gGag and Env have been previously identified to associate with EVs of similar buoyancy (310). Further to this point, Gag accumulation at the membrane seems more widespread than that of Env, implying some independence (528). While this particular dissection involved co-transfection of individual components in our two-plasmid system, with gGag transcription and translation being independent of Gag, this is not the case during a true infection. Nevertheless, the existence of another subpopulation capable of delivering capsid molecules to a cell may explain the substantial differences observed between gGag-sufficient and gGag-deficient viruses. By this, I refer to the bewildering observation that a gGag-sufficient virus delivered markedly increased levels of capsid to cells with no detectable difference in rate of infection when compared to a gGag-deficient virus. This was exposed by relating a fate of capsid assay to the viral infectivity assessments. The presence of such an abundant level of retroviral capsids, with no detectable Env, may indicate that these EVs represent a population of previously unidentified VLPs. Moreover, the orientation of gGag on these particles positions it with a cytoplasmic YXXL motif, which has been proven to markedly enhance endocytosis (529). Other groups have uncovered some phenotypical evidence to suggest this role for gGag, however the mechanism was unclear until now. By this, I refer to the illustration that Nef directs the trafficking of HIV-1 Gag and correspondingly gGag rescues Nef-deficient HIV-1 (314, 530). It remains to be determined if these VLPs or EVs contain substantial levels of SERINC. This may indicate another retroviral effort to remove SERINC from the producer cell or a consequence of a dysregulated endocytic system. Further investigation is required to confirm the presence of these so-called VLPs, or Gag delivering EVs, in a more natural setting.

Glycosylated Gag is an intriguing example of a convergent evolution between retroviruses; similar selective pressures within the hosts, both humans and mice, have pushed HIV and MLV to develop and maintain mechanisms to counteract intrinsic defenses. While gGag is functionally similar to Nef in terms of SERINC antagonism, the mechanism for resistance to APOBEC3 is still not entirely clear. The work presented herein provides further support to the hypothesis linking viral core stability directly with resistance to APOBEC3. Differences in susceptibility of MLV towards different APOBEC3 family members, such as the seven human members tested within these studies, has revealed the specificity of gGag towards mA3. The levels of mA3-induced deamination within MLV with a competent gGag is virtually undetectable, while the protection imposed towards human APOBEC3 (hA3) proteins is only partial. This finding may imply differing mechanisms of action of the APOBEC3 proteins, as gGag has evolved through selective pressures imposed exclusively by mA3. Therefore, the evolutionary pressure forced upon the HIV relative, SIV, to develop Vif, an antagonist capable of recognizing and ubiquitinating numerous hA3 proteins, was more complex than the pressure on MLV (531). In contrast, the antagonism of SERINC is remarkably similar between gGag and Nef. This is likely due to the numerous members of SERINC proteins within both mice and humans, though only two of which have detectable antiretroviral activity (213). An interesting difference between Nef and gGag, however, is the recognition and targeting of SERINC for degradation. While Nef selectively downregulates only antiviral SERINC, gGag has a broader approach (315, 532). It would be interesting to reveal if gGag, or MLV, has the potential to evolve a broader approach towards counteracting APOBEC3 under different evolutionary pressures. This can be provoked *in vitro* using murine cell lines expressing hA3 proteins, human cell lines expressing the MLV receptor (mCAT1) or through the use of transgenic mice. Additionally, the role of Nef can be functionally replaced by gGag, whereas Nef is not capable of rescuing gGag-deficient MLV under certain conditions (313). This is either reflective of the capsid stabilizing component, which should be provided by the Gag region of gGag, or an as of yet unidentified function of this protein. Regardless, its role in an

in vivo setting is undeniable. The strongest evidence for which is the reversion of gGag-deficient viruses to express a functional gGag *in vivo*, though not in the presence of mA3-deficient mice (224, 225, 238, 302-304, 423). Yet the selective pressure enforced by SERINC has not yet been proven in such a definitive manner.

Independently of gGag, in **Chapters 4 & 5** I sought to advance the scientific knowledge on MLV through the adaptation of small particle flow cytometry, also known as flow virometry. In **Chapter 4**, I collaborated with Dr. Vera Tang to develop this technique on MLV within the University of Ottawa Flow Cytometry and Virometry Core Facility (373). The laboratory strain of MLV chosen for this study has a GFP incorporated within the SU region of the Env (371, 372). Given the abundance of Env on the surface of virions, this acted as a robust distinguishing characteristic to highlight MLV from EVs (115). This selectivity is likely mediated by the cooperation of Env with multiple regions of Gag (93, 111). Using a transfection-based approach, I illustrated that Env does not freely associate with EVs in a high abundance. This is likely due to the coordination of Gag and Env within the endosomal sorting machinery (93, 108). Further discrimination was made possible by illustrating the discrepancy in side scattered light (SSC) profiles of MLV compared to EVs. While EVs vary in size, the homogenous nature of the SSC profile of MLV is attributed to its controlled assembly and consistent size (101). I also verified the apparent size of the virus population using nanoparticle tracking analysis and a microfiltration approach. While I sought to identify a staining technique that is capable of distinguishing MLV from EVs independently of the fluorescent Env, my efforts were ultimately unsuccessful using lipophilic and nucleic acid dyes, though I did verify the efficacy of this approach with a vaccinia virus. Ultimately, **I hypothesize that the lipid and nucleic acid content of the EVs and MLV particles may not be sufficiently different to target with such a broad dye-based approach**. This may be for the best, considering the illustration of the negative impacts of efficient staining on the replicative fitness of MLV.

In **Chapter 5**, I took advantage of the knowledge gained from **Chapter 4** to effectively enumerate MLV particles by flow virometry (374). By retroviral transduction of NIH 3T3 cells, the same cells used for virus production, I verified that MLV Env incorporation into EVs was minimal when compared to its directed association to MLV particles. This type of control was chosen for three main reasons: 1) Integration into the genome of the host cell occurs using the MLV machinery, 2) Transcription is directed under the control of the MLV LTR, and 3) Host origin is maintained (i.e. murine cells are used for production). Importantly, to illustrate the broad application of flow virometry, antibody surface staining of MLV was shown to be equally as effective to discern Env incorporation as inherent Env fluorescence. Furthermore, the SSC profiles of MLV were confirmed to be quite consistent when compared to the heterogeneity of EVs. Flow virometry with SSC triggering limits perceived events to those of adequate size, which suggests that MLV (approximate diameter 110-120nm) is near the limit of detection of our instrumentation using this approach (for more details, see Appendix 3). This does exclude the possibility of analyzing smaller viruses and EVs based on SSC triggering, however flow virometry has the advantage of ignoring the presence of free proteins and low magnitude protein aggregates. Furthermore, the two-pronged identification of MLV involves both size homogeneity and Env incorporation, which I illustrated to have an approximate 99% confidence in the selective identification of MLV over EVs and other particles. Thus, I have validated flow virometry as a rapid approach to discriminate intact MLV particles from soluble proteins and EVs based on SSC profiles and Env as a discrimination marker.

Through correlation of flow virometry quantification and total viral protein content, I revealed a substantial amount of soluble viral proteins within MLV preparations. On average, approximately 25% of total protein content was calculated to be associated with intact virus particles when considering both capsid (p30) and Env content within a sample. Importantly, these calculations are based on robust microscopy studies that have counted the levels of each of these proteins associated with an intact

virion (101, 115). This suggests that a striking majority of viral protein content within these biological samples are soluble. To gain an idea of the origin of these soluble proteins, one may bear in mind the theoretical ratio of capsid : Env within the context of an intact viral particle, as inferred from the aforementioned reports, which is 7.29. Within this study, I calculated the capsid : Env ratio within the viral supernatants to be approximately 7.4 ± 0.3. The conservation of this ratio within the supernatants implies the bulk of soluble proteins likely originates from degraded virions. This is likely due to the experimental settings which provided 72hrs of virus production time. Considering the half-life of MLV and disparities in virus production, proportions of soluble to virus-associated proteins are likely to vary (129). Thus, flow virometry has the added benefit to discriminate intact virus particles and provide more insight into viral titers when compared to ELISA, a conventionally used technique.

Determination of the genome packaging efficiency of a virus is of great interest to the field. However, this remains a challenging quantitative technique to achieve. Nonetheless, using high resolution microscopy-based analysis, the genome packaging efficiency of HIV-1 has been determined to be approximately 95% (355). Qualitatively, however, MLV is well-characterized to selectively incorporate dimeric genomes through interactions between the nucleocapsid region of Gag and the packaging signal (77, 78, 127, 507). Furthermore, the correlation of total MLV genomic content was related to the viral particle enumeration to infer a packaging efficiency. In this regard, virions were assumed to package either 0 or 2 copies of the viral genome. EV-associated viral nucleic acids were assumed to be negligible in this case, due to the non-significant difference between MLV and total particle counts when comparing flow virometry to nanoparticle tracking analysis. Altogether, genome packaging efficiency was calculated to be approximately 15-20% for MLV. Though this PCR-based approach is limited in the sense that it detects only fragments of the viral genome, both the packaging signal and Env regions were targeted to improve confidence. Especially considering the abundance of endogenous retroviruses (ERVs) within the murine genome, it is possible that MLV infection may reactivate their transcription

(377). Given the targeted activation of TLR4, and documented evidence of ERV reactivation in LPS-induced cells, this is highly likely (533). This has been illustrated in the context of HIV-1 infection and human ERVs (534). Thus, it is possible that the lack of detection of MLV genomes is due, at least in part, to the incorporation of ERV genomes with sequence variations that avoid this PCR-based detection. Moreover, if we consider the work from Dr. Alan Rein's group, it was originally posited that an MLV particle contains approximately 7-8 RNA bases per Gag molecule (109). Though originally thought to be half of the nucleic acid content within a viral particle, this can be revisited with the more robust knowledge of MLV structure and Gag composition (101). This suggests that a genome pair accounts for over 90% of the RNA capable of fitting within a single virion. Together with the levels of cellular mRNA species detected within MLV, some of which have enrichment as high as the viral genome, this indicates that some virions are lacking a genome pair in favour of cellular RNA (109). Overall, this leads me to theorize that the vast majority of MLV particles produced within these experimental settings are devoid of its specific genome pair, in favour of cellular RNA, such as mRNA and, possibly, ERV genomes. While this is in line with the current understanding of infectious units per viral particle based on microscopic studies, further work is required to determine the specific content of these virions (535).

Evidence of decoy or defective, interfering particles (DIPs) have been proposed for numerous other species of viruses (516-520). Similar evidence has even been illustrated for the case of HIV infection (376, 536). It is highly possible that a proportion of these MLV virions devoid of a genuine, full-length genome pair are representative of high levels of DIPs. Intracellularly, these DIPs have been suggested to competitively inhibit the virus of origin due to limiting resources. This type of inhibition is desirable in circumstances that would otherwise lead to cytotoxicity for the host cell. This represents a likely scenario, as despite variations in viral protein content at the producer cell level, all ten clones of virus producer cells released a similar magnitude of virus particles by all means of quantification. This phenomenon demonstrates that there must be a limiting resource or inhibiting factor within the cells. *In*

vivo, these decoy or DIPs may play several roles. As previously discussed, the MLV Env has the potential to activate immune cells through TLR4 interactions (526). This may be a priming of potential target cells, due to the mitotic requirement of MLV (139). Given the activation of immune cells, these incompetent particles may act as decoys to sequester the antibody response, reducing the likelihood of neutralization for true infectious virions. Contrarily, along the lines of expected roles for DIPs for other viruses, these particles may act in an immunostimulatory and MLV inhibitory fashion to curb viral pathogenesis and enhance host survival.

Though the presence of DIPs has not been conclusively shown for MLV, occurrence of defective genomes within the host chromatin has been recognized as a naturally occurring event (87, 515). This has been attributed to the alternative splicing sites within the viral genome (86). In direct support of these defective genomes acting as functional DIPs, mutational deletion of the respective splice sites results in an expanded pathogenic effect for multiple strains of MLV (85, 537). The sequence of these defective genomes encodes a partial Gag, missing the C-terminus of capsid and entire nucleocapsid, fused to a C-terminus of integrase. However, there is potential still for additional splicing and translation of Env. It is important to note that these proteins lack the independent capability for genome packaging, self-assembly and reverse transcription. Complementation alongside a functional viral genome, these defective genomes have been found to associate within virions. Accumulation of these defective polyproteins would result in a corresponding lack of replicative fitness for those virions, representing a competitive proteomic interaction. Furthermore, as these defective genomes have an intact Psi sequence, competitive genomic packaging will also occur. Even heterodimerization has been demonstrated between defective and full-length MLV genomes (515). Thus, these defective genomes have the potential to competitively inhibit productive infections in a dose-dependent manner, at both the RNA and protein levels. This is very much in accordance with the traditional functionality of DIPs and corresponds with mathematical modelling within the context of VSV infection, another RNA virus (376).

Given the lack of detection of a laboratory strain genome within 80-85% of these particles, this leads me to the hypothesis that many of these DIPs are generated from the activated transcription of ERVs within the infected cells. Additionally, the presence of several uncharacterized host proteins, Gm46894, Gm39972 Gm43305, that bear a remarkable resemblance to the coding sequences within this potential DIP genome indicates a true *in vivo* relevance (538, 539). Further work is essential to confirm and dissect the role of these particles within a host.

In closing, though we have come a long way from the original identification of MLV as a filterable pathogenic agent, there are still many questions left unanswered. With the culmination of knowledge acquired during the course of this thesis, we are now one step closer to understanding the many complexities of a simple retrovirus. The work demonstrated within this thesis has uncovered numerous aspects of the Moloney murine leukemia virus (MLV). With regards to the enigmatic accessory protein of MLV, Glycosylated Gag (gGag), I have revealed previously undiscovered functions that advance our knowledge about retroviral infection. Firstly, this work solidifies the use of MLV as a functional small animal model for the understanding of the intricacies of retrovirus-host interactions and antagonism. This is highlighted through striking examples of convergent evolution between MLV and HIV, developing differing mechanisms to similarly antagonize the pressures exerted by homologous restriction factors of mice and humans. On a more general note, the works presented herein emphasize the importance of viral core stability within any retrovirus species. Deciphering the mechanisms behind retroviral restriction factors and pathogen-associated antagonists represents a desirable, but as of yet clinically unexplored avenue of potential therapy. Development of therapeutics along these lines will have the benefit of a broader acting effect, potentiating the inhibitory phenotype of intrinsic factors on a wide range of retroviral threats. At the same time, I have underlined the capability of flow virometry to identify and quantify a viral agent based on size and antigenic composition. Secondly, from these results, I have provided convincing evidence on the presence of defective, interfering particles within the

context of MLV. Preparations of DIPs have become a promising avenue for treatment of existing viral infections, especially for those wherein vaccination strategies exhibit challenges and the viral evolutionary rate permits significant immune and therapeutic escape (i.e. influenza, dengue, HIV, etc.) (540). DIP prophylaxis will compete, inhibit and steal resources from the replicative virus, while at the same time stimulating the immune response to promote clearance. Flow virometry represents a uniquely positioned tool to both identify and purify DIPs from within any given viral stock. Thirdly, the rapidity, sensitivity and minimal manipulation required for this technique, enables it to be easily adapted into a clinical setting (361). While currently the clinical diagnosis of a viral infection is time consuming and error prone, this type of work has the potential to rapidly and accurately characterize viral infections from clinical samples, bridging the gap between diagnosis and treatment. Similar studies are currently underway to establish EVs with varying antigens as biomarkers for earlier diagnosis of cancers (541). Finally, though the applications herein were modelled after a murine retrovirus, we have demonstrated the broad capability of antibody staining for host markers on viral membranes in an additional study (503). Thus, through antigenic profiling there is a potential for the identification of the originating virus producer cell. This is highly desirable for the characterization of the latent reservoir in HIV-1 patients, allowing for a more targeted therapy rather than the current systemic approach.

References

1. Porter JR. 1976. Antony van Leeuwenhoek: tercentenary of his discovery of bacteria. Bacteriol Rev 40:260-9.
2. Pasteur L. May 1880. On the extension of the germ theory to the etiology of certain common diseases. Comptes rendus, de l'Academie des Sciences:1033-44.
3. Lecoq H. 2001. [Discovery of the first virus, the tobacco mosaic virus: 1892 or 1898?]. C R Acad Sci III 324:929-33.
4. Wherry WB. 1902. Experiments on the Permeability of the berkefeld Filter and the Pasteur-Chamberland bougie to Bacteria of Small Size. J Med Res 8:322-8.
5. Ackermann HW. 2011. The first phage electron micrographs. Bacteriophage 1:225-227.
6. Dulbecco R. 1952. Production of Plaques in Monolayer Tissue Cultures by Single Particles of an Animal Virus. Proc Natl Acad Sci U S A 38:747-52.
7. Baer A, Kehn-Hall K. 2014. Viral concentration determination through plaque assays: using traditional and novel overlay systems. J Vis Exp doi:10.3791/52065:e52065.
8. Koonin EV, Starokadomskyy P. 2016. Are viruses alive? The replicator paradigm sheds decisive light on an old but misguided question. Stud Hist Philos Biol Biomed Sci 59:125-34.
9. Koonin EV, Martin W. 2005. On the origin of genomes and cells within inorganic compartments. Trends Genet 21:647-54.
10. Baltimore D. 1971. Expression of animal virus genomes. Bacteriol Rev 35:235-41.
11. Wolf YI, Kazlauskas D, Iranzo J, Lucia-Sanz A, Kuhn JH, Krupovic M, Dolja VV, Koonin EV. 2018. Origins and Evolution of the Global RNA Virome. MBio 9.
12. Simmonds P, Adams MJ, Benko M, Breitbart M, Brister JR, Carstens EB, Davison AJ, Delwart E, Gorbalenya AE, Harrach B, Hull R, King AM, Koonin EV, Krupovic M, Kuhn JH, Lefkowitz EJ, Nibert ML, Orton R, Roossinck MJ, Sabanadzovic S, Sullivan MB, Suttle CA, Tesh RB, van der Vlugt RA, Varsani A, Zerbini FM. 2017. Consensus statement: Virus taxonomy in the age of metagenomics. Nat Rev Microbiol 15:161-168.
13. Rous P. 1911. A Sarcoma of the Fowl Transmissible by an Agent Separable from the Tumor Cells. J Exp Med 13:397-411.
14. Ellermann V. BO. 1908. Experimentelle Leukämie bei Hühnern. Zentralbl Bakteriol Parasitenkd Infectionskr Hyg Abt Orig 46:595-609.
15. Jarrett WF, Martin WB, Crighton GW, Dalton RG, Stewart MF. 1964. Transmission Experiments with Leukemia (Lymphosarcoma). Nature 202:566-7.
16. Theilen GH, Gould D, Fowler M, Dungworth DL. 1971. C-type virus in tumor tissue of a woolly monkey (Lagothrix spp.) with fibrosarcoma. J Natl Cancer Inst 47:881-9.
17. J.J. B. 1936. Some possible effects of nursing on the mammary gland tumour incidence in mice. Science 84:162.
18. Moloney JB. 1960. Biological studies on a lymphoid-leukemia virus extracted from sarcoma 37. I. Origin and introductory investigations. J Natl Cancer Inst 24:933-51.
19. Moloney JB. 1966. A virus-induced rhabdomyosarcoma of mice. Natl Cancer Inst Monogr 22:139-42.
20. Abelson HT, Rabstein LS. 1970. Lymphosarcoma: virus-induced thymic-independent disease in mice. Cancer Res 30:2213-22.
21. Friend C. 1957. Cell-free transmission in adult Swiss mice of a disease having the character of a leukemia. J Exp Med 105:307-18.
22. Gross L. 1957. Development and serial cellfree passage of a highly potent strain of mouse leukemia virus. Proc Soc Exp Biol Med 94:767-71.
23. L.N. P. 1992. Biology of avian retroviruses. In The Retroviridae 1:299-404.

24. Stehelin D, Varmus HE, Bishop JM, Vogt PK. 1976. DNA related to the transforming gene(s) of avian sarcoma viruses is present in normal avian DNA. Nature 260:170-3.
25. van Lohuizen M, Verbeek S, Scheijen B, Wientjens E, van der Gulden H, Berns A. 1991. Identification of cooperating oncogenes in E mu-myc transgenic mice by provirus tagging. Cell 65:737-52.
26. Poirier Y, Kozak C, Jolicoeur P. 1988. Identification of a common helper provirus integration site in Abelson murine leukemia virus-induced lymphoma DNA. J Virol 62:3985-92.
27. Tsatsanis C, Fulton R, Nishigaki K, Tsujimoto H, Levy L, Terry A, Spandidos D, Onions D, Neil JC. 1994. Genetic determinants of feline leukemia virus-induced lymphoid tumors: patterns of proviral insertion and gene rearrangement. J Virol 68:8296-303.
28. Dougherty RM, Di Stefano HS, Roth FK. 1967. Virus particles and viral antigens in chicken tissues free of infectious avian leukosis virus. Proc Natl Acad Sci U S A 58:808-17.
29. Hanafusa H, Hanafusa T, Rubin H. 1963. The defectiveness of Rous sarcoma virus. Proc Natl Acad Sci U S A 49:572-80.
30. Hanafusa H, Miyamoto T, Hanafusa T. 1970. A cell-associated factor essential for formation of an infectious form of Rous sarcoma virus. Proc Natl Acad Sci U S A 66:314-21.
31. Vogt PK. 1967. A virus released by "nonproducing" Rous sarcoma cells. Proc Natl Acad Sci U S A 58:801-8.
32. Temin HM. 1964. Nature of the provirus of Rous sarcoma. Nat Cancer Inst Monogr 17:557-570.
33. Temin HM. 1962. Separation of morphological conversion and virus production in Rous sarcoma virus infection. Cold Spring Harb Symp Quant Biol 27:407-14.
34. Rowe WP, Pincus T. 1972. Quantitative studies of naturally occurring murine leukemia virus infection of AKR mice. J Exp Med 135:429-36.
35. Aaronson SA, Hartley JW, Todaro GJ. 1969. Mouse leukemia virus: "spontaneous" release by mouse embryo cells after long-term in vitro cultivation. Proc Natl Acad Sci U S A 64:87-94.
36. Weiss RA, Friis RR, Katz E, Vogt PK. 1971. Induction of avian tumor viruses in normal cells by physical and chemical carcinogens. Virology 46:920-38.
37. Lowy DR, Rowe WP, Teich N, Hartley JW. 1971. Murine leukemia virus: high-frequency activation in vitro by 5-iododeoxyuridine and 5-bromodeoxyuridine. Science 174:155-6.
38. Baltimore D. 1970. RNA-dependent DNA polymerase in virions of RNA tumour viruses. Nature 226:1209-11.
39. Temin HM, Mizutani S. 1970. RNA-dependent DNA polymerase in virions of Rous sarcoma virus. Nature 226:1211-3.
40. Sambrook J, Westphal H, Srinivasan PR, Dulbecco R. 1968. The integrated state of viral DNA in SV40-transformed cells. Proc Natl Acad Sci U S A 60:1288-95.
41. Schwartzberg P, Colicelli J, Goff SP. 1984. Construction and analysis of deletion mutations in the pol gene of Moloney murine leukemia virus: a new viral function required for productive infection. Cell 37:1043-52.
42. Rethwilm A, Bodem J. 2013. Evolution of foamy viruses: the most ancient of all retroviruses. Viruses 5:2349-74.
43. Gartner K, Wiktorowicz T, Park J, Mergia A, Rethwilm A, Scheller C. 2009. Accuracy estimation of foamy virus genome copying. Retrovirology 6:32.
44. Hancks DC, Kazazian HH, Jr. 2016. Roles for retrotransposon insertions in human disease. Mob DNA 7:9.
45. Lavialle C, Cornelis G, Dupressoir A, Esnault C, Heidmann O, Vernochet C, Heidmann T. 2013. Paleovirology of 'syncytins', retroviral env genes exapted for a role in placentation. Philos Trans R Soc Lond B Biol Sci 368:20120507.

46. Grandi N, Tramontano E. 2018. Human Endogenous Retroviruses Are Ancient Acquired Elements Still Shaping Innate Immune Responses. Front Immunol 9:2039.
47. Nakaya Y, Lilue J, Stavrou S, Moran EA, Ross SR. 2017. AIM2-Like Receptors Positively and Negatively Regulate the Interferon Response Induced by Cytosolic DNA. MBio 8.
48. Xu X, Zhao H, Gong Z, Han GZ. 2018. Endogenous retroviruses of non-avian/mammalian vertebrates illuminate diversity and deep history of retroviruses. PLoS Pathog 14:e1007072.
49. Wendling F, Varlet P, Charon M, Tambourin P. 1986. MPLV: a retrovirus complex inducing an acute myeloproliferative leukemic disorder in adult mice. Virology 149:242-6.
50. Finkel MP, Biskis BO, Jinkins PB. 1966. Virus induction of osteosarcomas in mice. Science 151:698-701.
51. Chirigos MA, Scott D, Turner W, Perk K. 1968. Biological, pathological and physical characterization of a possible variant of a murine sarcoma virus (Moloney). Int J Cancer 3:223-7.
52. Ch'ang LY, Yang WK, Myer FE, Yang DM. 1989. Negative regulatory element associated with potentially functional promoter and enhancer elements in the long terminal repeats of endogenous murine leukemia virus-related proviral sequences. J Virol 63:2746-57.
53. Stocking C, Kollek R, Bergholz U, Ostertag W. 1986. Point mutations in the U3 region of the long terminal repeat of Moloney murine leukemia virus determine disease specificity of the myeloproliferative sarcoma virus. Virology 153:145-9.
54. Shinnick TM, Lerner RA, Sutcliffe JG. 1981. Nucleotide sequence of Moloney murine leukaemia virus. Nature 293:543-8.
55. Guntaka RV. 1993. Transcription termination and polyadenylation in retroviruses. Microbiol Rev 57:511-21.
56. Cleavinger PJ, Kandala JC, Guntaka RV. 1997. The GT-rich sequence in the U5 region of Rous sarcoma virus long terminal repeat is required for transcription termination and 3' processing. Folia Biol (Praha) 43:153-60.
57. Volkova NA, Fomina EG, Smolnikova VV, Zinovieva NA, Fomin IK. 2014. The U3 region of Moloney murine leukemia virus contains position-independent cis-acting sequences involved in the nuclear export of full-length viral transcripts. J Biol Chem 289:20158-69.
58. Swain A, Coffin JM. 1989. Polyadenylation at correct sites in genome RNA is not required for retrovirus replication or genome encapsidation. J Virol 63:3301-6.
59. Sokol M, Wabl M, Ruiz IR, Pedersen FS. 2014. Novel principles of gamma-retroviral insertional transcription activation in murine leukemia virus-induced end-stage tumors. Retrovirology 11:36.
60. Berlioz C, Darlix JL. 1995. An internal ribosomal entry mechanism promotes translation of murine leukemia virus gag polyprotein precursors. J Virol 69:2214-22.
61. Deffaud C, Darlix JL. 2000. Characterization of an internal ribosomal entry segment in the 5' leader of murine leukemia virus env RNA. J Virol 74:846-50.
62. Suomalainen M, Garoff H. 1994. Incorporation of homologous and heterologous proteins into the envelope of Moloney murine leukemia virus. J Virol 68:4879-89.
63. Rein A. 2011. Murine leukemia viruses: objects and organisms. Adv Virol 2011:403419.
64. Yoshinaka Y, Katoh I, Copeland TD, Oroszlan S. 1985. Murine leukemia virus protease is encoded by the gag-pol gene and is synthesized through suppression of an amber termination codon. Proc Natl Acad Sci U S A 82:1618-22.
65. Jamjoom GA, Naso RB, Arlinghaus RB. 1977. Further characterization of intracellular precursor polyproteins of Rauscher leukemia virus. Virology 78:11-34.
66. Houck-Loomis B, Durney MA, Salguero C, Shankar N, Nagle JM, Goff SP, D'Souza VM. 2011. An equilibrium-dependent retroviral mRNA switch regulates translational recoding. Nature 480:561-4.

67. Johnson SF, Collins JT, D'Souza VM, Telesnitsky A. 2014. Determinants of Moloney murine leukemia virus Gag-Pol and genomic RNA proportions. J Virol 88:7267-75.
68. Feher A, Boross P, Sperka T, Miklossy G, Kadas J, Bagossi P, Oroszlan S, Weber IT, Tozser J. 2006. Characterization of the murine leukemia virus protease and its comparison with the human immunodeficiency virus type 1 protease. J Gen Virol 87:1321-30.
69. Ragheb JA, Yu H, Hofmann T, Anderson WF. 1995. The amphotropic and ecotropic murine leukemia virus envelope TM subunits are equivalent mediators of direct membrane fusion: implications for the role of the ecotropic envelope and receptor in syncytium formation and viral entry. J Virol 69:7205-15.
70. Kraunus J, Zychlinski D, Heise T, Galla M, Bohne J, Baum C. 2006. Murine leukemia virus regulates alternative splicing through sequences upstream of the 5' splice site. J Biol Chem 281:37381-90.
71. Lee JT, Yu SS, Han E, Kim S, Kim S. 2004. Engineering the splice acceptor for improved gene expression and viral titer in an MLV-based retroviral vector. Gene Ther 11:94-9.
72. Fujisawa R, McAtee FJ, Zirbel JH, Portis JL. 1997. Characterization of glycosylated Gag expressed by a neurovirulent murine leukemia virus: identification of differences in processing in vitro and in vivo. J Virol 71:5355-60.
73. Bender W, Davidson N. 1976. Mapping of poly(A) sequences in the electron microscope reveals unusual structure of type C oncornavirus RNA molecules. Cell 7:595-607.
74. Mann R, Mulligan RC, Baltimore D. 1983. Construction of a retrovirus packaging mutant and its use to produce helper-free defective retrovirus. Cell 33:153-9.
75. Bender MA, Palmer TD, Gelinas RE, Miller AD. 1987. Evidence that the packaging signal of Moloney murine leukemia virus extends into the gag region. J Virol 61:1639-46.
76. Adam MA, Miller AD. 1988. Identification of a signal in a murine retrovirus that is sufficient for packaging of nonretroviral RNA into virions. J Virol 62:3802-6.
77. Hibbert CS, Mirro J, Rein A. 2004. mRNA molecules containing murine leukemia virus packaging signals are encapsidated as dimers. J Virol 78:10927-38.
78. D'Souza V, Summers MF. 2004. Structural basis for packaging the dimeric genome of Moloney murine leukaemia virus. Nature 431:586-90.
79. Basyuk E, Boulon S, Skou Pedersen F, Bertrand E, Vestergaard Rasmussen S. 2005. The packaging signal of MLV is an integrated module that mediates intracellular transport of genomic RNAs. J Mol Biol 354:330-9.
80. Smagulova F, Maurel S, Morichaud Z, Devaux C, Mougel M, Houzet L. 2005. The highly structured encapsidation signal of MuLV RNA is involved in the nuclear export of its unspliced RNA. J Mol Biol 354:1118-28.
81. Rasmussen SV, Pedersen FS. 2006. Co-localization of gammaretroviral RNAs at their transcription site favours co-packaging. J Gen Virol 87:2279-89.
82. Maurel S, Mougel M. 2010. Murine leukemia virus RNA dimerization is coupled to transcription and splicing processes. Retrovirology 7:64.
83. Nash MA, Meyer MK, Decker GL, Arlinghaus RB. 1993. A subset of Pr65gag is nucleus associated in murine leukemia virus-infected cells. J Virol 67:1350-6.
84. Sakuma T, Davila JI, Malcolm JA, Kocher JP, Tonne JM, Ikeda Y. 2014. Murine leukemia virus uses NXF1 for nuclear export of spliced and unspliced viral transcripts. J Virol 88:4069-82.
85. Sorensen AB, Lund AH, Kunder S, Quintanilla-Martinez L, Schmidt J, Wang B, Wabl M, Pedersen FS. 2007. Impairment of alternative splice sites defining a novel gammaretroviral exon within gag modifies the oncogenic properties of Akv murine leukemia virus. Retrovirology 4:46.

86. Dejardin J, Bompard-Marechal G, Audit M, Hope TJ, Sitbon M, Mougel M. 2000. A novel subgenomic murine leukemia virus RNA transcript results from alternative splicing. J Virol 74:3709-14.
87. Houzet L, Battini JL, Bernard E, Thibert V, Mougel M. 2003. A new retroelement constituted by a natural alternatively spliced RNA of murine replication-competent retroviruses. EMBO J 22:4866-75.
88. Pessel-Vivares L, Houzet L, Laine S, Mougel M. 2015. Insights into the nuclear export of murine leukemia virus intron-containing RNA. RNA Biol 12:942-9.
89. Rein A, McClure MR, Rice NR, Luftig RB, Schultz AM. 1986. Myristylation site in Pr65gag is essential for virus particle formation by Moloney murine leukemia virus. Proc Natl Acad Sci U S A 83:7246-50.
90. Soneoka Y, Kingsman SM, Kingsman AJ. 1997. Mutagenesis analysis of the murine leukemia virus matrix protein: identification of regions important for membrane localization and intracellular transport. J Virol 71:5549-59.
91. Leung J, Yueh A, Appah FS, Jr., Yuan B, de los Santos K, Goff SP. 2006. Interaction of Moloney murine leukemia virus matrix protein with IQGAP. EMBO J 25:2155-66.
92. Jin J, Sherer NM, Heidecker G, Derse D, Mothes W. 2009. Assembly of the murine leukemia virus is directed towards sites of cell-cell contact. PLoS Biol 7:e1000163.
93. Gregory DA, Lyddon TD, Johnson MC. 2013. Multiple Gag domains contribute to selective recruitment of murine leukemia virus (MLV) Env to MLV virions. J Virol 87:1518-27.
94. Yuan B, Li X, Goff SP. 1999. Mutations altering the moloney murine leukemia virus p12 Gag protein affect virion production and early events of the virus life cycle. EMBO J 18:4700-10.
95. Wight DJ, Boucherit VC, Nader M, Allen DJ, Taylor IA, Bishop KN. 2012. The gammaretroviral p12 protein has multiple domains that function during the early stages of replication. Retrovirology 9:83.
96. Auerbach MR, Brown KR, Singh IR. 2007. Mutational analysis of the N-terminal domain of Moloney murine leukemia virus capsid protein. J Virol 81:12337-47.
97. Hsu HW, Schwartzberg P, Goff SP. 1985. Point mutations in the P30 domain of the gag gene of Moloney murine leukemia virus. Virology 142:211-4.
98. Alin K, Goff SP. 1996. Mutational analysis of interactions between the Gag precursor proteins of murine leukemia viruses. Virology 216:418-24.
99. Wang MQ, Goff SP. 2003. Defects in virion production caused by mutations affecting the C-terminal portion of the Moloney murine leukemia virus capsid protein. J Virol 77:3339-44.
100. Cheslock SR, Poon DT, Fu W, Rhodes TD, Henderson LE, Nagashima K, McGrath CF, Hu WS. 2003. Charged assembly helix motif in murine leukemia virus capsid: an important region for virus assembly and particle size determination. J Virol 77:7058-66.
101. Qu K, Glass B, Dolezal M, Schur FKM, Murciano B, Rein A, Rumlova M, Ruml T, Krausslich HG, Briggs JAG. 2018. Structure and architecture of immature and mature murine leukemia virus capsids. Proc Natl Acad Sci U S A 115:E11751-E11760.
102. Henderson LE, Copeland TD, Sowder RC, Smythers GW, Oroszlan S. 1981. Primary structure of the low molecular weight nucleic acid-binding proteins of murine leukemia viruses. J Biol Chem 256:8400-6.
103. De Rocquigny H, Ficheux D, Gabus C, Allain B, Fournie-Zaluski MC, Darlix JL, Roques BP. 1993. Two short basic sequences surrounding the zinc finger of nucleocapsid protein NCp10 of Moloney murine leukemia virus are critical for RNA annealing activity. Nucleic Acids Res 21:823-9.

104. Gorelick RJ, Henderson LE, Hanser JP, Rein A. 1988. Point mutants of Moloney murine leukemia virus that fail to package viral RNA: evidence for specific RNA recognition by a "zinc finger-like" protein sequence. Proc Natl Acad Sci U S A 85:8420-4.
105. Muriaux D, Costes S, Nagashima K, Mirro J, Cho E, Lockett S, Rein A. 2004. Role of murine leukemia virus nucleocapsid protein in virus assembly. J Virol 78:12378-85.
106. Muriaux D, Mirro J, Harvin D, Rein A. 2001. RNA is a structural element in retrovirus particles. Proc Natl Acad Sci U S A 98:5246-51.
107. Miyazaki Y, Garcia EL, King SR, Iyalla K, Loeliger K, Starck P, Syed S, Telesnitsky A, Summers MF. 2010. An RNA structural switch regulates diploid genome packaging by Moloney murine leukemia virus. J Mol Biol 396:141-52.
108. Basyuk E, Galli T, Mougel M, Blanchard JM, Sitbon M, Bertrand E. 2003. Retroviral genomic RNAs are transported to the plasma membrane by endosomal vesicles. Dev Cell 5:161-74.
109. Rulli SJ, Jr., Hibbert CS, Mirro J, Pederson T, Biswal S, Rein A. 2007. Selective and nonselective packaging of cellular RNAs in retrovirus particles. J Virol 81:6623-31.
110. Opstelten DJ, Wallin M, Garoff H. 1998. Moloney murine leukemia virus envelope protein subunits, gp70 and Pr15E, form a stable disulfide-linked complex. J Virol 72:6537-45.
111. Lucas TM, Lyddon TD, Grosse SA, Johnson MC. 2010. Two distinct mechanisms regulate recruitment of murine leukemia virus envelope protein to retroviral assembly sites. Virology 405:548-55.
112. Sjoberg M, Wallin M, Lindqvist B, Garoff H. 2006. Furin cleavage potentiates the membrane fusion-controlling intersubunit disulfide bond isomerization activity of leukemia virus Env. J Virol 80:5540-51.
113. Li M, Yang C, Tong S, Weidmann A, Compans RW. 2002. Palmitoylation of the murine leukemia virus envelope protein is critical for lipid raft association and surface expression. J Virol 76:11845-52.
114. Beer C, Pedersen L, Wirth M. 2005. Amphotropic murine leukaemia virus envelope protein is associated with cholesterol-rich microdomains. Virol J 2:36.
115. Kuznetsov YG, Low A, Fan H, McPherson A. 2004. Atomic force microscopy investigation of wild-type Moloney murine leukemia virus particles and virus particles lacking the envelope protein. Virology 323:189-96.
116. Bartusch C, Prange R. 2016. ESCRT Requirements for Murine Leukemia Virus Release. Viruses 8:103.
117. Segura MM, Garnier A, Di Falco MR, Whissell G, Meneses-Acosta A, Arcand N, Kamen A. 2008. Identification of host proteins associated with retroviral vector particles by proteomic analysis of highly purified vector preparations. J Virol 82:1107-17.
118. Segura-Morales C, Pescia C, Chatellard-Causse C, Sadoul R, Bertrand E, Basyuk E. 2005. Tsg101 and Alix interact with murine leukemia virus Gag and cooperate with Nedd4 ubiquitin ligases during budding. J Biol Chem 280:27004-12.
119. Jadwin JA, Rudd V, Sette P, Challa S, Bouamr F. 2010. Late domain-independent rescue of a release-deficient Moloney murine leukemia virus by the ubiquitin ligase itch. J Virol 84:704-15.
120. Sherer NM, Lehmann MJ, Jimenez-Soto LF, Ingmundson A, Horner SM, Cicchetti G, Allen PG, Pypaert M, Cunningham JM, Mothes W. 2003. Visualization of retroviral replication in living cells reveals budding into multivesicular bodies. Traffic 4:785-801.
121. Martin-Serrano J, Neil SJ. 2011. Host factors involved in retroviral budding and release. Nat Rev Microbiol 9:519-31.
122. Katoh I, Yoshinaka Y, Rein A, Shibuya M, Odaka T, Oroszlan S. 1985. Murine leukemia virus maturation: protease region required for conversion from "immature" to "mature" core form and for virus infectivity. Virology 145:280-92.

123. Crawford S, Goff SP. 1985. A deletion mutation in the 5' part of the pol gene of Moloney murine leukemia virus blocks proteolytic processing of the gag and pol polyproteins. J Virol 53:899-907.
124. Hayakawa T, Misumi Y, Kobayashi M, Yamamoto Y, Fujisawa Y. 1992. Requirement of N- and C-terminal regions for enzymatic activity of human T-cell leukemia virus type I protease. Eur J Biochem 206:919-25.
125. Menendez-Arias L, Gotte D, Oroszlan S. 1993. Moloney murine leukemia virus protease: bacterial expression and characterization of the purified enzyme. Virology 196:557-63.
126. Kol N, Gladnikoff M, Barlam D, Shneck RZ, Rein A, Rousso I. 2006. Mechanical properties of murine leukemia virus particles: effect of maturation. Biophys J 91:767-74.
127. Fu W, Rein A. 1993. Maturation of dimeric viral RNA of Moloney murine leukemia virus. J Virol 67:5443-9.
128. Loving R, Wu SR, Sjoberg M, Lindqvist B, Garoff H. 2012. Maturation cleavage of the murine leukemia virus Env precursor separates the transmembrane subunits to prime it for receptor triggering. Proc Natl Acad Sci U S A 109:7735-40.
129. Higashikawa F, Chang L. 2001. Kinetic analyses of stability of simple and complex retroviral vectors. Virology 280:124-31.
130. Riedel C, Vasishtan D, Siebert CA, Whittle C, Lehmann MJ, Mothes W, Grunewald K. 2017. Native structure of a retroviral envelope protein and its conformational change upon interaction with the target cell. J Struct Biol 197:172-180.
131. Kamiyama H, Kakoki K, Yoshii H, Iwao M, Igawa T, Sakai H, Hayashi H, Matsuyama T, Yamamoto N, Kubo Y. 2011. Infection of XC cells by MLVs and Ebola virus is endosome-dependent but acidification-independent. PLoS One 6:e26180.
132. Kumar P, Nachagari D, Fields C, Franks J, Albritton LM. 2007. Host cell cathepsins potentiate Moloney murine leukemia virus infection. J Virol 81:10506-14.
133. Sjoberg M, Loving R, Lindqvist B, Garoff H. 2017. Sequential activation of the three protomers in the Moloney murine leukemia virus Env. Proc Natl Acad Sci U S A 114:2723-2728.
134. Wu SR, Sjoberg M, Wallin M, Lindqvist B, Ekstrom M, Hebert H, Koeck PJ, Garoff H. 2008. Turning of the receptor-binding domains opens up the murine leukaemia virus Env for membrane fusion. EMBO J 27:2799-808.
135. Doms RW, Moore JP. 2000. HIV-1 membrane fusion: targets of opportunity. J Cell Biol 151:F9-14.
136. Stavrou S, Blouch K, Kotla S, Bass A, Ross SR. 2015. Nucleic acid recognition orchestrates the anti-viral response to retroviruses. Cell Host Microbe 17:478-88.
137. Fassati A, Goff SP. 1999. Characterization of intracellular reverse transcription complexes of Moloney murine leukemia virus. J Virol 73:8919-25.
138. Valle-Tenney R, Opazo T, Cancino J, Goff SP, Arriagada G. 2016. Dynein Regulators Are Important for Ecotropic Murine Leukemia Virus Infection. J Virol 90:6896-6905.
139. Roe T, Reynolds TC, Yu G, Brown PO. 1993. Integration of murine leukemia virus DNA depends on mitosis. EMBO J 12:2099-108.
140. Yueh A, Leung J, Bhattacharyya S, Perrone LA, de los Santos K, Pu SY, Goff SP. 2006. Interaction of moloney murine leukemia virus capsid with Ubc9 and PIASy mediates SUMO-1 addition required early in infection. J Virol 80:342-52.
141. Wanaguru M, Barry DJ, Benton DJ, O'Reilly NJ, Bishop KN. 2018. Murine leukemia virus p12 tethers the capsid-containing pre-integration complex to chromatin by binding directly to host nucleosomes in mitosis. PLoS Pathog 14:e1007117.
142. Henderson LE, Gilden RV, Oroszlan S. 1979. Amino acid sequence homology between histone H5 and murine leukemia virus phosphoprotein p12. Science 203:1346-8.

143. Schneider WM, Brzezinski JD, Aiyer S, Malani N, Gyuricza M, Bushman FD, Roth MJ. 2013. Viral DNA tethering domains complement replication-defective mutations in the p12 protein of MuLV Gag. Proc Natl Acad Sci U S A 110:9487-92.
144. Tanese N, Goff SP. 1988. Domain structure of the Moloney murine leukemia virus reverse transcriptase: mutational analysis and separate expression of the DNA polymerase and RNase H activities. Proc Natl Acad Sci U S A 85:1777-81.
145. Peters G, Harada F, Dahlberg JE, Panet A, Haseltine WA, Baltimore D. 1977. Low-molecular-weight RNAs of Moloney murine leukemia virus: identification of the primer for RNA-directed DNA synthesis. J Virol 21:1031-41.
146. Peters G, Dahlberg JE. 1979. RNA-directed DNA synthesis in Moloney murine leukemia virus: interaction between the primer tRNA and the genome RNA. J Virol 31:398-407.
147. Levin JG, Seidman JG. 1979. Selective packaging of host tRNA's by murine leukemia virus particles does not require genomic RNA. J Virol 29:328-35.
148. Eckwahl MJ, Sim S, Smith D, Telesnitsky A, Wolin SL. 2015. A retrovirus packages nascent host noncoding RNAs from a novel surveillance pathway. Genes Dev 29:646-57.
149. Arhel N. 2010. Revisiting HIV-1 uncoating. Retrovirology 7:96.
150. Levin JG, Seidman JG. 1981. Effect of polymerase mutations on packaging of primer tRNAPro during murine leukemia virus assembly. J Virol 38:403-8.
151. Palmer MT, Kirkman R, Kosloff BR, Eipers PG, Morrow CD. 2007. tRNA isoacceptor preference prior to retrovirus Gag-Pol junction links primer selection and viral translation. J Virol 81:4397-404.
152. Fu W, Ortiz-Conde BA, Gorelick RJ, Hughes SH, Rein A. 1997. Placement of tRNA primer on the primer-binding site requires pol gene expression in avian but not murine retroviruses. J Virol 71:6940-6.
153. Miller SB, Yildiz FZ, Lo JA, Wang B, D'Souza VM. 2014. A structure-based mechanism for tRNA and retroviral RNA remodelling during primer annealing. Nature 515:591-5.
154. Gonsky J, Bacharach E, Goff SP. 2001. Identification of residues of the Moloney murine leukemia virus nucleocapsid critical for viral DNA synthesis in vivo. J Virol 75:2616-26.
155. Gorelick RJ, Chabot DJ, Ott DE, Gagliardi TD, Rein A, Henderson LE, Arthur LO. 1996. Genetic analysis of the zinc finger in the Moloney murine leukemia virus nucleocapsid domain: replacement of zinc-coordinating residues with other zinc-coordinating residues yields noninfectious particles containing genomic RNA. J Virol 70:2593-7.
156. Gorelick RJ, Fu W, Gagliardi TD, Bosche WJ, Rein A, Henderson LE, Arthur LO. 1999. Characterization of the block in replication of nucleocapsid protein zinc finger mutants from moloney murine leukemia virus. J Virol 73:8185-95.
157. Georgiadis MM, Jessen SM, Ogata CM, Telesnitsky A, Goff SP, Hendrickson WA. 1995. Mechanistic implications from the structure of a catalytic fragment of Moloney murine leukemia virus reverse transcriptase. Structure 3:879-92.
158. Molling K, Bolognesi DP, Bauer H, Busen W, Plassmann HW, Hausen P. 1971. Association of viral reverse transcriptase with an enzyme degrading the RNA moiety of RNA-DNA hybrids. Nat New Biol 234:240-3.
159. Allain B, Lapadat-Tapolsky M, Berlioz C, Darlix JL. 1994. Transactivation of the minus-strand DNA transfer by nucleocapsid protein during reverse transcription of the retroviral genome. EMBO J 13:973-81.
160. Schultz SJ, Zhang M, Champoux JJ. 2003. Specific cleavages by RNase H facilitate initiation of plus-strand RNA synthesis by Moloney murine leukemia virus. J Virol 77:5275-85.
161. Kelleher CD, Champoux JJ. 1998. Characterization of RNA strand displacement synthesis by Moloney murine leukemia virus reverse transcriptase. J Biol Chem 273:9976-86.

162. Hwang CK, Svarovskaia ES, Pathak VK. 2001. Dynamic copy choice: steady state between murine leukemia virus polymerase and polymerase-dependent RNase H activity determines frequency of in vivo template switching. Proc Natl Acad Sci U S A 98:12209-14.
163. Lanciault C, Champoux JJ. 2006. Pausing during reverse transcription increases the rate of retroviral recombination. J Virol 80:2483-94.
164. Roberts JD, Bebenek K, Kunkel TA. 1988. The accuracy of reverse transcriptase from HIV-1. Science 242:1171-3.
165. Halvas EK, Svarovskaia ES, Pathak VK. 2000. Role of murine leukemia virus reverse transcriptase deoxyribonucleoside triphosphate-binding site in retroviral replication and in vivo fidelity. J Virol 74:10349-58.
166. Roth MJ, Schwartzberg PL, Goff SP. 1989. Structure of the termini of DNA intermediates in the integration of retroviral DNA: dependence on IN function and terminal DNA sequence. Cell 58:47-54.
167. Craigie R, Fujiwara T, Bushman F. 1990. The IN protein of Moloney murine leukemia virus processes the viral DNA ends and accomplishes their integration in vitro. Cell 62:829-37.
168. Daniel R, Kao G, Taganov K, Greger JG, Favorova O, Merkel G, Yen TJ, Katz RA, Skalka AM. 2003. Evidence that the retroviral DNA integration process triggers an ATR-dependent DNA damage response. Proc Natl Acad Sci U S A 100:4778-83.
169. Sloan RD, Wainberg MA. 2011. The role of unintegrated DNA in HIV infection. Retrovirology 8:52.
170. Lee MS, Craigie R. 1994. Protection of retroviral DNA from autointegration: involvement of a cellular factor. Proc Natl Acad Sci U S A 91:9823-7.
171. Lee MS, Craigie R. 1998. A previously unidentified host protein protects retroviral DNA from autointegration. Proc Natl Acad Sci U S A 95:1528-33.
172. Suzuki Y, Craigie R. 2002. Regulatory mechanisms by which barrier-to-autointegration factor blocks autointegration and stimulates intermolecular integration of Moloney murine leukemia virus preintegration complexes. J Virol 76:12376-80.
173. Margalit A, Brachner A, Gotzmann J, Foisner R, Gruenbaum Y. 2007. Barrier-to-autointegration factor--a BAFfling little protein. Trends Cell Biol 17:202-8.
174. Li L, Olvera JM, Yoder KE, Mitchell RS, Butler SL, Lieber M, Martin SL, Bushman FD. 2001. Role of the non-homologous DNA end joining pathway in the early steps of retroviral infection. EMBO J 20:3272-81.
175. Serhan F, Penaud M, Petit C, Leste-Lasserre T, Trajcevski S, Klatzmann D, Duisit G, Sonigo P, Moullier P. 2004. Early detection of a two-long-terminal-repeat junction molecule in the cytoplasm of recombinant murine leukemia virus-infected cells. J Virol 78:6190-9.
176. Suzuki Y, Ogawa K, Koyanagi Y, Suzuki Y. 2010. Functional disruption of the moloney murine leukemia virus preintegration complex by vaccinia-related kinases. J Biol Chem 285:24032-43.
177. De Rijck J, de Kogel C, Demeulemeester J, Vets S, El Ashkar S, Malani N, Bushman FD, Landuyt B, Husson SJ, Busschots K, Gijsbers R, Debyser Z. 2013. The BET family of proteins targets moloney murine leukemia virus integration near transcription start sites. Cell Rep 5:886-94.
178. LaFave MC, Varshney GK, Gildea DE, Wolfsberg TG, Baxevanis AD, Burgess SM. 2014. MLV integration site selection is driven by strong enhancers and active promoters. Nucleic Acids Res 42:4257-69.
179. Tsuruyama T, Liu W, Yoshikawa K. 2012. In vitro murine leukemia retroviral integration and structure fluctuation of target DNA. PLoS One 7:e31533.
180. Benleulmi MS, Matysiak J, Henriquez DR, Vaillant C, Lesbats P, Calmels C, Naughtin M, Leon O, Skalka AM, Ruff M, Lavigne M, Andreola ML, Parissi V. 2015. Intasome architecture and chromatin density modulate retroviral integration into nucleosome. Retrovirology 12:13.

181. Studamire B, Goff SP. 2008. Host proteins interacting with the Moloney murine leukemia virus integrase: multiple transcriptional regulators and chromatin binding factors. Retrovirology 5:48.
182. Miklik D, Senigl F, Hejnar J. 2018. Proviruses with Long-Term Stable Expression Accumulate in Transcriptionally Active Chromatin Close to the Gene Regulatory Elements: Comparison of ASLV-, HIV- and MLV-Derived Vectors. Viruses 10.
183. Albritton LM, Tseng L, Scadden D, Cunningham JM. 1989. A putative murine ecotropic retrovirus receptor gene encodes a multiple membrane-spanning protein and confers susceptibility to virus infection. Cell 57:659-66.
184. Rein A. 1982. Interference grouping of murine leukemia viruses: a distinct receptor for the MCF-recombinant viruses in mouse cells. Virology 120:251-7.
185. Ikeda H, Sugimura H. 1989. Fv-4 resistance gene: a truncated endogenous murine leukemia virus with ecotropic interference properties. J Virol 63:5405-12.
186. Jung YT, Lyu MS, Buckler-White A, Kozak CA. 2002. Characterization of a polytropic murine leukemia virus proviral sequence associated with the virus resistance gene Rmcf of DBA/2 mice. J Virol 76:8218-24.
187. Wu T, Yan Y, Kozak CA. 2005. Rmcf2, a xenotropic provirus in the Asian mouse species Mus castaneus, blocks infection by polytropic mouse gammaretroviruses. J Virol 79:9677-84.
188. Malfavon-Borja R, Feschotte C. 2015. Fighting fire with fire: endogenous retrovirus envelopes as restriction factors. J Virol 89:4047-50.
189. Lu J, Pan Q, Rong L, He W, Liu SL, Liang C. 2011. The IFITM proteins inhibit HIV-1 infection. J Virol 85:2126-37.
190. Brass AL, Huang IC, Benita Y, John SP, Krishnan MN, Feeley EM, Ryan BJ, Weyer JL, van der Weyden L, Fikrig E, Adams DJ, Xavier RJ, Farzan M, Elledge SJ. 2009. The IFITM proteins mediate cellular resistance to influenza A H1N1 virus, West Nile virus, and dengue virus. Cell 139:1243-54.
191. Liu SY, Aliyari R, Chikere K, Li G, Marsden MD, Smith JK, Pernet O, Guo H, Nusbaum R, Zack JA, Freiberg AN, Su L, Lee B, Cheng G. 2013. Interferon-inducible cholesterol-25-hydroxylase broadly inhibits viral entry by production of 25-hydroxycholesterol. Immunity 38:92-105.
192. Liu Y, Wei Z, Zhang Y, Ma X, Chen Y, Yu M, Ma C, Li X, Cao Y, Liu J, Han J, Yang X, Duan Y. 2018. Activation of liver X receptor plays a central role in antiviral actions of 25-hydroxycholesterol. J Lipid Res 59:2287-2296.
193. Fackler OT. 2015. Spotlight on HIV-1 Nef: SERINC3 and SERINC5 Identified as Restriction Factors Antagonized by the Pathogenesis Factor. Viruses 7:6730-8.
194. Harris RS, Perrino FW, Shaban NM. 2015. The multidimensional nature of antiviral innate immunity. Cell Host Microbe 17:423-5.
195. Stavrou S, Aguilera AN, Blouch K, Ross SR. 2018. DDX41 Recognizes RNA/DNA Retroviral Reverse Transcripts and Is Critical for In Vivo Control of Murine Leukemia Virus Infection. MBio 9.
196. Best S, Le Tissier P, Towers G, Stoye JP. 1996. Positional cloning of the mouse retrovirus restriction gene Fv1. Nature 382:826-9.
197. Perron MJ, Stremlau M, Lee M, Javanbakht H, Song B, Sodroski J. 2007. The human TRIM5alpha restriction factor mediates accelerated uncoating of the N-tropic murine leukemia virus capsid. J Virol 81:2138-48.
198. Nisole S, Stoye JP, Saib A. 2005. TRIM family proteins: retroviral restriction and antiviral defence. Nat Rev Microbiol 3:799-808.
199. Goujon C, Moncorge O, Bauby H, Doyle T, Ward CC, Schaller T, Hue S, Barclay WS, Schulz R, Malim MH. 2013. Human MX2 is an interferon-induced post-entry inhibitor of HIV-1 infection. Nature 502:559-62.

200. Harris RS, Liddament MT. 2004. Retroviral restriction by APOBEC proteins. Nat Rev Immunol 4:868-77.
201. Wang X, Han Y, Dang Y, Fu W, Zhou T, Ptak RG, Zheng YH. 2010. Moloney leukemia virus 10 (MOV10) protein inhibits retrovirus replication. J Biol Chem 285:14346-55.
202. Gramberg T, Kahle T, Bloch N, Wittmann S, Mullers E, Daddacha W, Hofmann H, Kim B, Lindemann D, Landau NR. 2013. Restriction of diverse retroviruses by SAMHD1. Retrovirology 10:26.
203. Gao G, Guo X, Goff SP. 2002. Inhibition of retroviral RNA production by ZAP, a CCCH-type zinc finger protein. Science 297:1703-6.
204. Woods MW, Kelly JN, Hattlmann CJ, Tong JG, Xu LS, Coleman MD, Quest GR, Smiley JR, Barr SD. 2011. Human HERC5 restricts an early stage of HIV-1 assembly by a mechanism correlating with the ISGylation of Gag. Retrovirology 8:95.
205. Krapp C, Hotter D, Gawanbacht A, McLaren PJ, Kluge SF, Sturzel CM, Mack K, Reith E, Engelhart S, Ciuffi A, Hornung V, Sauter D, Telenti A, Kirchhoff F. 2016. Guanylate Binding Protein (GBP) 5 Is an Interferon-Inducible Inhibitor of HIV-1 Infectivity. Cell Host Microbe 19:504-14.
206. Zhou T, Dang Y, Zheng YH. 2014. The mitochondrial translocator protein, TSPO, inhibits HIV-1 envelope glycoprotein biosynthesis via the endoplasmic reticulum-associated protein degradation pathway. J Virol 88:3474-84.
207. Zhou T, Frabutt DA, Moremen KW, Zheng YH. 2015. ERManI (Endoplasmic Reticulum Class I alpha-Mannosidase) Is Required for HIV-1 Envelope Glycoprotein Degradation via Endoplasmic Reticulum-associated Protein Degradation Pathway. J Biol Chem 290:22184-92.
208. Neil SJ, Zang T, Bieniasz PD. 2008. Tetherin inhibits retrovirus release and is antagonized by HIV-1 Vpu. Nature 451:425-30.
209. Liberatore RA, Bieniasz PD. 2011. Tetherin is a key effector of the antiretroviral activity of type I interferon in vitro and in vivo. Proc Natl Acad Sci U S A 108:18097-101.
210. Li M, Ablan SD, Miao C, Zheng YM, Fuller MS, Rennert PD, Maury W, Johnson MC, Freed EO, Liu SL. 2014. TIM-family proteins inhibit HIV-1 release. Proc Natl Acad Sci U S A 111:E3699-707.
211. Inuzuka M, Hayakawa M, Ingi T. 2005. Serinc, an activity-regulated protein family, incorporates serine into membrane lipid synthesis. J Biol Chem 280:35776-83.
212. Trautz B, Wiedemann H, Luchtenborg C, Pierini V, Kranich J, Glass B, Krausslich HG, Brocker T, Pizzato M, Ruggieri A, Brugger B, Fackler OT. 2017. The host-cell restriction factor SERINC5 restricts HIV-1 infectivity without altering the lipid composition and organization of viral particles. J Biol Chem 292:13702-13713.
213. Beitari S, Ding S, Pan Q, Finzi A, Liang C. 2017. Effect of HIV-1 Env on SERINC5 Antagonism. J Virol 91.
214. Trautz B, Pierini V, Wombacher R, Stolp B, Chase AJ, Pizzato M, Fackler OT. 2016. The Antagonism of HIV-1 Nef to SERINC5 Particle Infectivity Restriction Involves the Counteraction of Virion-Associated Pools of the Restriction Factor. J Virol 90:10915-10927.
215. Sood C, Marin M, Chande A, Pizzato M, Melikyan GB. 2017. SERINC5 protein inhibits HIV-1 fusion pore formation by promoting functional inactivation of envelope glycoproteins. J Biol Chem 292:6014-6026.
216. Schulte B, Selyutina A, Opp S, Herschhorn A, Sodroski JG, Pizzato M, Diaz-Griffero F. 2018. Localization to detergent-resistant membranes and HIV-1 core entry inhibition correlate with HIV-1 restriction by SERINC5. Virology 515:52-65.
217. Li M, Waheed AA, Yu J, Zeng C, Chen HY, Zheng YM, Feizpour A, Reinhard BM, Gummuluru S, Lin S, Freed EO, Liu SL. 2019. TIM-mediated inhibition of HIV-1 release is antagonized by Nef but potentiated by SERINC proteins. Proc Natl Acad Sci U S A 116:5705-5714.

218. Teng B, Burant CF, Davidson NO. 1993. Molecular cloning of an apolipoprotein B messenger RNA editing protein. Science 260:1816-9.
219. Espinosa R, 3rd, Funahashi T, Hadjiagapiou C, Le Beau MM, Davidson NO. 1994. Assignment of the gene encoding the human apolipoprotein B mRNA editing enzyme (APOBEC1) to chromosome 12p13.1. Genomics 24:414-5.
220. Jarmuz A, Chester A, Bayliss J, Gisbourne J, Dunham I, Scott J, Navaratnam N. 2002. An anthropoid-specific locus of orphan C to U RNA-editing enzymes on chromosome 22. Genomics 79:285-96.
221. Suspene R, Sommer P, Henry M, Ferris S, Guetard D, Pochet S, Chester A, Navaratnam N, Wain-Hobson S, Vartanian JP. 2004. APOBEC3G is a single-stranded DNA cytidine deaminase and functions independently of HIV reverse transcriptase. Nucleic Acids Res 32:2421-9.
222. Yu Q, Konig R, Pillai S, Chiles K, Kearney M, Palmer S, Richman D, Coffin JM, Landau NR. 2004. Single-strand specificity of APOBEC3G accounts for minus-strand deamination of the HIV genome. Nat Struct Mol Biol 11:435-42.
223. Vetter ML, D'Aquila RT. 2009. Cytoplasmic APOBEC3G restricts incoming Vif-positive human immunodeficiency virus type 1 and increases two-long terminal repeat circle formation in activated T-helper-subtype cells. J Virol 83:8646-54.
224. Kolokithas A, Rosenke K, Malik F, Hendrick D, Swanson L, Santiago ML, Portis JL, Hasenkrug KJ, Evans LH. 2010. The glycosylated Gag protein of a murine leukemia virus inhibits the antiretroviral function of APOBEC3. J Virol 84:10933-6.
225. Stavrou S, Nitta T, Kotla S, Ha D, Nagashima K, Rein AR, Fan H, Ross SR. 2013. Murine leukemia virus glycosylated Gag blocks apolipoprotein B editing complex 3 and cytosolic sensor access to the reverse transcription complex. Proc Natl Acad Sci U S A 110:9078-83.
226. Alce TM, Popik W. 2004. APOBEC3G is incorporated into virus-like particles by a direct interaction with HIV-1 Gag nucleocapsid protein. J Biol Chem 279:34083-6.
227. Navarro F, Bollman B, Chen H, Konig R, Yu Q, Chiles K, Landau NR. 2005. Complementary function of the two catalytic domains of APOBEC3G. Virology 333:374-86.
228. Svarovskaia ES, Xu H, Mbisa JL, Barr R, Gorelick RJ, Ono A, Freed EO, Hu WS, Pathak VK. 2004. Human apolipoprotein B mRNA-editing enzyme-catalytic polypeptide-like 3G (APOBEC3G) is incorporated into HIV-1 virions through interactions with viral and nonviral RNAs. J Biol Chem 279:35822-8.
229. Burnett A, Spearman P. 2007. APOBEC3G multimers are recruited to the plasma membrane for packaging into human immunodeficiency virus type 1 virus-like particles in an RNA-dependent process requiring the NC basic linker. J Virol 81:5000-13.
230. Zhang L, Li X, Ma J, Yu L, Jiang J, Cen S. 2008. The incorporation of APOBEC3 proteins into murine leukemia viruses. Virology 378:69-78.
231. Sanchez-Martinez S, Aloia AL, Harvin D, Mirro J, Gorelick RJ, Jern P, Coffin JM, Rein A. 2012. Studies on the restriction of murine leukemia viruses by mouse APOBEC3. PLoS One 7:e38190.
232. Abudu A, Takaori-Kondo A, Izumi T, Shirakawa K, Kobayashi M, Sasada A, Fukunaga K, Uchiyama T. 2006. Murine retrovirus escapes from murine APOBEC3 via two distinct novel mechanisms. Curr Biol 16:1565-70.
233. Rulli SJ, Jr., Mirro J, Hill SA, Lloyd P, Gorelick RJ, Coffin JM, Derse D, Rein A. 2008. Interactions of murine APOBEC3 and human APOBEC3G with murine leukemia viruses. J Virol 82:6566-75.
234. Bishop KN, Holmes RK, Malim MH. 2006. Antiviral potency of APOBEC proteins does not correlate with cytidine deamination. J Virol 80:8450-8.
235. Holmes RK, Koning FA, Bishop KN, Malim MH. 2007. APOBEC3F can inhibit the accumulation of HIV-1 reverse transcription products in the absence of hypermutation. Comparisons with APOBEC3G. J Biol Chem 282:2587-95.

236. Albin JS, Brown WL, Harris RS. 2014. Catalytic activity of APOBEC3F is required for efficient restriction of Vif-deficient human immunodeficiency virus. Virology 450-451:49-54.
237. Gillick K, Pollpeter D, Phalora P, Kim EY, Wolinsky SM, Malim MH. 2013. Suppression of HIV-1 infection by APOBEC3 proteins in primary human CD4(+) T cells is associated with inhibition of processive reverse transcription as well as excessive cytidine deamination. J Virol 87:1508-17.
238. Stavrou S, Zhao W, Blouch K, Ross SR. 2018. Deaminase-Dead Mouse APOBEC3 Is an In Vivo Retroviral Restriction Factor. J Virol 92.
239. Guo F, Cen S, Niu M, Saadatmand J, Kleiman L. 2006. Inhibition of tRNA(3)(Lys)-primed reverse transcription by human APOBEC3G during human immunodeficiency virus type 1 replication. J Virol 80:11710-22.
240. Luo K, Wang T, Liu B, Tian C, Xiao Z, Kappes J, Yu XF. 2007. Cytidine deaminases APOBEC3G and APOBEC3F interact with human immunodeficiency virus type 1 integrase and inhibit proviral DNA formation. J Virol 81:7238-48.
241. Wang X, Ao Z, Chen L, Kobinger G, Peng J, Yao X. 2012. The cellular antiviral protein APOBEC3G interacts with HIV-1 reverse transcriptase and inhibits its function during viral replication. J Virol 86:3777-86.
242. Morse M, Huo R, Feng Y, Rouzina I, Chelico L, Williams MC. 2017. Dimerization regulates both deaminase-dependent and deaminase-independent HIV-1 restriction by APOBEC3G. Nat Commun 8:597.
243. Ara A, Love RP, Follack TB, Ahmed KA, Adolph MB, Chelico L. 2017. Mechanism of Enhanced HIV Restriction by Virion Coencapsidated Cytidine Deaminases APOBEC3F and APOBEC3G. J Virol 91.
244. Iwatani Y, Chan DS, Wang F, Maynard KS, Sugiura W, Gronenborn AM, Rouzina I, Williams MC, Musier-Forsyth K, Levin JG. 2007. Deaminase-independent inhibition of HIV-1 reverse transcription by APOBEC3G. Nucleic Acids Res 35:7096-108.
245. Kobayashi T, Koizumi Y, Takeuchi JS, Misawa N, Kimura Y, Morita S, Aihara K, Koyanagi Y, Iwami S, Sato K. 2014. Quantification of deaminase activity-dependent and -independent restriction of HIV-1 replication mediated by APOBEC3F and APOBEC3G through experimental-mathematical investigation. J Virol 88:5881-7.
246. Belanger K, Langlois MA. 2015. Comparative analysis of the gene-inactivating potential of retroviral restriction factors APOBEC3F and APOBEC3G. J Gen Virol 96:2878-87.
247. Boi S, Kolokithas A, Shepard J, Linwood R, Rosenke K, Van Dis E, Malik F, Evans LH. 2014. Incorporation of mouse APOBEC3 into murine leukemia virus virions decreases the activity and fidelity of reverse transcriptase. J Virol 88:7659-62.
248. Mohammadzadeh N, Love RP, Gibson R, Arts EJ, Poon AFY, Chelico L. 2019. Role of co-expressed APOBEC3F and APOBEC3G in inducing HIV-1 drug resistance. Heliyon 5:e01498.
249. Venkatesan S, Rosenthal R, Kanu N, McGranahan N, Bartek J, Quezada SA, Hare J, Harris RS, Swanton C. 2018. Perspective: APOBEC mutagenesis in drug resistance and immune escape in HIV and cancer evolution. Ann Oncol 29:563-572.
250. Mulder LC, Harari A, Simon V. 2008. Cytidine deamination induced HIV-1 drug resistance. Proc Natl Acad Sci U S A 105:5501-6.
251. Sadler HA, Stenglein MD, Harris RS, Mansky LM. 2010. APOBEC3G contributes to HIV-1 variation through sublethal mutagenesis. J Virol 84:7396-404.
252. Cuevas JM, Geller R, Garijo R, Lopez-Aldeguer J, Sanjuan R. 2015. Extremely High Mutation Rate of HIV-1 In Vivo. PLoS Biol 13:e1002251.
253. Jern P, Stoye JP, Coffin JM. 2007. Role of APOBEC3 in genetic diversity among endogenous murine leukemia viruses. PLoS Genet 3:2014-22.
254. Kim EY, Lorenzo-Redondo R, Little SJ, Chung YS, Phalora PK, Maljkovic Berry I, Archer J, Penugonda S, Fischer W, Richman DD, Bhattacharya T, Malim MH, Wolinsky SM. 2014. Human

APOBEC3 induced mutation of human immunodeficiency virus type-1 contributes to adaptation and evolution in natural infection. PLoS Pathog 10:e1004281.
255. Borzooee F, Joris KD, Grant MD, Larijani M. 2018. APOBEC3G Regulation of the Evolutionary Race Between Adaptive Immunity and Viral Immune Escape Is Deeply Imprinted in the HIV Genome. Front Immunol 9:3032.
256. Delviks-Frankenberry KA, Nikolaitchik OA, Burdick RC, Gorelick RJ, Keele BF, Hu WS, Pathak VK. 2016. Minimal Contribution of APOBEC3-Induced G-to-A Hypermutation to HIV-1 Recombination and Genetic Variation. PLoS Pathog 12:e1005646.
257. Sharp PM, Hahn BH. 2011. Origins of HIV and the AIDS pandemic. Cold Spring Harb Perspect Med 1:a006841.
258. Kluge SF, Sauter D, Kirchhoff F. 2015. SnapShot: antiviral restriction factors. Cell 163:774-774 e1.
259. Gabuzda DH, Lawrence K, Langhoff E, Terwilliger E, Dorfman T, Haseltine WA, Sodroski J. 1992. Role of vif in replication of human immunodeficiency virus type 1 in CD4+ T lymphocytes. J Virol 66:6489-95.
260. Mariani R, Chen D, Schrofelbauer B, Navarro F, Konig R, Bollman B, Munk C, Nymark-McMahon H, Landau NR. 2003. Species-specific exclusion of APOBEC3G from HIV-1 virions by Vif. Cell 114:21-31.
261. Conticello SG, Harris RS, Neuberger MS. 2003. The Vif protein of HIV triggers degradation of the human antiretroviral DNA deaminase APOBEC3G. Curr Biol 13:2009-13.
262. Hultquist JF, Lengyel JA, Refsland EW, LaRue RS, Lackey L, Brown WL, Harris RS. 2011. Human and rhesus APOBEC3D, APOBEC3F, APOBEC3G, and APOBEC3H demonstrate a conserved capacity to restrict Vif-deficient HIV-1. J Virol 85:11220-34.
263. Yu X, Yu Y, Liu B, Luo K, Kong W, Mao P, Yu XF. 2003. Induction of APOBEC3G ubiquitination and degradation by an HIV-1 Vif-Cul5-SCF complex. Science 302:1056-60.
264. Binning JM, Smith AM, Hultquist JF, Craik CS, Caretta Cartozo N, Campbell MG, Burton L, La Greca F, McGregor MJ, Ta HM, Bartholomeeusen K, Peterlin BM, Krogan NJ, Sevillano N, Cheng Y, Gross JD. 2018. Fab-based inhibitors reveal ubiquitin independent functions for HIV Vif neutralization of APOBEC3 restriction factors. PLoS Pathog 14:e1006830.
265. Anderson BD, Harris RS. 2015. Transcriptional regulation of APOBEC3 antiviral immunity through the CBF-beta/RUNX axis. Sci Adv 1:e1500296.
266. Stopak K, de Noronha C, Yonemoto W, Greene WC. 2003. HIV-1 Vif blocks the antiviral activity of APOBEC3G by impairing both its translation and intracellular stability. Mol Cell 12:591-601.
267. Luciw PA, Cheng-Mayer C, Levy JA. 1987. Mutational analysis of the human immunodeficiency virus: the orf-B region down-regulates virus replication. Proc Natl Acad Sci U S A 84:1434-8.
268. Aiken C. 1997. Pseudotyping human immunodeficiency virus type 1 (HIV-1) by the glycoprotein of vesicular stomatitis virus targets HIV-1 entry to an endocytic pathway and suppresses both the requirement for Nef and the sensitivity to cyclosporin A. J Virol 71:5871-7.
269. Usami Y, Wu Y, Gottlinger HG. 2015. SERINC3 and SERINC5 restrict HIV-1 infectivity and are counteracted by Nef. Nature 526:218-23.
270. Rosa A, Chande A, Ziglio S, De Sanctis V, Bertorelli R, Goh SL, McCauley SM, Nowosielska A, Antonarakis SE, Luban J, Santoni FA, Pizzato M. 2015. HIV-1 Nef promotes infection by excluding SERINC5 from virion incorporation. Nature 526:212-7.
271. Shi J, Xiong R, Zhou T, Su P, Zhang X, Qiu X, Li H, Li S, Yu C, Wang B, Ding C, Smithgall TE, Zheng YH. 2018. HIV-1 Nef Antagonizes SERINC5 Restriction by Downregulation of SERINC5 via the Endosome/Lysosome System. J Virol 92.
272. Dai W, Usami Y, Wu Y, Gottlinger H. 2018. A Long Cytoplasmic Loop Governs the Sensitivity of the Anti-viral Host Protein SERINC5 to HIV-1 Nef. Cell Rep 22:869-875.

273. de Sousa-Pereira P, Abrantes J, Bauernfried S, Pierini V, Esteves PJ, Keppler OT, Pizzato M, Hornung V, Fackler OT, Baldauf HM. 2019. The antiviral activity of rodent and lagomorph SERINC3 and SERINC5 is counteracted by known viral antagonists. J Gen Virol 100:278-288.
274. Wu Y, Olety B, Weiss ER, Popova E, Yamanaka H, Gottlinger H. 2019. Potent Enhancement of HIV-1 Replication by Nef in the Absence of SERINC3 and SERINC5. MBio 10.
275. Varthakavi V, Smith RM, Bour SP, Strebel K, Spearman P. 2003. Viral protein U counteracts a human host cell restriction that inhibits HIV-1 particle production. Proc Natl Acad Sci U S A 100:15154-9.
276. Van Damme N, Goff D, Katsura C, Jorgenson RL, Mitchell R, Johnson MC, Stephens EB, Guatelli J. 2008. The interferon-induced protein BST-2 restricts HIV-1 release and is downregulated from the cell surface by the viral Vpu protein. Cell Host Microbe 3:245-52.
277. Iwabu Y, Fujita H, Kinomoto M, Kaneko K, Ishizaka Y, Tanaka Y, Sata T, Tokunaga K. 2009. HIV-1 accessory protein Vpu internalizes cell-surface BST-2/tetherin through transmembrane interactions leading to lysosomes. J Biol Chem 284:35060-72.
278. Goffinet C, Allespach I, Homann S, Tervo HM, Habermann A, Rupp D, Oberbremer L, Kern C, Tibroni N, Welsch S, Krijnse-Locker J, Banting G, Krausslich HG, Fackler OT, Keppler OT. 2009. HIV-1 antagonism of CD317 is species specific and involves Vpu-mediated proteasomal degradation of the restriction factor. Cell Host Microbe 5:285-97.
279. Lewinski MK, Jafari M, Zhang H, Opella SJ, Guatelli J. 2015. Membrane Anchoring by a C-terminal Tryptophan Enables HIV-1 Vpu to Displace Bone Marrow Stromal Antigen 2 (BST2) from Sites of Viral Assembly. J Biol Chem 290:10919-33.
280. Miyagi E, Andrew AJ, Kao S, Strebel K. 2009. Vpu enhances HIV-1 virus release in the absence of Bst-2 cell surface down-modulation and intracellular depletion. Proc Natl Acad Sci U S A 106:2868-73.
281. Belzile JP, Duisit G, Rougeau N, Mercier J, Finzi A, Cohen EA. 2007. HIV-1 Vpr-mediated G2 arrest involves the DDB1-CUL4AVPRBP E3 ubiquitin ligase. PLoS Pathog 3:e85.
282. Zhou D, Wang Y, Tokunaga K, Huang F, Sun B, Yang R. 2015. The HIV-1 accessory protein Vpr induces the degradation of the anti-HIV-1 agent APOBEC3G through a VprBP-mediated proteasomal pathway. Virus Res 195:25-34.
283. Schrofelbauer B, Yu Q, Zeitlin SG, Landau NR. 2005. Human immunodeficiency virus type 1 Vpr induces the degradation of the UNG and SMUG uracil-DNA glycosylases. J Virol 79:10978-87.
284. Weil AF, Ghosh D, Zhou Y, Seiple L, McMahon MA, Spivak AM, Siliciano RF, Stivers JT. 2013. Uracil DNA glycosylase initiates degradation of HIV-1 cDNA containing misincorporated dUTP and prevents viral integration. Proc Natl Acad Sci U S A 110:E448-57.
285. Yan N, O'Day E, Wheeler LA, Engelman A, Lieberman J. 2011. HIV DNA is heavily uracilated, which protects it from autointegration. Proc Natl Acad Sci U S A 108:9244-9.
286. Yan J, Shun MC, Hao C, Zhang Y, Qian J, Hrecka K, DeLucia M, Monnie C, Ahn J, Skowronski J. 2018. HIV-1 Vpr Reprograms CLR4(DCAF1) E3 Ubiquitin Ligase to Antagonize Exonuclease 1-Mediated Restriction of HIV-1 Infection. MBio 9.
287. Yan J, Shun MC, Zhang Y, Hao C, Skowronski J. 2019. HIV-1 Vpr counteracts HLTF-mediated restriction of HIV-1 infection in T cells. Proc Natl Acad Sci U S A 116:9568-9577.
288. Bergamaschi A, Ayinde D, David A, Le Rouzic E, Morel M, Collin G, Descamps D, Damond F, Brun-Vezinet F, Nisole S, Margottin-Goguet F, Pancino G, Transy C. 2009. The human immunodeficiency virus type 2 Vpx protein usurps the CUL4A-DDB1 DCAF1 ubiquitin ligase to overcome a postentry block in macrophage infection. J Virol 83:4854-60.
289. Laguette N, Sobhian B, Casartelli N, Ringeard M, Chable-Bessia C, Segeral E, Yatim A, Emiliani S, Schwartz O, Benkirane M. 2011. SAMHD1 is the dendritic- and myeloid-cell-specific HIV-1 restriction factor counteracted by Vpx. Nature 474:654-7.

290. Hofmann H, Logue EC, Bloch N, Daddacha W, Polsky SB, Schultz ML, Kim B, Landau NR. 2012. The Vpx lentiviral accessory protein targets SAMHD1 for degradation in the nucleus. J Virol 86:12552-60.
291. Baldauf HM, Stegmann L, Schwarz SM, Ambiel I, Trotard M, Martin M, Burggraf M, Lenzi GM, Lejk H, Pan X, Fregoso OI, Lim ES, Abraham L, Nguyen LA, Rutsch F, Konig R, Kim B, Emerman M, Fackler OT, Keppler OT. 2017. Vpx overcomes a SAMHD1-independent block to HIV reverse transcription that is specific to resting CD4 T cells. Proc Natl Acad Sci U S A 114:2729-2734.
292. Ledbetter J, Nowinski RC, Emery S. 1977. Viral proteins expressed on the surface of murine leukemia cells. J Virol 22:65-73.
293. Schultz AM, Rabin EH, Oroszlan S. 1979. Post-translational modification of Rauscher leukemia virus precursor polyproteins encoded by the gag gene. J Virol 30:255-66.
294. Edwards SA, Fan H. 1979. gag-Related polyproteins of Moloney murine leukemia virus: evidence for independent synthesis of glycosylated and unglycosylated forms. J Virol 30:551-63.
295. Schultz AM, Oroszlan S. 1978. Murine leukemia virus gag polyproteins: the peptide chain unique to Pr80 is located at the amino terminus. Virology 91:481-6.
296. Schwartzberg P, Colicelli J, Goff SP. 1983. Deletion mutants of Moloney murine leukemia virus which lack glycosylated gag protein are replication competent. J Virol 46:538-46.
297. Prats AC, De Billy G, Wang P, Darlix JL. 1989. CUG initiation codon used for the synthesis of a cell surface antigen coded by the murine leukemia virus. J Mol Biol 205:363-72.
298. Saris CJ, van Eenbergen J, Liskamp RM, Bloemers HP. 1983. Structure of glycosylated and unglycosylated gag and gag-pol precursor proteins of Moloney murine leukemia virus. J Virol 46:841-59.
299. Hampe A, Gobet M, Even J, Sherr CJ, Galibert F. 1983. Nucleotide sequences of feline sarcoma virus long terminal repeats and 5' leaders show extensive homology to those of other mammalian retroviruses. J Virol 45:466-72.
300. Kende M, Hill R, Dinowitz M, Stephenson JR, Kelloff GJ. 1979. Naturally occurring lymphocyte-mediated immunity to endogenous type-C virus in the mouse. Blocking of the lymphocyte reactivity with antisera to the virus. J Exp Med 149:358-71.
301. Masuda M, Hoffman PM, Ruscetti SK. 1993. Viral determinants that control the neuropathogenicity of PVC-211 murine leukemia virus in vivo determine brain capillary endothelial cell tropism of the virus in vitro. J Virol 67:4580-7.
302. Corbin A, Prats AC, Darlix JL, Sitbon M. 1994. A nonstructural gag-encoded glycoprotein precursor is necessary for efficient spreading and pathogenesis of murine leukemia viruses. J Virol 68:3857-67.
303. Portis JL, Spangrude GJ, McAtee FJ. 1994. Identification of a sequence in the unique 5' open reading frame of the gene encoding glycosylated Gag which influences the incubation period of neurodegenerative disease induced by a murine retrovirus. J Virol 68:3879-87.
304. Fujisawa R, McAtee FJ, Wehrly K, Portis JL. 1998. The neuroinvasiveness of a murine retrovirus is influenced by a dileucine-containing sequence in the cytoplasmic tail of glycosylated Gag. J Virol 72:5619-25.
305. Fan H, Chute H, Chao E, Feuerman M. 1983. Construction and characterization of Moloney murine leukemia virus mutants unable to synthesize glycosylated gag polyprotein. Proc Natl Acad Sci U S A 80:5965-9.
306. van der Hoorn FA, Lahaye T, Muller V, Ogle MA, Engers HD. 1985. Characterization of gP85gag as an antigen recognized by Moloney leukemia virus-specific cytolytic T cell clones that function in vivo. J Exp Med 162:128-44.

307. Schultz AM, Lockhart SM, Rabin EM, Oroszlan S. 1981. Structure of glycosylated and unglycosylated gag polyproteins of Rauscher murine leukemia virus: carbohydrate attachment sites. J Virol 38:581-92.
308. Ng VL, Wood TG, Lyons DD, Arlinghaus RB. 1979. Characterization of intracellular precursor polyproteins of Moloney murine leukemia virus. J Virol 32:1051-6.
309. Naso RB, Stanker LH, Kopchick JJ, Ng VL, Karshin WL, Arlinghaus RB. 1983. Further studies on the glycosylated gag gene products of Rauscher murine leukemia virus: identification of an N-terminal 45,000-dalton cleavage product. J Virol 45:1200-6.
310. Fujisawa R, McAtee FJ, Favara C, Hayes SF, Portis JL. 2001. N-terminal cleavage fragment of glycosylated Gag is incorporated into murine oncornavirus particles. J Virol 75:11239-43.
311. Low A, Datta S, Kuznetsov Y, Jahid S, Kothari N, McPherson A, Fan H. 2007. Mutation in the glycosylated gag protein of murine leukemia virus results in reduced in vivo infectivity and a novel defect in viral budding or release. J Virol 81:3685-92.
312. Nitta T, Kuznetsov Y, McPherson A, Fan H. 2010. Murine leukemia virus glycosylated Gag (gPr80gag) facilitates interferon-sensitive virus release through lipid rafts. Proc Natl Acad Sci U S A 107:1190-5.
313. Pizzato M. 2010. MLV glycosylated-Gag is an infectivity factor that rescues Nef-deficient HIV-1. Proc Natl Acad Sci U S A 107:9364-9.
314. Usami Y, Popov S, Gottlinger HG. 2014. The Nef-like effect of murine leukemia virus glycosylated gag on HIV-1 infectivity is mediated by its cytoplasmic domain and depends on the AP-2 adaptor complex. J Virol 88:3443-54.
315. Li S, Ahmad I, Shi J, Wang B, Yu C, Zhang L, Zheng YH. 2019. Murine Leukemia Virus Glycosylated Gag Reduces Murine SERINC5 Protein Expression at Steady-State Levels via the Endosome/Lysosome Pathway to Counteract SERINC5 Antiretroviral Activity. J Virol 93.
316. Usami Y, Gottlinger H. 2013. HIV-1 Nef responsiveness is determined by Env variable regions involved in trimer association and correlates with neutralization sensitivity. Cell Rep 5:802-12.
317. Ahi YS, Zhang S, Thappeta Y, Denman A, Feizpour A, Gummuluru S, Reinhard B, Muriaux D, Fivash MJ, Rein A. 2016. Functional Interplay Between Murine Leukemia Virus Glycogag, Serinc5, and Surface Glycoprotein Governs Virus Entry, with Opposite Effects on Gammaretroviral and Ebolavirus Glycoproteins. MBio 7.
318. Nitta T, Lee S, Ha D, Arias M, Kozak CA, Fan H. 2012. Moloney murine leukemia virus glyco-gag facilitates xenotropic murine leukemia virus-related virus replication through human APOBEC3-independent mechanisms. Retrovirology 9:58.
319. Langlois MA, Kemmerich K, Rada C, Neuberger MS. 2009. The AKV murine leukemia virus is restricted and hypermutated by mouse APOBEC3. J Virol 83:11550-9.
320. Goffinet C, Schmidt S, Kern C, Oberbremer L, Keppler OT. 2010. Endogenous CD317/Tetherin limits replication of HIV-1 and murine leukemia virus in rodent cells and is resistant to antagonists from primate viruses. J Virol 84:11374-84.
321. Wolf P. 1967. The nature and significance of platelet products in human plasma. Br J Haematol 13:269-88.
322. Thery C, Witwer KW, Aikawa E, Alcaraz MJ, Anderson JD, Andriantsitohaina R, Antoniou A, Arab T, Archer F, Atkin-Smith GK, Ayre DC, Bach JM, Bachurski D, Baharvand H, Balaj L, Baldacchino S, Bauer NN, Baxter AA, Bebawy M, Beckham C, Bedina Zavec A, Benmoussa A, Berardi AC, Bergese P, Bielska E, Blenkiron C, Bobis-Wozowicz S, Boilard E, Boireau W, Bongiovanni A, Borras FE, Bosch S, Boulanger CM, Breakefield X, Breglio AM, Brennan MA, Brigstock DR, Brisson A, Broekman ML, Bromberg JF, Bryl-Gorecka P, Buch S, Buck AH, Burger D, Busatto S, Buschmann D, Bussolati B, Buzas EI, Byrd JB, Camussi G, et al. 2018. Minimal information for studies of

extracellular vesicles 2018 (MISEV2018): a position statement of the International Society for Extracellular Vesicles and update of the MISEV2014 guidelines. J Extracell Vesicles 7:1535750.
323. Pan BT, Teng K, Wu C, Adam M, Johnstone RM. 1985. Electron microscopic evidence for externalization of the transferrin receptor in vesicular form in sheep reticulocytes. J Cell Biol 101:942-8.
324. Halicka HD, Bedner E, Darzynkiewicz Z. 2000. Segregation of RNA and separate packaging of DNA and RNA in apoptotic bodies during apoptosis. Exp Cell Res 260:248-56.
325. Yanez-Mo M, Siljander PR, Andreu Z, Zavec AB, Borras FE, Buzas EI, Buzas K, Casal E, Cappello F, Carvalho J, Colas E, Cordeiro-da Silva A, Fais S, Falcon-Perez JM, Ghobrial IM, Giebel B, Gimona M, Graner M, Gursel I, Gursel M, Heegaard NH, Hendrix A, Kierulf P, Kokubun K, Kosanovic M, Kralj-Iglic V, Kramer-Albers EM, Laitinen S, Lasser C, Lener T, Ligeti E, Line A, Lipps G, Llorente A, Lotvall J, Mancek-Keber M, Marcilla A, Mittelbrunn M, Nazarenko I, Nolte-'t Hoen EN, Nyman TA, O'Driscoll L, Olivan M, Oliveira C, Pallinger E, Del Portillo HA, Reventos J, Rigau M, Rohde E, Sammar M, et al. 2015. Biological properties of extracellular vesicles and their physiological functions. J Extracell Vesicles 4:27066.
326. Hanson PI, Cashikar A. 2012. Multivesicular body morphogenesis. Annu Rev Cell Dev Biol 28:337-62.
327. Colombo M, Raposo G, Thery C. 2014. Biogenesis, secretion, and intercellular interactions of exosomes and other extracellular vesicles. Annu Rev Cell Dev Biol 30:255-89.
328. van Niel G, Charrin S, Simoes S, Romao M, Rochin L, Saftig P, Marks MS, Rubinstein E, Raposo G. 2011. The tetraspanin CD63 regulates ESCRT-independent and -dependent endosomal sorting during melanogenesis. Dev Cell 21:708-21.
329. Kanada M, Bachmann MH, Contag CH. 2016. Signaling by Extracellular Vesicles Advances Cancer Hallmarks. Trends Cancer 2:84-94.
330. Beer KB, Wehman AM. 2017. Mechanisms and functions of extracellular vesicle release in vivo-What we can learn from flies and worms. Cell Adh Migr 11:135-150.
331. Zaborowski MP, Balaj L, Breakefield XO, Lai CP. 2015. Extracellular Vesicles: Composition, Biological Relevance, and Methods of Study. Bioscience 65:783-797.
332. O'Neill CP, Gilligan KE, Dwyer RM. 2019. Role of Extracellular Vesicles (EVs) in Cell Stress Response and Resistance to Cancer Therapy. Cancers (Basel) 11.
333. Bernard MA, Zhao H, Yue SC, Anandaiah A, Koziel H, Tachado SD. 2014. Novel HIV-1 miRNAs stimulate TNFalpha release in human macrophages via TLR8 signaling pathway. PLoS One 9:e106006.
334. Dreux M, Garaigorta U, Boyd B, Decembre E, Chung J, Whitten-Bauer C, Wieland S, Chisari FV. 2012. Short-range exosomal transfer of viral RNA from infected cells to plasmacytoid dendritic cells triggers innate immunity. Cell Host Microbe 12:558-70.
335. Khatua AK, Taylor HE, Hildreth JE, Popik W. 2009. Exosomes packaging APOBEC3G confer human immunodeficiency virus resistance to recipient cells. J Virol 83:512-21.
336. de Carvalho JV, de Castro RO, da Silva EZ, Silveira PP, da Silva-Januario ME, Arruda E, Jamur MC, Oliver C, Aguiar RS, daSilva LL. 2014. Nef neutralizes the ability of exosomes from CD4+ T cells to act as decoys during HIV-1 infection. PLoS One 9:e113691.
337. Lenassi M, Cagney G, Liao M, Vaupotic T, Bartholomeeusen K, Cheng Y, Krogan NJ, Plemenitas A, Peterlin BM. 2010. HIV Nef is secreted in exosomes and triggers apoptosis in bystander CD4+ T cells. Traffic 11:110-22.
338. Feng Z, Hensley L, McKnight KL, Hu F, Madden V, Ping L, Jeong SH, Walker C, Lanford RE, Lemon SM. 2013. A pathogenic picornavirus acquires an envelope by hijacking cellular membranes. Nature 496:367-71.

339. Nagashima S, Jirintai S, Takahashi M, Kobayashi T, Tanggis, Nishizawa T, Kouki T, Yashiro T, Okamoto H. 2014. Hepatitis E virus egress depends on the exosomal pathway, with secretory exosomes derived from multivesicular bodies. J Gen Virol 95:2166-75.
340. Prescher J, Baumgartel V, Ivanchenko S, Torrano AA, Brauchle C, Muller B, Lamb DC. 2015. Super-resolution imaging of ESCRT-proteins at HIV-1 assembly sites. PLoS Pathog 11:e1004677.
341. Dorjbal B, Derse D, Lloyd P, Soheilian F, Nagashima K, Heidecker G. 2011. The role of ITCH protein in human T-cell leukemia virus type 1 release. J Biol Chem 286:31092-104.
342. Mazurov D, Heidecker G, Derse D. 2007. The inner loop of tetraspanins CD82 and CD81 mediates interactions with human T cell lymphotrophic virus type 1 Gag protein. J Biol Chem 282:3896-903.
343. Grigorov B, Attuil-Audenis V, Perugi F, Nedelec M, Watson S, Pique C, Darlix JL, Conjeaud H, Muriaux D. 2009. A role for CD81 on the late steps of HIV-1 replication in a chronically infected T cell line. Retrovirology 6:28.
344. Nolte-'t Hoen E, Cremer T, Gallo RC, Margolis LB. 2016. Extracellular vesicles and viruses: Are they close relatives? Proc Natl Acad Sci U S A 113:9155-61.
345. Cantin R, Diou J, Belanger D, Tremblay AM, Gilbert C. 2008. Discrimination between exosomes and HIV-1: purification of both vesicles from cell-free supernatants. J Immunol Methods 338:21-30.
346. Kim SH, Lim KI. 2017. Stability of Retroviral Vectors Against Ultracentrifugation Is Determined by the Viral Internal Core and Envelope Proteins Used for Pseudotyping. Mol Cells 40:339-345.
347. Ott DE. 2009. Purification of HIV-1 virions by subtilisin digestion or CD45 immunoaffinity depletion for biochemical studies. Methods Mol Biol 485:15-25.
348. Esser MT, Graham DR, Coren LV, Trubey CM, Bess JW, Jr., Arthur LO, Ott DE, Lifson JD. 2001. Differential incorporation of CD45, CD80 (B7-1), CD86 (B7-2), and major histocompatibility complex class I and II molecules into human immunodeficiency virus type 1 virions and microvesicles: implications for viral pathogenesis and immune regulation. J Virol 75:6173-82.
349. Trubey CM, Chertova E, Coren LV, Hilburn JM, Hixson CV, Nagashima K, Lifson JD, Ott DE. 2003. Quantitation of HLA class II protein incorporated into human immunodeficiency type 1 virions purified by anti-CD45 immunoaffinity depletion of microvesicles. J Virol 77:12699-709.
350. Orentas RJ, Hildreth JE. 1993. Association of host cell surface adhesion receptors and other membrane proteins with HIV and SIV. AIDS Res Hum Retroviruses 9:1157-65.
351. Konadu KA, Huang MB, Roth W, Armstrong W, Powell M, Villinger F, Bond V. 2016. Isolation of Exosomes from the Plasma of HIV-1 Positive Individuals. J Vis Exp doi:10.3791/53495.
352. Reiter K, Aguilar PP, Wetter V, Steppert P, Tover A, Jungbauer A. 2019. Separation of virus-like particles and extracellular vesicles by flow-through and heparin affinity chromatography. J Chromatogr A 1588:77-84.
353. Pankaj K. 2013. Virus Identification and Quantification. Labome: Materials and Methods 3.
354. Osteikoetxea X, Sodar B, Nemeth A, Szabo-Taylor K, Paloczi K, Vukman KV, Tamasi V, Balogh A, Kittel A, Pallinger E, Buzas EI. 2015. Differential detergent sensitivity of extracellular vesicle subpopulations. Org Biomol Chem 13:9775-82.
355. Chen J, Nikolaitchik O, Singh J, Wright A, Bencsics CE, Coffin JM, Ni N, Lockett S, Pathak VK, Hu WS. 2009. High efficiency of HIV-1 genomic RNA packaging and heterozygote formation revealed by single virion analysis. Proc Natl Acad Sci U S A 106:13535-40.
356. Szakacs Z, Meszaros T, de Jonge MI, Gyurcsanyi RE. 2018. Selective counting and sizing of single virus particles using fluorescent aptamer-based nanoparticle tracking analysis. Nanoscale 10:13942-13948.
357. Hercher M, Mueller W, Shapiro HM. 1979. Detection and discrimination of individual viruses by flow cytometry. J Histochem Cytochem 27:350-2.

358. Lippe R. 2018. Flow Virometry: a Powerful Tool To Functionally Characterize Viruses. J Virol 92.
359. Libregts S, Arkesteijn GJA, Nemeth A, Nolte-'t Hoen ENM, Wauben MHM. 2018. Flow cytometric analysis of extracellular vesicle subsets in plasma: impact of swarm by particles of non-interest. J Thromb Haemost 16:1423-1436.
360. van der Pol E, Hoekstra AG, Sturk A, Otto C, van Leeuwen TG, Nieuwland R. 2010. Optical and non-optical methods for detection and characterization of microparticles and exosomes. J Thromb Haemost 8:2596-607.
361. Bonar MM, Tilton JC. 2017. High sensitivity detection and sorting of infectious human immunodeficiency virus (HIV-1) particles by flow virometry. Virology 505:80-90.
362. Landowski M, Dabundo J, Liu Q, Nicola AV, Aguilar HC. 2014. Nipah virion entry kinetics, composition, and conformational changes determined by enzymatic virus-like particles and new flow virometry tools. J Virol 88:14197-206.
363. Marie D, Brussaard CPD, Thyrhaug R, Bratbak G, Vaulot D. 1999. Enumeration of marine viruses in culture and natural samples by flow cytometry. Appl Environ Microbiol 65:45-52.
364. Zicari S, Arakelyan A, Fitzgerald W, Zaitseva E, Chernomordik LV, Margolis L, Grivel JC. 2016. Evaluation of the maturation of individual Dengue virions with flow virometry. Virology 488:20-7.
365. Gaudin R, Barteneva NS. 2015. Sorting of small infectious virus particles by flow virometry reveals distinct infectivity profiles. Nat Commun 6:6022.
366. Cadima-Couto I, Goncalves J. 2010. Towards Inhibition of Vif-APOBEC3G Interaction: Which Protein to Target? Adv Virol 2010:649315.
367. Sharkey M, Sharova N, Mohammed I, Huff SE, Kummetha IR, Singh G, Rana TM, Stevenson M. 2019. HIV-1 Escape from Small-Molecule Antagonism of Vif. MBio 10.
368. Rosales Gerpe MC, Renner TM, Belanger K, Lam C, Aydin H, Langlois MA. 2015. N-linked glycosylation protects gammaretroviruses against deamination by APOBEC3 proteins. J Virol 89:2342-57.
369. Renner TM, Belanger K, Lam C, Gerpe MCR, McBane JE, Langlois MA. 2018. Full-Length Glycosylated Gag of Murine Leukemia Virus Can Associate with the Viral Envelope as a Type I Integral Membrane Protein. J Virol 92.
370. Tang VA, Renner TM, Varette O, Le Boeuf F, Wang J, Diallo JS, Bell JC, Langlois MA. 2016. Single-particle characterization of oncolytic vaccinia virus by flow virometry. Vaccine 34:5082-5089.
371. Sliva K, Erlwein O, Bittner A, Schnierle BS. 2004. Murine leukemia virus (MLV) replication monitored with fluorescent proteins. Virol J 1:14.
372. Erlwein O, Buchholz CJ, Schnierle BS. 2003. The proline-rich region of the ecotropic Moloney murine leukaemia virus envelope protein tolerates the insertion of the green fluorescent protein and allows the generation of replication-competent virus. J Gen Virol 84:369-73.
373. Tang VA, Renner TM, Fritzsche AK, Burger D, Langlois MA. 2017. Single-Particle Discrimination of Retroviruses from Extracellular Vesicles by Nanoscale Flow Cytometry. Sci Rep 7:17769.
374. Renner TM, Tang VA, Burger D, Langlois MA. 2019. Intact Viral Particle Counts Measured by Flow Virometry Provides Insight into the Infectivity and Genome Packaging Efficiency of the Moloney Murine Leukemia Virus. J Virol doi:10.1128/JVI.01600-19.
375. Finzi D, Plaeger SF, Dieffenbach CW. 2006. Defective virus drives human immunodeficiency virus infection, persistence, and pathogenesis. Clin Vaccine Immunol 13:715-21.
376. Thompson KA, Yin J. 2010. Population dynamics of an RNA virus and its defective interfering particles in passage cultures. Virol J 7:257.
377. Stoye JP. 2012. Studies of endogenous retroviruses reveal a continuing evolutionary saga. Nat Rev Microbiol 10:395-406.

378. Duggal NK, Malik HS, Emerman M. 2011. The breadth of antiviral activity of Apobec3DE in chimpanzees has been driven by positive selection. J Virol 85:11361-71.
379. Rehwinkel J. 2014. Mouse knockout models for HIV-1 restriction factors. Cell Mol Life Sci 71:3749-66.
380. Compton AA, Hirsch VM, Emerman M. 2012. The host restriction factor APOBEC3G and retroviral Vif protein coevolve due to ongoing genetic conflict. Cell Host Microbe 11:91-8.
381. Meyerson NR, Sawyer SL. 2011. Two-stepping through time: mammals and viruses. Trends Microbiol 19:286-94.
382. Hrecka K, Hao C, Gierszewska M, Swanson SK, Kesik-Brodacka M, Srivastava S, Florens L, Washburn MP, Skowronski J. 2011. Vpx relieves inhibition of HIV-1 infection of macrophages mediated by the SAMHD1 protein. Nature 474:658-61.
383. Sheehy AM, Gaddis NC, Choi JD, Malim MH. 2002. Isolation of a human gene that inhibits HIV-1 infection and is suppressed by the viral Vif protein. Nature 418:646-50.
384. Stremlau M, Owens CM, Perron MJ, Kiessling M, Autissier P, Sodroski J. 2004. The cytoplasmic body component TRIM5alpha restricts HIV-1 infection in Old World monkeys. Nature 427:848-53.
385. Li Y, Li X, Stremlau M, Lee M, Sodroski J. 2006. Removal of arginine 332 allows human TRIM5alpha to bind human immunodeficiency virus capsids and to restrict infection. J Virol 80:6738-44.
386. Sokolskaja E, Berthoux L, Luban J. 2006. Cyclophilin A and TRIM5alpha independently regulate human immunodeficiency virus type 1 infectivity in human cells. J Virol 80:2855-62.
387. Yap MW, Nisole S, Lynch C, Stoye JP. 2004. Trim5alpha protein restricts both HIV-1 and murine leukemia virus. Proc Natl Acad Sci U S A 101:10786-91.
388. Kozak CA, Chakraborti A. 1996. Single amino acid changes in the murine leukemia virus capsid protein gene define the target of Fv1 resistance. Virology 225:300-5.
389. Ohkura S, Goldstone DC, Yap MW, Holden-Dye K, Taylor IA, Stoye JP. 2011. Novel escape mutants suggest an extensive TRIM5alpha binding site spanning the entire outer surface of the murine leukemia virus capsid protein. PLoS Pathog 7:e1002011.
390. Refsland EW, Harris RS. 2013. The APOBEC3 family of retroelement restriction factors. Curr Top Microbiol Immunol 371:1-27.
391. Newman EN, Holmes RK, Craig HM, Klein KC, Lingappa JR, Malim MH, Sheehy AM. 2005. Antiviral function of APOBEC3G can be dissociated from cytidine deaminase activity. Curr Biol 15:166-70.
392. Belanger K, Savoie M, Rosales Gerpe MC, Couture JF, Langlois MA. 2013. Binding of RNA by APOBEC3G controls deamination-independent restriction of retroviruses. Nucleic Acids Res 41:7438-52.
393. MacMillan AL, Kohli RM, Ross SR. 2013. APOBEC3 inhibition of mouse mammary tumor virus infection: the role of cytidine deamination versus inhibition of reverse transcription. J Virol 87:4808-17.
394. Nowarski R, Prabhu P, Kenig E, Smith Y, Britan-Rosich E, Kotler M. 2014. APOBEC3G Inhibits HIV-1 RNA Elongation by Inactivating the Viral Trans-Activation Response Element. J Mol Biol doi:10.1016/j.jmb.2014.05.012.
395. Guo F, Cen S, Niu M, Yang Y, Gorelick RJ, Kleiman L. 2007. The interaction of APOBEC3G with human immunodeficiency virus type 1 nucleocapsid inhibits tRNA3Lys annealing to viral RNA. J Virol 81:11322-31.
396. Conticello SG, Thomas CJ, Petersen-Mahrt SK, Neuberger MS. 2005. Evolution of the AID/APOBEC family of polynucleotide (deoxy)cytidine deaminases. Mol Biol Evol 22:367-77.

397. Bishop KN, Holmes RK, Sheehy AM, Davidson NO, Cho SJ, Malim MH. 2004. Cytidine deamination of retroviral DNA by diverse APOBEC proteins. Curr Biol 14:1392-6.
398. Santiago ML, Montano M, Benitez R, Messer RJ, Yonemoto W, Chesebro B, Hasenkrug KJ, Greene WC. 2008. Apobec3 encodes Rfv3, a gene influencing neutralizing antibody control of retrovirus infection. Science 321:1343-6.
399. Takeda E, Tsuji-Kawahara S, Sakamoto M, Langlois MA, Neuberger MS, Rada C, Miyazawa M. 2008. Mouse APOBEC3 restricts friend leukemia virus infection and pathogenesis in vivo. J Virol 82:10998-1008.
400. Okeoma CM, Lovsin N, Peterlin BM, Ross SR. 2007. APOBEC3 inhibits mouse mammary tumour virus replication in vivo. Nature 445:927-30.
401. Okeoma CM, Low A, Bailis W, Fan HY, Peterlin BM, Ross SR. 2009. Induction of APOBEC3 in vivo causes increased restriction of retrovirus infection. J Virol 83:3486-95.
402. Low A, Okeoma CM, Lovsin N, de las Heras M, Taylor TH, Peterlin BM, Ross SR, Fan H. 2009. Enhanced replication and pathogenesis of Moloney murine leukemia virus in mice defective in the murine APOBEC3 gene. Virology 385:455-63.
403. Browne EP, Littman DR. 2008. Species-specific restriction of apobec3-mediated hypermutation. J Virol 82:1305-13.
404. Evans LH, Dresler S, Kabat D. 1977. Synthesis and glycosylation of polyprotein precursors to the internal core proteins of Friend murine leukemia virus. J Virol 24:865-74.
405. Edwards SA, Fan H. 1980. Sequence relationship of glycosylated and unglycosylated gag polyproteins of Moloney murine leukemia virus. J Virol 35:41-51.
406. Portis JL, Fujisawa R, McAtee FJ. 1996. The glycosylated gag protein of MuLV is a determinant of neuroinvasiveness: analysis of second site revertants of a mutant MuLV lacking expression of this protein. Virology 226:384-92.
407. Mikl MC, Watt IN, Lu M, Reik W, Davies SL, Neuberger MS, Rada C. 2005. Mice deficient in APOBEC2 and APOBEC3. Mol Cell Biol 25:7270-7.
408. Langlois M, Beale R, Conticello S, Neuberger M. 2005. Mutational comparison of the single-domained APOBEC3C and double-domained APOBEC3F/G anti-retroviral cytidine deaminases provides insight into their DNA target site specificities. Nucleic Acids Research 33:1913-1923.
409. Belanger K, Savoie M, Aydin H, Renner TM, Montazeri Z, Langlois MA. 2014. Deamination intensity profiling of human APOBEC3 protein activity along the near full-length genomes of HIV-1 and MoMLV by HyperHRM analysis. Virology 448:168-75.
410. Suspene R, Henry M, Guillot S, Wain-Hobson S, Vartanian JP. 2005. Recovery of APOBEC3-edited human immunodeficiency virus G->A hypermutants by differential DNA denaturation PCR. J Gen Virol 86:125-9.
411. Gherghe C, Weeks KM. 2006. The SL1-SL2 (stem-loop) domain is the primary determinant for stability of the gamma retroviral genomic RNA dimer. J Biol Chem 281:37952-61.
412. Paprotka T, Venkatachari NJ, Chaipan C, Burdick R, Delviks-Frankenberry KA, Hu WS, Pathak VK. 2010. Inhibition of xenotropic murine leukemia virus-related virus by APOBEC3 proteins and antiviral drugs. J Virol 84:5719-29.
413. Paprotka T, Delviks-Frankenberry KA, Cingoz O, Martinez A, Kung HJ, Tepper CG, Hu WS, Fivash MJ, Jr., Coffin JM, Pathak VK. 2011. Recombinant origin of the retrovirus XMRV. Science 333:97-101.
414. Wirth S, Vessaz A, Krummenacher C, Baribaud F, Acha-Orbea H, Diggelmann H. 2002. Regions of mouse mammary tumor virus superantigen involved in interaction with the major histocompatibility complex class II I-A molecule. J Virol 76:11172-5.

415. Nitta T, Tam R, Kim JW, Fan H. 2011. The cellular protein La functions in enhancement of virus release through lipid rafts facilitated by murine leukemia virus glycosylated Gag. MBio 2:e00341-10.
416. Simon V, Zennou V, Murray D, Huang Y, Ho DD, Bieniasz PD. 2005. Natural variation in Vif: differential impact on APOBEC3G/3F and a potential role in HIV-1 diversification. PLoS Pathog 1:e6.
417. Haché G, Mansky LM, Harris RS. 2006. Human APOBEC3 proteins, retrovirus restriction, and HIV drug resistance. AIDS Rev 8:148-57.
418. Monajemi M, Woodworth CF, Benkaroun J, Grant M, Larijani M. 2012. Emerging complexities of APOBEC3G action on immunity and viral fitness during HIV infection and treatment. Retrovirology 9:35.
419. Jern P, Russell RA, Pathak VK, Coffin JM. 2009. Likely role of APOBEC3G-mediated G-to-A mutations in HIV-1 evolution and drug resistance. PLoS Pathog 5:e1000367.
420. Kim EY, Bhattacharya T, Kunstman K, Swantek P, Koning FA, Malim MH, Wolinsky SM. 2010. Human APOBEC3G-mediated editing can promote HIV-1 sequence diversification and accelerate adaptation to selective pressure. J Virol 84:10402-5.
421. Harris RS, Dudley JP. 2015. APOBECs and virus restriction. Virology 479-480:131-45.
422. Pillemer EA, Kooistra DA, Witte ON, Weissman IL. 1986. Monoclonal antibody to the amino-terminal L sequence of murine leukemia virus glycosylated gag polyproteins demonstrates their unusual orientation in the cell membrane. J Virol 57:413-21.
423. Chun R, Fan H. 1994. Recovery of Glycosylated gag Virus from Mice Infected with a Glycosylated gag-Negative Mutant of Moloney Murine Leukemia Virus. J Biomed Sci 1:218-223.
424. Nair S, Sanchez-Martinez S, Ji X, Rein A. 2014. Biochemical and biological studies of mouse APOBEC3. J Virol 88:3850-60.
425. Harris RS, Bishop KN, Sheehy AM, Craig HM, Petersen-Mahrt SK, Watt IN, Neuberger MS, Malim MH. 2003. DNA deamination mediates innate immunity to retroviral infection. Cell 113:803-9.
426. Rausch JW, Chelico L, Goodman MF, Le Grice SF. 2009. Dissecting APOBEC3G substrate specificity by nucleoside analog interference. J Biol Chem 284:7047-58.
427. Yang Y, Luban J, Diaz-Griffero F. 2014. The fate of HIV-1 capsid: a biochemical assay for HIV-1 uncoating. Methods Mol Biol 1087:29-36.
428. Wight DJ, Boucherit VC, Wanaguru M, Elis E, Hirst EM, Li W, Ehrlich M, Bacharach E, Bishop KN. 2014. The N-terminus of murine leukaemia virus p12 protein is required for mature core stability. PLoS Pathog 10:e1004474.
429. Stremlau M, Perron M, Lee M, Li Y, Song B, Javanbakht H, Diaz-Griffero F, Anderson DJ, Sundquist WI, Sodroski J. 2006. Specific recognition and accelerated uncoating of retroviral capsids by the TRIM5alpha restriction factor. Proc Natl Acad Sci U S A 103:5514-9.
430. Cen S, Guo F, Niu M, Saadatmand J, Deflassieux J, Kleiman L. 2004. The interaction between HIV-1 Gag and APOBEC3G. J Biol Chem 279:33177-84.
431. Luo K, Liu B, Xiao Z, Yu Y, Yu X, Gorelick R, Yu XF. 2004. Amino-terminal region of the human immunodeficiency virus type 1 nucleocapsid is required for human APOBEC3G packaging. J Virol 78:11841-52.
432. Schafer A, Bogerd HP, Cullen BR. 2004. Specific packaging of APOBEC3G into HIV-1 virions is mediated by the nucleocapsid domain of the gag polyprotein precursor. Virology 328:163-8.
433. Zennou V, Perez-Caballero D, Gottlinger H, Bieniasz PD. 2004. APOBEC3G incorporation into human immunodeficiency virus type 1 particles. J Virol 78:12058-61.
434. Tung JS, Yoshiki T, Fleissner E. 1976. A core polyprotein of murine leukemia virus on the surface of mouse leukemia cells. Cell 9:573-8.

435. Wilk T, Gross I, Gowen BE, Rutten T, de Haas F, Welker R, Krausslich HG, Boulanger P, Fuller SD. 2001. Organization of immature human immunodeficiency virus type 1. J Virol 75:759-71.
436. Yeager M, Wilson-Kubalek EM, Weiner SG, Brown PO, Rein A. 1998. Supramolecular organization of immature and mature murine leukemia virus revealed by electron cryo-microscopy: implications for retroviral assembly mechanisms. Proc Natl Acad Sci U S A 95:7299-304.
437. Kingston RL, Olson NH, Vogt VM. 2001. The organization of mature Rous sarcoma virus as studied by cryoelectron microscopy. J Struct Biol 136:67-80.
438. Hammarstedt M, Garoff H. 2004. Passive and active inclusion of host proteins in human immunodeficiency virus type 1 gag particles during budding at the plasma membrane. J Virol 78:5686-97.
439. Tremblay MJ, Fortin JF, Cantin R. 1998. The acquisition of host-encoded proteins by nascent HIV-1. Immunol Today 19:346-51.
440. Steppert P, Burgstaller D, Klausberger M, Berger E, Aguilar PP, Schneider TA, Kramberger P, Tover A, Nobauer K, Razzazi-Fazeli E, Jungbauer A. 2016. Purification of HIV-1 gag virus-like particles and separation of other extracellular particles. J Chromatogr A 1455:93-101.
441. Arakelyan A, Fitzgerald W, King DF, Rogers P, Cheeseman HM, Grivel JC, Shattock RJ, Margolis L. 2017. Flow virometry analysis of envelope glycoprotein conformations on individual HIV virions. Sci Rep 7:948.
442. Arakelyan A, Fitzgerald W, Margolis L, Grivel JC. 2013. Nanoparticle-based flow virometry for the analysis of individual virions. J Clin Invest 123:3716-27.
443. van der Pol E, Boing AN, Harrison P, Sturk A, Nieuwland R. 2012. Classification, functions, and clinical relevance of extracellular vesicles. Pharmacol Rev 64:676-705.
444. Robbins PD, Morelli AE. 2014. Regulation of immune responses by extracellular vesicles. Nat Rev Immunol 14:195-208.
445. Bobrie A, Colombo M, Krumeich S, Raposo G, Thery C. 2012. Diverse subpopulations of vesicles secreted by different intracellular mechanisms are present in exosome preparations obtained by differential ultracentrifugation. J Extracell Vesicles 1.
446. Hill AF, Pegtel DM, Lambertz U, Leonardi T, O'Driscoll L, Pluchino S, Ter-Ovanesyan D, Nolte-'t Hoen EN. 2013. ISEV position paper: extracellular vesicle RNA analysis and bioinformatics. J Extracell Vesicles 2.
447. Kowal J, Arras G, Colombo M, Jouve M, Morath JP, Primdal-Bengtson B, Dingli F, Loew D, Tkach M, Thery C. 2016. Proteomic comparison defines novel markers to characterize heterogeneous populations of extracellular vesicle subtypes. Proc Natl Acad Sci U S A 113:E968-77.
448. Belov L, Matic KJ, Hallal S, Best OG, Mulligan SP, Christopherson RI. 2016. Extensive surface protein profiles of extracellular vesicles from cancer cells may provide diagnostic signatures from blood samples. J Extracell Vesicles 5:25355.
449. Izquierdo-Useros N, Puertas MC, Borras FE, Blanco J, Martinez-Picado J. 2011. Exosomes and retroviruses: the chicken or the egg? Cell Microbiol 13:10-7.
450. Sampey GC, Saifuddin M, Schwab A, Barclay R, Punya S, Chung MC, Hakami RM, Zadeh MA, Lepene B, Klase ZA, El-Hage N, Young M, Iordanskiy S, Kashanchi F. 2016. Exosomes from HIV-1-infected Cells Stimulate Production of Pro-inflammatory Cytokines through Trans-activating Response (TAR) RNA. J Biol Chem 291:1251-66.
451. Arakelyan A, Fitzgerald W, Zicari S, Vanpouille C, Margolis L. 2017. Extracellular Vesicles Carry HIV Env and Facilitate Hiv Infection of Human Lymphoid Tissue. Sci Rep 7:1695.
452. Li M, Aliotta JM, Asara JM, Tucker L, Quesenberry P, Lally M, Ramratnam B. 2012. Quantitative proteomic analysis of exosomes from HIV-1-infected lymphocytic cells. Proteomics 12:2203-11.

453. Raab-Traub N, Dittmer DP. 2017. Viral effects on the content and function of extracellular vesicles. Nat Rev Microbiol 15:559-572.
454. Brussaard CPD, Marie D, Bratbak G. 2000. Flow cytometric detection of viruses. Journal of Virological Methods 85:175-182.
455. Musich T, Jones JC, Keele BF, Jenkins LM, Demberg T, Uldrick TS, Yarchoan R, Robert-Guroff M. 2017. Flow virometric sorting and analysis of HIV quasispecies from plasma. JCI Insight 2:e90626.
456. Steen HB. 2004. Flow cytometer for measurement of the light scattering of viral and other submicroscopic particles. Cytometry A 57:94-9.
457. Loret S, El Bilali N, Lippe R. 2012. Analysis of herpes simplex virus type I nuclear particles by flow cytometry. Cytometry A 81:950-9.
458. Groot Kormelink T, Arkesteijn GJ, Nauwelaers FA, van den Engh G, Nolte-'t Hoen EN, Wauben MH. 2016. Prerequisites for the analysis and sorting of extracellular vesicle subpopulations by high-resolution flow cytometry. Cytometry A 89:135-47.
459. Mateescu B, Kowal EJ, van Balkom BW, Bartel S, Bhattacharyya SN, Buzas EI, Buck AH, de Candia P, Chow FW, Das S, Driedonks TA, Fernandez-Messina L, Haderk F, Hill AF, Jones JC, Van Keuren-Jensen KR, Lai CP, Lasser C, Liegro ID, Lunavat TR, Lorenowicz MJ, Maas SL, Mager I, Mittelbrunn M, Momma S, Mukherjee K, Nawaz M, Pegtel DM, Pfaffl MW, Schiffelers RM, Tahara H, Thery C, Tosar JP, Wauben MH, Witwer KW, Nolte-'t Hoen EN. 2017. Obstacles and opportunities in the functional analysis of extracellular vesicle RNA - an ISEV position paper. J Extracell Vesicles 6:1286095.
460. Morales-Kastresana A, Telford B, Musich TA, McKinnon K, Clayborne C, Braig Z, Rosner A, Demberg T, Watson DC, Karpova TS, Freeman GJ, DeKruyff RH, Pavlakis GN, Terabe M, Robert-Guroff M, Berzofsky JA, Jones JC. 2017. Labeling Extracellular Vesicles for Nanoscale Flow Cytometry. Sci Rep 7:1878.
461. Arraud N, Gounou C, Turpin D, Brisson AR. 2016. Fluorescence triggering: A general strategy for enumerating and phenotyping extracellular vesicles by flow cytometry. Cytometry A 89:184-95.
462. Inglis HC, Danesh A, Shah A, Lacroix J, Spinella PC, Norris PJ. 2015. Techniques to improve detection and analysis of extracellular vesicles using flow cytometry. Cytometry A 87:1052-63.
463. Stoner SA, Duggan E, Condello D, Guerrero A, Turk JR, Narayanan PK, Nolan JP. 2016. High sensitivity flow cytometry of membrane vesicles. Cytometry A 89:196-206.
464. Cloutier N, Tan S, Boudreau LH, Cramb C, Subbaiah R, Lahey L, Albert A, Shnayder R, Gobezie R, Nigrovic PA, Farndale RW, Robinson WH, Brisson A, Lee DM, Boilard E. 2013. The exposure of autoantigens by microparticles underlies the formation of potent inflammatory components: the microparticle-associated immune complexes. EMBO Mol Med 5:235-49.
465. Zhu P, Chertova E, Bess J, Jr., Lifson JD, Arthur LO, Liu J, Taylor KA, Roux KH. 2003. Electron tomography analysis of envelope glycoprotein trimers on HIV and simian immunodeficiency virus virions. Proc Natl Acad Sci U S A 100:15812-7.
466. Zhu P, Liu J, Bess J, Jr., Chertova E, Lifson JD, Grise H, Ofek GA, Taylor KA, Roux KH. 2006. Distribution and three-dimensional structure of AIDS virus envelope spikes. Nature 441:847-52.
467. Stano A, Leaman DP, Kim AS, Zhang L, Autin L, Ingale J, Gift SK, Truong J, Wyatt RT, Olson AJ, Zwick MB. 2017. Dense Array of Spikes on HIV-1 Virion Particles. J Virol 91.
468. Gyorgy B, Modos K, Pallinger E, Paloczi K, Pasztoi M, Misjak P, Deli MA, Sipos A, Szalai A, Voszka I, Polgar A, Toth K, Csete M, Nagy G, Gay S, Falus A, Kittel A, Buzas EI. 2011. Detection and isolation of cell-derived microparticles are compromised by protein complexes resulting from shared biophysical parameters. Blood 117:e39-48.
469. van der Pol E, van Gemert MJ, Sturk A, Nieuwland R, van Leeuwen TG. 2012. Single vs. swarm detection of microparticles and exosomes by flow cytometry. J Thromb Haemost 10:919-30.

470. Nolan JP, Stoner SA. 2013. A trigger channel threshold artifact in nanoparticle analysis. Cytometry A 83:301-5.
471. Anonymous. 2010. BD Biosciences. An Introduction to Window Extension on Digital Flow Cytometers. BD Technical Bulletin doi:https://www.bdbiosciences.com/documents/techbulletin_lsr_window_ext.pdf.
472. Gray WD, Mitchell AJ, Searles CD. 2015. An accurate, precise method for general labeling of extracellular vesicles. MethodsX 2:360-7.
473. San-Juan-Vergara H, Sampayo-Escobar V, Reyes N, Cha B, Pacheco-Lugo L, Wong T, Peeples ME, Collins PL, Castano ME, Mohapatra SS. 2012. Cholesterol-rich microdomains as docking platforms for respiratory syncytial virus in normal human bronchial epithelial cells. J Virol 86:1832-43.
474. Zhang S, Chan KR, Tan HC, Ooi EE. 2014. Dengue virus growth, purification, and fluorescent labeling. Methods Mol Biol 1138:3-14.
475. Xu H, Hao X, Wang S, Wang Z, Cai M, Jiang J, Qin Q, Zhang M, Wang H. 2015. Real-time Imaging of Rabies Virus Entry into Living Vero cells. Sci Rep 5:11753.
476. Lakadamyali M, Rust MJ, Babcock HP, Zhuang X. 2003. Visualizing infection of individual influenza viruses. Proc Natl Acad Sci U S A 100:9280-5.
477. Berkowitz R, Fisher J, Goff SP. 1996. RNA packaging. Curr Top Microbiol Immunol 214:177-218.
478. Li M, Zeringer E, Barta T, Schageman J, Cheng A, Vlassov AV. 2014. Analysis of the RNA content of the exosomes derived from blood serum and urine and its potential as biomarkers. Philos Trans R Soc Lond B Biol Sci 369.
479. Chevillet JR, Kang Q, Ruf IK, Briggs HA, Vojtech LN, Hughes SM, Cheng HH, Arroyo JD, Meredith EK, Gallichotte EN, Pogosova-Agadjanyan EL, Morrissey C, Stirewalt DL, Hladik F, Yu EY, Higano CS, Tewari M. 2014. Quantitative and stoichiometric analysis of the microRNA content of exosomes. Proc Natl Acad Sci U S A 111:14888-93.
480. Goebel SJ, Johnson GP, Perkus ME, Davis SW, Winslow JP, Paoletti E. 1990. The complete DNA sequence of vaccinia virus. Virology 179:247-66, 517-63.
481. McFadden G. 2005. Poxvirus tropism. Nat Rev Microbiol 3:201-13.
482. Smith GL, Benfield CT, Maluquer de Motes C, Mazzon M, Ember SW, Ferguson BJ, Sumner RP. 2013. Vaccinia virus immune evasion: mechanisms, virulence and immunogenicity. J Gen Virol 94:2367-92.
483. Cassetti MC, Merchlinsky M, Wolffe EJ, Weisberg AS, Moss B. 1998. DNA packaging mutant: repression of the vaccinia virus A32 gene results in noninfectious, DNA-deficient, spherical, enveloped particles. J Virol 72:5769-80.
484. Chandler WL, Yeung W, Tait JF. 2011. A new microparticle size calibration standard for use in measuring smaller microparticles using a new flow cytometer. J Thromb Haemost 9:1216-24.
485. van der Pol E, Coumans FA, Grootemaat AE, Gardiner C, Sargent IL, Harrison P, Sturk A, van Leeuwen TG, Nieuwland R. 2014. Particle size distribution of exosomes and microvesicles determined by transmission electron microscopy, flow cytometry, nanoparticle tracking analysis, and resistive pulse sensing. J Thromb Haemost 12:1182-92.
486. van der Pol E, Coumans FA, Sturk A, Nieuwland R, van Leeuwen TG. 2014. Refractive index determination of nanoparticles in suspension using nanoparticle tracking analysis. Nano Lett 14:6195-201.
487. Houzet L, Gay B, Morichaud Z, Briant L, Mougel M. 2006. Intracellular assembly and budding of the Murine Leukemia Virus in infected cells. Retrovirology 3:12.
488. Cyrklaff M, Risco C, Fernandez JJ, Jimenez MV, Esteban M, Baumeister W, Carrascosa JL. 2005. Cryo-electron tomography of vaccinia virus. Proc Natl Acad Sci U S A 102:2772-7.

489. Dragovic RA, Gardiner C, Brooks AS, Tannetta DS, Ferguson DJ, Hole P, Carr B, Redman CW, Harris AL, Dobson PJ, Harrison P, Sargent IL. 2011. Sizing and phenotyping of cellular vesicles using Nanoparticle Tracking Analysis. Nanomedicine 7:780-8.
490. Carroll MW, Moss B. 1997. Host range and cytopathogenicity of the highly attenuated MVA strain of vaccinia virus: propagation and generation of recombinant viruses in a nonhuman mammalian cell line. Virology 238:198-211.
491. Vanderplasschen A, Mathew E, Hollinshead M, Sim RB, Smith GL. 1998. Extracellular enveloped vaccinia virus is resistant to complement because of incorporation of host complement control proteins into its envelope. Proc Natl Acad Sci U S A 95:7544-9.
492. Burger D, Turner M, Xiao F, Munkonda MN, Akbari S, Burns KD. 2017. High glucose increases the formation and pro-oxidative activity of endothelial microparticles. Diabetologia doi:10.1007/s00125-017-4331-2.
493. Weiss RA. 2013. On the concept and elucidation of endogenous retroviruses. Philos Trans R Soc Lond B Biol Sci 368:20120494.
494. Coffin JM, Fan H. 2016. The Discovery of Reverse Transcriptase. Annu Rev Virol 3:29-51.
495. Guan R, Aiyer S, Cote ML, Xiao R, Jiang M, Acton TB, Roth MJ, Montelione GT. 2017. X-ray crystal structure of the N-terminal region of Moloney murine leukemia virus integrase and its implications for viral DNA recognition. Proteins 85:647-656.
496. Dubois N, Marquet R, Paillart JC, Bernacchi S. 2018. Retroviral RNA Dimerization: From Structure to Functions. Front Microbiol 9:527.
497. Studamire B, Goff SP. 2010. Interactions of host proteins with the murine leukemia virus integrase. Viruses 2:1110-45.
498. Cote ML, Roth MJ. 2008. Murine leukemia virus reverse transcriptase: structural comparison with HIV-1 reverse transcriptase. Virus Res 134:186-202.
499. Cavazzana M, Six E, Lagresle-Peyrou C, Andre-Schmutz I, Hacein-Bey-Abina S. 2016. Gene Therapy for X-Linked Severe Combined Immunodeficiency: Where Do We Stand? Hum Gene Ther 27:108-16.
500. Masciopinto F, Giovani C, Campagnoli S, Galli-Stampino L, Colombatto P, Brunetto M, Yen TS, Houghton M, Pileri P, Abrignani S. 2004. Association of hepatitis C virus envelope proteins with exosomes. Eur J Immunol 34:2834-42.
501. Timmins J, Scianimanico S, Schoehn G, Weissenhorn W. 2001. Vesicular release of ebola virus matrix protein VP40. Virology 283:1-6.
502. Gould SJ, Booth AM, Hildreth JE. 2003. The Trojan exosome hypothesis. Proc Natl Acad Sci U S A 100:10592-7.
503. Vera A. Tang AKF, Tyler M. Renner, Dylan Burger, Edwin van der Pol, Joanne A. Lannigan, George C. Brittain, Joshua A. Welsh, Jennifer C. Jones and Marc-André Langlois. 2019. Engineered Retroviruses as Fluorescent Biological Reference Particles for Small Particle Flow Cytometry. bioRxiv doi:https://doi.org/10.1101/614461.
504. Langlois MA, Beale RC, Conticello SG, Neuberger MS. 2005. Mutational comparison of the single-domained APOBEC3C and double-domained APOBEC3F/G anti-retroviral cytidine deaminases provides insight into their DNA target site specificities. Nucleic Acids Res 33:1913-23.
505. Longo PA, Kavran JM, Kim MS, Leahy DJ. 2013. Transient mammalian cell transfection with polyethylenimine (PEI). Methods Enzymol 529:227-40.
506. Forster F, Medalia O, Zauberman N, Baumeister W, Fass D. 2005. Retrovirus envelope protein complex structure in situ studied by cryo-electron tomography. Proc Natl Acad Sci U S A 102:4729-34.
507. Fisher J, Goff SP. 1998. Mutational analysis of stem-loops in the RNA packaging signal of the Moloney murine leukemia virus. Virology 244:133-45.

508. Andrawiss M, Takeuchi Y, Hewlett L, Collins M. 2003. Murine leukemia virus particle assembly quantitated by fluorescence microscopy: role of Gag-Gag interactions and membrane association. J Virol 77:11651-60.
509. Bachrach E, Marin M, Pelegrin M, Karavanas G, Piechaczyk M. 2000. Efficient cell infection by Moloney murine leukemia virus-derived particles requires minimal amounts of envelope glycoprotein. J Virol 74:8480-6.
510. El Bilali N, Duron J, Gingras D, Lippe R. 2017. Quantitative Evaluation of Protein Heterogeneity within Herpes Simplex Virus 1 Particles. J Virol 91.
511. Vlasak J, Hoang VM, Christanti S, Peluso R, Li F, Culp TD. 2016. Use of flow cytometry for characterization of human cytomegalovirus vaccine particles. Vaccine 34:2321-8.
512. Morales-Kastresana A, Musich TA, Welsh JA, Telford W, Demberg T, Wood JCS, Bigos M, Ross CD, Kachynski A, Dean A, Felton EJ, Van Dyke J, Tigges J, Toxavidis V, Parks DR, Overton WR, Kesarwala AH, Freeman GJ, Rosner A, Perfetto SP, Pasquet L, Terabe M, McKinnon K, Kapoor V, Trepel JB, Puri A, Kobayashi H, Yung B, Chen X, Guion P, Choyke P, Knox SJ, Ghiran I, Robert-Guroff M, Berzofsky JA, Jones JC. 2019. High-fidelity detection and sorting of nanoscale vesicles in viral disease and cancer. J Extracell Vesicles 8:1597603.
513. Musich T, Jones JC, Keele BF, Jenkins LMM, Demberg T, Uldrick TS, Yarchoan R, Robert-Guroff M. 2017. Flow virometric sorting and analysis of HIV quasispecies from plasma. JCI Insight 2:e90626.
514. Koch P, Lampe M, Godinez WJ, Muller B, Rohr K, Krausslich HG, Lehmann MJ. 2009. Visualizing fusion of pseudotyped HIV-1 particles in real time by live cell microscopy. Retrovirology 6:84.
515. Maurel S, Houzet L, Garcia EL, Telesnitsky A, Mougel M. 2007. Characterization of a natural heterodimer between MLV genomic RNA and the SD' retroelement generated by alternative splicing. RNA 13:2266-76.
516. Frensing T. 2015. Defective interfering viruses and their impact on vaccines and viral vectors. Biotechnol J 10:681-9.
517. Lukhovitskaya NI, Thaduri S, Garushyants SK, Torrance L, Savenkov EI. 2013. Deciphering the mechanism of defective interfering RNA (DI RNA) biogenesis reveals that a viral protein and the DI RNA act antagonistically in virus infection. J Virol 87:6091-103.
518. Sun Y, Jain D, Koziol-White CJ, Genoyer E, Gilbert M, Tapia K, Panettieri RA, Jr., Hodinka RL, Lopez CB. 2015. Immunostimulatory Defective Viral Genomes from Respiratory Syncytial Virus Promote a Strong Innate Antiviral Response during Infection in Mice and Humans. PLoS Pathog 11:e1005122.
519. Easton AJ, Scott PD, Edworthy NL, Meng B, Marriott AC, Dimmock NJ. 2011. A novel broad-spectrum treatment for respiratory virus infections: influenza-based defective interfering virus provides protection against pneumovirus infection in vivo. Vaccine 29:2777-84.
520. Yang Y, Lyu T, Zhou R, He X, Ye K, Xie Q, Zhu L, Chen T, Shen C, Wu Q, Zhang B, Zhao W. 2019. The Antiviral and Antitumor Effects of Defective Interfering Particles/Genomes and Their Mechanisms. Front Microbiol 10:1852.
521. Klasse PJ. 2015. Molecular determinants of the ratio of inert to infectious virus particles. Prog Mol Biol Transl Sci 129:285-326.
522. Chuck AS, Clarke MF, Palsson BO. 1996. Retroviral infection is limited by Brownian motion. Hum Gene Ther 7:1527-34.
523. Chen J, MacCarthy T. 2017. The preferred nucleotide contexts of the AID/APOBEC cytidine deaminases have differential effects when mutating retrotransposon and virus sequences compared to host genes. PLoS Comput Biol 13:e1005471.
524. Cook JD, Lee JE. 2013. The secret life of viral entry glycoproteins: moonlighting in immune evasion. PLoS Pathog 9:e1003258.

525. Mukhamedova N, Hoang A, Dragoljevic D, Dubrovsky L, Pushkarsky T, Low H, Ditiatkovski M, Fu Y, Ohkawa R, Meikle PJ, Horvath A, Brichacek B, Miller YI, Murphy A, Bukrinsky M, Sviridov D. 2019. Exosomes containing HIV protein Nef reorganize lipid rafts potentiating inflammatory response in bystander cells. PLoS Pathog 15:e1007907.
526. Rassa JC, Meyers JL, Zhang Y, Kudaravalli R, Ross SR. 2002. Murine retroviruses activate B cells via interaction with toll-like receptor 4. Proc Natl Acad Sci U S A 99:2281-6.
527. Ardavin C, Luthi F, Andersson M, Scarpellino L, Martin P, Diggelmann H, Acha-Orbea H. 1997. Retrovirus-induced target cell activation in the early phases of infection: the mouse mammary tumor virus model. J Virol 71:7295-9.
528. Satake M, McMillan PN, Luftig RB. 1981. Effect of vinblastine on distribution of murine leukemia virus-derived membrane-associated antigens. Proc Natl Acad Sci U S A 78:6266-70.
529. Day JR, Munk C, Guatelli JC. 2004. The membrane-proximal tyrosine-based sorting signal of human immunodeficiency virus type 1 gp41 is required for optimal viral infectivity. J Virol 78:1069-79.
530. Malbec M, Sourisseau M, Guivel-Benhassine F, Porrot F, Blanchet F, Schwartz O, Casartelli N. 2013. HIV-1 Nef promotes the localization of Gag to the cell membrane and facilitates viral cell-to-cell transfer. Retrovirology 10:80.
531. Feng Y, Baig TT, Love RP, Chelico L. 2014. Suppression of APOBEC3-mediated restriction of HIV-1 by Vif. Front Microbiol 5:450.
532. Matheson NJ, Sumner J, Wals K, Rapiteanu R, Weekes MP, Vigan R, Weinelt J, Schindler M, Antrobus R, Costa AS, Frezza C, Clish CB, Neil SJ, Lehner PJ. 2015. Cell Surface Proteomic Map of HIV Infection Reveals Antagonism of Amino Acid Metabolism by Vpu and Nef. Cell Host Microbe 18:409-23.
533. Kwon DN, Lee YK, Greenhalgh DG, Cho K. 2011. Lipopolysaccharide stress induces cell-type specific production of murine leukemia virus type-endogenous retroviral virions in primary lymphoid cells. J Gen Virol 92:292-300.
534. van der Kuyl AC. 2012. HIV infection and HERV expression: a review. Retrovirology 9:6.
535. Pizzato M, Marlow SA, Blair ED, Takeuchi Y. 1999. Initial binding of murine leukemia virus particles to cells does not require specific Env-receptor interaction. J Virol 73:8599-611.
536. Bernier R, Tremblay M. 1995. Homologous interference resulting from the presence of defective particles of human immunodeficiency virus type 1. J Virol 69:291-300.
537. Audit M, Dejardin J, Hohl B, Sidobre C, Hope TJ, Mougel M, Sitbon M. 1999. Introduction of a cis-acting mutation in the capsid-coding gene of moloney murine leukemia virus extends its leukemogenic properties. J Virol 73:10472-9.
538. Altschul SF, Madden TL, Schaffer AA, Zhang J, Zhang Z, Miller W, Lipman DJ. 1997. Gapped BLAST and PSI-BLAST: a new generation of protein database search programs. Nucleic Acids Res 25:3389-402.
539. Altschul SF, Wootton JC, Gertz EM, Agarwala R, Morgulis A, Schaffer AA, Yu YK. 2005. Protein database searches using compositionally adjusted substitution matrices. FEBS J 272:5101-9.
540. Tanner EJ, Kirkegaard KA, Weinberger LS. 2016. Exploiting Genetic Interference for Antiviral Therapy. PLoS Genet 12:e1005986.
541. Lane RE, Korbie D, Hill MM, Trau M. 2018. Extracellular vesicles as circulating cancer biomarkers: opportunities and challenges. Clin Transl Med 7:14.

Rights and Permissions

Figure licenses and permissions.

Figure 1.2. License #: 4674930178483

Figure 1.5. License #: 4674921498531

Figure 1.6. License #: 4674941205962

Figure 1.7.

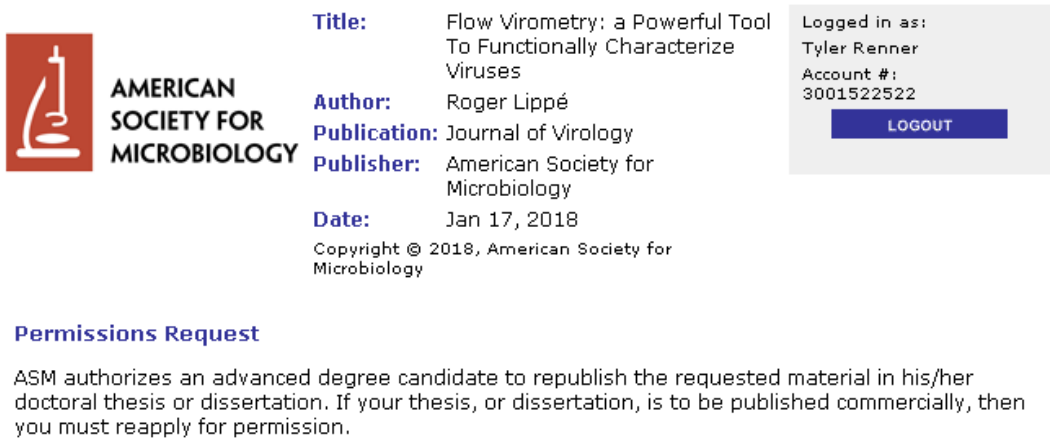

The following excerpt is applicable to **Chapters 2 & 3**. It is taken from the American Society for Microbiology (ASM) which states the authors rights and permissions for reuse of publications:

Authors may republish/adapt portions of their articles

ASM also grants the author the right to republish discrete portions of his/her article in any other publication (including print, CD-ROM, and other electronic formats) of which he or she is author or editor, provided that proper credit is given to the original ASM publication. An ASM author also retains the right to reuse the full article in his/her dissertation or thesis. "Proper credit" means either the copyright lines shown on the top of the first page of the PDF version, or "Copyright © American Society for Microbiology, [insert journal name, volume number, year, page numbers and DOI]" of the HTML version.

https://journals.asm.org/content/statement-author-rights

In the cases of these ASM journals, this excerpt should also be noted:

ASM publishes Microbiology Resource Announcements content under a Creative Commons Attribution 4.0 International license. The author(s) retains copyright under this license. Others may read, download, copy, distribute, print, search, adapt, link to, reorganize, and build upon the published work for any purpose, even commercially, as long as credit to the author and original article is given.

https://journals.asm.org/content/licensing

Reprint of **Chapter 4** within this thesis is in accordance with the Creative Commons Attribution 4.0 International License (http://creativecommons.org/licenses/by/4.0/).

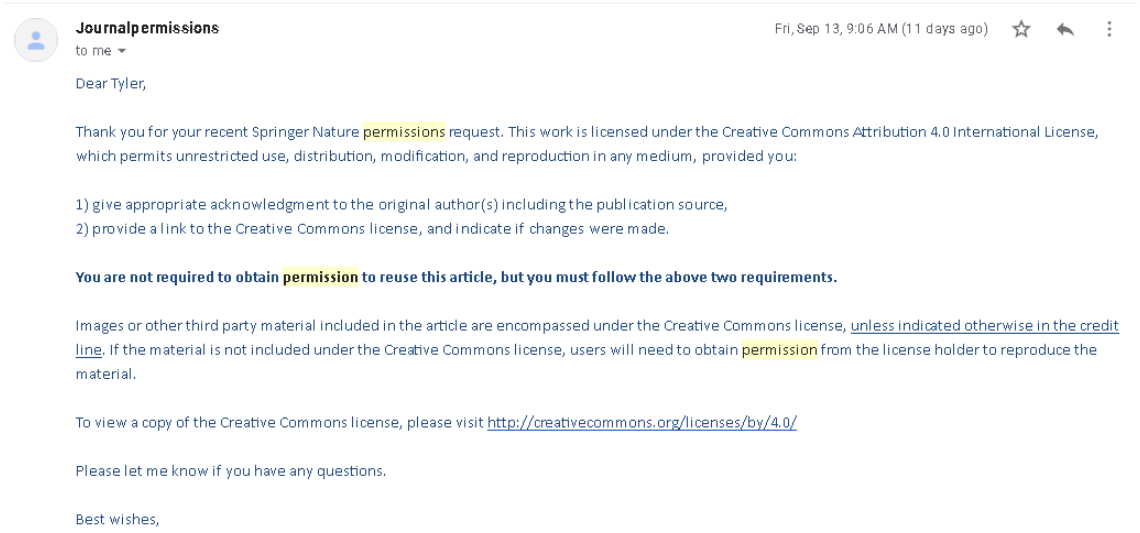

Journalpermissions Fri, Sep 13, 9:06 AM (11 days ago)

to me

Dear Tyler,

Thank you for your recent Springer Nature permissions request. This work is licensed under the Creative Commons Attribution 4.0 International License, which permits unrestricted use, distribution, modification, and reproduction in any medium, provided you:

1) give appropriate acknowledgment to the original author(s) including the publication source,
2) provide a link to the Creative Commons license, and indicate if changes were made.

You are not required to obtain permission to reuse this article, but you must follow the above two requirements.

Images or other third party material included in the article are encompassed under the Creative Commons license, unless indicated otherwise in the credit line. If the material is not included under the Creative Commons license, users will need to obtain permission from the license holder to reproduce the material.

To view a copy of the Creative Commons license, please visit http://creativecommons.org/licenses/by/4.0/

Please let me know if you have any questions.

Best wishes,

Permissions for reprint of article from Vaccine within the Appendix:
https://www.elsevier.com/about/policies/copyright#Author-rights

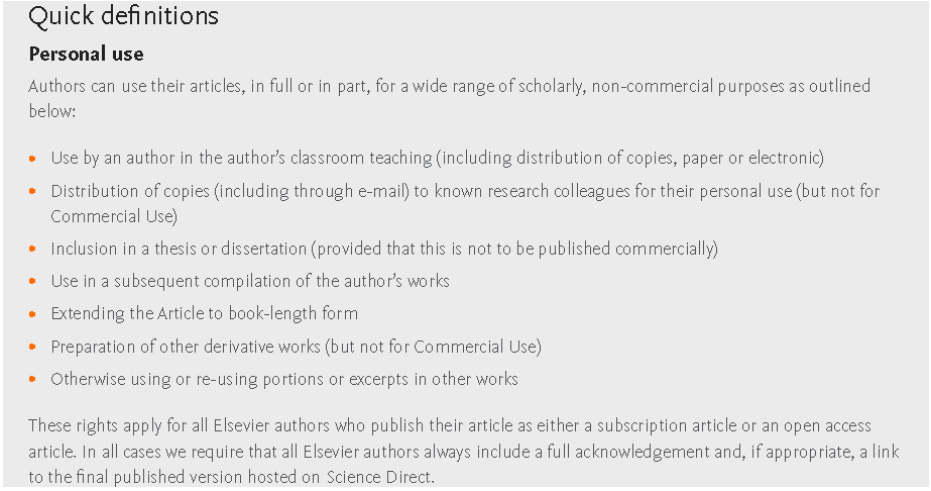

Quick definitions

Personal use

Authors can use their articles, in full or in part, for a wide range of scholarly, non-commercial purposes as outlined below:

- Use by an author in the author's classroom teaching (including distribution of copies, paper or electronic)
- Distribution of copies (including through e-mail) to known research colleagues for their personal use (but not for Commercial Use)
- Inclusion in a thesis or dissertation (provided that this is not to be published commercially)
- Use in a subsequent compilation of the author's works
- Extending the Article to book-length form
- Preparation of other derivative works (but not for Commercial Use)
- Otherwise using or re-using portions or excerpts in other works

These rights apply for all Elsevier authors who publish their article as either a subscription article or an open access article. In all cases we require that all Elsevier authors always include a full acknowledgement and, if appropriate, a link to the final published version hosted on Science Direct.

Appendix 1

Preface: This chapter has been previously published as a research article:

Tang VA, **Renner TM**, Varette O, Le Boeuf F, Wang J, Diallo JS, Bell JC, Langlois MA. 2016. Single-particle characterization of oncolytic vaccinia virus by flow virometry. Vaccine. 34(42):5082-5089. https://doi.org/10.1016/j.vaccine.2016.08.074

Vaccine 34 (2016) 5082–5089

Contents lists available at ScienceDirect

Vaccine

journal homepage: www.elsevier.com/locate/vaccine

Single-particle characterization of oncolytic vaccinia virus by flow virometry

Vera A. Tang [a], Tyler M. Renner [b], Oliver Varette [b,c], Fabrice Le Boeuf [c], Jiahu Wang [c], Jean-Simon Diallo [b,c], John C. Bell [b,c], Marc-André Langlois [a,b,*]

[a] University of Ottawa Flow Cytometry and Virometry Core Facility, Canada
[b] Department of Biochemistry, Microbiology and Immunology, Faculty of Medicine, University of Ottawa, Canada
[c] Centre for Innovative Cancer Therapeutics, Ottawa Hospital Research Institute, Canada

ARTICLE INFO

Article history:
Received 9 June 2016
Received in revised form 27 July 2016
Accepted 23 August 2016
Available online 8 September 2016

Keywords:
Oncolytic virus
Vaccinia virus
Submicron-sized particles
Extracellular vesicles
Microparticles
Flow cytometry
Flow virometry
Viral sorting
Quality control
Vaccine

ABSTRACT

Vaccinia virus (VV) is an oncolytic virus that is currently being evaluated as a promising cancer vaccine in several phase I, II and III clinical trials. Although several quality control tests are performed on each new batch of virus, these do not routinely include a systematic characterization of virus particle homogeneity, or relate the infectious titer to the total number of submicron sized particles (SSPs) present in the sample. SSPs are comprised of infectious virus and non-infectious viral particles, but also cell contaminants derived from the virus isolation procedures, such as cellular vesicles and debris. Here we have employed flow virometry (FV) analysis and sorting to isolate and characterize distinct SSP populations in therapeutic oncolytic VV preparations. We show that VV preparations contain SSPs heterogeneous in size and include large numbers of non-infectious VV particles. Furthermore, we used FV to illustrate how VV has a propensity to aggregate over time and under various handling and storage procedures. Accordingly, we find that together the infectious titer, the total number of SSPs, the number of viral genomes and the level of particle aggregation in a sample constitute useful parameters that greatly facilitate inter-sample assessment of physical quality, and also provides a means to monitor sample deterioration over time. Additionally, we have successfully employed FV sorting to further isolate virus from other particles by identifying a lipophilic dye that preferentially stains VV over other SSPs in the sample. Overall, we demonstrate that FV is a fast and effective tool that can be used to perform quality, and consistency control assessments of oncolytic VV vaccine preparations.

1. Introduction

Viruses are best known as harmful pathogens that cause disease. However, some viruses are uniquely capable of promoting anti-tumor activity and cancer remission, these are called oncolytic viruses (OVs). Cancer cells commonly display defects in interferon signaling which is a critical mechanism for antiviral defense. OVs exploit this deficiency to infect and destroy cancer cells specifically [1,2]. Vaccinia virus (VV) is an enveloped double-stranded DNA virus of the poxviridae family that is best known as the active ingredient in the smallpox vaccine used for global eradication of the disease. The potential of VV as an OV was revealed by showing that it displayed a natural tropism for a broad range of tumors when injected in experimental animals [3–7]. Further engineering of VV to increase safety and tumor-specificity was achieved by removing its genes coding for thymidine kinase (TK, J2R) and Vaccinia growth factor (VGF, C11R). The resulting double-deleted VV (VVDD) is unable to replicate in healthy cells or induce the proliferation of nearby cells [4]. Replication of VV in cancer cells leads to tumor regression, tumor antigen exposure, and stimulation of host anti-tumor immunity, thereby positioning it as a promising anti-cancer biotherapeutic agent [2,8,9]. The US Food and Drug Administration has recently approved the first OV treatment for melanoma, with an increasing number of OVs in clinical development [10,11].

In contrast to some viruses that are released from infected cells in large quantities, the infectious pool of VV particles exists primarily as intracellular mature virions (IMVs), also sometimes referred to as mature virions (MVs) [12,13]. However, small amounts of VV particles also bud from infected cells as cell-associated enveloped viruses (CEV) and extracellular enveloped

* Corresponding author at: Department of Biochemistry, Microbiology and Immunology, Faculty of Medicine, University of Ottawa, 451 Smyth Road, Ottawa, Ontario K1H 8M5, Canada.
E-mail address: langlois@uottawa.ca (M.-A. Langlois).

http://dx.doi.org/10.1016/j.vaccine.2016.08.074
0264-410X/

viruses (EEVs) [14,15]. To prepare VV stocks, IMVs are harvested by lysing infected cells and then purifying the virus by density gradient centrifugation or tangential flow filtration [16,17]. Lysis of infected cells releases large amounts of cellular debris and molecules that may bind and co-purify with the virus if not properly eliminated. Additionally, it has long been established that VV self-aggregates, thereby altering the biophysical properties of the virus during the purification process [18,19]. As such, a reliable, accurate and rapid method to assess OV sample purity and integrity would be of significant value, especially for clinical and therapeutic applications.

Use of a flow cytometer to analyse individual viral particles is called *flow virometry* (FV) [20]. The ability to perform single-particle analysis on cell-derived vesicles and viruses smaller than 300 nm is relatively new and only possible on customized instruments equipped with more powerful lasers, improved optics and photomultiplier tubes (PMTs) optimized for small particles. The advantages of FV over other submicron-sized particle (SSP) analysis technologies are the abilities to estimate the size of virion by light scatter, to visualize the different particle subpopulations, and perform multi-parameter profiling analyses of surface antigens. Additionally, FV can be used to isolate and sort virus subpopulations [21,22]. As such, FV can be employed to characterize a virus preparation, especially for sensitive applications such as vaccine development [23].

Here we demonstrate FV as an effective method to quantify and characterize SSPs and inter-sample variability of VV stocks used in OV vaccine preparations. By sorting the various subpopulations of particles in a sample, we were able to measure the ratio of particles to viral genomes and correlate this with the infectious titer. Additionally, we show that virus aggregation can be used as a physical indicator of sample deterioration. Finally, we identified a lipophilic dye that preferentially stains the infectious pool of VV that could prove to be a useful tool in the future for carrying out a detailed characterization of VV surface antigens by FV.

2. Material and methods

2.1. Calibration beads

The following beads were used as per manufacturer's instruction: Fluoresbrite Plain YG, Silica Microspheres (Polysciences), Calibration Bead Mix (Apogee), Latex/polystyrene beads (Sigma-Aldrich), SPHERO™ Fluorescent Yellow Particles, and Nano Fluorescent Yellow Particles (Spherotech). 123count eBeads were used as per manufacturer's instruction to determine particle count in virus samples (eBiosciences).

2.2. Viruses: strains, production and purification

VVDD-eGFP, derived from Vaccinia virus VSC20 [4,5], is the parent strain of VVDD-mCherry (named VVDD for simplicity) used throughout this study. We created VVDD-mCherry by homologous recombination by transfecting VVDD-eGFP infected cells with a plasmid expressing mCherry cloned within the VV TK gene. IMVs were isolated and mCherry-expressing plaques were selected on U2OS cells. Additional details about VVDD-eGFP and how the viruses were cloned are published in the following references [1,24–27]. To produce stocks of the VVDD-eGFP, VVDD-mCherry and B5R-eGFP stains, HeLa cells were grown in 15 cm dishes and infected at a multiplicity of infection of 0.01. Infected cells were pelleted by centrifugation at 2000 rpm for 10mins and resuspended in Tris 1 mM, pH 8.0. Cell pellets underwent three freeze-thaw cycles (−80 °C/37 °C) before cell debris were pelleted. Supernatants containing virions were then purified by centrifugation on a 36% sucrose cushion (11,500 rpm, JS-13.1 Swinging Bucket Rotor, 80 min., 4 °C) [28]. Concentrated VV was then resuspended in Tris buffer (1 mM, pH 8.0), aliquoted and stored at −80 °C. For Modified Vaccinia Ankara (MVA) stocks, BHK21 cells were used instead of HeLa. Clinical grade JX594 was purified by tangential flow filtration. After extensive buffer exchange, purified virus was resuspended in Tris 1 mM, pH 8.0.

2.3. Virus titration

Purified VV stocks were serially diluted in serum-free DMEM and 500 μl of each dilution was plated onto a monolayer of U2OS cells, established by seeding 10^6 cells/well in a 6-well plate the day before initiating the plaque assay. After 2 h of incubation at 37 °C, 5% CO_2, the plates were overlaid with a semi-solid 1:1 ratio of carboxymethylcellulose 3% and DMEM 2× supplemented with 20% FBS. Plates were then incubated for an additional 48 h, fixed with 80% methanol, stained with 0.1% Crystal violet and plaques counted.

2.4. FV analysis and sorting

Analysis and sorting were performed on a MoFlo® Astrios™ EQ (Beckman) equipped with 405 nm (55 mW), 488 nm (200 mW), 532 nm (150 mW), 561 nm (200 mW), 592 nm (200 mW), and 640 nm (100 mW) lasers. A 100 μm nozzle was used for both analysis and sorting at a sheath pressure of 27 psi, with a sample differential pressure of 0.3 psi. We triggered off of FSC with a threshold of 0.006%, which routinely gives <50eps with no sample being run. Data were analyzed using FlowJo data analysis software.

All virus stocks were diluted to 10^6 PFU/ml with 0.1 μm-filtered PBS (Gibco) prior to analysis unless otherwise indicated. Where filtration was required, unless otherwise indicated, stocks were diluted to 10^7 PFU/ml prior to filtration using 0.45 μm, 0.22 μm (Millipore), or 0.1 μm (Pall) syringe filters. All virus samples labeled with dye were stained for 20 min at 4 °C and analyzed immediately post-labeling. DiO/DiD labeling solutions from Vybrant®Multicolor Cell Labeling Kit were used at 5 μl/mL of virus sample. Virus was labeled with 1 μl/ml of CellTraceViolet Cell Proliferation dye. FM4-64FX fixable lipophilic styryl dye was used at a concentration of 5 μg/ml (ThermoFisher). VV was passed through a 0.45 μm filter and labeled with rabbit polyclonal anti-VV-FITC (Abcam, #ab19970) and a polyclonal isotype control with no known specificity (Abcam, #ab37406). VV was incubated with antibodies for 18 h at 4 °C for all indicated dilutions.

2.5. Vaccinia genome extractions and quantification

Viral genomes were extracted using QIAamp UltraSens Virus Kit (Qiagen) according to manufacturer's methods and used as the template for droplet digital PCR (ddPCR) quantification. The 20 μL reaction mix consisted of 5 μL of purified viral DNA, EvaGreen ddPCR MasterMix (BioRad) and a final concentration of 200 nM of the primer set targeting the DNA polymerase gene (E9L) (Forward: 5′-GAACATTTTTGGCAGAGAGAGCC-3′, Reverse: 5′-CAACTCTTAGCCGAAGCGTATGAG-3′). The ddPCR reaction was carried out using a QX200 ddPCR System (BioRad) and following a previously described protocol [29]. The absolute viral genome copy number in each reaction was related back to the input DNA volume.

3. Results

3.1. SSP characterization

To evaluate the ability of our flow cytometer to characterize VV particles, we first needed to set our acquisition gates. The lower limit was positioned immediately above that of instrument noise (Fig. 1A), and below the debris in 0.1 μm-filtered PBS (Fig. 1B). As a mock control, we purified SSPs released from uninfected cells in the same way as if they were infected with VV. Mock samples were passed through a 0.45 μm filter (Fig. 1C), or left unfiltered (Fig. 1D) and then analyzed. We detected a large number of particles derived from the cell lysis procedure required to release IMVs, despite sample purification. Filtration of the samples did little to reduce the number of particles, indicating that the majority are smaller than 450 nm. We then set the lower acquisition gate to encompass the filtered mock particles and the upper gate to encompass the rest of the acquisition spectrum.

VV-containing samples were passed through 0.22 μm (Fig. 1E) and 0.45 μm (Fig. 1F) filters and analyzed. A VV particle has an expected overall dimension between 250 nm and 360 nm [30,31]. Therefore, VV particles are retained by the 0.22 μm filter, leaving but the smallest SSPs in the sample to pass through (Fig. 1E). We also confirmed that these particles did not form plaques (Suppl. Fig. 1). Passing the sample through a 0.45 μm filter yielded a population of particles assumed to be singlet virions and cell-derived SSPs (Fig. 1F). The unfiltered stock of this same VV preparation contained particles of a broader range of sizes, spanning most of the dynamic range of the FSC detector (Fig. 1G). To demonstrate that larger SSPs are in fact aggregates, we attempted to dissociate them by sonication and by enzymatic subtilisin digestion. Sonication was modestly successful at reducing aggregates (Suppl. Fig. 2A–D), resulting in a 1.8-fold increase in the infectious titer (Suppl. Fig. 2H). Subtilisin treatment almost completely dissolved the aggregates by digesting proteins expressed on the surface of the viral envelope (Suppl. Fig. 2E–G) [32], but was also detrimental to viral infectivity (Suppl. Fig. 2I). These data confirm that singlet viruses are detected in our lower gate and aggregated virus appears in our upper gate.

3.2. Estimation of VV size by FV

Light scatter, as measured by FSC or SSC, provides a relative indication of size compared to a known standard, which is inferred from the amount of light collected at a specific angle of detection. The refractive index of a given particle strongly influences the way light is scattered and is determined for the most part by its material composition. Here we used commercial size calibration beads to estimate the size of particles as measured by FSC. Beads in the submicron size range were selected from four manufacturers. The fluorescence intensities of the beads were measured and plotted against FSC (Fig. 2A). Silica and polystyrene have different refractive indices (Fig. 2B), it is therefore not surprising that beads of similar physical size made from these different materials exhibit different FSC values (Fig. 2C).

The reported physical size of wild type VV is $250 \times 270 \times 360$ nm, as measured by cryo-electron tomography (Fig. 2D) [30,31]. FV analysis of VVDD virions passed through a 0.45 μm filter revealed three populations of defined sizes by FSC (Fig. 2E). We estimate that the sizes of populations 2 and 3 are respectively 204 nm and 268 nm using silica beads, and 214 and 262 nm using polystyrene beads (Fig. 2E). These populations possibly represent two of the planar dimensions of the virus passing through the flow cell of the cytometer. We were unable to accurately estimate the apparent size of population 1 because of the lack of an appropriate standard in that size range. The underestimation of the size of the virus is likely due to the differences in refractive indices between synthetic beads (1.59 polystyrene, 1.43 silica) and virus (1.36) [33]. To gain further insight into the makeup of these three SSP populations, we sorted them followed

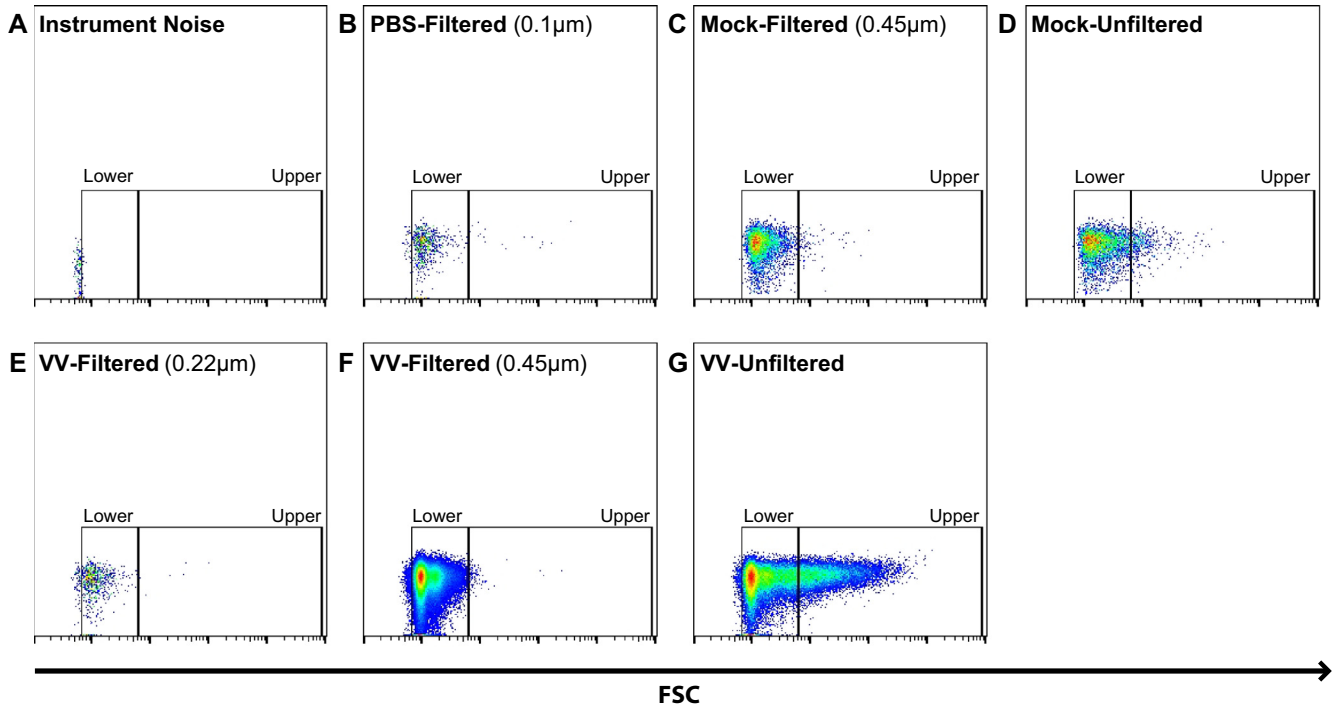

Fig. 1. Gating strategy for flow virometry analysis of VV. (A) Instrument noise; delineates the lower limit of the lower gate. (B) Filtered PBS (0.10 μm). (C) Mock control, filtered (0.45 μm); delineates the upper limit of the lower gate. (D) Mock control, unfiltered. (E) VV, filtered (0.22 μm). (F) VV, filtered (0.45 μm). (G) VV, unfiltered. Sample run time was the same for all samples analyzed.

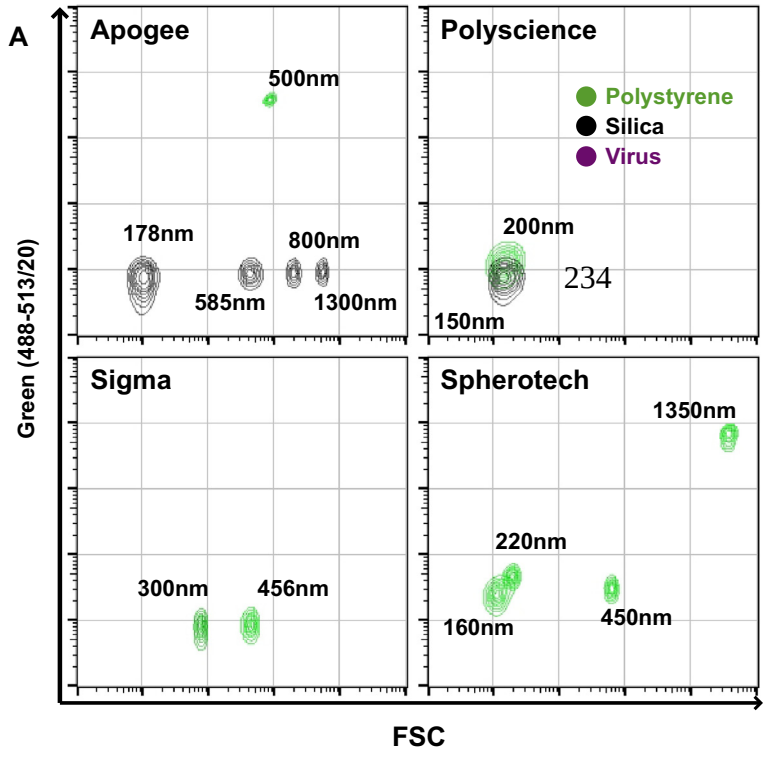

B

Refractive Index	
Vaccinia Virus	1.36
Whole Cells	1.38
Cell Membrane & Organelles	1.43-1.51
Beads: Polystyrene	1.59
Silica	1.43

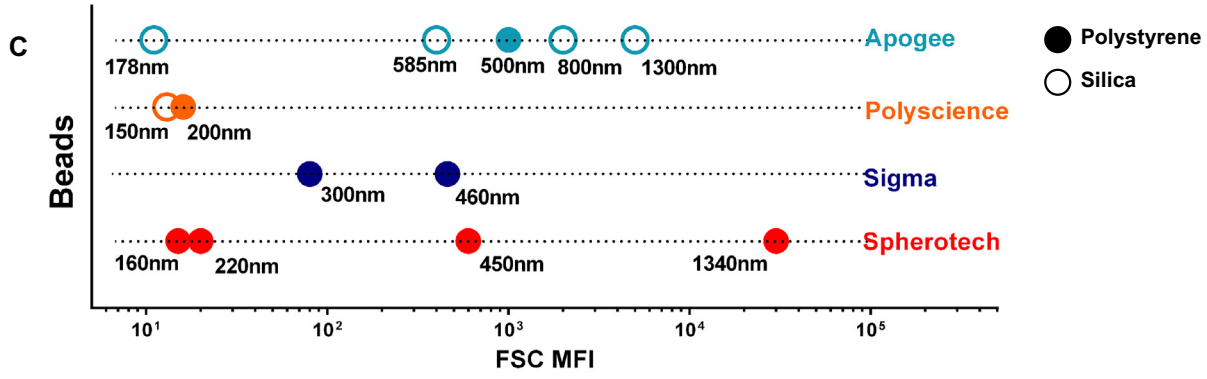

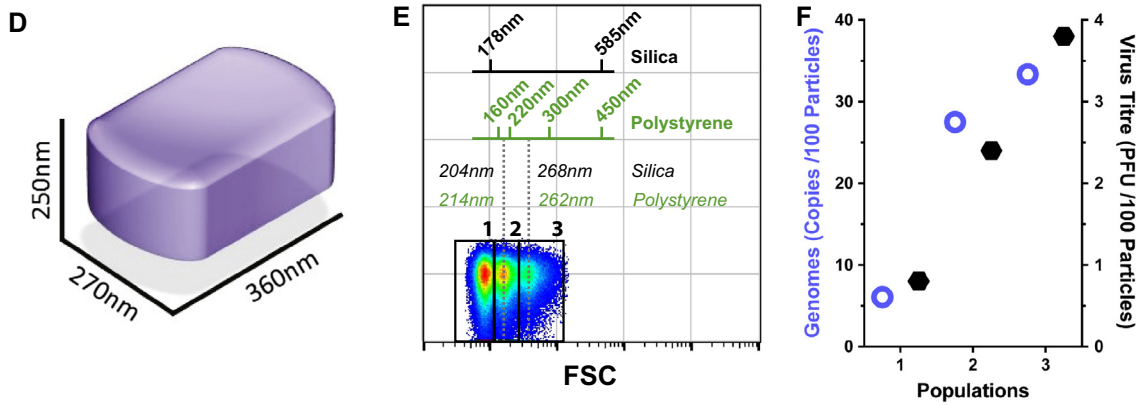

Fig. 2. Filtered VV appears as distinct populations by flow virometry. (A) Apparent size distribution of commercial fluorescent beads displayed as fluorescence intensity as a function of Forward Scatter (FSC). (B) Refractive indices of VV, whole cells, cellular components, polystyrene and silica beads. (C) Relative FSC mean fluorescence intensity (MFI) in respect to bead manufacturer, reported size, and composition. (D) Graphical representation of the dimensions of a VV capsid. (E) Size estimate of VV using polystyrene and silica beads. Linear regression was used to calculate VV size values for both types of beads. (F) The three dominant SSP populations of panel E were sorted by flow virometry and analyzed. Open blue circles: vgDNA copies in each sorted population was evaluated by ddPCR; black hexagons: the viral titer was measured by plaque assay. (For interpretation of the references to color in this figure legend, the reader is referred to the web version of this article.)

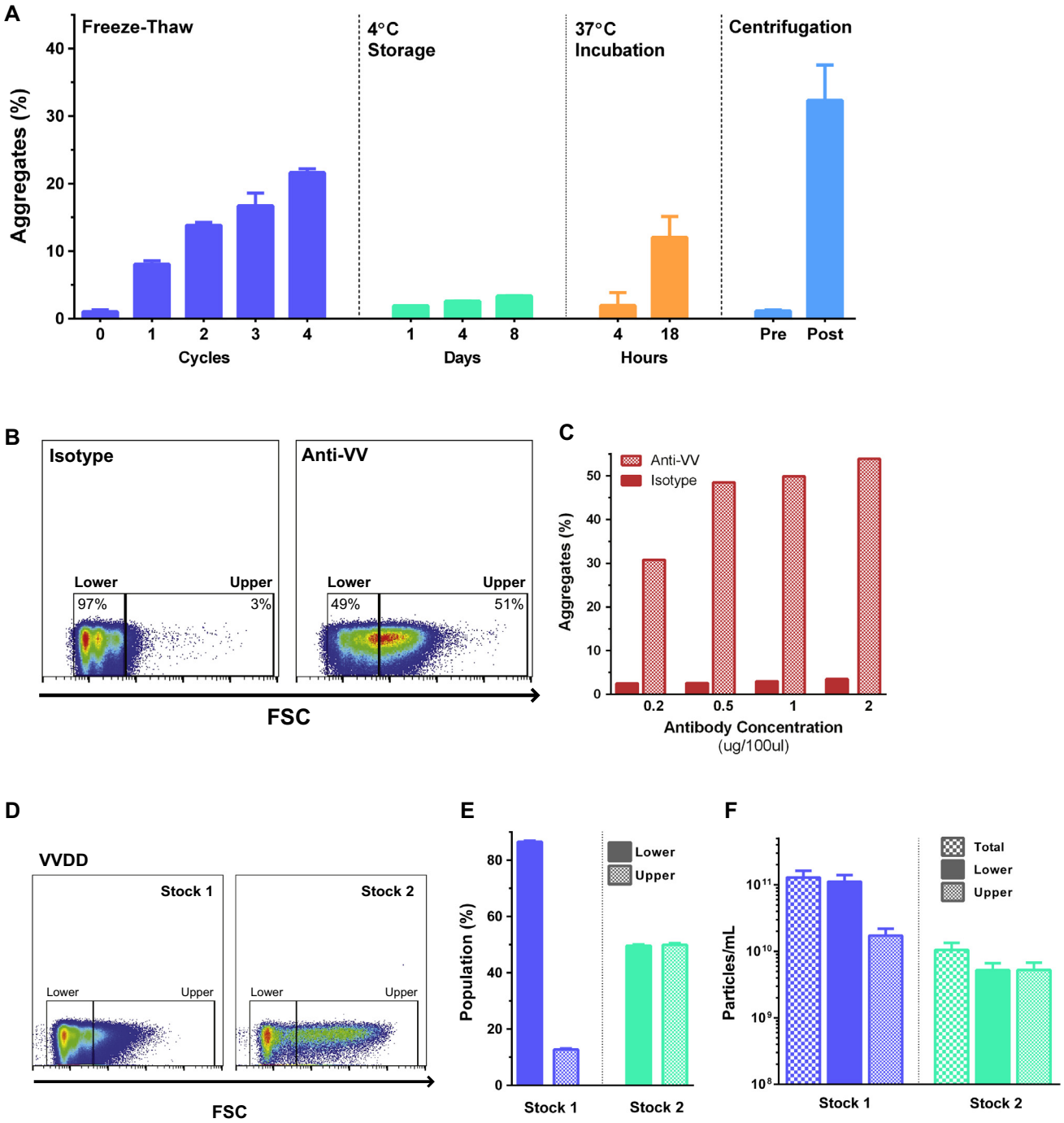

Fig. 3. Conditions promoting VV aggregation. (A) A filtered VVDD stock was subjected to: up to 4 cycles of freeze-thaw (−80 °C/37 °C); stored at 4 °C and sampled over 8 days; incubated at 37 °C and sampled over 18 h; centrifuged at 26,000g for 90 min. (B) A representative FSC scatterplot displays the degree of aggregation post anti-VV and isotype labeling of 0.45 μm-filtered VVDD (left: 0.5 μg/100 μl of isotype control antibody; right: 0.5 μg/100 μl anti-VV). (C) Aggregation as a function of the antibody concentration used for staining (isotype control and anti-VV antibodies). (D) Two unfiltered VVDD stock preparations were compared using FSC to evaluate the degree of particle aggregation. (E) Analysis of the proportion of SSPs in the upper and lower gates. (F) Concentration of SSPs in the lower and upper gates for the two different VVDD stock preparations.

by ddPCR amplification of the VVDD viral genomic DNA (vgDNA). Our results revealed that all three SSP populations contained viral genomes, with the two larger populations containing the highest ratio of vgDNA-to-particles (Fig. 2F). The abundance of infectious viral particles was approximately 10-fold lower than that of the genomes, indicating a large percentage of defective viruses (Fig. 2F).

3.3. Experimental conditions that influence VV aggregation

We next sought to determine whether VV aggregation is influenced by various experimental procedures. A stock of VVDD was passed through a 0.45 μm filter to generate singlet particles, then submitted to conditions presented in Fig. 3A. All conditions tested induced the formation of aggregates to varying degrees, with

Table 1
Characterization of various VV stock preparations by flow virometry.

Stock VV strain	Viral titer (PFU/mL)	Total particles (particles/mL)	Infectious particles (%)	Singlets (%)
VVDD stock 1[a]	3.3E+09	1.3E+11	3	87
VVDD stock 2[a]	2.5E+09	1.1E+10	24	50
B5R-eGFP	2.7E+09	2.6E+10	11	90
JX594	2.0E+09	2.6E+10	8	75
MVA	1.2E+09	1.7E+10	7	84
VVDD-eGFP	4.9E+08	1.1E+10	4	88

[a] VVDD-mCherry.

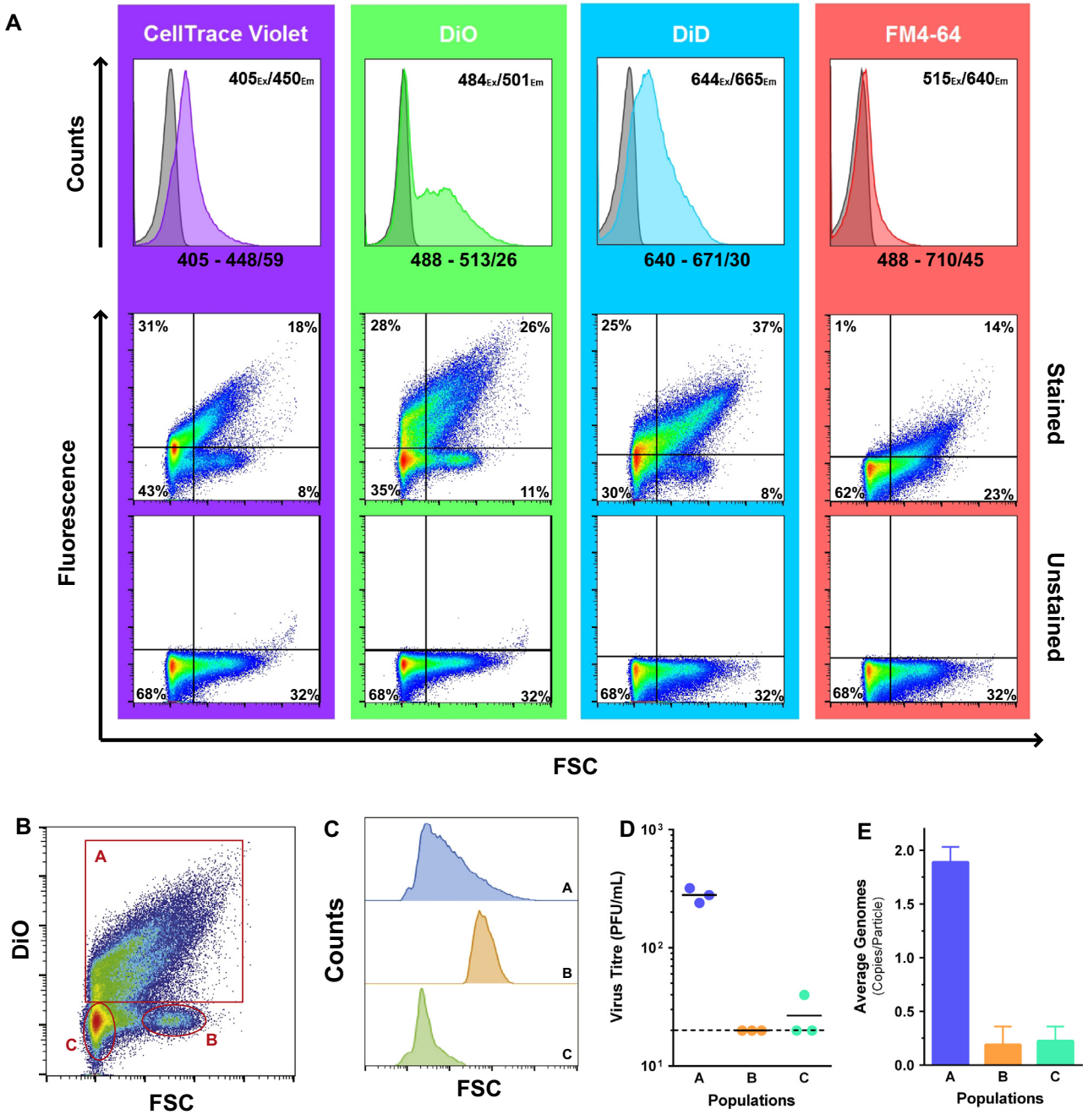

Fig. 4. Labeling and sorting of VV using membrane dyes. (A) *Top row*, histogram overlays of labeled (gray) vs. unlabeled (color) virus. The optimal excitation and emission wavelengths of the dyes are indicated on the histogram plot. The laser and filters used for detection are indicated below the plots. *Middle row*, scatter plots of stained VV displayed as fluorescence intensity as a function of FSC. *Bottom row*, unstained VVDD using the optimal laser and filter for each dye. (B) Scatter plot of DiO-stained VVDD shows three distinctly labeled particle populations: A: (DiO+), B: (DiO-FSC^{high}) and C: (DiO-FSC^{low}). (C) Histogram plots comparing FSC of populations A, B, and C. (D) Virus titer determined by plaque assay for each of the three sorted particle populations. (E) VVDD genome copies per particle in each of the sorted particle populations, n = 3. For interpretation of the references to color in this figure legend, the reader is referred to the web version of this article.)

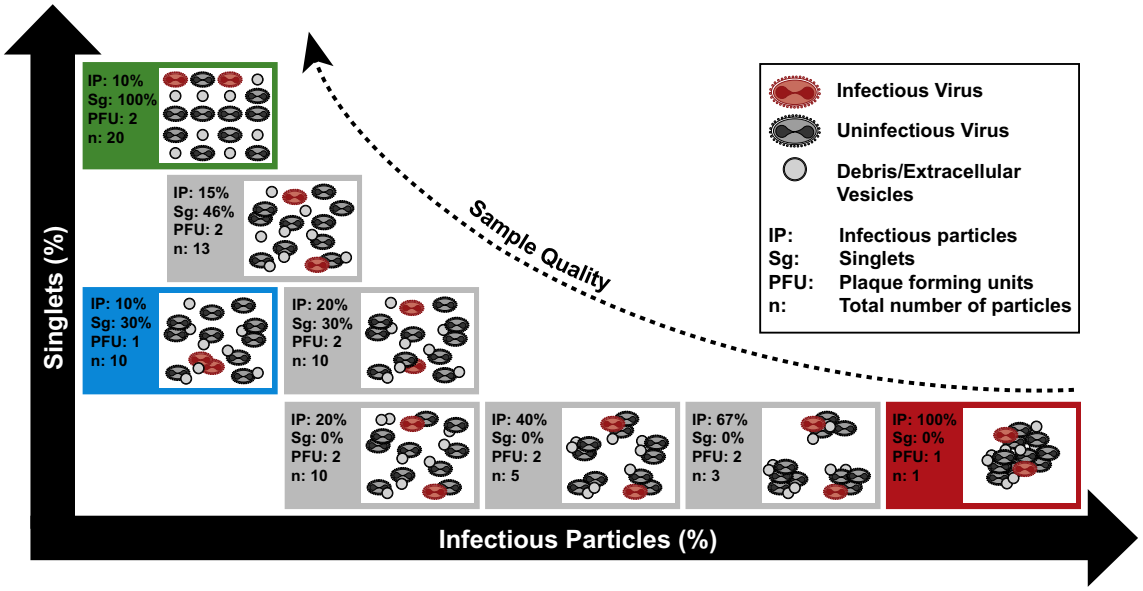

Fig. 5. Assessing virus sample quality by flow virometry. Graphical simulation of the relationship between infectious particles (IP), singlets (Sg), plaque forming units (PFU) and the number of total particles in a sample (n). The green box indicates a high quality sample with low particle aggregation, and the red box indicates a poor sample with high aggregation and a low infectious titer. The blue box represents a possible, but statistically disfavoured aggregation event where all infectious particles aggregate to form a single particle. For interpretation of the references to color in this figure legend, the reader is referred to the web version of this article.)

storage at 4 °C having the smallest impact on aggregation. Interestingly, centrifugation at 26,000*g* for 90 min had the most pronounced effect, whereby over 30% of SSPs became aggregated.

Staining of VVDD using a polyclonal antibody also induced aggregation, but to a greater extent. Over 50% of SSPs analyzed appeared as aggregates when treated with an antibody at a concentration of 0.5 μg/100 μl (Fig. 3B). Higher amounts of antibody did not increase aggregate formation, indicating viral epitope saturation by the antibody (Fig. 3B and C).

3.4. Assessment of viral stock consistency

Here we asked whether aggregate composition and the total number of SSPs in different VV stock preparations were consistent. We randomly selected two VVDD stocks prepared on different dates for analysis (Fig. 3D). Aggregates accounted for 13% of total SSPs in Stock 1 and about 50% in Stock 2 (Fig. 3E), while the total particle count was 1.3×10^{11} particles/mL for Stock 1 and 1.1×10^{10} particles/mL for Stock 2 (Fig. 3F and Table 1). Investigation of the physical characteristics of other VV strains in our collection by FV followed a similar trend where the infectious titer of the stocks were similar, but demonstrated a large variability in the percentage of infectious particles and particle aggregation (Table 1). Differences in sample characteristics may be of significant importance for vaccine preparations as total SSPs and aggregation intensity could influence immunogenicity, infectivity and oncolytic efficacy of the viruses in patients.

3.5. Enhancing VV detection using lipid dyes

We next sought alternative methods of labeling VV that do not induce aggregation. We tested three cell permeable fluorescent lipid dyes (DiO, DiD and FM4-64) and one amine dye (CellTrace Violet). Fig. 4A depicts histogram overlays of labeled (coloured) and unlabeled (gray) VVDD Stock 2 using various dyes (*top row*), scatter plot of labeled virus presented as fluorescence vs. FSC (*middle row*), and unlabeled virus analyzed by FSC with the relevant filters (*bottom row*). SSP labeling was achieved with all dyes, however DiO was the only dye that selectively labeled a specific population of the sample and created a bimodal distribution. This resulted in three distinct particle populations when displayed against FSC: DiO+ (54%), DiO-FSC^{low} (35%), DiO-FSC^{high} (11%) (Fig. 4B). Importantly, DiO staining did not induce further aggregation of the sample compared to the unstained control as judged by the total events in the upper gates (Fig. 4A, *bottom row*).

VVDD stained with DiO was then sorted into three populations labeled as A: DiO+, B: DiO-FSC^{high} and C: DiO-FSC^{low} (Fig. 4B). A comparison of populations A, B, and C using FSC shows that particles in population A have a broad size distribution, while particles in B and C are more homogeneous (Fig. 4C). The sorted SSP populations were next analyzed for infectivity and vgDNA content. Almost all of the infectious particles localized in population A (Fig. 4D), as well as the bulk of the vgDNA (Fig. 4E).

4. Conclusion

Virus aggregation and cell-derived contaminants such as vesicles and debris are recurrent concerns when preparing stocks of VV for therapeutic use, primarily because of the risk of adverse immunological effects in the recipient. Additionally, there is a need for a rapid and simple test to monitor the integrity of VV stocks overtime, and control inter-sample variations when preparing new batches of the virus. Here we have provided experimental evidence that FV is an effective method to measure the abundance and heterogeneity of SSPs in a VV sample. Furthermore, we have demonstrated that it is possible to sort VV in a sample, which allows for further downstream analyses such as the quantification of vgDNA. These measurable characteristics of a VV sample, together with the infectious titer, can provide information to assess the physical quality of VV particles in a sample.

In Fig. 5, we modelled the relationship between the percentage of infectious particles (IP) in a sample in relation to total SSPs (n), the infectious titer (PFU), and the percentage of singlet particles measured in the lower gate (Sg). If we postulate that aggregates form randomly, then infectious virus will bind equally to virus and other particles. As the particles in a sample aggregate, the percentage of IP increases but the infectious titer drops, as all the

infectious particles aggregate together to create one large infectious unit (Fig. 5, Red box).

One of the challenges in FV is locating the particle population of interest. Fluorescent beads are often used as size markers. The caveat to this approach is that commercial silica or polystyrene beads have different light refraction properties than biological materials. In the case of the VV, the beads lead to an underestimation of the published size of the virus (Fig. 2). These observations are consistent with other studies that attempted to measure the size of viruses and SSPs using flow cytometry [21,23,34]. Development of size standards that more closely mimic the refractive indices of biological material could prove to be highly useful for the analysis of small particles by flow cytometers.

An alternative way of locating VV in a cluster of SSPs is by selectively staining the virus with fluorescent antibodies. However, staining of VV poses a special challenge as anti-VV antibodies cause the virus to aggregate (Fig. 3B and C). To overcome this problem, we tested a number of fluorescent dyes and determined that DiO can preferentially stain VV particles (Fig. 4). However, because DiO is a lipid dye, it will likely also stain extracellular vesicles, as well as other types of particles with a high lipid content.

In conclusion, here we have showcased the utility of FV as an effective method to sort and evaluate the physical properties of VV sample preparations. FV stands out as a potentially valuable tool for carrying out routine quality control assessments for a broad range of OVs used in therapeutic applications.

Acknowledgements

M.-A.L. holds a Canada Research Chair in Molecular Virology and Intrinsic Immunity. This work was supported by a research and development Grant from the University of Ottawa Faculty of Medicine to the FCV Core Facility and to M.-A.L. JB and JSD are supported by the Terry Fox Research Institute, and the Canadian Cancer Society. JB is also supported by the Ontario Institute for Cancer Research (Ontario Regional BioTherapeutics Program - ORBiT). The B5R-eGFP VV strain was kindly provided by Bernard Moss and Brian Ward (NIAID, NIH).

Appendix A. Supplementary material

Supplementary data associated with this article can be found, in the online version, at http://dx.doi.org/10.1016/j.vaccine.2016.08.074.

References

[1] Parato KA, Breitbach CJ, Le Boeuf F, Wang J, Storbeck C, Ilkow C, et al. The oncolytic poxvirus JX-594 selectively replicates in and destroys cancer cells driven by genetic pathways commonly activated in cancers. Mol Therapy: J Am Soc Gene Therapy 2012;20:749–58.
[2] Ilkow CS, Swift SL, Bell JC, Diallo JS. From scourge to cure: tumour-selective viral pathogenesis as a new strategy against cancer. PLoS Pathog 2014;10:e1003836.
[3] Diallo JS, Le Boeuf F, Lai F, Cox J, Vaha-Koskela M, Abdelbary H, et al. A high-throughput pharmacoviral approach identifies novel oncolytic virus sensitizers. Mol Therapy: J Am Soc Gene Therapy 2010;18:1123–9.
[4] McCart JA, Ward JM, Lee J, Hu Y, Alexander HR, Libutti SK, et al. Systemic cancer therapy with a tumor-selective vaccinia virus mutant lacking thymidine kinase and vaccinia growth factor genes. Cancer Res 2001;61:8751–7.
[5] Le Boeuf F, Diallo JS, McCart JA, Thorne S, Falls T, Stanford M, et al. Synergistic interaction between oncolytic viruses augments tumor killing. Mol Therapy: J Am Soc Gene Therapy 2010;18:888–95.
[6] Breitbach CJ, Burke J, Jonker D, Stephenson J, Haas AR, Chow LQ, et al. Intravenous delivery of a multi-mechanistic cancer-targeted oncolytic poxvirus in humans. Nature 2011;477:99–102.
[7] Breitbach CJ, Arulanandam R, De Silva N, Thorne SH, Patt R, Daneshmand M, et al. Oncolytic vaccinia virus disrupts tumor-associated vasculature in humans. Cancer Res 2013;73:1265–75.
[8] Lichty BD, Breitbach CJ, Stojdl DF, Bell JC. Going viral with cancer immunotherapy. Nat Rev Cancer 2014;14:559–67.
[9] Kim MK, Breitbach CJ, Moon A, Heo J, Lee YK, Cho M, et al. Oncolytic and immunotherapeutic vaccinia induces antibody-mediated complement-dependent cancer cell lysis in humans. Sci Transl Med 2013;5. 185ra63.
[10] Kaufman HL, Kohlhapp FJ, Zloza A. Oncolytic viruses: a new class of immunotherapy drugs. Nat Rev Drug Discovery 2015;14:642–62.
[11] Kim M. Replicating poxviruses for human cancer therapy. J Microbiol 2015;53:209–18.
[12] Hollinshead M, Vanderplasschen A, Smith GL, Vaux DJ. Vaccinia virus intracellular mature virions contain only one lipid membrane. J Virol 1999;73:1503–17.
[13] Smith GL, Vanderplasschen A, Law M. The formation and function of extracellular enveloped vaccinia virus. J Gen Virol 2002;83:2915–31.
[14] Blasco R, Moss B. Role of cell-associated enveloped vaccinia virus in cell-to-cell spread. J Virol 1992;66:4170–9.
[15] Appleyard G, Hapel AJ, Boulter EA. An antigenic difference between intracellular and extracellular rabbitpox virus. J Gen Virol 1971;13:9–17.
[16] Earl PL, Cooper N, Wyatt LS, Moss B, Carroll MW. Preparation of cell cultures and vaccinia virus stocks. Ausubel Frederick M et al., editors. Current protocols in molecular biology, Chapter 16, 2001. Unit16.
[17] Ungerechts G, Bossow S, Leuchs B, Holm PS, Rommelaere J, Coffey M, et al. Moving oncolytic viruses into the clinic: clinical-grade production, purification, and characterization of diverse oncolytic viruses. Mol Therapy Methods Clin Dev 2016;3:16018.
[18] Sharp DG, McGuire PM. Spectrum of physical properties among the virions of a whole population of vaccinia virus particles. J Virol 1970;5:275–81.
[19] Kim KS, Sharp DG. Electron microscopic observations on the nature of vaccinia virus particle aggregation. J Immunol 1966;97:197–202.
[20] Arakelyan A, Fitzgerald W, Margolis L, Grivel JC. Nanoparticle-based flow virometry for the analysis of individual virions. J Clin Investig 2013;123:3716–27.
[21] Gaudin R, Barteneva NS. Sorting of small infectious virus particles by flow virometry reveals distinct infectivity profiles. Nat Commun 2015;6:6022.
[22] Loret S, El Bilali N, Lippe R. Analysis of herpes simplex virus type I nuclear particles by flow cytometry. Cytomet Part A: J Int Soc Anal Cytol 2012;81:950–9.
[23] Vlasak J, Hoang VM, Christanti S, Peluso R, Li F, Culp TD. Use of flow cytometry for characterization of human cytomegalovirus vaccine particles. Vaccine 2016;34:2321–8.
[24] Carroll MW, Moss B. Host range and cytopathogenicity of the highly attenuated MVA strain of vaccinia virus: propagation and generation of recombinant viruses in a nonhuman mammalian cell line. Virology 1997;238:198–211.
[25] Roy DG, Power AT, Bourgeois-Daigneault MC, Falls T, Ferreira L, Stern A, et al. Programmable insect cell carriers for systemic delivery of integrated cancer biotherapy. J Controll Release: Off J Controll Release Soc 2015;220:210–21.
[26] Zeh HJ, Downs-Canner S, McCart JA, Guo ZS, Rao UN, Ramalingam L, et al. First-in-man study of Western Reserve strain oncolytic vaccinia virus: safety, systemic spread, and antitumor activity. Mol Therapy: J Am Soc Gene Therapy 2015;23:202–14.
[27] Heo J, Reid T, Ruo L, Breitbach CJ, Rose S, Bloomston M, et al. Randomized dose-finding clinical trial of oncolytic immunotherapeutic vaccinia JX-594 in liver cancer. Nat Med 2013;19:329–36.
[28] Vanderplasschen A, Mathew E, Hollinshead M, Sim RB, Smith GL. Extracellular enveloped vaccinia virus is resistant to complement because of incorporation of host complement control proteins into its envelope. Proc Natl Acad Sci USA 1998;95:7544–9.
[29] Albano F, Zagaria A, Anelli L, Coccaro N, Tota G, Brunetti C, et al. Absolute quantification of the pretreatment PML-RARA transcript defines the relapse risk in acute promyelocytic leukemia. Oncotarget 2015;6:13269–77.
[30] Condit RC, Moussatche N, Traktman P. In a nutshell: structure and assembly of the vaccinia virion. Adv Virus Res 2006;66:31–124.
[31] Cyrklaff M, Risco C, Fernandez JJ, Jimenez MV, Esteban M, Baumeister W, et al. Cryo-electron tomography of vaccinia virus. Proc Natl Acad Sci USA 2005;102:2772–7.
[32] Ott DE. Purification of HIV-1 virions by subtilisin digestion or CD45 immunoaffinity depletion for biochemical studies. Methods Mol Biol 2009;485:15–25.
[33] Katz E, Wolffe E, Moss B. Identification of second-site mutations that enhance release and spread of vaccinia virus. J Virol 2002;76:11637–44.
[34] van der Pol E, Coumans FA, Grootemaat AE, Gardiner C, Sargent IL, Harrison P, et al. Particle size distribution of exosomes and microvesicles determined by transmission electron microscopy, flow cytometry, nanoparticle tracking analysis, and resistive pulse sensing. J Thromb Haemost: JTH 2014;12:1182–92.

Appendix 2

Preface: This chapter has been uploaded to the bioRxiv preprint server. Submitted for peer-review.

http://dx.doi.org/10.1101/614461

Vera A. Tang, Anna K. Fritzsche, **Tyler M. Renner**, Dylan Burger, Edwin van der Pol, Joanne A. Lannigan, George C. Brittain, Joshua A. Welsh, Jennifer C. Jones, and Marc-André Langlois

Engineered Retroviruses as Fluorescent Biological Reference Particles for Small Particle Flow Cytometry

Vera A. Tang[1,2,*], Anna K. Fritzsche[1,2], Tyler M. Renner[2], Dylan Burger[3], Edwin van der Pol[4,5,6], Joanne A. Lannigan[7], George C. Brittain[8], Joshua A. Welsh[9], Jennifer C. Jones[9], and Marc-André Langlois[1,2,10,*]

ABSTRACT

There has been renewed interest in the use of flow cytometry for single particle phenotypic analysis of particles in the nanometer size-range such as viruses, organelles, bacteria and extracellular vesicles (EVs). However, many of these particles are smaller than 200 nm in diameter, which places them at the limit of detection for many commercial flow cytometers. The use of reference particles of diameter, fluorescence, and light-scattering properties akin to those of the small biological particles being studied is therefore imperative for accurate and reproducible data acquisition and reporting across different instruments and analytical technologies. We show here that an engineered murine leukemia virus (MLV) can act as a fluorescence reference particle for other small particles such as retroviruses and EVs. More specifically, we show that engineered MLV is a highly monodisperse enveloped particle that can act as a surrogate to demonstrate the various effects of antibody labeling on the physical properties of small biological particles in a similar diameter range.

KEY TERMS: Small particle flow cytometry (FCM), nanoscale flow cytometry (NFC), retroviruses, biological reference particles, extracellular vesicles (EVs), exosomes.

Flow cytometry (FCM) analysis of viruses less than 500 nm in diameter has been reported since the late 70's (1-3). Much of this foundational work required customized cytometer configurations, including high powered lasers, large collection angles, and very low sampling rates. Advances in the technology of modern cytometers now allow for some conventional commercial instruments to detect biological particles down to the 100 nm diameter range with minor to no modifications to default instrument configurations (4-14). However, several key challenges remain for small particle FCM and these include: variations in instrument configurations and detection capabilities across platforms and facilities, widely differing sample processing and labeling methods, and a lack of consensus for data reporting (15).

One of the major factors impeding these efforts for standardization is the paucity of available reference particles with fluorescence intensities relevant to that of biological samples (16). Reference particles are important for daily quality control of instrument performance, as well as internal positive controls for

[1]University of Ottawa Flow Cytometry and Virometry Core Facility. [2]Department of Biochemistry, Microbiology and Immunology, Faculty of Medicine, University of Ottawa. [3]Department of Cellular and Molecular Medicine, Faculty of Medicine, University of Ottawa. [4]Vesicle Observation Center, [5]Biomedical Engineering & Physics, [6]Laboratory Experimental Clinical Chemistry, Amsterdam University Medical Centres, Netherlands. [7]University of Virginia Flow Cytometry Core Facility. [8]Life Science Research, Beckman Coulter Life Sciences, Miami, FL. [9]Translational Nanobiology Section, Laboratory of Pathology, Center for Cancer Research, National Cancer Institute, National Institutes of Health, Bethesda, USA, [10]uOttawa Center for Infection, Immunity and Inflammation (CI3). *Correspondence to be addressed to vtang@uottawa.ca and langlois@uottawa.ca. Request for materials to be addressed to langlois@uottawa.ca.

optimization of sample labeling protocols. Particles with low levels of fluorescence are needed to ensure optimal signal to noise resolution for dim signals. Biological reference particles have the advantage of possessing similar biochemical composition and antigen density levels, and can therefore act as suitable positive staining controls for antibody and dye labeling assays.

The development of calibration particles is also critical for the standardization of reference particle and sample data analysis and reporting in standard units. Although fluorescent reference particles in the form of polystyrene beads are commonly available, these are several microns in diameter and generally do not exhibit comparable fluorescence intensities (i.e., they are too bright) as EVs or even viruses. The calibration of fluorescence axes for small particle analysis using molecules of equivalent soluble fluorophore (MESF) units will require a set of populations that are smaller and dimmer than those currently available. Light scatter calibration using Mie modeling on the other hand requires homogeneous, well-characterized particles, with a variety of diameters and refractive indices (RIs) that are not necessarily the same as biological particles. Currently there are few sources of well-characterized light scatter reference materials for small particle FCM. Calibration particles and reference particles are therefore two distinct groups of materials that fulfill different roles with small particle standardization; the development of both, however, is required in the pursuit of standardized small particle FCM assays.

The murine leukemia virus (MLV) is symmetric and roughly spherical in shape, with a diameter of 124±14 nm as measured by electron cryo-microscopy (17). The specific strain used in this current study, Moloney MLV, is an ecotropic murine gammaretrovirus, meaning that it can only infect certain strains of susceptible mice(18). The viral envelope is primarily derived from the plasma membrane of infected cells, acquired during viral egress; a process that shares several common pathways with EV release into the extracellular medium (19,20). The precise and consistent stoichiometry involved in virion capsid assembly results in the release of particles that are monodisperse in structure. This is a critical and highly desirable feature, which distinguishes viruses from other biological reference particles. MLV naturally expresses on its surface host cell-derived markers, along with the viral envelope glycoprotein (Env). Env is expressed as a trimeric structure with a transmembrane domain (TM) and a surface (SU) antibody-accessible subunit (21,22). For most retroviruses, Env constitutes the only viral protein expressed on their surface. The number of Env trimeric structures, termed spikes, is a feature that has been characterized for several retroviral species. For example, while the human immunodeficiency virus type I (HIV-1) expresses approximately 14 - 21 spikes per particle, the simian immunodeficiency virus (SIV) was shown to have 73-98, the Rous sarcoma virus (RSV) ~82, and MLV ~100 (23-26).

For this study, we engineered a fluorescent MLV expressing superfolder GFP (sfGFP) as a fusion protein with Env (8,27). The fluorescence of Env-sfGFP was quantified using MESF beads (28,29). The unique features of viral homogeneity for both diameter and Env-sfGFP expression levels enabled the use of MLVsfGFP as a prototypic small vesicular particle to demonstrate quantification of fluorescence expression as a means to enumerate viral surface protein expression, as well as address pertinent questions regarding antibody labeling of small particles using Env-sfGFP as the target antigen. These include: 1) the relationship of fluorophore diameter and brightness to the resolution of small particle populations, 2) the impact of antibody labeling on diameter and RI, and 3) whether the use of multiple antibodies can impede optimal labeling and fluorescence intensities.

The use of this strain of MLV as a reference particle poses no biosafety concerns since they are ecotropic mouse viruses that are readily inactivated with formalin. They can also be lyophilized for stable storage and transport. The ability for them to be engineered to express surface epitopes of choice, fluorescent or otherwise, make these ideal controls for EV and virus immunophenotyping experiments. Based on these characteristics, we conclude that MLV particles exhibit essential features of a biological reference particle, and provide a much-

needed tool for daily quality control, positive controls for select protein markers, and a simple method for evaluating cytometer sensitivity.

MATERIALS AND METHODS

MLV production. Generation of chronically infected NIH 3T3 cells and the production and preparation of MLV samples for flow cytometry analyses were described previously (8). MLVsfGFP was engineered from a glycogag-deficient MLV using overlapping primers to insert the sfGFP sequence into the proline-rich region of Env using a restriction-free cloning strategy, hence allowing for its surface expression as a chimera with the viral protein (27). Viruses were harvested from the supernatant of chronically infected NIH 3T3 mouse fibroblasts and directly analyzed by FCM. Briefly, for virus production, 2.5 x 10^6 chronically infected cells were seeded into a 10-cm dish and cultured for 12 hrs. Cells were then washed to remove the serum-containing media and further cultured for 72 hrs in 10ml of phenol red-free DMEM (WISENT Inc.) supplemented with 10% (*v/v*) EV-depleted fetal bovine serum. The cell supernatant was collected and passed through a 0.45 µm filter. The supernatant was then diluted with 0.1 µm-filtered PBS (WISENT Inc.) as required for analysis.

Quantification of MLV particle concentration and coincidence detection. Viruses are produced at a constant rate by chronically infected cell lines. The concentration of virus in the supernatant from infected cells correlates directly with the number of infected cells seeded (Suppl. Fig. 1A). Particle concentration of viruses was determined based on virus-gated events using 1:1000 dilution, which usually yields a concentration of particles ~1-5x10^6 particles/ml as determined by the Beckman Coulter CytoFLEX S with a sampling rate of 10µl/min. Volumetric counts obtained from the CytoFLEX were validated by NTA (Suppl. Fig. 1B and 1C). Serial dilutions of the MLV containing supernatants show consistent SSC and fluorescence intensities at dilutions below 1:500, with ≤1% electronic abort rate (Suppl. Fig. 1D to 1F).

Flow cytometer set-up, beads, and data acquisition. Unless otherwise indicated, all samples were acquired on a Beckman Coulter CytoFLEX S with 4 lasers (405 nm, 488 nm, 561 nm, 640 nm), using 405 nm SSC-H (405-SSC-H) as the threshold parameter (threshold at 1400 a.u.). Detector gain for fluorescence and SSC detection were optimized using MLVsfGFP, with 0.1 µm-filtered PBS used as the background control for threshold determination. The gains for the respective detectors associated with the following spectral filters: 405-SSC, 405-450/50, 488-525/40, 561-580/30, and 640-670/30 were 1400, 1200, 3000, 1600, and 1200 a.u. respectively. A 405-SSC vs. time plot was used during acquisition to monitor, and ensure, consistency of the event rates. All samples were acquired for 1 min at a sampling rate of 10 µl/min. The sampling volume was validated by weight using the CytExpert volumetric calibration tool. The CytoFLEX Sizing Mix (prototype) (Beckman Coulter, Brea, CA) was analyzed undiluted and ApogeeMix (Apogee Flow Systems, Hemel Hempstead, UK) was diluted 1:5 with 0.1 µm-filtered PBS for analysis. FlowJo v.10 (FlowJo, LLC, Ashland, OR) was used for analysis of flow cytometry data.

Imaging Flow Cytometry (IFC). All MLV samples were acquired on a two camera ImageStreamX MKII (LuminexCorp.) according to the method previously described (12), with the modification of using the 405 nm laser (120 mW) for scatter measurements. Briefly, samples were acquired with 60X magnification, eGFP excitation with a 200 mW 488 nm laser, and scatter with the 405 nm laser described above. Emissions were collected for scatter in CH07 (bandpass 405-505nm) and CH02 for eGFP (bandpass 480-560 nm). All samples were acquired using the Inspire software and collected for a period of two minutes using a scatter acquisition gate that eliminated the speed beads (1µm polystyrene beads used for camera synchronization). Instrument sheath and sample dilution buffer was a 0.1 µm sterile filtered DPBS/Modified (HyClone cat. #SH30028.02). Buffer only controls were also run for the same amount of time to be sure that the same volumes were acquired as the samples. All virus samples were run in triplicate. 500 nm Si 7 peak FITC-MESF beads were also acquired using the same instrument settings as the virus samples. Data was processed using IDEAS 6.2 software (LuminexCorp) and FCS data files created for the scatter and GFP parameters and submitted for further analysis by the

University of Ottawa Flow Cytometry and Virometry Core Facility.

Fluorescence standardization and quantification using MESF beads. Calibration curves were generated using a linear fit by plotting the known MESF values vs. their respective fluorescence intensities in linear scale for each of the MESF bead sets used in these studies. The beads used were 500nm Si FITC-MESF (30), BD QuantiBrite PE (Lot 73318, BD Biosciences, Mississauga, ON), and Quantum-5 FITC MESF Beads (Bang Laboratories, Fishers, IN). Autofluorescence was measured using the blank bead population, and this was subtracted from the fluorescent-bead values. The uncertainties of the fluorescence values for each bead population was accounted for in the generation of the calibration curve and is represented as the standard error (SE), derived from the division of the standard of deviation (SD) by the square-root of counts obtained in each gated bead population. The linear fit of the calibration curve was weighted with the SEM of each bead population. The slope and intercept of each calibration curve for the 500 nm Si FITC-MESF and 7 µm PS FITC-MESF beads (Suppl. Fig. 2), was used to deduce the molecules of FITC equivalence for MLVsfGFP.

The virus population used for fluorescence quantification was identified based on its SSC and GFP fluorescence intensity and background fluorescence of the virus was subtracted using the fluorescence values of the gated MLVnoGFP. The mode of the sfGFP fluorescence intensities was used in determining the FITC-MESF value of MLVsfGFP. This statistic was chosen because it best represents the maximum of the unimodal distribution of our monodisperse virus population and is also the statistic most resistant to contributions from background noise events, which can be variable between day-to-day flow cytometer operations. The reported MFI and MESF values for MLVsfGFP was based on three separate experiments with a total of n=8 and n=9 samples. Calibration fits were produced using a C++ macro compiled with ROOT under the general public license (https://root.cern.ch/downloading-root). The slope and intercepts from the calibration fits were inputted into FlowJo to display the data as a derived parameter in terms of MESF units.

Antibody labeling of MLV and MLV infected cells. For antibody labeling of MLV, the concentration of viral particles harvested from the supernatants of cells infected with MLVsfGFP and MLVnoGFP was adjusted to 10^9 viral particles/ml for staining. Fluorophore-conjugated antibody aliquots were centrifuged at 17,000 x g for 10 min prior to use to reduce the presence of aggregates. For each antibody labeling reaction, 50 µl of virus supernatant was labeled with anti-GFP antibodies unconjugated or conjugated with PE, AF647 (clone FM264G, Bio Legend, San Diego, CA), or BV421 (clone 1A12-6-18), anti-mCD63-PE (clone NVG-2), anti-mCD81-PE or BV421 (clone Eat2), or anti-mCD9 PE (clone KMC8, BD Biosciences, Mississauga, ON) at the indicated concentrations for 1 hour at 37 °C in a total volume of 100 µl. For titration of all anti-GFP antibodies, 5 x 10^7 MLVsfGFP viral particles were mixed with an equal number of MLVnoGFP particles, and a range of antibody staining concentrations from 0.0125µg/ml to 1.6µg/ml was tested for each anti-GFP conjugate. Unlabeled virus and antibody alone samples were run as controls for antibody labeling experiments. Labeled virus and controls were diluted 1:500 (~10^6 particles/ml) for analysis in 0.1 µm-filtered PBS for analysis by FCM. For antibody labeling of MLV infected cells, 10^6 cells were labeled with a concentration of 1 µg/ml of the same anti-tetraspanin antibodies used for MLV labeling in a 200 µl staining volume of 0.2% BSA-PBS for 20 min at 4°C. Excess antibody was removed by washing with 0.2% BSA-PBS. The SI was calculated for each anti-GFP conjugate at each concentration and the optimal staining concentrations associated with the highest SI value for anti-GFP PE, BV421, and AF647 were 0.2 µg/ml, 0.8 µg/ml, and 0.4 µg/ml respectively. The SI is defined as the difference of the MFI of the stained MLVsfGFP and MLVnoGFP divided by the standard of deviation of MLVnoGFP.

To assess the expression of cell-derived tetraspanins on MLV, MLVsfGFP was labeled with anti-mouse CD9, CD63, or CD81 antibodies conjugated with PE because this fluorophore was found to produce the highest SI. Gating strategy used to identify tetraspanin stained vs. negative particles is shown in

Supplementary Figure 3 (panels A & B). Non-specific labeling with rat IgG-PE on MLV occurs at antibody concentrations greater than 1.6 μg/ml (Suppl. Fig. 4A). Lower concentrations of each antibody were also tested and confirmed that the optimal staining concentration (highest SI) was indeed 1.6 μg/ml (Suppl. Fig. 3C). Virus was identified by SSC intensity and gated to remove antibody aggregates using the antibody-only control samples (Suppl. Fig. 5A: red gates, and 5B: red events). PE and GFP intensities of anti-tetraspanin PE labeled fluorescent virus was converted to MESF using QuantiBrite PE and 500nm Si FITC MESF beads. QuantiBrite PE beads were chosen in this case because there are no commercially available small particle PE MESF beads.

Nanoparticle Tracking Analysis. NTA was carried out as previously described (8). Briefly, samples were diluted with 0.1 μm-filtered PBS and analysed using the ZetaView PMX110 Multiple Parameter Particle Tracking Analyzer (Particle Metrix, Meerbusch, Germany) in diameter mode using ZetaView software version 8.02.28. Camera gain: 938, Shutter: 70, Frame Rate 30 fps, Temperature 24.5, Brightness: 30. Videos were taken from all 11 camera positions.

Light scatter modelling using Mie Scatter. Effective RI was approximated using the scatter-diameter curves based on the CytoFLEX S collection geometry as previously published (31). Briefly, instrument light scatter calibration was performed by fitting acquired 405 nm light scatter data to predicted values using the reported diameters and refractive indices of Apogee Mix beads (Apogee info) and NIST-traceable beads (Beckman Coulter, Brea, CA). These ranged in diameter from 80 nm polystyrene to 1300 nm silica (Fig. 1C).

Data Sharing. All List-mode data files have been made available on *FlowRepository.org* in compliance MIFlowCyt Checklist item 4.1. Repository ID: http://flowrepository.org/id/FR-FCM-Z24Y.

RESULTS

MLV virions are monodisperse. The ecotropic Moloney MLV used for this study was modified to prevent the expression of the membrane-associated accessory glycogag protein (27). This alteration ensured that the only viral protein expressed on its surface is Env. This virus is termed MLVnoGFP in our study. MLVsfGFP consists on this same virus but with the insertion of sfGFP in the Env protein sequence. MLV virions were detected as a highly monodisperse population that could be resolved by side-scatter (SSC) intensity alone and further identified by GFP expression (Fig. 1A, red gates). Next, the 405-SSC intensity of the virus was compared to two types of sizing beads: CytoFLEX Sizing Mix (prototype, Beckman Coulter) (Fig. 1B) and ApogeeMix (Fig. 1C). The virus gate (red) from Figure 1A was superimposed to panels 1B and 1C to delineate where the fluorescent MLV population would appear with reference to the bead populations on our instrument system. MLV has a similar SSC intensity to 80 nm polystyrene beads (Fig. 1D). A comparison of the standard deviation (SD) in diameter distribution of MLVsfGFP and 100 nm polystyrene bead by nanoparticle tracking analysis (NTA) show a greater variability in diameter sizes in the beads versus virus, 44.3 and 32.9, respectively (Fig. 1E). This reflects the homogeneous and consistent stoichiometry of virus assembly, and suggests that formation of monodisperse MLVs is more consistent than the manufacturing methods currently used for production of NIST-traceable 100 nm polystyrene beads.

Fluorescence quantification and enumeration of GFP molecule expression on MLVsfGFP. The fluorescence signal was analyzed from MLVsfGFP viral particles, using MLVnoGFP as the auto-fluorescence control and MESF calibration beads for fluorescence quantification (Fig. 2A). 500 nm silica spheres containing known MESF values of fluorescein isothiocyanate (500 nm Si FITC-MESF) (30) were used in lieu of GFP given that GFP-MESF beads in the relevant diameter and fluorescence-intensity range are currently not commercially available. The GFP intensity expressed by MLVsfGFP, quantified using the 500nm Si FITC-MESF beads, was found to be 637±3 FITC-equivalent molecules. Due to the mismatch of fluorophores between the FITC-MESF calibration beads and the MLVsfGFP, we could not report the

fluorescence intensity of the virus in terms of GFP-MESF. Env-sfGFP expression was therefore quantified on MLV by an alternate method using anti-GFP-PE antibody labeling and fluorophore-matched QuantiBrite PE beads (Fig. 2B). A titration of the anti-GFP-PE antibody was performed to determine the concentration that would produce optimal labeling of Env-sfGFP using MLVnoGFP as an internal non-specific binding control (Fig. 4B and 4E). The brightest population of QuantiBrite PE beads were off-scale and only the first three populations were used. Anti-GFP-PE labeled MLVsfGFP had a PE-MESF value of 306±13, corresponding to 102 Env spikes. However, this quantification method also has potential limitations because it could underestimate the expression level of Env-sfGFP for several reasons: 1) inaccuracies associated with the use of MESF beads that are not calibrated for use with small particles, 2) quenching of PE molecules due to the proximity of target epitopes, 3) steric hindrance could prevent binding of all available epitopes, and 4) the bivalent nature of the antibody.

Cross-institution and cross-platform assessment of fluorescence quantification. To compare the impact of 1) instrument variability, 2) user data acquisition variability, and 3) technological platform variations on the consistency of fluorescence quantification of the viruses, MLVsfGFP and MLVnoGFP viruses were sent to two different research institutions. The first institution operated a Beckman Coulter CytoFLEX S (Inst. 1) where virus fluorescence was quantified using 7 μm PS FITC-MESF beads (Fig. 3A). The second institution (Inst 2), operated a Luminex ImageStream X (ISX) where fluorescence quantifications were performed using 500 nm Si FITC-MESF beads (Fig. 3B). The values for FITC-MESF obtained on the sfGFP-expressing virus by Inst. 1 were very similar to our own, within a 0.25-fold difference, while Inst. 2 (ISX) produced values that were 2.6-fold higher (Fig. 3C). This apparent disparity was most likely due to differences in spectral filters between the two platforms. The width of the 525/40 bandpass filter used in the CytoFLEX S for collection of signal from FITC and GFP limits the collection of emitted photons to 62.7% and 59.2%, respectively (Fig. 3D and 3E). The wider filter on the ISX (520/80) is collecting 83.3% and 88.9% of photons emitted from FITC and GFP, respectively. This would suggest that the ISX was disproportionately collecting more signal from GFP than FITC (1.5-fold more compared to 1.3-fold), which could contribute to MLVsfGFP appearing brighter with respect to the FITC-MESF beads, highlighting a potential caveat of using mismatched fluorophores for fluorescence quantification.

Antibody labeling of MLV surface antigens. FCM is the preferred method for immunophenotyping of cells. However, immunophenotyping of small particle populations, such as EVs and viruses, is inherently challenging due to low surface antigen abundance as a result of their restricted surface area. For optimal resolution of these populations, fluorophore selections are therefore limited to the brightest options, with minimal spectral spillover, thereby reducing the number of antigens that can be targeted in one antibody panel. In cells, fewer than 1000 molecules/cell is considered low antigen abundance (32). According to our own measurements, Env-sfGFP expression on MLV is potentially in the order of 10^2 molecules (Fig. 2). Compared to a cell, this may seem low in total abundance, yet when integrated over surface area, this amount of antigen on a nanoparticle of ~100 nm in diameter actually translates to very high antigen density; the equivalent of several millions of molecules on a 10 μm cell. As a result, labeling of small particles with high antigen density could potentially present the challenge of steric hindrance issues that may occur for antibodies conjugated to larger fluorophores.

Many factors contribute to the number of photons detected by a flow cytometer from a fluorescently-labeled particle. These factors include: excitation wavelength, spectral filters, quantum efficiencies of detectors at increasing wavelengths, and the fluorophore to protein ratio (F:P ratio) of antibodies used to label the particles of interest. For the purposes of our study, instrument-specific

considerations, such as excitation wavelength and spectral filters, are negated since analyses were performed on the same instrument. Avalanche photodiodes (APDs), the detectors used in the CytoFLEX S, also have a similar quantum efficiency over the range of visible light (400-800 nm) (33). The F:P ratio of conjugated antibodies, however, is a factor that should be considered, aside from the brightness, when choosing fluorophore conjugates since it is affected by the size of the fluorophore. Larger fluorophores such as PE typically have a 1:1 ratio due to steric hindrance, whereas smaller fluorophores could have a higher F:P ratio (34). Hence, a particle labeled with an antibody conjugated to the brightest fluorophore maybe not necessarily result in the greatest number of photons detected if the F:P ratio is low.

To assess the contributions of fluorophore size and brightness to resolving MLVsfGFP, an antibody against the high-density Env-sfGFP surface antigen was tested. Three different fluorophores that range in diameter and emission spectra, conjugated to an anti-GFP antibody were tested: PE, Brilliant Violet 421 (BV421), and Alexa Fluor 647 (AF647). The characteristics of each fluorophore, including brightness ($\varepsilon\phi$) and size (kDa), are summarized in Figure 4A. PE is the largest and brightest of the three fluorophores, followed by BV421, and AF647. A titration was performed for the three conjugates of anti-GFP antibodies and the stain index (SI) was calculated for each (Fig. 4B to 4E). At optimal staining concentrations (highest SI), both the PE and BV421 conjugates identified an equivalent frequency of GFP^+ viruses (52%), while the AF647 conjugate labeled slightly fewer GFP^+ viruses than the other two fluorophore conjugates (46%) (Fig. 4F). As with labeling of cells, increase of the cell or particle concentration will decrease the SI of optimized antibody concentrations. We confirmed that at the optimal staining concentration of 0.2 µg/ml for anti-GFP PE, increasing the particle concentration of the sample does indeed decrease the SI, however this was only observed when particle concentrations increased by more than a factor of 2 (Suppl. Fig. 4B and 4C). We also observed that staining saturation is reached for the MLVsfGFP virus at a concentration of 1.6 µg/ml of the anti-GFP antibody (Suppl. Fig. 4A).

Although PE is a very bright fluorophore, one major caveat in using PE-conjugated antibodies for small particle FCM is its potential to form aggregates (35). In fact, PE^+ particles were detected in samples containing only anti-GFP PE antibody which increased in number with rising concentrations of antibody used (Suppl. Fig. 5A). The majority of these PE^+ aggregates were located in two populations (coloured events); one lower and the other higher than the labeled virus in SSC intensity (gray events) (Suppl. Fig. 5B). At the optimal staining concentration of 0.2 µg/ml for anti-GFP PE, the number of aggregates was negligible in comparison to the number of stained particles (Suppl. Fig. 5A & B). However, it is important to note that these samples were stained at 0.2 µg/ml, but then further diluted 1:500 for analysis, resulting in an actual antibody concentration of 0.4 ng/ml when analysed on the flow cytometer. Aggregates can also be seen with the anti-GPF BV421 conjugate, but not with the AF647 conjugate (Suppl. Fig. 5C and D).

Antibody labeling of MLV modulates scatter intensity, hydrodynamic diameter, and the refractive index. During the analysis of our antibody-labeled MLVs in the previous section, we noted that the GFP^+ virus populations increased in SSC intensity with increasing amounts of anti-GFP PE antibody (Fig. 5A; red gates). This increase in SSC was also observed with BV421 and to a lesser extent the AF647 conjugate (Fig. 5B). Conceptually, it is feasible that labeling with antibodies could significantly increase the apparent diameter of a small particle such as MLV. The diameter of an IgG antibody has been reported to range from 14 to 40 nm in diameter by 2 to 4 nm in height depending on the measurement method used (36,37). IgG conjugated with PE, which is 250 kDa and considered one of the larger fluorophores used in flow cytometry, has been reported to measure 60 nm in diameter by 5 nm in height by atomic force microscopy (35). To determine if the increase in SSC

intensity is due to an increase in particle diameter, NTA was used to determine the hydrodynamic diameter of antibody-labeled MLVsfGFP at the over-saturating concentration of 1.6μg/ml. The median particle diameter and distribution were compared for unstrained MLVsfGFP and MLVsfGFP labeled with unconjugated anti-GFP, as well as PE, BV421, and AF647-conjugated antibodies (Fig. 5C). A scatter-modeling program based on Mie theory was used to calibrate the SSC intensity, to relate the SSC intensity to the measured hydrodynamic diameters of antibody-labeled and unlabeled MLVsfGFP determined with NTA (38), and to infer the RI. Data on the 405 nm scatter intensities acquired from polystyrene (RI=1.6333) and silica (RI=1.448) beads of known diameter (NIST-traceable) were used for calibration of our instrument (Fig. 1B). Our analyses showed high correlation (R^2=0.9999) of acquired values (geometric symbols) with theoretical values (solid lines) down to 80 nm for PS (Fig. 5D). Theoretical lines represent Mie-theory simulations for materials of specific RIs with increasing particle diameter, scatter intensity, and scattering cross-section. Measured values for the diameters and scatter intensities of particles with the same RI are predicted to fall on the same lines as seen with the PS, fluorescent PS (FL PS), and Si beads (Fig. 5D). Figure 5E, generated from the gray inset in Figure 5D, depicts the collected data of antibody labeled MLV with respect to the RI values for PS (solid blue line) and Si (dashed red line).

Although individual MLV particles are not homogeneous in composition like a bead, their *effective RI* was calculated with this assumption to simplify the modeling of particles with multiple refractive indices due to mixed compositions (Fig. 5F). Here, the effective RI assumes the scattering intensity of each particle is related only to its refractive index and has no contributing extinction coefficient, as seen with fluorescent polystyrene beads (Fig. 5E). The dotted line, which passes through the unstained MLVsfGFP represents the effective RI of unstained virus (RI=1.519). The SSC intensity of antibody-labeled viruses falls below the iso-RI line of the unlabeled virus, indicating that labeled viruses have a lower effective RI than unlabeled virus. These results clearly show that antibody labeling can increase the diameter and, interestingly, reduces the effective RI, and therefore light scattering properties, of small particles. This may be related to the extinction coefficient of the fluorophore conjugated antibodies.

Quantification of host cell-derived tetraspanins on MLV. Host-derived antigen expression on the surface of the virus by antibody labeling was next assessed to determine whether the observations from anti-Env-sfGFP labeling held true for other antigens on the surface of the virus. We chose to target cell-derived tetraspanins on the surface of MLV because these transmembrane glycoproteins are ubiquitously expressed as they contribute to fundamental processes of cellular trafficking (39). Tetraspanins CD9, CD63, and CD81 have been used as markers to identify subtypes of EVs due to their association with mechanisms of EV egress, such as the endosomal sorting complexes required for the transport (ESCRT) pathway (39). More specifically, these pathways have also been implicated in both cellular entry and egress of retroviruses (40-44).

The PE MESF of anti-tetraspanin-labeled viral particles were compared to show the relative expression levels of CD9, CD63, and CD81 on MLV (Fig. 6A-E). This comparison is possible because, in contrast to other fluorophores, only one PE molecule is likely to be conjugated per IgG due to its large diameter (34). CD81 was most abundantly expressed on MLVsfGFP with a median PE MESF of 18.7±0.2, followed by CD63 with 13.1±0.3 PE MESF, and CD9 with 6.4±0.02 PE MESF. It is important to note that these values should be taken as a measure of relative tetraspanin abundance between the three types, and not as actual molecules of tetraspanins expressed per virus, since QuantiBrite PE beads were not intended for use with such dimly expressed antigens and so are not accurately calibrated for this purpose (45). It is unclear whether CD9 expression was actually present on MLVsfGFP since the signal was similar to unstained virus (3.6±0.02 PE MESF) and could potentially be the result of non-specific labeling.

However, CD9 was confirmed to be expressed on the cells producing MLVsfGFP, therefore it is possible that MLVsfGFP indeed express CD9 at very low levels, below the detection limit of our flow cytometer (Suppl. Fig. 3D).

The level of staining produced by the same anti-CD81 antibody conjugated to PE vs. BV421 was compared (Fig. 6F). Labeling of MLVsfGFP with anti-GFP-PE resulted in a higher SI than with the BV421 conjugate, although both equally resolved the MLVsfGFP population at optimal staining concentrations (Fig. 4B, 4C, and 4F). At optimal staining concentrations, labeling MLVsfGFP with anti-CD81-PE resulted in approximately 20% higher frequency of $CD81^{+}GFP^{+}$ viruses than anti-CD81-BV421 (Fig. 6G). The resolution of CD81 expression, an antigen expressed at lower levels than Env-sfGFP, benefited significantly from the use of a brighter fluorophore.

To assess whether double-labeling, the targeting of two different antigens with two different antibodies, would result in reduced staining for each individual antigen due to possible steric hindrance between the fluorophore-conjugated antibodies. A comparison was made between the percent of resulting $CD81^{+}GFP^{+}$ and $CD63^{+}GFP^{+}$ viruses (based on the gating strategy used in Fig. 6F; dashed gates) when the virus was labeled with anti-CD63 PE and anti-CD81 BV421 individually or with both antibodies together. There was no significant difference between the numbers of $CD81^{+}$MLVsfGFP or $CD63^{+}$MLVsfGFP events, or in the percentage of $CD81^{+}$ or $CD63^{+}$ GFP^{+} events, obtained using single versus double-labeling (Fig. 6H and 6I). This suggests that steric hindrance did not affect in this case the individual binding of two antibodies targeting distinct antigens.

SSC intensities for single and double-labeled virus populations (Fig. 6J) were compared to determine if fluorescence labeling of lower-density antigens would similarly impact scatter intensity and, thus, the apparent diameter and RI. Although there was an appearance of a correlation between the highest SSC intensities and the highest degree of labeling (CD81+CD63>CD81>CD63>CD9), these values were not statistically different from those of the unlabeled virus. Therefore, these observations suggest that the labeling of low-density antigens with fluorophore-conjugated antibodies does not significantly alter the scatter intensities of small particles.

DISCUSSION

Current challenges for the analysis of small biological particles by flow cytometry are multi-faceted. To reliably achieve single-molecule resolution, technological advancements are needed to further improve instrument sensitivity. Development of brighter and smaller fluorophores is required for multi-parameter analyses of small particles where surface area is highly restricted. But more urgently, different types of reference particles with low fluorescence levels relevant to small particles are also needed for: 1) positive controls for stainings (antibodies and dyes), and 2) instrument calibration to allow standardized data reporting across instruments and technological platforms.

At present, few references particles are available for small particle FCM. Many FCM reference beads, such as compensation beads, are made mostly of polystyrene and exhibit fluorescence and autofluorescence intensity levels that are much higher than those attainable with small biological particles. Chemical conjugation of biological molecules to synthetic beads for use as positive controls can be technically challenging and often result in very high levels of expression that are biologically irrelevant. Currently available calibration beads are also too large and too bright for accurate small particle fluorescence standardization using MESF axes calibration. Biological particles, such as retroviruses, on the other hand, have long been adapted for use as vectors to safely express proteins of interest in cells. MLV particles are small, monodisperse, and have minimal autofluorescence. The potential of MLVs for use as fluorescence calibration particles in FCM is obvious because they

can be engineered or labeled to have multiple levels of fluorescence expression. We showed here, with titrating levels of anti-GFP antibody, that MLVsfGFP can be easily labeled with different intensities of fluorescence.

In this study, MLV was engineered to express sfGFP in fusion with the viral surface glycoprotein, Env. These virus particles were used to showcase the importance of FCM best practices, such as antibody titration and fluorophore selection, when conducting immunophenotyping assays on small biological particles. Additionally, we demonstrated that when a highly-expressed surface antigen on a small particle is labeled with an excess of fluorophore-conjugated antibodies, these can change the physical properties, including the diameter and effective RI of that small particle. Additionally, this study emphasized the importance of fluorescence standardization with matching fluorophores to compare data between different flow cytometry platforms. Taken together, our observations on antibody labeling using MLV as a prototypical small particle, enabled us to identify and address specific challenges relevant to the antibody-labeling of small biological particles. These observations were only made possible due to the stringent uniformity in diameter and fluorescence, and high viral surface antigen expression on MLV particles. These critical features decisively qualify MLV as a candidate biological reference particle for the FCM analysis of other enveloped viruses and small biological particles such as EVs.

ACKNOWLEDGEMENTS

The authors would especially like to thank members of the Beckman Coulter technical support team, Dominic Therrien and Marc Simard, for valuable assistance throughout this study. We would like to acknowledge Sergei Gulnik and Maria Gentile of the Beckman Coulter Research and Marketing Teams for their helpful discussions. We would like to thank Christian Ouellet for providing the C++ scripts for MESF calibration. V.A.T. is an International Society for Advancement of Cytometry (ISAC) Shared Resource Lab Emerging Leader. T.M.R. holds a Queen Elizabeth II Graduate Scholarship in Science and Technology (QEII- GSST). E.v.d.P. was supported by the Netherlands Organization for Scientific Research-Domain Applied and Engineering Sciences (NWO-TTW), research programs VENI 15924. M.-A.L. holds a Canada Research Chair in Molecular Virology and Intrinsic Immunity. This work was supported by a research and development grant from the University of Ottawa Faculty of Medicine to the FCV Core Facility, and by a Discovery Grant and an Idea to Innovation (I2I) Grant by the Natural Sciences and Engineering Research Council of Canada (NSERC) to M.-A.L.

CONFLICTS OF INTERESTS

M.-A.L. is the CEO, and V.A.T. is the CSO of ViroFlow Technologies. G.C.B is a Beckman Coulter research scientist. E.v.d.P. is CSO of Exometry.

REFERENCES

1. Hercher M, Mueller W, Shapiro HM. Detection and discrimination of individual viruses by flow cytometry. J Histochem Cytochem 1979;27:350-2.
2. Sanders CA, Yajko DM, Nassos PS, Hyun WC, Fulwyler MJ, Hadley WK. Detection and analysis by dual-laser flow cytometry of bacteriophage T4 DNA inside Escherichia coli. Cytometry 1991;12:167-71.
3. Steen HB. Flow cytometer for measurement of the light scattering of viral and other submicroscopic particles. Cytometry A 2004;57:94-9.
4. Lian H, He S, Chen C, Yan X. Flow Cytometric Analysis of Nanoscale Biological Particles and Organelles. Annu Rev Anal Chem (Palo Alto Calif) 2019.
5. Marcoux G, Duchez AC, Cloutier N, Provost P, Nigrovic PA, Boilard E. Revealing the diversity of extracellular vesicles using high-dimensional flow cytometry analyses. Sci Rep 2016;6:35928.
6. Lippe R. Flow Virometry: a Powerful Tool To Functionally Characterize Viruses. J Virol 2018;92.
7. Nolan JP, Duggan E. Analysis of Individual Extracellular Vesicles by Flow Cytometry.

Methods Mol Biol 2018;1678:79-92.

8. Tang VA, Renner TM, Fritzsche AK, Burger D, Langlois MA. Single-Particle Discrimination of Retroviruses from Extracellular Vesicles by Nanoscale Flow Cytometry. Sci Rep 2017;7:17769.
9. Bonar MM, Tilton JC. High sensitivity detection and sorting of infectious human immunodeficiency virus (HIV-1) particles by flow virometry. Virology 2017;505:80-90.
10. Musich T, Jones JC, Keele BF, Jenkins LM, Demberg T, Uldrick TS, Yarchoan R, Robert-Guroff M. Flow virometric sorting and analysis of HIV quasispecies from plasma. JCI Insight 2017;2:e90626.
11. Cloutier N, Tan S, Boudreau LH, Cramb C, Subbaiah R, Lahey L, Albert A, Shnayder R, Gobezie R, Nigrovic PA and others. The exposure of autoantigens by microparticles underlies the formation of potent inflammatory components: the microparticle-associated immune complexes. EMBO Mol Med 2013;5:235-49.
12. Lannigan J, Erdbruegger U. Imaging flow cytometry for the characterization of extracellular vesicles. Methods 2017;112:55-67.
13. van der Pol E, de Rond L, Coumans FAW, Gool EL, Boing AN, Sturk A, Nieuwland R, van Leeuwen TG. Absolute sizing and label-free identification of extracellular vesicles by flow cytometry. Nanomedicine 2018;14:801-810.
14. Welsh JA, Holloway JA, Wilkinson JS, Englyst NA. Extracellular Vesicle Flow Cytometry Analysis and Standardization. Front Cell Dev Biol 2017;5:78.
15. Parks DR, Moore WA, Brinkman RR, Chen Y, Condello D, El Khettabi F, Nolan JP, Perfetto SP, Redelman D, Spidlen J and others. Methodology for evaluating and comparing flow cytometers: A multisite study of 23 instruments. Cytometry A 2018;93:1087-1091.
16. Nolan JP. Flow Cytometry of Extracellular Vesicles: Potential, Pitfalls, and Prospects. Curr Protoc Cytom 2015;73:13 14 1-16.
17. Yeager M, Wilson-Kubalek EM, Weiner SG, Brown PO, Rein A. Supramolecular organization of immature and mature murine leukemia virus revealed by electron cryo-microscopy: implications for retroviral assembly mechanisms. Proc Natl Acad Sci U S A 1998;95:7299-304.
18. Kozak CA. Origins of the endogenous and infectious laboratory mouse gammaretroviruses. Viruses 2014;7:1-26.
19. Wurdinger T, Gatson NN, Balaj L, Kaur B, Breakefield XO, Pegtel DM. Extracellular vesicles and their convergence with viral pathways. Adv Virol 2012;2012:767694.
20. Nolte-'t Hoen E, Cremer T, Gallo RC, Margolis LB. Extracellular vesicles and viruses: Are they close relatives? Proc Natl Acad Sci U S A 2016;113:9155-61.
21. Liu J, Bartesaghi A, Borgnia MJ, Sapiro G, Subramaniam S. Molecular architecture of native HIV-1 gp120 trimers. Nature 2008;455:109-13.
22. Kwong PD, Wyatt R, Robinson J, Sweet RW, Sodroski J, Hendrickson WA. Structure of an HIV gp120 envelope glycoprotein in complex with the CD4 receptor and a neutralizing human antibody. Nature 1998;393:648-59.
23. Stano A, Leaman DP, Kim AS, Zhang L, Autin L, Ingale J, Gift SK, Truong J, Wyatt RT, Olson AJ and others. Dense Array of Spikes on HIV-1 Virion Particles. J Virol 2017;91.
24. Zhu P, Chertova E, Bess J, Jr., Lifson JD, Arthur LO, Liu J, Taylor KA, Roux KH. Electron tomography analysis of envelope glycoprotein trimers on HIV and simian immunodeficiency virus virions. Proc Natl Acad Sci U S A 2003;100:15812-7.
25. Zhu P, Liu J, Bess J, Jr., Chertova E, Lifson JD, Grise H, Ofek GA, Taylor KA, Roux KH. Distribution and three-dimensional structure of AIDS virus envelope spikes. Nature 2006;441:847-52.
26. Butan C, Winkler DC, Heymann JB, Craven RC, Steven AC. RSV capsid polymorphism correlates with polymerization efficiency and envelope glycoprotein content: implications that nucleation controls morphogenesis. J Mol Biol 2008;376:1168-

81.
27. Renner TM, Belanger K, Lam C, Gerpe MCR, McBane JE, Langlois MA. Full-Length Glycosylated Gag of Murine Leukemia Virus Can Associate with the Viral Envelope as a Type I Integral Membrane Protein. J Virol 2018;92.
28. Schwartz A, Wang L, Early E, Gaigalas A, Zhang YZ, Marti GE, Vogt RF. Quantitating Fluorescence Intensity from Fluorophore: The Definition of MESF Assignment. J Res Natl Inst Stand Technol 2002;107:83-91.
29. Wood JC, Hoffman RA. Evaluating fluorescence sensitivity on flow cytometers: an overview. Cytometry 1998;33:256-9.
30. Zhang S, Zhu S, Yang L, Zheng Y, Gao M, Wang S, Zeng JZ, Yan X. High-throughput multiparameter analysis of individual mitochondria. Anal Chem 2012;84:6421-8.
31. van der Pol E, Sturk A, van Leeuwen T, Nieuwland R, Coumans F, group I-S-VW. Standardization of extracellular vesicle measurements by flow cytometry through vesicle diameter approximation. J Thromb Haemost 2018;16:1236-1245.
32. Balderas B. Optimization of Multicolor Panel Design Incorporating Low Receptor Density Antigens. BD Biosciences Webinar; 2013.
33. Hergert E. Detectors: Guideposts on the Road to Selection. 2019.
34. Davis KA, Abrams B, Iyer SB, Hoffman RA, Bishop JE. Determination of CD4 antigen density on cells: role of antibody valency, avidity, clones, and conjugation. Cytometry 1998;33:197-205.
35. Chen Y, Cai J, Xu Q, Chen ZW. Atomic force bio-analytics of polymerization and aggregation of phycoerythrin-conjugated immunoglobulin G molecules. Mol Immunol 2004;41:1247-52.
36. Hansma HG. Varieties of imaging with scanning probe microscopes. Proc Natl Acad Sci U S A 1999;96:14678-80.
37. Leatherbarrow RJ, Stedman M, Wells TN. Structure of immunoglobulin G by scanning tunnelling microscopy. J Mol Biol 1991;221:361-5.
38. van der Pol E, Coumans FA, Sturk A, Nieuwland R, van Leeuwen TG. Refractive index determination of nanoparticles in suspension using nanoparticle tracking analysis. Nano Lett 2014;14:6195-201.
39. Martin-Serrano J, Neil SJ. Host factors involved in retroviral budding and release. Nat Rev Microbiol 2011;9:519-31.
40. Nydegger S, Foti M, Derdowski A, Spearman P, Thali M. HIV-1 egress is gated through late endosomal membranes. Traffic 2003;4:902-10.
41. Molle D, Segura-Morales C, Camus G, Berlioz-Torrent C, Kjems J, Basyuk E, Bertrand E. Endosomal trafficking of HIV-1 gag and genomic RNAs regulates viral egress. J Biol Chem 2009;284:19727-43.
42. Deneka M, Pelchen-Matthews A, Byland R, Ruiz-Mateos E, Marsh M. In macrophages, HIV-1 assembles into an intracellular plasma membrane domain containing the tetraspanins CD81, CD9, and CD53. J Cell Biol 2007;177:329-41.
43. Grigorov B, Attuil-Audenis V, Perugi F, Nedelec M, Watson S, Pique C, Darlix JL, Conjeaud H, Muriaux D. A role for CD81 on the late steps of HIV-1 replication in a chronically infected T cell line. Retrovirology 2009;6:28.
44. Martin-Serrano J, Yarovoy A, Perez-Caballero D, Bieniasz PD. Divergent retroviral late-budding domains recruit vacuolar protein sorting factors by using alternative adaptor proteins. Proc Natl Acad Sci U S A 2003;100:12414-9.
45. Pannu KK, Joe ET, Iyer SB. Performance evaluation of QuantiBRITE phycoerythrin beads. Cytometry 2001;45:250-8.

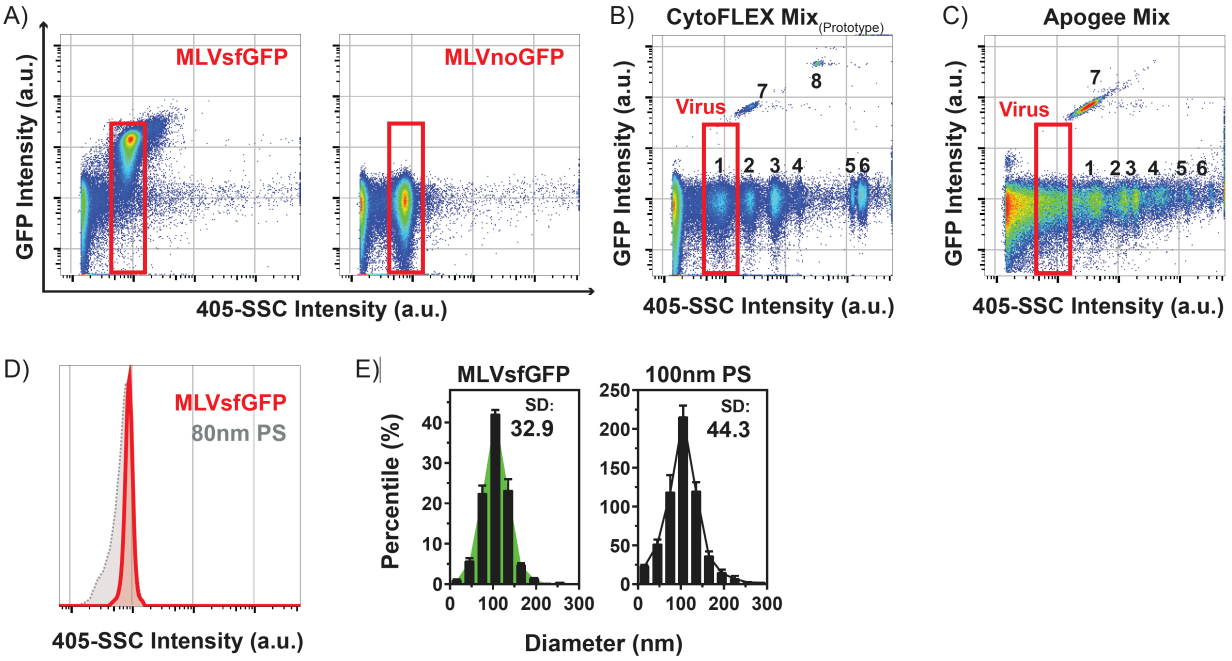

FIGURE 1. MLV virions are highly monodisperse. (A) MLVsfGFP and MLVnoGFP virions are a discrete population that can be resolved by 405-SSC intensity (a.u.) and green fluorescence intensity (a.u.). (B) Prototype CytoFLEX Sizing Mix (1: 80 nm PS, 2: 100 nm PS, 3: 214 nm Si, 4: 152nm PS, 5: 296 nm PS, 6: 1020 nm Si, 7: 100 nm PS fluorescent, 8: 196 nm PS fluorescent) and (C) ApogeeMix (1: 180 nm Si, 2: 240 nm Si, 3: 300 nm Si, 4: 590 nm Si, 5: 880 nm Si, 6: 1300 nm Si, 7: 110nm PS fluorescent) were analysed using the same settings as those for the MLV viruses. The "Virus" gate in red is the same from panel A. (D) Comparison of the 405-SSC intensity (a.u.) of MLVsfGFP and 80 nm polystyrene (PS) beads. (E) NTA on the diameter distribution of 100 nm PS beads and MLVsfGFP; SD: standard deviation.

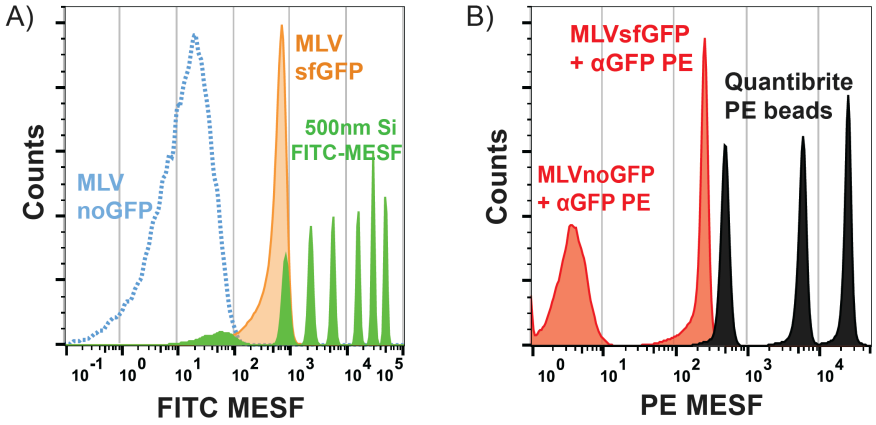

FIGURE 2. Fluorescence quantification of GFP expression on MLVsfGFP. (A) Green fluorescence from MLVsfGFP was quantified with 500nm Si FITC-MESF beads with MLVnoGFP as an autofluorescence control. Representative histogram overlay of MLVsfGFP and MLVnoGFP in FITC-MESF units with FITC-MESF beads (n=5). (B) Fluorescence quantification of anti-GFP PE labeled MLVsfGFP with QuantiBrite PE beads using MLVnoGFP as an internal control for non-specific labeling (n=3).

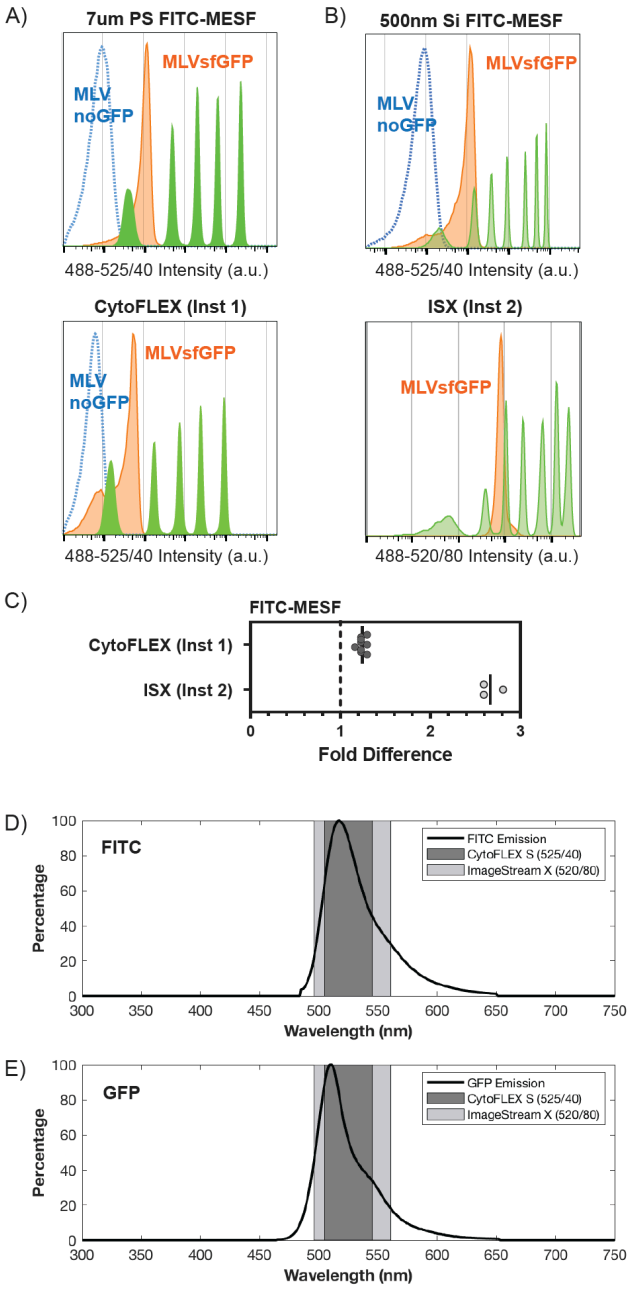

FIGURE 3. Cross-institution and cross-platform comparison of fluorescence intensity quantification of MLVsfGFP. (A) Comparative analysis of MLVsfGFP and MLVnoGFP viruses on two CytoFLEX S flow cytometers from two different institutions using 7µm PS FITC-MESF beads (top panel: uOttawa, bottom panel: Beckman Coulter (Inst1)). (B) Comparative analysis of MLVsfGFP and MLVnoGFP viruses on a Luminex ImageStream X (ISX) and a CytoFLEX S using 500nm Si FITC-MESF beads (top panel uOttawa CytoFLEX S, bottom panel uVirginia (Inst2) ISX). MLVnoGFP was not detected on the ISX. Data is displayed as fluorescence intensity. C) FITC-MESF values were calibrated for MLVsfGFP on both platforms and compared to values obtained with uOttawa CytoFLEX S, with uOttawa values set to "1" (dashed line). (D and E) Filter sets for the ISX and CytoFLEX S that were used for detection overlaid with the emission spectrums of FITC (D) and GFP (E); CytoFLEX S: n= 9; ISX; n = 3.

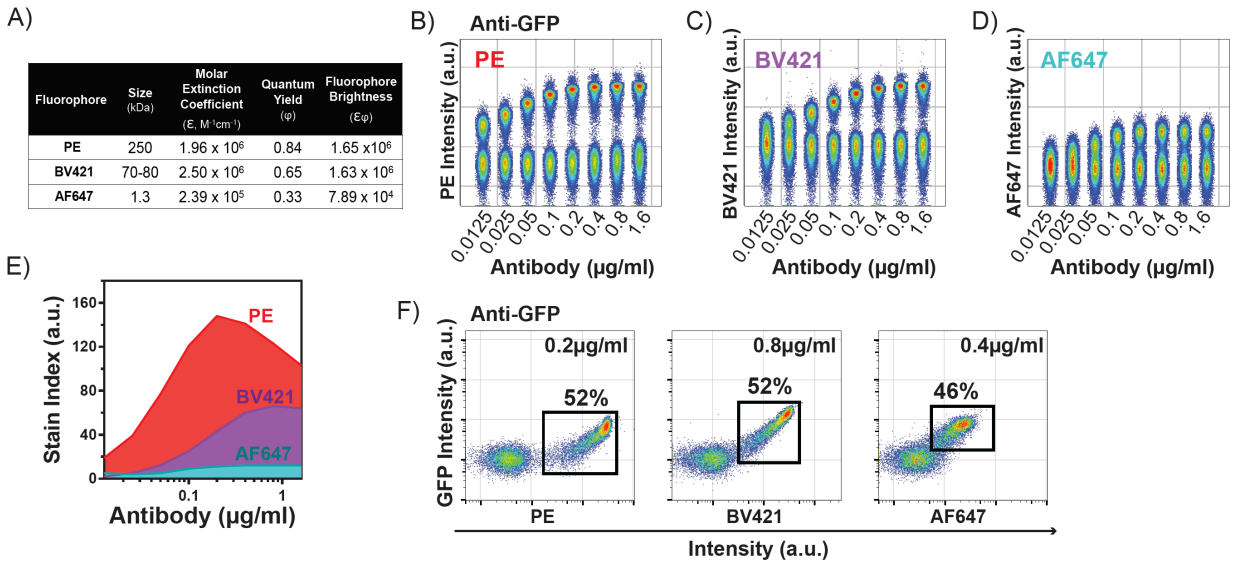

Fluorophore	Size (kDa)	Molar Extinction Coefficient (ε, $M^{-1}cm^{-1}$)	Quantum Yield (φ)	Fluorophore Brightness (εφ)
PE	250	1.96×10^6	0.84	1.65×10^6
BV421	70-80	2.50×10^6	0.65	1.63×10^6
AF647	1.3	2.39×10^5	0.33	7.89×10^4

FIGURE 4. Evaluation of antibody-fluorophore conjugates for the detection of MLV. (A) Diameter and brightness information for PE, BV421, and AF647. Titration of anti-GFP (B) PE, (C) BV421, and (D) AF647 antibodies from 0.0125 µg/ml to 1.6 µg/ml, performed on a mixture of equal proportions of MLVnoGFP and MLVsfGFP virus particles. (E) The SI, displayed is a representative graph of n=6, was calculated for each antibody at each concentration to determine the optimal staining concentration. (F) Representative dot-plots showing the frequency of anti-GFP$^+$ events labeled at optimal staining concentrations for each fluorophore conjugate.

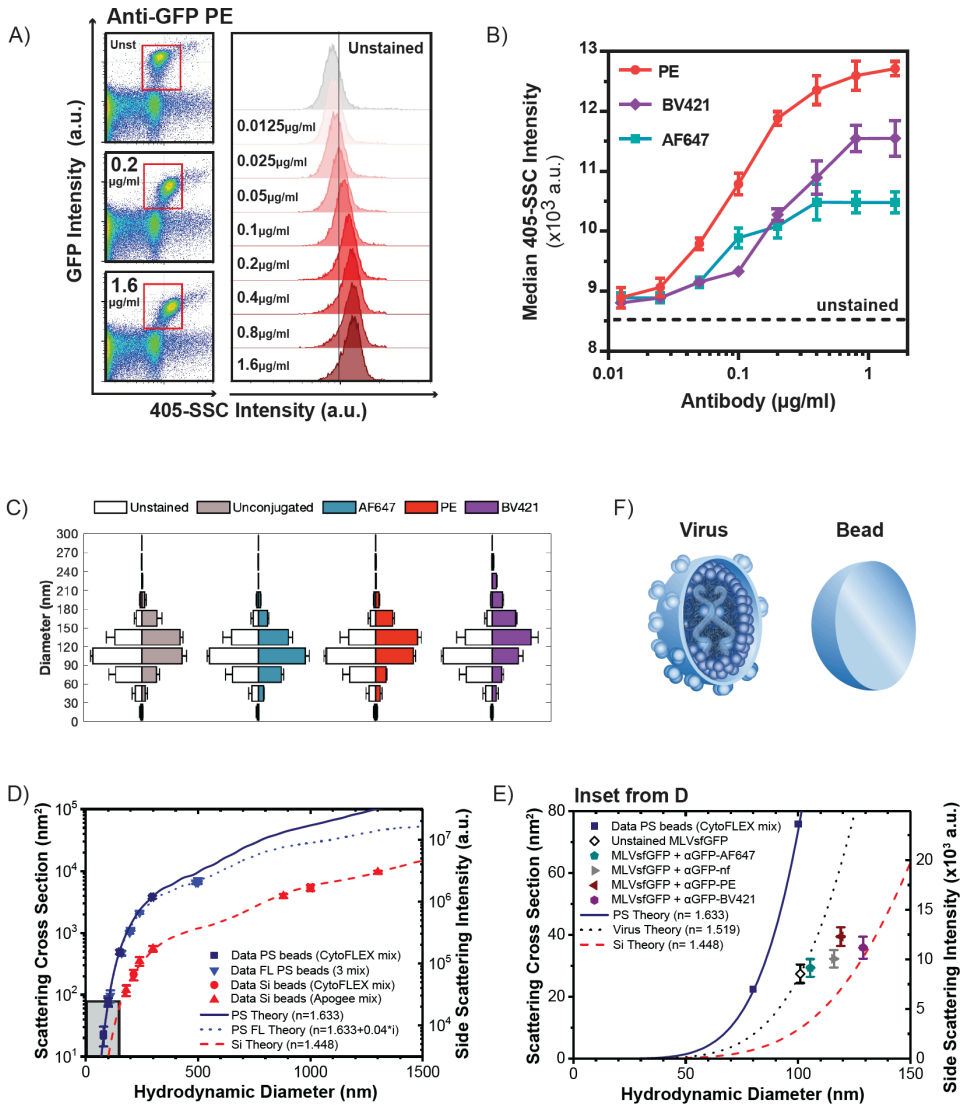

FIGURE 5. Antibody-fluorophore conjugates impact SSC intensity, hydrodynamic diameter, and effective refractive index of labeled viruses. (A) Antibody labeling of MLVsfGFP increases the SSC intensity of virus particles in a concentration-dependent manner. Representative scatter plots of MLVsfGFP (gated) mixed with MLVnoGFP that were unstained (Unst) or labeled with anti-GFP PE antibody at 0.2ug/ml and 1.6ug/ml (left panels). Histogram overlay of the gated GFP$^+$ populations that were labeled with anti-GFP PE, for all antibody concentrations from 0.0125ug/ml to 1.6ug/ml (right panel). (B) SSC intensity of GFP$^+$ viruses labeled with anti-GFP conjugated with PE, BV421, and AF647 at increasing antibody concentrations. Dashed line denotes SSC intensity of unstained MLVsfGFP. (C) NTA-measured diameter distribution of unstained MLVsfGFP separately compared to MLVsfGFP labeled with unconjugated anti-GPF, anti-GFP-PE, BV421, or AF647 at a concentration of 1.6µg/ml; n=3. (D) Mie-theory analysis for the calculation of the RIs for data points acquired using different silica (Si; red) and polystyrene (PS; blue) beads. The plot represents a correlation of the scattering cross section, hydrodynamic diameter, and SSC intensity of the virus particles. The gray-shaded box indicates the range where the MLV data points were acquired. (E) Gray-shaded box inset from (D), Mie-theory analysis of unstained MLVsfGFP and viruses labeled with various anti-GFP conjugated antibodies. The estimated effective RI of unlabeled virus is demonstrated as a dotted black line; n=3. (F) Cartoon to illustrate the complex and heterogeneous composition of a virus compared to the homogenous composition of a bead.

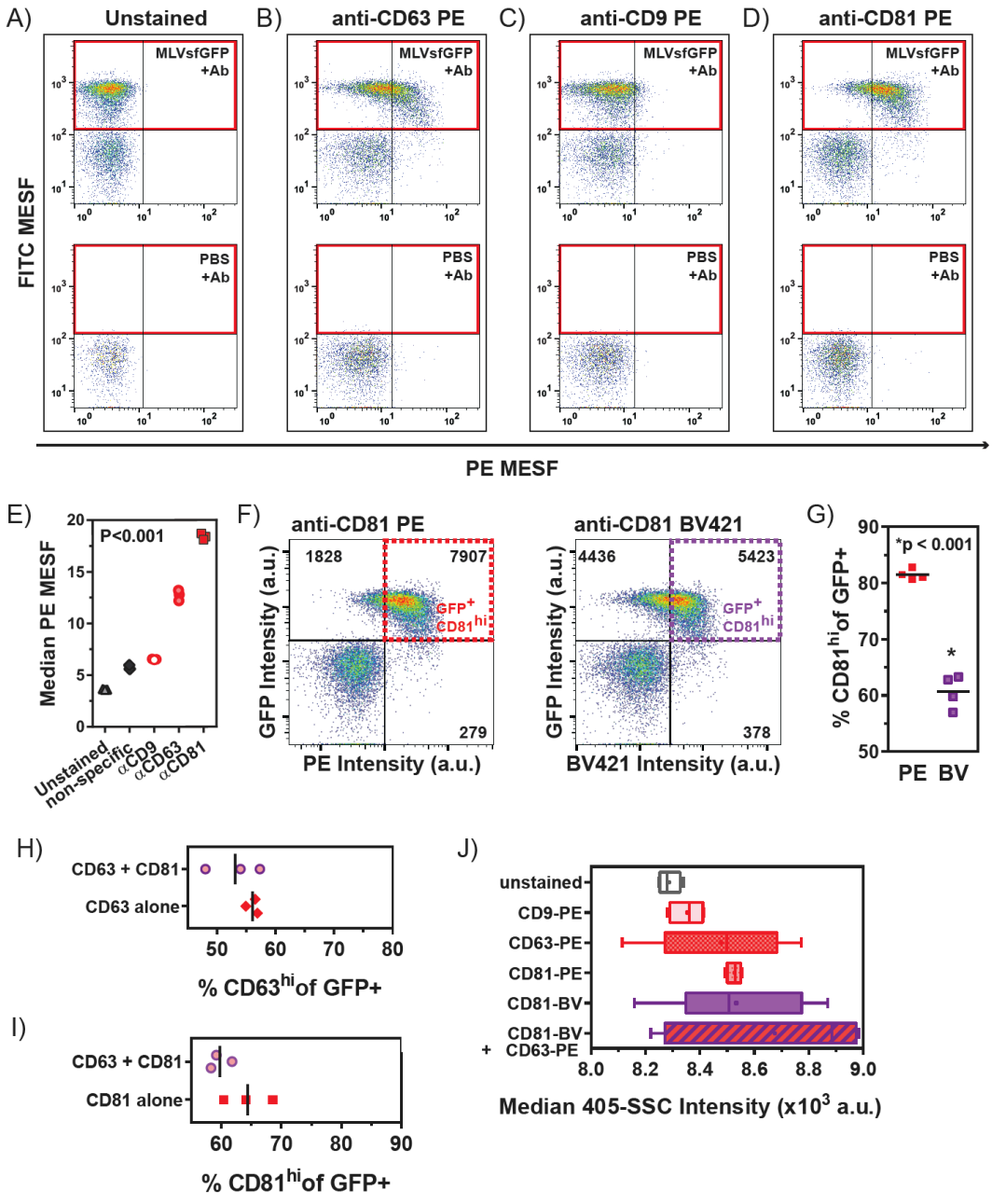

FIGURE 6. Phenotypic analysis of cell-derived tetraspanins expressed on the surface of MLV virions. (A) Unstained MLVsfGFP was compared to virus labeled with (B) anti-CD63-PE, (C) anti-CD9-PE, and (D) anti-CD81-PE at a concentration of 1.6 µg/ml of antibody per sample. QuantiBrite PE beads and 500nm Si FITC MESF were used to convert fluorescence intensity to PE and FITC MESF. (E) Median PE-MESF values of anti-tetraspanin labeled MLVsfGFP (n=3), 1-way ANOVA, P<0.001. (F) Gating strategy for identification of $GFP^{+}CD81^{hi}$ population from MLVsfGFP labeled with anti-CD81 BV421 and anti-CD81 BV421. (G) Comparison of $GFP^{+}CD81^{hi}$ events from anti-CD81 PE and anti-CD81 BV421 labeling, n=3, Unpaired t-Test, p<0.001. (H) Comparison of the frequency of $CD63^{hi}GFP^{+}$ virus in single- (anti-CD63 alone) vs. double-labeled (anti-CD63 + anti-CD81) viruses, Unpaired t-Test, non-significant, p = 0.34. (I) Frequency of $CD81^{hi}GFP^{+}$ virus in single- (anti-CD81 alone) vs. double-labeled (anti-CD63 + anti-CD81) viruses, Unpaired t-Test, non-significant, p = 0.15. (J) SSC intensities (405-SSC) for anti-tetraspanin labeled viruses, 1-way ANOVA, non-significant, P = 0.16.

SUPPLEMENTARY MATERIAL

Engineered Retroviruses as Fluorescent Biological Reference Particles for Small Particle Flow Cytometry

Vera A. Tang[1,2,*], Anna K. Fritzsche[1,2], Tyler M. Renner[2], Dylan Burger[3], Edwin van der Pol[4,5,6], Joanne A. Lannigan[7], George C. Brittain[8], Joshua A. Welsh[9], Jennifer C. Jones[9], and Marc-André Langlois[1,2,10,*]

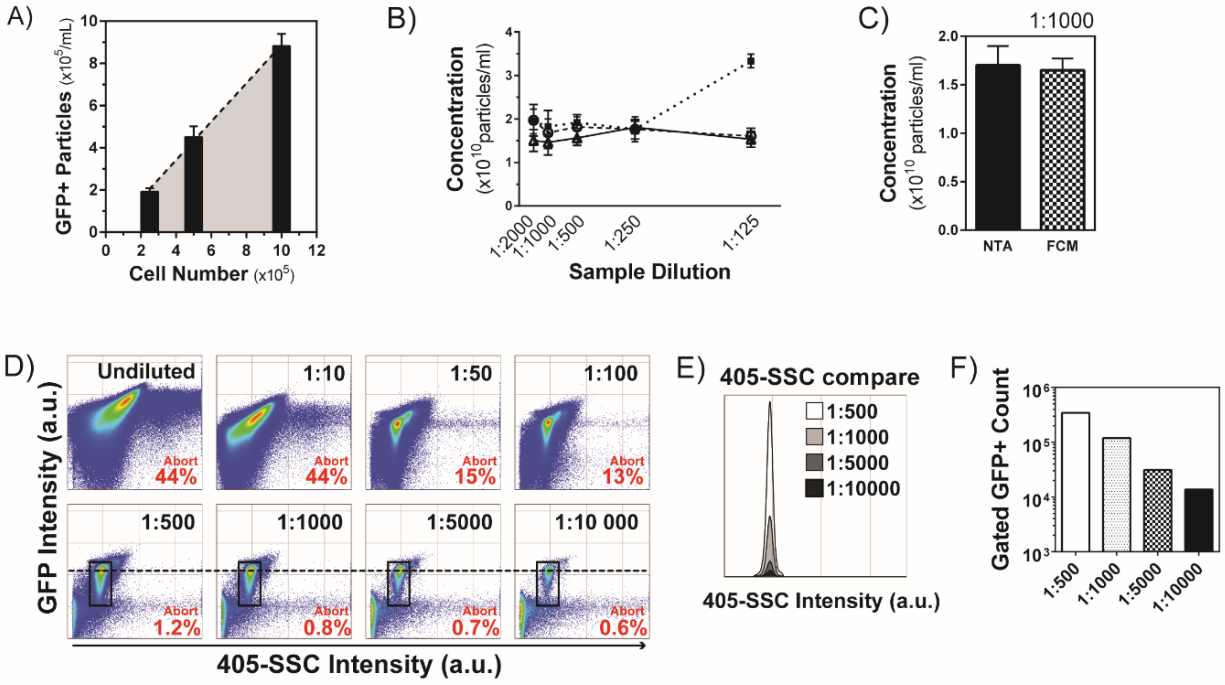

Supplementary Figure 1. Coincidence detection and determination of virus particle concentration through serial dilutions using FCM and NTA. A) Analysis of equivalent volumes of supernatants collected from an MLV infected cell line correlating seeding densities of cells to the amount of virus produced; n=6. B) Calculated particle concentration of MLVsfGFP in undiluted supernatant based on concentrations measured by NTA in serial dilutions (n=3). C) The calculated concentration of undiluted MLVsfGFP supernatant based on measurements determined by NTA and FCM using samples diluted 1:1000 (n=3). D) Flow cytometry analysis of MLV dilutions showing the abort rates and increase in measured GFP fluorescence intensity and 405-SSC intensity of MLVsfGFP at the highest concentrations. E) An overlay of the events from the highest dilutions to compare 405-SSC scatter intensities. F) Linear correlation of GFP+ events (gated in (Fig. 1A) with dilution factor.

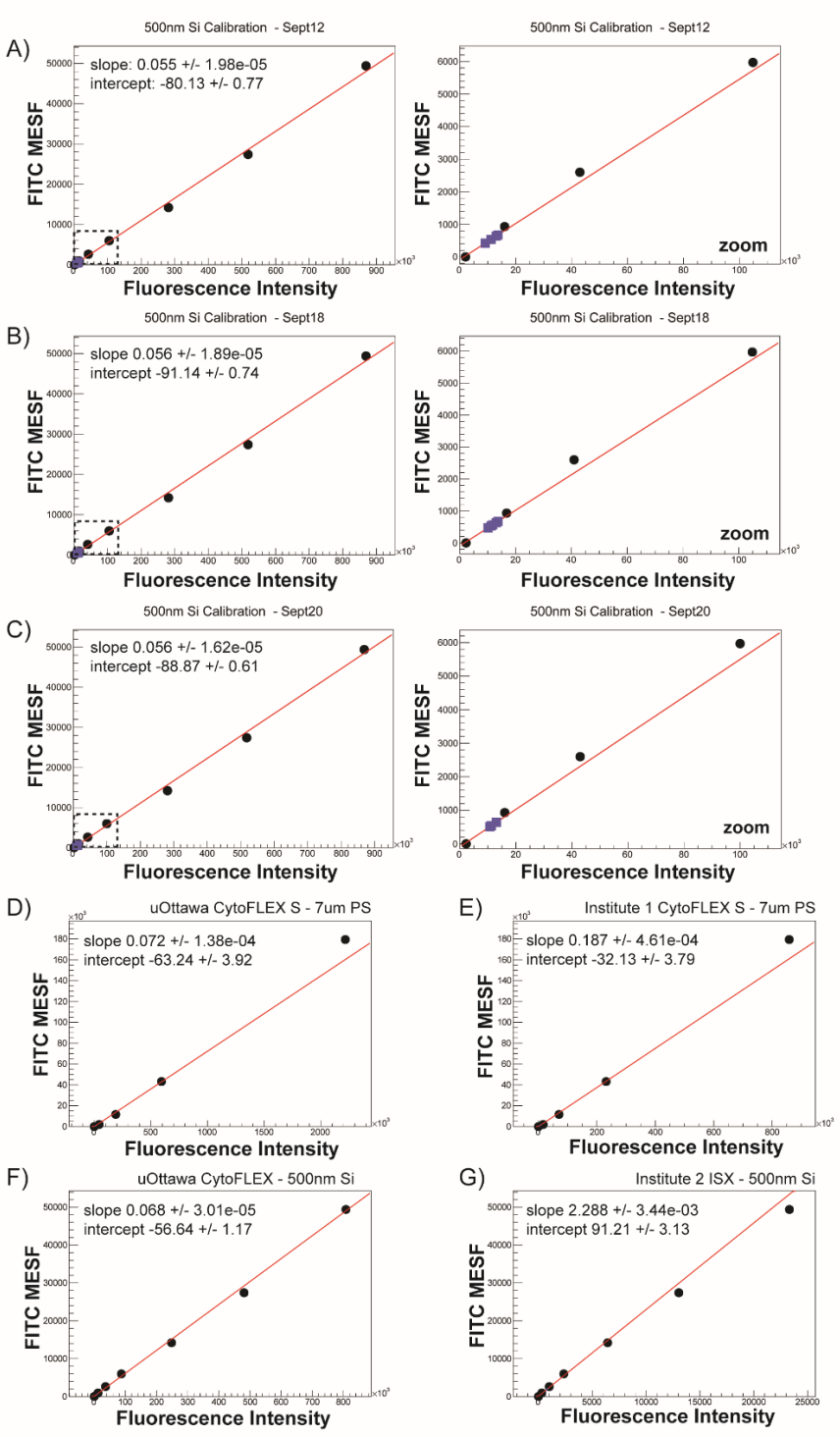

Supplementary Figure 2. Calibration Curves for MESF calculations for Figures 2 & 3. (A to C) Calibration curves for 500nm Si MESF beads for data collected on 3 separate dates for MESF values summarized in Figure 2G. (D) Calibration curve for uOttawa CytoFLEX S using 7 µm PS FITC MESF Beads. (E) Calibration curve for Institute 1 CytoFLEX S using 7 µm PS FITC MESF Beads. (F) Calibration curve for uOttawa CytoFLEX S using 500 nm Si FITC MESF Beads. (G) Calibration curve from Institute 2 ISX using 500 nm Si FITC MESF Beads.

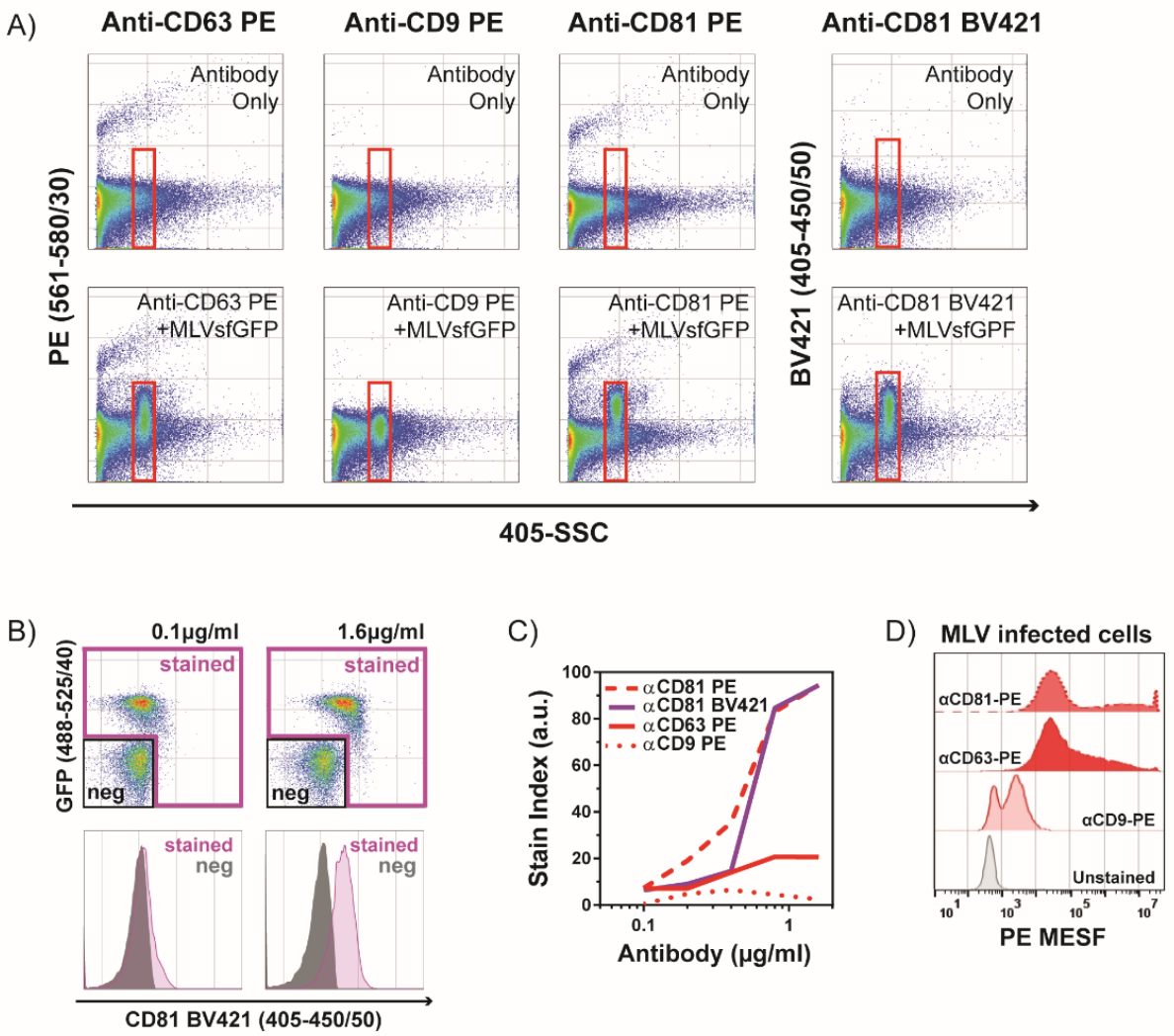

Supplementary Figure 3. Anti-tetraspanin labeling of MLVsfGFP and MLVsfGFP infected cells. (A) Gating strategy for virus events to remove antibody aggregates using antibody only controls. All events are displayed as PE Intensity vs. 405-SSC Intensity for anti-mouse PE conjugates for CD9, CD63, and CD81. (B) Gated events from (A) are displayed as GFP vs. PE Intensity. These events were then calibrated to be displayed as FITC MESF vs PE MESF in Figure 6. (B) Gating strategy used to identify stained and negative populations used to calculate SI. (C) SI for anti-CD81-PE, anti-CD81-BV421, anti-CD63-PE, and anti-CD9-PE at concentrations from 0.1 µg/ml to 1.6 µg/ml. D) Anti-tetraspanin labeling of chronically infected producer cells for MLVsfGFP, representative histogram of n=3.

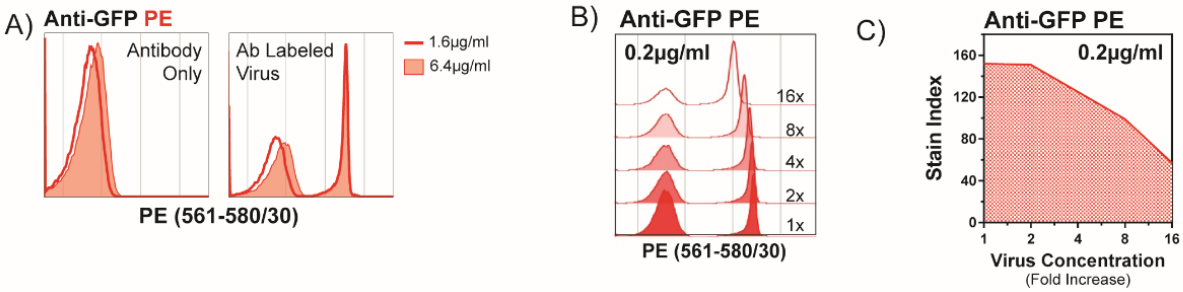

Supplementary Figure 4. Effect of changes in particle and antibody concentration on the stain index of antibody labeled MLVsfGFP. (A) Histogram overlay of MLVsfGFP labeled with anti-GFP-PE at increasing virus concentrations while maintaining staining concentration of 0.2 µg/ml. 1x is the original virus concentration used to obtained optimal stain index at 0.2 µg/ml. (B) Stain index calculated from (A). (C) Histogram overlay of anti-GFP-PE antibody-alone at 1.6 µg/ml and 6.4 µg/ml (left panel) and anti-GFP-PE labeled MLVsfGFP + MLVnoGFP (right panel) showing staining of the MLVsfGFP population is saturated at 1.6 µg/ml.

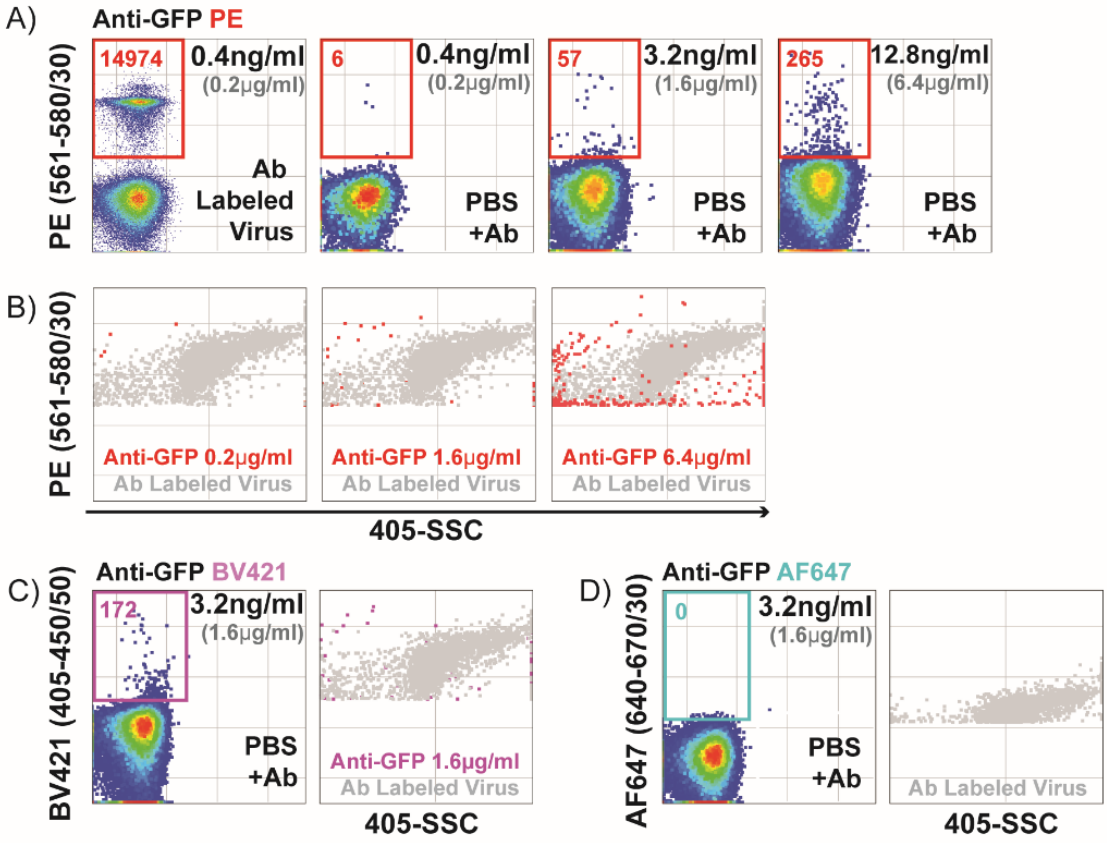

Supplementary Figure 5. Detection of antibody aggregates in anti-GFP conjugates. (A) Dilutions of anti-GFP-PE antibody alone were analyzed at 0.2µg/ml (optimal staining concentration), 1.6µg/ml and 6.4µg/ml. The first panel on the left denotes MLVsfGFP stained at a concentration of 0.2µg/ml. Concentrations in black indicate the actual concentration of antibody as it is diluted for analysis on the cytometer. Values in red are PE+ event counts within the red gate. (B-D) Overlays of MLVsfGFP labeled at optimal staining concentration (gray events) with increasing concentrations of (B) anti-GFP-PE; (C) 1.6µg/ml of anti-GFP-BV421; and (D) anti-GFP-AF647. Representative plots for three independent experiments are shown.

Appendix 3

Preface: This chapter has been previously published as a research article:

Brittain, G.C., Chen, Y.Q., Martinez, E. et al. A Novel Semiconductor-Based Flow Cytometer with Enhanced Light-Scatter Sensitivity for the Analysis of Biological Nanoparticles. Sci Rep 9, 16039 (2019) http://doi:10.1038/s41598-019-52366-4.

SCIENTIFIC REPORTS
nature research

OPEN

A Novel Semiconductor-Based Flow Cytometer with Enhanced Light-Scatter Sensitivity for the Analysis of Biological Nanoparticles

George C. Brittain IV[1], Yong Q. Chen[1], Edgar Martinez[2], Vera A. Tang[3,4], Tyler M. Renner[4], Marc-André Langlois[3,4,5] & Sergei Gulnik[1*]

The CytoFLEX is a novel semiconductor-based flow cytometer that utilizes avalanche photodiodes, wavelength-division multiplexing, enhanced optics, and diode lasers to maximize light capture and minimize optical and electronic noise. Due to an increasing interest in the use of extracellular vesicles (EVs) as disease biomarkers, and the growing desire to use flow cytometry for the analyses of biological nanoparticles, we assessed the light-scatter sensitivity of the CytoFLEX for small-particle detection. We found that the CytoFLEX can fully resolve 70 nm polystyrene and 98.6 nm silica beads by violet side scatter (VSSC). We further analyzed the detection limit for biological nanoparticles, including viruses and EVs, and show that the CytoFLEX can detect viruses down to 81 nm and EVs at least as small as 65 nm. Moreover, we could immunophenotype EV surface antigens, including directly in blood and plasma, demonstrating the double labeling of platelet EVs with CD61 and CD9, as well as triple labeling with CD81 for an EV subpopulation in one donor. In order to assess the refractive indices (RIs) of the viruses and EVs, we devised a new method to inversely calculate the RIs using the intensity vs. size data together with Mie-theory scatter efficiencies scaled to reference-particle measurements. Each of the viruses tested had an equivalent RI, approximately 1.47 at 405 nm, which suggests that flow cytometry can be more broadly used to easily determine virus sizes. We also found that the RIs of EVs increase as the particle diameters decrease below 150 nm, increasing from 1.37 for 200 nm EVs up to 1.61 for 65 nm EVs, expanding the lower range of EVs that can be detected by light scatter. Overall, we demonstrate that the CytoFLEX has an unprecedented level of sensitivity compared to conventional flow cytometers. Accordingly, the CytoFLEX can be of great benefit to virology and EV research, and will help to expand the use of flow cytometry for minimally invasive liquid biopsies by allowing for the direct analysis of antigen expression on biological nanoparticles within patient samples, including blood, plasma, urine and bronchoalveolar lavages.

Extracellular vesicles (EVs) are small, naturally occurring cell fragments that range in size between 30–1000 nm. They are generated in large numbers by living cells throughout the body, and are released as part of both normal and pathological processes. EVs are present in all bodily fluids, and their potential for use as disease biomarkers is the subject of active research in areas of major therapeutic importance, including cancer and cardiovascular disease. However, due to their small size, EVs are difficult to purify and analyze by traditional techniques[1–4].

The most commonly used techniques for purifying EVs from blood and other bodily fluids are ultracentrifugation, size-exclusion chromatography, and PEG precipitation. Each of these are known to have biases for particular small-particle populations based on their densities, sizes, surface charges, or other properties, and each result in variable levels of residual protein and lipoprotein contamination[5,6]. Moreover, experimental characterization of the resulting samples generally consists of bulk methods, including western blots, bead-based

[1]Beckman Coulter Life Sciences, Life Science Research, Miami, FL, USA. [2]Beckman Coulter Life Sciences, Particle Characterization, Miami, FL, USA. [3]University of Ottawa Flow Cytometry and Virometry Core Facility, Ottawa, Canada. [4]Department of Biochemistry, Microbiology and Immunology, Faculty of Medicine, University of Ottawa, Ottawa, Canada. [5]uOttawa Center for Infection, Immunity and Inflammation (CI3), University of Ottawa, Ottawa, Canada. *email: sgulnik@beckman.com

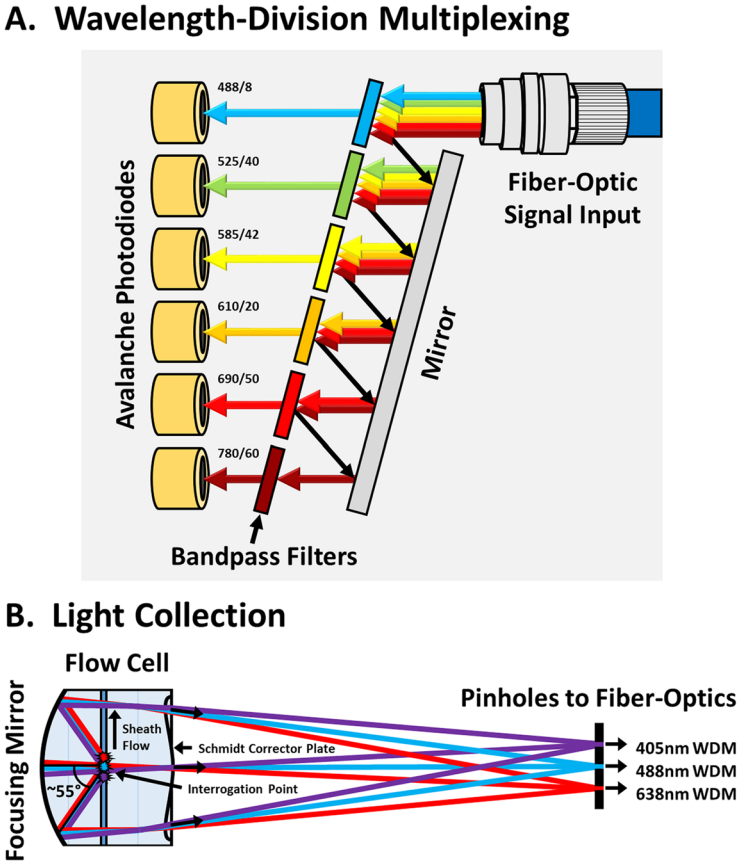

Figure 1. Optical Innovations in the CytoFLEX. (**A**) Wavelength-division multiplexing is a method for parsing ranges of light wavelengths, adapted from fiber-optics technology used in the telecommunications industry. Input light from the fiber-optic cable is sequentially reflected by bandpass filters until the particular wavelength range encounters a permissive filter that allows the light to pass through to its associated APD. This design minimizes the loss of light, as occurs with dichroic mirrors. (**B**) The catadioptric flow-cell design maximizes light collection. Approximately 110° of side-scatter and fluorescent light is focused by a plano-concave mirror on the back of the flow cell. The light path is then shaped by a lens designed similar to a Schmidt corrector plate, which directs light originating from the different lasers to their respective fiber-optic pinholes, while also minimizing the cross-mixing of light.

sandwich assays, genomic assays, dynamic light scattering (DLS) and nanoparticle tracking analysis[4,7,8]. While these methods may provide insights into EV biology, they ultimately obscure individual particle characteristics and, thus, the ability to properly analyze EV populations and subpopulations. In contrast, flow cytometry is the method of choice for single-particle analyses within suspension samples, and may be uniquely suited to address the needs of the EV field[1,3].

Flow cytometry can enable the quantitative, multiparametric characterization of EVs and other biological particles, including viruses and bacteria[9,10]. However, EVs and other biological nanoparticles typically fall within the background noise of conventional flow cytometers, which limits how useful they may be for analyzing such samples. In fact, the most sensitive conventional flow cytometers have been suggested to be unable to detect EVs smaller than roughly 300 nm in diameter[8,11,12]. Since the microvesicle size range actually extends down to 150 nm, and exosomes are said to be between 30–150 nm in diameter, this results in the common notion that only the tip of the EV iceberg can be detected by flow cytometry[1,4].

Improving upon the sensitivity of conventional flow cytometers, we have developed a semiconductor-based flow cytometer, called the CytoFLEX, which pairs silicon avalanche photodiodes (APDs) with wavelength-division multiplexing (WDM), an optimized flow-cell design, and diode lasers in order to maximize signal and minimize noise. Silicon APDs are semiconductor photodetectors that have a higher quantum efficiency and lower electronic noise than traditional photomultiplier tubes, resulting in increased light-detection sensitivity across a larger wavelength range[13–15]. The WDM design, adapted from fiber-optic technology used in the telecommunications industry, eliminates the dichroic mirrors that are traditionally used to divide light into color bands within filter trees, preventing the 20–50+% signal losses that occurs in a typical flow cytometer prior to even reaching the bandpass filters (Fig. 1A)[16]. The CytoFLEX flow cell is specially designed to maximize light capture using catadioptric optical features similar to those found within astronomical telescopes, collecting approximately 110° of side-scatter and fluorescent light, while also reducing optical noise that normally results from the cross-mixing of

light from alternative laser sources (Fig. 1B)[17]. Collectively, these innovations enable the use of low-power diode lasers and small-area APDs, which further reduce electronic and thermal noise[13,18]. As a result, the performance of light-scatter detection on the CytoFLEX is so sensitive that the blue side-scatter (SSC, 488 nm) channel actually requires an attenuation filter to reduce the signal to a range useful for cells and other large particles. As an alternative, violet SSC (VSSC, 405 nm) on the CytoFLEX is unfiltered and can be used to take full advantage of the increased sensitivity for small-particle detection. Using VSSC versus SSC for small-particle detection has an added benefit that the shorter-wavelength light actually increases the amount of light scattered by small particles due to increasing the relative refractive index (RI)[19].

In order to formally assess the light-scatter sensitivity of the CytoFLEX, we set up a series of experiments to test the detection limit for a variety of synthetic and biological nanoparticles. First, we analyzed the different modes of light-scatter detection on the CytoFLEX using a mixture of polystyrene (PS) and silica (Si) size standards, with a size range extending from 81 nm to 2 μm. We then tested a variety of small and low-scatter particles, including both synthetic beads and viruses, in order to better assess the resolution limit for VSSC on the CytoFLEX. Next, we developed a new method for converting scatter-intensity measurements to sizes and/or RIs using scaled Mie-theory curves in order to enable better characterization, and even the prediction of the sensitivity limits, for particles of different compositions. Using this method, we determined the RI of a variety of viruses and then determined the precise sizes and size ranges for the viruses. Finally, we analyzed plasma-derived EVs and compared the VSSC intensity measurements to dynamic light scattering (DLS) in order to correlate the median scatter intensities to bulk size measurements. These measurements were also used to analyze the distribution of RIs for EVs of different sizes, and we confirmed prior observations in literature suggesting that the RI of EVs increases with decreasing size.

Results

Assessing the different modes of light-scatter detection on the CytoFLEX. The CytoFLEX flow cytometer has 3 modes of light-scatter detection: FSC, SSC, and VSSC, which increase in sensitivity in that order. In Supplementary Fig. 1, we demonstrate the differential sensitivity of these 3 modes using a prototype mix of micro- and nanoparticles, called the CytoFLEX Standards Mix.

FSC on the CytoFLEX is not traditional small-angle light scatter, but rather a comparative signal analysis called axial light loss detection[13,20]. It functions by directly analyzing the 488 nm laser beam without an obscuration bar in order to calculate intensity differences as particles pass through the interrogation point, similar to how transit photometry is used in astrophysics to discover and characterize exoplanets in distant star systems[21]. This method has been optimized for larger particles and cell-sized events, with baseline separation for particles larger than 500 nm in diameter (Supplementary Fig. 1A). While this level of FSC sensitivity is lower than some flow cytometers, this approach was specifically designed to minimize variance and eliminate the need for routine alignment, making it more user friendly. This approach also has an added benefit that the resolution of different-sized particles using FSC is mostly independent of the RI of the particle. Indeed, while 1020 nm Si beads (RI = 1.45 at 488 nm)[22] had a lower SSC intensity than 490 nm PS beads (RI = 1.6 at 488 nm)[23], the FSC intensities were proportional to the volume of the particles regardless of the RI. This can be very helpful for reducing the variations in the FSC signatures of biological particles that occur due to differences in membrane integrity, such as with damaged or apoptotic cells[24,25].

The sensitivity of SSC and VSSC on the CytoFLEX can be seen in Supplementary Fig. 1B. We found that SSC could resolve down to 214 nm Si and at least 152 nm PS particles with complete baseline resolution. The unfiltered VSSC detection was even more sensitive and could fully resolve 81 nm PS particles. Both SSC and VSSC on the CytoFLEX are true scatter-based detection methods, and the sizes of the particles that can be detected and resolved depends on their RI.

Assessing the sensitivity of VSSC on the CytoFLEX. In order to better assess the baseline sensitivity of VSSC on the CytoFLEX, we next tested a variety of synthetic and biological nanoparticles with different RIs (Fig. 2). For PS nanoparticles, we found that the CytoFLEX could detect PS beads as small as 60 nm, though these beads did not achieve baseline separation (Fig. 2A). PS beads as small as 70 nm were resolved from noise. For Si nanoparticles, the CytoFLEX could fully resolve 98.6 nm Si beads with a RI of 1.44 (Fig. 2B). Analyses of viral particles revealed that the CytoFLEX can fully resolve Human Adenovirus-5 (HAdV-5), Human Immunodeficiency Virus-1 (HIV-1), and Murine Leukemia Virus (MLV) (Fig. 2C). HAdV-5 is a non-enveloped DNA virus that is approximately 95 nm in diameter[26,27]. HIV-1 is an enveloped retrovirus that has a peak diameter of approximately 100 nm[28,29], but a broad size range resulting in a heavily skewed mean. MLV is another enveloped retrovirus with a diameter of approximately 110 nm[9,30,31]. Herpes Simplex Virus-1 (HSV-1) is a larger DNA virus, with a diameter range between 125 to 250 nm, and a peak tegument distribution between 138 to 176 nm, averaging 157 nm[32,33]. Vaccinia Virus (VV) is a large, ellipsoidal DNA virus, with highly variable size characteristics in literature. In order to assign an approximate spherical diameter to VV for Mie-theory analysis, we calculated the ellipsoidal volumes for VV with size characteristics from 5 references, estimated the diameters for spheres of equivalent volumes, and then determined the average spherical diameter to be 237.5 nm (Supplementary Table 1)[34–38]. The average measurements for each particle are listed in Supplementary Table 2, and more detailed information is in Supplementary Fig. 2.

A method for converting scatter intensity to size or RI. The quantity of light scatter produced by particles depends directly on their RI, which complicates the ability to determine the size of particles based on reference standards with a different RI. Synthetic reference standards are still useful, though, because they have well-defined characteristics that remain constant regardless of the instrument or detection method. In order to help improve the characterization of small particles with different compositions by flow cytometry, we devised

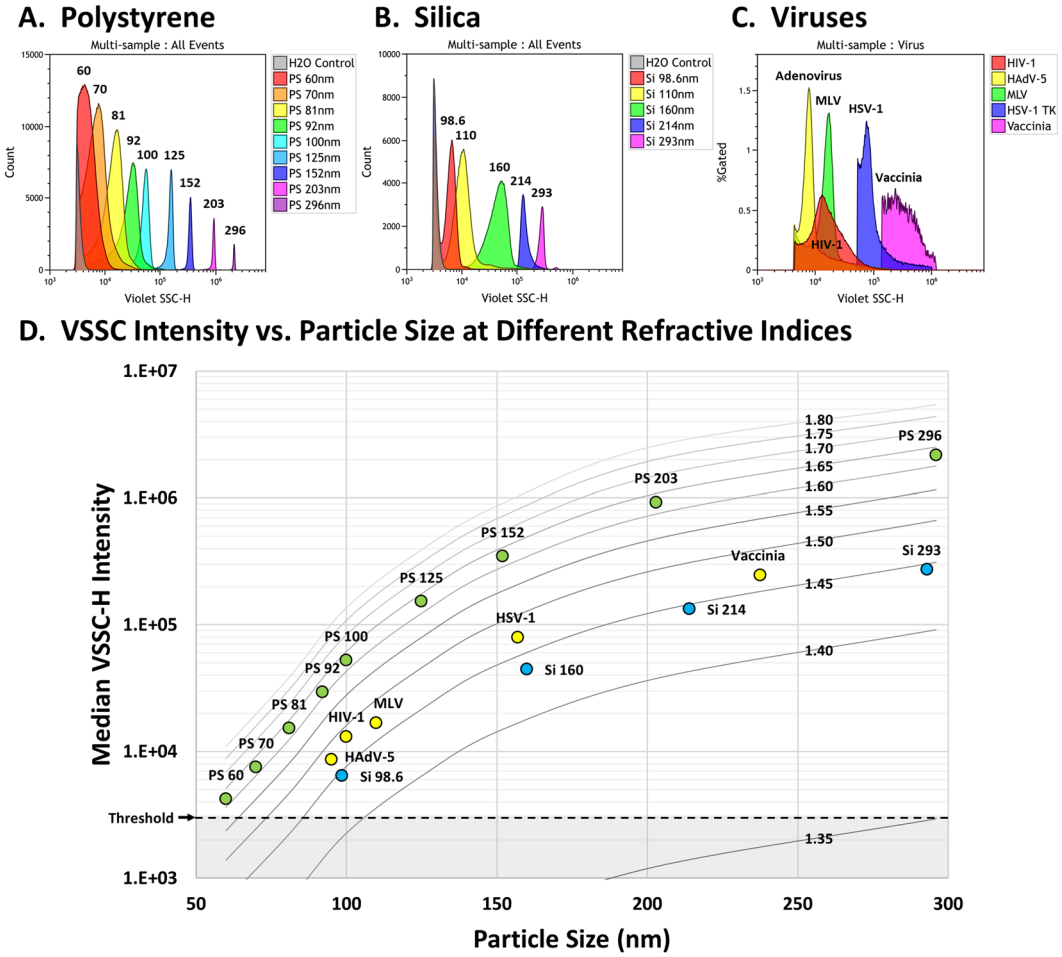

Figure 2. VSSC Sensitivity. (**A**) The detection of 60–296 nm PS particles by VSSC. The CytoFLEX can detect as small as 60 nm PS nanoparticles, and can resolve as small as 70 nm. (**B**) The detection of 98.6–293 nm Si particles by VSSC. 98.6 nm Si particles with a RI of 1.44 can be fully resolved by VSSC. (**C**) VSSC detection of viruses. Unlabeled 95 nm HAdV-5, 100 nm HIV-1, and 110 nm MLV can be fully resolved by light scatter on the CytoFLEX. (**D**) A contour plot prepared using Mie-theory RI curves scaled to the CytoFLEX VSSC intensities. The data from (**A–C**) were overlaid on the plot to verify the accuracy of the scaling. All samples were collected in triplicate and these data represent the population means. VSSC gain = 400; VSSC-H threshold = 3000. The VSSC-H threshold for HSV-1 and Vaccinia was 40 K and 100 K, respectively.

a simple method for approximating the size or RI of particles based on their scatter intensity and one or the other parameter. Standard approaches to determining particle characteristics based on light scatter and inverse Mie-theory calculations require a variety of instrument variables that may not be known or readily available[39,40]. Because all of these variables are contained within the real scatter intensities produced by the instrument, we hypothesized that we could actually use reference standards to scale Mie-theory curves to the scatter intensities expected for the flow cytometer. We calculated the expected scatter intensities by creating ratio equivalencies of the real intensities for the reference particles divided by their theoretical scatter efficiencies, and then solving for the intensities of particles of the same sizes but different RIs. Since the conversion of scatter intensities between RIs involves a simple ratio of real-versus-calculated intensities, any unknown variables that contribute to the signal cancel out as constants.

A proof of concept for our conversion method is demonstrated in Fig. 2D for the VSSC detection of a variety of nanoparticles on the CytoFLEX. We first measured a set of reference particles with known characteristics, including 60, 81, 100, 125, 152, 203 and 296 nm NIST-traceable PS beads (Supplementary Fig. 3). The RI of PS was calculated to be 1.627 at 405 nm[41], while the RI for water was calculated to be 1.3388[42]. The average scatter intensities and theoretical scatter efficiencies for each particle are listed in Supplementary Fig. 4A. Next, we prepared a matrix of theoretical scatter efficiencies for the particle sizes with RIs between 1.35 and 1.80 (Supplementary Fig. 4B), and then calculated the approximate VSSC intensities for each particle at the different RIs (Supplementary Fig. 4C). Finally, the matrix of calculated VSSC intensities was plotted versus size, with the different curves representing contours of RI equivalencies (Fig. 2D). The accuracy of our method was confirmed by plotting the nanoparticles from Fig. 2A–C into the contour plot: the PS and Si particles fall right into their expected RI ranges, around 1.63 and 1.44, respectively[43]. Interestingly, the RIs for all of the viruses were found

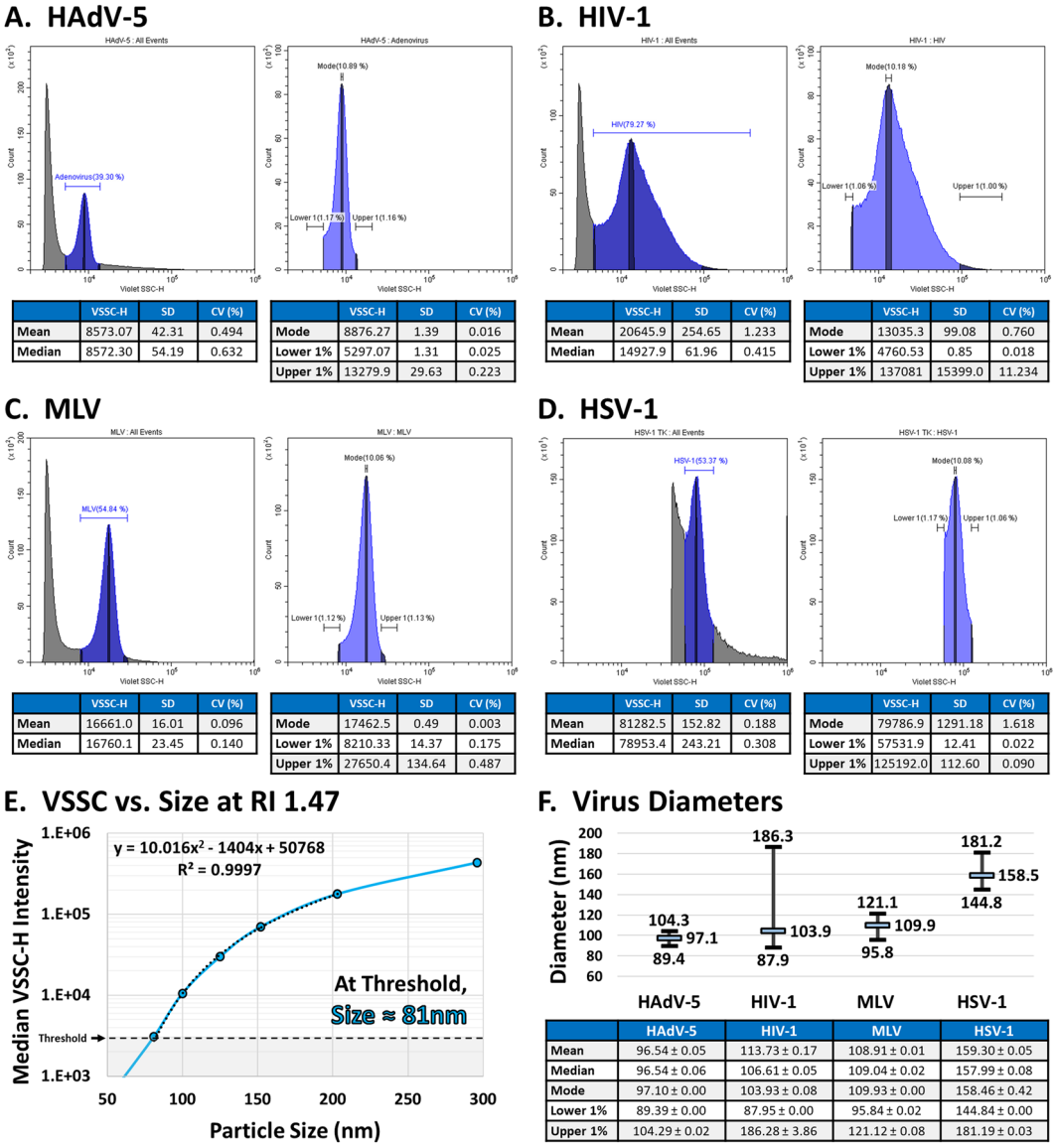

	VSSC-H	SD	CV (%)
Mean	8573.07	42.31	0.494
Median	8572.30	54.19	0.632

	VSSC-H	SD	CV (%)
Mode	8876.27	1.39	0.016
Lower 1%	5297.07	1.31	0.025
Upper 1%	13279.9	29.63	0.223

	VSSC-H	SD	CV (%)
Mean	20645.9	254.65	1.233
Median	14927.9	61.96	0.415

	VSSC-H	SD	CV (%)
Mode	13035.3	99.08	0.760
Lower 1%	4760.53	0.85	0.018
Upper 1%	137081	15399.0	11.234

	VSSC-H	SD	CV (%)
Mean	16661.0	16.01	0.096
Median	16760.1	23.45	0.140

	VSSC-H	SD	CV (%)
Mode	17462.5	0.49	0.003
Lower 1%	8210.33	14.37	0.175
Upper 1%	27650.4	134.64	0.487

	VSSC-H	SD	CV (%)
Mean	81282.5	152.82	0.188
Median	78953.4	243.21	0.308

	VSSC-H	SD	CV (%)
Mode	79786.9	1291.18	1.618
Lower 1%	57531.9	12.41	0.022
Upper 1%	125192.0	112.60	0.090

	HAdV-5	HIV-1	MLV	HSV-1
Mean	96.54 ± 0.05	113.73 ± 0.17	108.91 ± 0.01	159.30 ± 0.05
Median	96.54 ± 0.06	106.61 ± 0.05	109.04 ± 0.02	157.99 ± 0.08
Mode	97.10 ± 0.00	103.93 ± 0.08	109.93 ± 0.00	158.46 ± 0.42
Lower 1%	89.39 ± 0.00	87.95 ± 0.00	95.84 ± 0.02	144.84 ± 0.00
Upper 1%	104.29 ± 0.02	186.28 ± 3.86	121.12 ± 0.08	181.19 ± 0.03

Figure 3. Sizing Viruses by Flow Cytometry. (**A–D**) VSSC-H population statistics for (**A**) HAdV-5, (**B**) HIV-1, (**C**) MLV, and (**D**) HSV-1. Each virus was read in triplicate and the data represent the average. (**E**) Fitting a VSSC-H Intensity vs. Size curve for RI 1.47 at 405 nm in order to calculate virus sizes. (**F**) The calculated size characteristics for each virus in (**A–D**). In the chart above, the calculated peak diameter is displayed along with the size range. The mean and median sizes are also included in the table below, ±the SEM.

to be approximately 1.47 based on the contours. While the RIs for these viruses are not available in literature, and viral characteristics vary, this value is within the middle range for viruses that have been characterized by alternative methods[44]. The exact sizes and RIs can be more precisely calculated by fitting equations to the curves and solving for the unknown variable. In this case, using more precise calculations based on the virus sizes from literature, we determined the RIs at 405 nm to be: 1.474 for HAdV-5, 1.484 for HIV-1, 1.469 for MLV, 1.470 for HSV-1, and 1.466 for VV (Supplementary Figs 5 and 6), averaging 1.473. A common refractive index between viruses would appear to suggest that it correlates to their protein content because the differences in virus size largely represent different quantities of protein. The minor differences in the calculated RIs may be due in part to the imprecision of using approximate sizes from literature. The lower detection limit for additional particles with a RI of 1.47 would be approximately 81 nm at the threshold and 86 nm at the level of 60 nm PS beads (Supplementary Fig. 7).

Characterizing virus sizes by flow cytometry. Since each virus appears to have a common refractive index, and because virus sizes are variable and sometimes imprecise in literature, we next set out to calculate the size characteristics for each virus tested based on their VSSC measurements. The mean, median, and mode VSSC measurements, as well as upper and lower limits can be found in Fig. 3: HAdV-5 (A), HIV-1 (B), MLV (C), and HSV-1 (D). VV was excluded simply due to its asymmetrical shape. The equation fitting the estimated

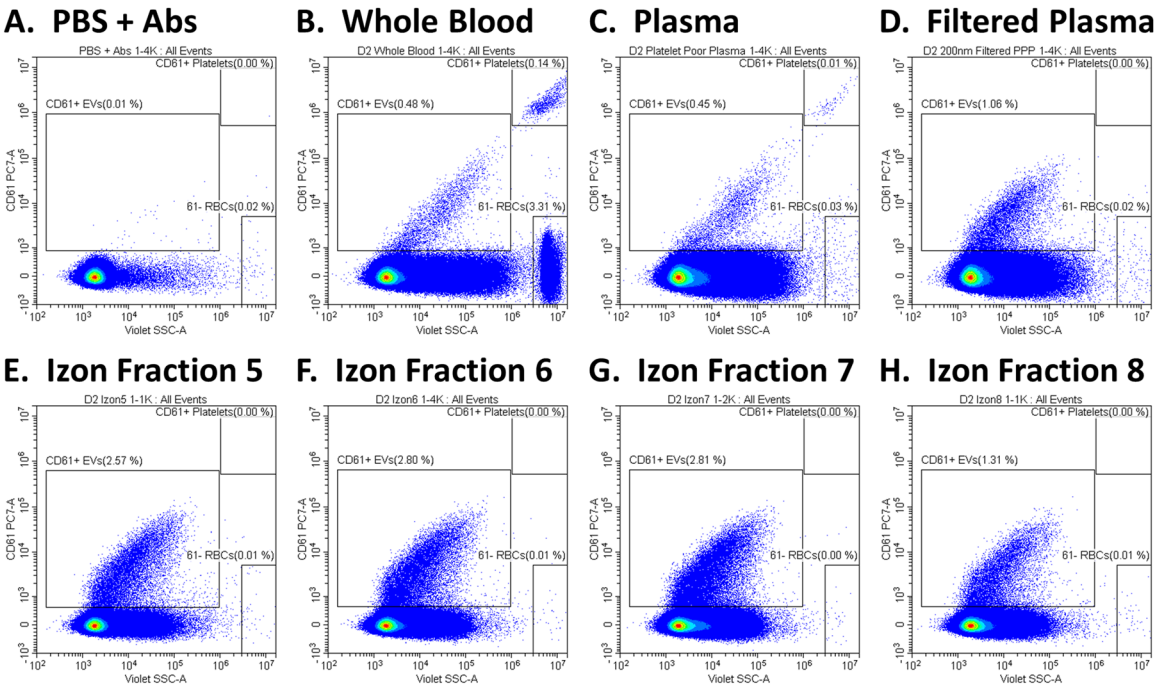

Figure 4. Preparation of Plasma EVs. (**A**) PBS + antibody cocktail as a control to demonstrate the absence of fluorescent-antibody aggregates. (**B**) $CD61^+$ EVs and platelets in whole blood. (**C**) $CD61^+$ EVs in PPP, with RBCs eliminated and platelets depleted. (**D**) $CD61^+$ EVs in PPP filtered through a 0.2 μm filter, with platelets eliminated. (**E–H**) $CD61^+$ EVs in the 5th through 8th 200 μL fraction from 0.2 μm-filtered PPP passed through an Izon qEV column. Serial dilutions were performed and all samples were acquired in triplicate. VSSC gain = 400; VSSC-H threshold = 3000.

VSSC intensities for 81–200 nm particles at a 1.47 RI can be found in Fig. 3E. Using this equation, the sizes of the viruses were calculated in Fig. 3F. Each of the calculated diameters and size ranges conforms well to literature, and may actually have improved accuracy due to sampling hundreds of thousands of intact events rather than a few-hundred hand-selected events from micrographs of highly-processed samples.

Analyzing plasma-derived EVs on the CytoFLEX. In order to determine the detection limit for plasma-derived EVs on the CytoFLEX, we combined a series of sample-preparation approaches to narrow down the size range of the plasma-EV sample fractions. First, we prepared platelet-poor plasma (PPP) by centrifugation. Then, we filtered out any residual large particles using a 0.2 μm filter. Finally, we performed size-exclusion chromatography (SEC), using Izon columns with a 70 nm pore size, to reduce proteins and lipoproteins. Using this approach, we narrowed the size range down to roughly 70–200 nm for comparison between DLS and flow cytometry.

The effectiveness of this approach can be seen in Fig. 4. $CD61^+$ platelets and platelet EVs in whole blood are shown in Fig. 4B[45]. The RBCs were then eliminated, and the platelets reduced, by centrifugation to prepare PPP (Fig. 4C). By filtering the PPP through a 0.2 μm filter, the residual platelets and larger microvesicles were eliminated (Fig. 4D). The filtered PPP samples were then passed through Izon columns, and fractions 5 to 8 were collected as the purified-EV sample fractions. In each of these samples, the amount of background protein and lipoprotein appears reduced, and the relative % of $CD61^+$ EVs increased between 2- to 5-fold over plasma (Fig. 4E–H). Titrations of the Izon fractions, together with the population statistics, can be found in Supplementary Fig. 8. The $CD61^+$ EVs prepared using this method were roughly 50% CD9 double positive, while they were predominantly CD63 and CD81 negative (Fig. 5A and Supplementary Fig. 9). Approximately 8.7% of the $CD61^+$ EVs from Donor 2 were CD81 double positive, including 7.5% that were CD9, CD81 and CD61 triple positive (Fig. 5B). However, the majority of donors appear more similar to Donors 1, 3 and 4. The RBC marker, CD235a, was included as a negative control for platelet EVs, while the PE conjugate was specifically used to control for antibody or protein aggregation in the case of multi-labeled events, since PE is particularly prone to aggregate: the $CD61^+$ EVs were all negative for CD235a-PE, which supports the specificity of the double and triple labeling.

A portion of each sample from Fig. 4E–H was also analyzed by DLS in order to characterize the sizes of each sample fraction. Figure 6A shows representative overlays for both the flow-cytometry and DLS data from the EV fractions. The average median VSSC and size readings can be found in Supplementary Figs 8 and 10. The median sizes for the EV fractions were determined to be between 65–194 nm, confirming the expected bounds for the purification approach. These data were plotted on the scaled Mie-theory RI contour plot prepared in Fig. 2, and interestingly had a perfect linear correlation for each donor within this size range, with R^2 values between 0.930–0.997 (Fig. 6B). If this linear trend for the EV fractions extends lower, then EV detection on the CytoFLEX

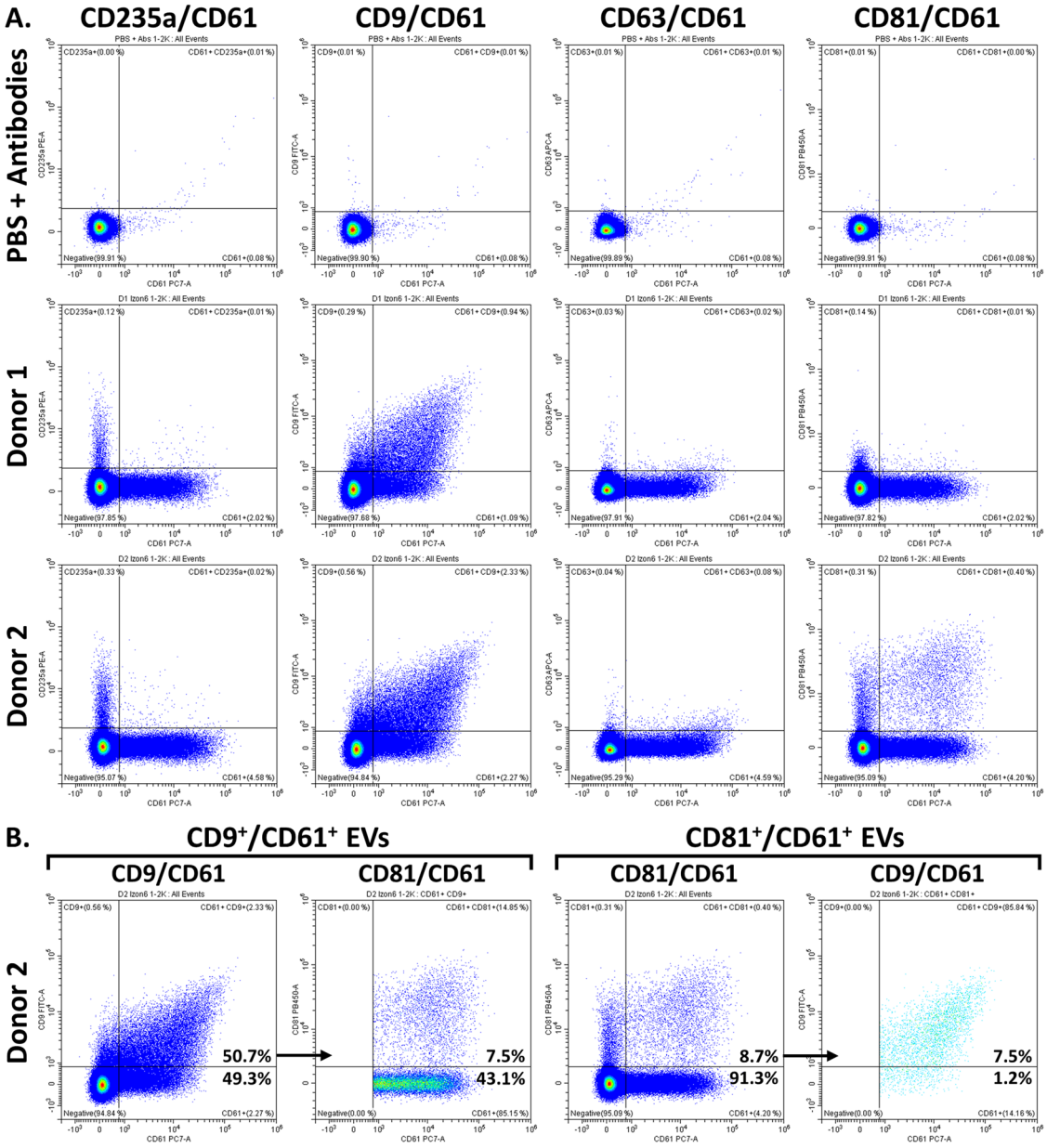

Figure 5. Tetraspanin Expression on the CD61$^+$ plasma EVs. (**A**) CD61$^+$ plasma EVs from human donors were tested for their expression of CD9, CD63 and CD81. The CD61$^+$ EVs were around 50% CD9$^+$, while CD63 and CD81 expression was mostly absent. 8.7% of the CD61$^+$ EVs from Donor 2 were CD81$^+$. The PBS + antibody control demonstrates the lack of fluorescent-antibody aggregates. (**B**) Further analysis of the CD81$^+$ EVs revealed that these were predominantly CD9, CD81 and CD61 triple positive. This is reciprocally demonstrated by analyzing the CD81 expression on CD9$^+$ CD61$^+$ EVs, and the CD9 expression on CD81$^+$ CD61$^+$ EVS. In total, 7.5% of the CD61 EVs from Donor 2 were triple positive. The percentages in bold are in reference to the overall CD61$^+$ EV population. These samples were serially diluted and acquired in triplicate. VSSC gain = 400; VSSC-H threshold = 3000.

should extend down to at least 32.6 nm at the level of 60 nm PS beads, and 12 nm at the threshold level, depending on donor-specific differences in the EV RIs. However, it must be noted that these EV characteristics are average population statistics composed of a distribution of many individual characteristics. We actually calculated the RIs for each EV fraction and found them to range between 1.608 at 64.8 nm and 1.367 at 194.3 nm (Fig. 6C). Further details on the RI calculations for each donor can be found in Supplementary Figs 11–14. This increase in the RI of EVs at smaller sizes is expected due to the increasing ratio of macromolecules to H_2O content[43], and comports well with literature[46].

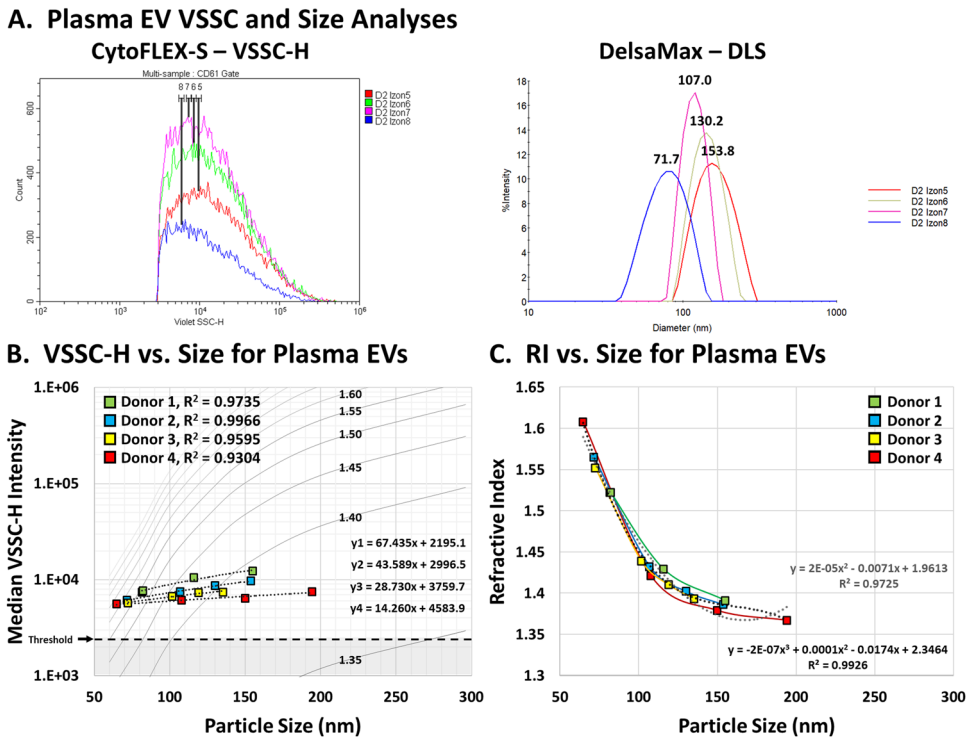

Figure 6. Analysis of the VSSC Sensitivity for EV Detection. (**A**) Analysis of the purified EV fractions by VSSC intensity and DLS sizing. The overlay plots demonstrate the differential VSSC intensities and DLS sizes for representative measurements of the EV fractions from Donor 2. (**B**) Overlay of the average VSSC intensity vs. DLS size measurements for each EV fraction on the scaled Mie-theory RI curves prepared in Fig. 2. The sample distributions are almost perfectly linear, with R^2 values between 0.930 and 0.997 relative to linear trendlines. (**C**) The RIs of the EV fractions increase progressively as their sizes decrease. All samples were serially diluted and the VSSC-H intensity measurements were acquired in triplicate or quadruplicate, while 100 DLS measurements were acquired per sample. VSSC gain = 400; VSSC-H threshold = 3000.

Discussion

We demonstrated that the CytoFLEX flow cytometer can effectively detect and resolve nanoparticles and plasma-derived EVs well in to the exosome range: 30–150 nm. By VSSC, we were able to fully resolve 70 nm PS beads and 98.6 nm Si beads, as well as HAdV-5, HIV-1 and MLV. To our knowledge, no other flow cytometer has ever been demonstrated to resolve adenoviruses and HIV, or PS and Si beads within this size range, by light scatter. MLV detection has been demonstrated on another flow cytometer[9], but the CytoFLEX has much improved resolution and consistency by comparison. Moreover, we found that the CytoFLEX can detect EVs at least as small as 65 nm, triggering with VSSC and immunophenotyping to identify the smallest EV populations. This level of sensitivity can greatly benefit exosome and EV research, as most flow cytometers have been suggested to be unable to detect EVs smaller than 300 nm in diameter[11]. In fact, while our results demonstrate that the CytoFLEX is more sensitive than even dedicated microparticle analyzers[45,47,48], it is indeed a full-fledged flow cytometer with a complete dynamic range for cells and other large particles.

The single biggest innovation that enables such dramatic performance improvement on the CytoFLEX is the use of small-area APDs for signal detection. Small-area APDs have a higher quantum yield, increased linear dynamic range, and minimal dark-current electronic noise[13–15]. The CytoFLEX was the first-in-class flow cytometer to replace traditional PMTs with APDs, and the performance and sensitivity improvements that have been demonstrated ever since have paved the way for others to follow suit. Due to the enhanced sensitivity provided by the APDs, the rest of the optical bench was built around enhancing performance on the lower end of the signal spectrum, rather than brute-force modifications to increase signals, such as with the use of higher-powered lasers. The design of the WDM module on the CytoFLEX, another first-in-class, is an innovative adaptation of fiber-optic technology from the telecommunications industry, allowing for the light signals on the CytoFLEX to be directed to their respective APDs without passing through any light filters or mirrors prior to reaching their final destination (Fig. 1A)[16]. This design allows for maximal signal collection. Conversely, the filter trees in traditional flow cytometers lose 20% or more light per dichroic mirror used to divide the light into color bands, which can result in >50% signal losses for some channels. The design of the flow cell similar to a miniature catadioptric telescope is another first-in-class innovation to maximize light collection, enabling the collection of 110° of side-scatter and fluorescent light (Fig. 1B)[17]. Traditional flow cytometers generally collect only 30–60° of side-scatter and fluorescent light, typically using focusing lenses. Finally, the enhanced signal collection and sensitivity improvements provided by the combined use of small-area APDs, WDMs and the optimized flow-cell design allows for the use of low-power diode lasers, which results in less electronic and thermal noise[18]. The

combined result is a novel, 21st-century, semiconductor-based flow cytometer with robust performance, extreme reliability without the need for constant maintenance and alignment, and improved light-scatter and fluorescence sensitivity, largely enhancing the signal detection on the lower end of a 7-decade dynamic range.

Interestingly, there has been a recent trend where researchers and companies are shifting toward utilizing VSSC for small-particle detection on a variety of instruments. This is presumably due to an increased awareness of the enhanced VSSC sensitivity found on the CytoFLEX, together with knowledge of the Sellmeier observation that the refractive index of a material depends on the wavelength of incident light, particularly that using lower-wavelength light can increase the light scatter of small particles[19]. However, VSSC alone may not provide much benefit toward increasing the sensitivity of such instruments beyond a marginal enhancement in light refraction, which can be easily offset by differences in laser power and other factors. The biggest factor contributing to the enhanced sensitivity of VSSC on the CytoFLEX is simply that the VSSC signal is not attenuated like SSC. The enhanced sensitivity of the CytoFLEX vs. other instruments, even when using diode lasers with less than half of the power output of traditional lasers, is again due to the enhanced optics collecting approximately 110° of orthogonally scattered light, the WDMs minimizing signal losses, and the small-area APDs having a high quantum yield with minimal electronic noise. Some of these factors may have no substantial benefit on their own, but they combine to great effect.

The approach that we developed for converting light-scatter intensity measurements to approximate sizes or RIs is relatively simple and should work with any light-scatter parameter. While forward Mie-theory calculations to predict the light-scatter efficiency of particles can be complex, they are much easier than the inverse calculations needed to determine particle characteristics based on light scatter[49,50]. Indeed, solving Mie-theory equations to determine specific particle characteristics typically requires a variety of complex variables pertaining to the internal engineering of the flow cytometer, which may not be readily available[39,40,45,51,52]. Moreover, Mie-theory solutions have been said to provide a lot more information than necessary, such that relying too heavily on theoretical calculations rather than real measurements can complicate the interpretation of results; e.g., predicting ripples in scatter profiles that may be due to imaginary or radiative components, but are not observed in actual measurements[49,53]. With our approach, scaling the forward Mie-theory calculations to actual reference-particle intensities, we addressed the inverse source problem by simply canceling out any unknown instrument variables as constants. Using this approach, we were able to effectively characterize the sensitivity of the CytoFLEX for biological and synthetic particles of different compositions, and even found that flow cytometry can be an effective tool for rapidly and accurately sizing viruses based on their apparent common RI: approximately 1.47 at 405 nm. Further testing will be needed to verify this result since it is certainly possible that there are deviations, particularly outside of the size range tested or with different experimental conditions.

Our current research on the CytoFLEX optics involves further improving the scatter and fluorescence sensitivity, with the goal of developing an analyzer that can provide complete baseline resolution for the smallest biological nanoparticles, including exosomes and small viruses. However, with thoughtful sample preparation and proper instrument operation, we have found that the current state-of-the-art CytoFLEX can already enable the detection and analysis of a variety of nanoscale viruses and EVs at the single-particle level, including EVs directly in whole blood and plasma. This enhanced functionality is perhaps uniquely capable of helping scientists and clinicians to achieve their goal of developing EV-based liquid biopsies for hard-to-detect diseases, such as tissue-resident cancers, minimal residual disease, and even neurological disorders. EV-based companion diagnostics also promise to provide for earlier diagnoses of diseases, such as heart attacks and strokes, better stratification and prediction of therapeutic outcomes, and improved analyses of disease progression, any one of which would revolutionize the future of personalized medicine[1,2,4].

Methods

Blood. Fresh blood was collected onsite daily by Blood Services using K3-EDTA Vacutainers (Becton Dickinson, Franklin Lakes, NJ). All samples were obtained from normal adult human donors under signed informed consent, as per Western Institutional Review Board-reviewed and -approved protocol. All methods were performed in accordance with the relevant guidelines and regulations.

Reagents. The CytoFLEX Standards Mix is a prototype bead mix from Beckman Coulter (Brea, CA), consisting of 81, 100, 152, and 296 nm NIST-traceable polystyrene (PS) beads, 214, 1020 and 2000 nm NIST-traceable silica (Si) beads, and 100, 196 and 490 nm green-fluorescent PS beads. The 60 (3060A), 70 (3070A), 81 (3080A), 92 (3090A), 100 (3100A), 125 (3125A), 152 (3150A), 203 (3200A) and 296 nm (3300A) NIST-traceable PS beads were from ThermoFisher Scientific (Waltham, MA). The 68.6 (NS-0070A) and 98.6 nm (NS-0100A) NIST-traceable Nanosilica beads were from MSP Corporation (Shoreview, MN). The 110 nm Si beads were from Sigma Aldrich (803308, St. Louis, MO). The 160 (SS02000) and 293 nm (SS02001) Si beads were from Bangs Laboratories (Fishers, IN). The 214 nm Si beads were obtained from Corpuscular (140140-10, Cold Spring, NY). Live HAdV-5 was purchased from Vector Biolabs (1060, Malvern, PA). Formalin-inactivated HIV-1 (HV-H-Zero) and MLV (MV-M-Zero) were obtained from ViroFlow Technologies, Inc. (Ottawa, Canada). The HSV-1 and VV were custom viral preparations prepared by freeze/thaw cell fracturing[10], also from ViroFlow Technologies, Inc. CD9-FITC (IM1775U), CD235a-PE (IM2211U), CD61-PC7 (IM3761), and CD81-PB (B19717) were from Beckman Coulter (Brea, CA). CD63-APC was from BioLegend (353008, San Diego, CA). Izon qEVsingle/70 nm SEC columns were purchased from Izon Science LTD (SP2, Oxford, United Kingdom).

Nanoparticle preparation. Nanoparticles were diluted from their stock concentrations into HPLC water (WX0008-1, MilliporeSigma, Burlington, MA) before running on the flow cytometer. In order to find the appropriate working concentrations, initial 1:100 or 1:1000 concentrations were prepared, and these were then serial diluted at a 1:2 ratio until swarming was minimized or eliminated and the signal-to-noise ratios were optimal.

Plasma EV sample preparation. Plasma was prepared from fresh human blood by a combination of centrifugation and filtration. Whole blood was aliquotted into 12 × 75 mm tubes and then PPP was prepared using a 2-step process. First, the blood was centrifuged for 5 min at 160 × g in an Allegra 6 R Centrifuge (366816, Beckman Coulter, Brea, CA), and the upper supernatant was collected as PPP, careful to avoid collection of platelet-rich plasma near the WBC layer[54]. Rather than subjecting the PPP to additional centrifugation steps that can also eliminate EVs, the residual platelets and larger particles were then eliminated by filtering the collected PPP through a 0.2 μm Acrodisc syringe filter #4612 (Pall Corporation, Port Washington, NY). The filtered PPP was then passed through Izon qEVsingle SEC columns with a 70 nm pore cutoff in order to eliminate the abundance of proteins and lipoproteins present below the size cutoff for the columns, while further narrowing the size distributions in the different column fractions. SEC was performed according to the manufacturer's instructions. Briefly, the columns were first flushed with 1x PBS (1408, Sigma-Aldrich, St. Louis, MO), 150–200 μL of PPP was then applied to the column, and this was followed by the addition of PBS to elute the sample fractions. The initial 800 μL of column eluate was voided, while further 200 μL fractions were collected for analysis by both DLS and flow cytometry.

Antibody labeling. Immunophenotyping was performed on the plasma-EV samples to identify the populations of interest. To label with antibodies, the antibodies were first mixed in their appropriate concentrations in a master mix. The optimal concentrations were empirically determined for each antibody. 50 μL of plasma or EV samples were aliquotted into different 12 × 75 mm tubes, and an aliquot of the antibody mixture was added to each sample. The samples were then allowed to incubate for at least 1-hour in the dark at RT. After labeling, the samples were diluted into flow-cytometry resuspension buffer (1x PBS + 0.2% PFA) and aliquotted into a 96-well plate for flow-cytometric analyses. Depending on the preparation method and particular donor, the appropriate dilution for the plasma-EV samples prior to analysis was typically within the range of 1:1 K to 1:4 K relative to the initial plasma when running at a medium sample rate (30 μL/min). In order to accommodate for donor-to-donor differences, all samples were serially diluted and acquired at a variety of dilutions between 1:250 and 1:4 K.

Flow cytometry. All experiments in this study were performed using a 13-color, 4-laser CytoFLEX S N-V-B-R Flow Cytometer, equipped with 375 nm, 405 nm, 488 nm and 638 nm lasers (B78557, Beckman Coulter, Brea, CA) (research use only; not for diagnostics), and operated using CytExpert Software v1.2 (Beckman Coulter, Brea, CA). For small-particle analysis, the configuration was modified for VSSC detection. Briefly, the 405/10 VSSC filter was moved to the V450 channel in the WDM, while the V450 and V525 channels were each shifted (eliminating the V610 channel), and the detector configuration was modified in the CytExpert software to assign the VSSC channel within the WDM. The Event-Rate Setting was set to High prior to initiating analyses, tightening the pulse window and thus reducing the background for small-particle analyses. Finally, the trigger channel was set to VSSC-Height and the threshold level was manually set as appropriate for the small particles. The particular threshold setting for different instruments directly correlates to the laser power and VSSC gain, and depends on how much optical noise the particular user prefers in the background, but it is usually in the range of 10x the gain setting. The optimal threshold setting for the CytoFLEX S N-V-B-R was determined empirically using 81 nm PS nanoparticles at their optimal dilution. Most experiments in this study were conducted using a VSSC gain of 400 with a VSSC-H threshold of 3000.

Prior to running the small-particle experiments, the sample probe was cleaned to reduce any debris. This step is particularly important for small-particle experimentation because any debris in the sample lines will increase the background noise and potentially swarm with the population of interest. Most noise of this nature resides in the scatter range below 100 nm PS beads, so this may not be a notable issue for less sensitive flow cytometers. For semi-automatic acquisition mode, cleansing was performed using a panel of bleach, FlowClean Cleaning Agent (A64669, Beckman Coulter, Brea, CA) and then two tubes of clean water to flush out the remaining detergent and debris, at the max rate for 1–2 minutes each. For plate-loader mode, this was performed using 2x alternating wells of FlowClean and water, followed by two additional wells of water to finish flushing any residual detergent and debris prior to the first sample. These steps were repeated if necessary.

Dynamic light scatter. DLS experiments were performed using a DelsaMax Pro Analyzer (B29164, Beckman Coulter, Brea, CA) according to the manufacturer's instructions. Following SEC, 100 μL of sample was aliquotted into a cuvette, and each sample was read 10x with 10 acquisitions per read (100 acquisitions in total). If necessary, the samples were diluted as much as 1:20 in 1x PBS. All acquisitions were performed for 2-seconds each at 25 °C, with the peak radius between 0.5 to 10,000 nm and the autocorrelation function set to between 2.0 to 200,000 μs. The median diameter for each sample was calculated using cumulants analyses on the % Intensity measurements from Brownian motion using the Rayleigh Spheres model. Outliers and skewing were minimized for the DLS readings by preparing the samples with narrow size distributions, as previously described. The DelsaMax Pro was standardized using 68.6 (NIST), 98.6 (NIST), 160 and 214 nm Si particles (Supplementary Fig. 15).

Data analyses. All flow cytometry data were analyzed using CytExpert v2.3 and Kaluza v1.5 (Beckman Coulter, Brea, CA). First, the compensation matrix was fine-tuned for the samples, if applicable. Next, the population gates were adjusted for each sample, a statistics table was prepared, and the population data were then exported to prepare charts and graphs using Excel 2013 (Microsoft, Redmond, WA). DLS data were analyzed using DelsaMax Software v1.6.1.17 (Beckman Coulter, Brea, CA).

Statistical analyses. All statistical analyses were performed in Excel 2013. Each sample was read in triplicate or more, and the population means were calculated by averaging the median or mean intensity measurements from each individual data point. The standard deviation for each sample was calculated using the STDEV

function, which calculates $SD = \sqrt{\frac{\sum_{i=1}^{N}(x_i - \bar{x})^2}{N-1}}$. The coefficients of variation (CVs) as a percentage, $CV(\%) = \left(\frac{SD}{Mean}\right) \times 100\%$. The standard error margin (SEM) $= \frac{SD}{\sqrt{N}}$.

Mie-theory conversions. The scatter efficiencies were calculated using the Fortran-based, Wiscombe Mie-theory code, MIEV0, available online from the Oregon Medical Laser Center (omlc.org/software/mie/). The theoretical scatter efficiencies at 405 nm were calculated for a variety of particles sizes (equivalent to the PS standards), and at multiple RIs between 1.35 and 1.80 (in 0.05 increments). The RI for PS was calculated to be 1.627 at 405 nm[41], and the RI for water was calculated to be 1.3388 at 405 nm[42]. After the VSSC-H intensities were measured for the PS reference particles, the matrix of Mie-theory scatter efficiencies was converted to scaled VSSC intensities by calculating equivalency ratios between the reference standards and the values for equivalently size particles at the different RIs. The theoretical intensities were calculated by solving the equivalency ratios for the unknown variable, as follows:

$$Theoretical\ Intensity = \left(\frac{Actual\ VSSC\ Intensity}{Reference\ Scatter\ Efficiency}\right) \times Theoretical\ Scatter\ Efficency.$$

This scaling approach does not require an exhaustive number of reference beads, but the more points that are included within the targeted size range, the more accurate the contours and calculations will be.

Calculations of either the RIs or the sizes of the different particles can be accomplished in a similar manner. If multidimensional analysis software is not available, the unknown values can be calculated manually by focusing in on one dimension at a time. In order to calculate the RI of particles based on their intensity measurement and size, an equation should first be best fit to the reference curve. This equation can then be solved for the approximate scatter intensity of a reference particle at the size of interest. Next, a matrix of Mie-theory scatter efficiencies is prepared for different RIs using the size of interest, and this matrix is converted to scaled instrument intensities as above, using the approximate scatter intensity previously calculated as the reference intensity. The best-fit equation for this intensity curve can be solved to determine the RI of the particle at the experimentally measured intensity. Since determining small differences in the decimal places of a RI vs. non-linear differences in scatter intensities many orders of magnitude greater can be difficult and inaccurate using polynomial equations, a simpler alternative is to focus in on the estimated RI range based on the main contour plot, and then use smaller RI increments, such as 0.01, focused within the range of interest. The 2 RI increments on either side of the experimentally measured intensity can be identified, and a linear equation between these 2 points can be easily solved to closely approximate the RI of the sample. This method is similar to solving for the tangent of a curve in calculus, where the tighter the interval gets, the more the curve approaches a straight line that provides for a reasonably accurate localized slope. Curves demonstrating such a linear tangential fit were prepared by overlaying 2 separate charts with equivalent scales: one with the main curve and the second with a linear trendline connecting only the two RIs closest to the target range. Equations with scatter intensity as one of the variables will be specific to the instrument and settings used for analysis, and will need to be scaled using empirical reference-particle measurements.

Data availability

All of the flow-cytometry data are archived at FlowRepository.org. Other data are available upon request.

Received: 23 June 2019; Accepted: 15 October 2019;
Published online: 05 November 2019

References

1. Welsh, J. A., Holloway, J. A., Wilkinson, J. S. & Englyst, N. A. Extracellular vesicle flow cytometry analysis and standardization. *Front. Cell Dev. Biol.* **5**, 78, https://doi.org/10.3389/fcell.2017.00078 (2017).
2. Willms, E., Cabañas, C., Mäger, I., Wood, M. J. A. & Vader, P. Extracellular vesicle heterogeneity: subpopulations, isolation techniques, and diverse functions in cancer progression. *Front. Immunol.* **9**, 738, https://doi.org/10.3389/fimmu.2018.00738 (2018).
3. Stoner, S. A. *et al*. High sensitivity flow cytometry of membrane vesicles. *Cytometry A* **89**(2), 196–206 (2016).
4. Van der Pol, E., Böing, A. N., Harrison, P., Sturk, A. & Nieuwland, R. Classification, functions, and clinical relevance of extracellular vesicles. *Pharmacol. Rev.* **64**, 676–705 (2012).
5. Sodar, B. W. *et al*. Low-density lipoprotein mimics blood plasma-derived exosomes and microvesicles during isolation and detection. *Sci. Rep.* **6**, 24316, https://doi.org/10.1038/srep24316 (2016).
6. Simonsen, J. B. What are we looking at? Extracellular vesicles, lipoproteins, or both? *Circ. Res.* **121**, 920–922 (2017).
7. Shao, H. *et al*. New technologies for analysis of extracellular vesicles. *Chem. Rev.* **118**, 1917–1950 (2018).
8. Van der Pol, E. *et al*. Optical and non-optical methods for detection and characterization of microparticles and exosomes. *J. Thromb. Haemost.* **8**, 2596–2607 (2010).
9. Tang, V. A., Renner, T. M., Fritzsche, A. K., Burger, D. & Langlois, M.-A. Single-particle discrimination of retroviruses from extracellular vesicles by nanoscale flow cytometry. *Sci. Rep.* **7**, 17769, https://doi.org/10.1038/s41598-017-18227-8 (2017).
10. Tang, V. A. *et al*. Single-particle characterization of oncolytic vaccinia virus by flow virometry. *Vaccine* **34**(42), 5082–5089 (2016).
11. Van der Pol, E., Sturk, A., van Leeuwen, T., Nieuwland, R. & Coumans, F. Standardization of extracellular vesicle measurements by flow cytometry through vesicle diameter approximation. *J. Thromb. Haemost.* **16**, 1236–1245 (2018).
12. Zwicker, J. I. *et al*. Tumor-derived tissue factor-bearing microparticles are associated with venous thromboembolic events in malignancy. *Clin. Cancer Res.* **15**(22), 6830–6840 (2009).
13. Chen, Y. Q. Flow cytometer. *US Patent* 10,330,582 B2. June 25th (2019).
14. McClish, M., Farrell, R., Vanderpuye, K. & Shah, K. S. A reexamination of silicon avalanche photodiode gain and quantum efficiency. *IEEE Nucl. Sci. Symp. Conf. Rec.* **J03-49**, 2959–2962 (2005).
15. Lawrence, W. G., Varadi, G., Entine, G., Podniesinski, E. & Wallace, P. K. A comparison of avalanche photodiode and photomultiplier tube detectors for flow cytometry. *Proc. SPIE* **6859**, 68590M, https://doi.org/10.1117/12.758958 (2008).
16. Chen, Y. Q. Flow cytometer. *US Patent* 9,746,412 B2. Aug. 29th (2017).

17. Chen, Y. Q. Flow cytometer. *US Patent* 10,209,174 B2. Feb. 19th (2019).
18. Chen, Y. Q. Flow cytometer. *US Patent* 10,126,227 B2. Nov. 13th (2018).
19. Sellmeier, W. Zur erklarung der abnormen farbenfolge im spectrum einiger substanzen. *Ann. Phys.* **219**(6), 272–282 (1871).
20. Stewart, C. C., Stewart, S. J. & Habbersett, R. C. Resolving leukocytes using axial light loss. *Cytometry* **10**, 426–432 (1989).
21. Charbonneau, D., Brown, T. M., Latham, D. W. & Mayor, M. Detection of planetary transits across a Sun-like star. *Astrophys. J. Lett.* **529**(1), L45–L48 (2000).
22. Malitson, I. H. Interspecimen comparison of the refractive index of fused silica. *J. Opt. Soc. Am.* **55**(10), 1205–1209 (1965).
23. Nikolov, I. D. & Ivanov, C. D. Optical plastic refractive measurements in the visible and the near-infrared regions. *Appl. Opt.* **39**(13), 2069–2070 (2000).
24. Terstappen, L. W. M. M., Shah, V. O., Conrad, M. P., Recktenwald, D. & Loken, M. R. Discriminating between damaged and intact cells in fixed flow cytometric samples. *Cytometry* **9**, 477–484 (1988).
25. Wlodkowic, D., Telford, W., Skommer, J. & Darzynkiewicz, Z. Apoptosis and beyond: cytometry in studies of programmed cell death. *Methods Cell. Biol.* **103**, 55–98 (2011).
26. Yu, X. *et al*. Cryo-EM structure of human adenovirus D26 reveals the conservation of structural organization among human adenoviruses. *Sci. Adv.* **3**(5), e1602670, https://doi.org/10.1126/sciadv.1602670 (2017).
27. Condezo, G. N. *et al*. Structures of adenovirus incomplete particles clarify capsid architecture and show maturation changes of packaging protein L1 52/55k. *J. Virol.* **89**(18), 9653–9664 (2015).
28. Faivre-Moskalenko, C. *et al*. RNA control of HIV-1 particle size polydispersity. *PLoS One* **9**(1), e83874, https://doi.org/10.1371/journal.pone.0083874 (2014).
29. Floderer, C. *et al*. Single molecule localization microscopy reveals how HIV-1 gag proteins sense membrane virus assembly sites in living host CD4 T cells. *Sci. Rep.* **8**, 16283, https://doi.org/10.1038/s41598-018-34536-y (2018).
30. Förster, F., Medalia, O., Zauberman, N., Baumeister, W. & Fass, D. Retrovirus envelope protein complex structure *in situ* studied by cryo-electron tomography. *Proc. Natl. Acad. Sci. USA* **102**(13), 4729–4734 (2005).
31. Yeager, M., Wilson-Kubalek, E. M., Weiner, S. G., Brown, P. O. & Rein, A. Supramolecular organization of immature and mature murine leukemia virus revealed by electron cryo-microscopy: implications for retroviral assembly mechanisms. *Proc. Natl. Acad. Sci. USA* **95**, 7299–7304 (1998).
32. Zhou, Z. H., Chen, D. H., Jakana, J., Rixon, F. J. & Chiu, W. Visualization of tegument-capsid interactions and DNA in intact herpes simplex virus type 1 virions. *J. Virol.* **73**(4), 3210–3218 (1999).
33. Laine, R. F. *et al*. Structural analysis of herpes simplex virus by optical super-resolution imaging. *Nat. Commun.* **6**, 5980, https://doi.org/10.1038/ncomms6980 (2015).
34. Müller, G. & Williamson, J. D. Poxviridae. (Nermut, M. V. & Steven, A. C., eds.) *Perspectives in Medical Virology, Volume 3: Animal Virus Structure*. Ch. 26, pg. 425. (Elsevier Science, New York, 1987).
35. Roos, N. *et al*. A novel immunogold cryoelectron microscopic approach to investigate the structure of the intracellular and extracellular forms of vaccinia virus. *EMBO J.* **15**(10), 2343–2355 (1996).
36. Griffiths, G. *et al*. Structure and assembly of intracellular mature vaccinia virus: isolated-particle analysis. *J. Virol.* **75**(22), 11034–11055 (2001).
37. Malkin, A. J., McPherson, A. & Gershon, P. D. Structure of intracellular mature vaccinia virus visualized by *in situ* atomic force microscopy. *J. Virol.* **77**(11), 6332–6340 (2003).
38. Cyrklaff, M. *et al*. Whole cell cryo-electron tomography reveals distinct disassembly intermediates of vaccinia virus. *PLoS One* **2**(5), e420, https://doi.org/10.1371/journal.pone.0000420 (2007).
39. Bohren, C. F. & Huffman, D. R. *Absorption and Scattering of Light by Small Particles*. (John Wiley & Sons, New York, 1983).
40. Ye, Z., Jiang, X. & Wang, Z. Measurements of particle size distribution based on Mie scattering theory and Markov chain inversion algorithm. *J. Softw.* **7**(10), 2309–2316 (2012).
41. Kasarova, S. N., Sultanova, N. G., Ivanov, C. D. & Nikolov, I. D. Analysis of the dispersion of optical plastic materials. *Opt. Mater. (Amst.)* **29**, 1481–1490 (2007).
42. Hale, G. M. & Querry, M. R. Optical constants of water in the 200-nm to 200-μm wavelength region. *Appl. Opt.* **12**(3), 555–563 (1973).
43. Varga, Z. *et al*. Hollow organosilica beads as reference particles for optical detection of extracellular vesicles. *J. Thromb. Haemost.* **16**, 1646–1655 (2018).
44. Pang, Y., Song, H. & Cheng, W. Using optical trap to measure the refractive index of a single animal virus in culture fluid with high precision. *Biomed. Opt. Express* **7**(5), 1672–1689 (2016).
45. Van der Pol, E. *et al*. Absolute sizing and label-free identification of extracellular vesicles by flow cytometry. *Nanomedicine* **14**(3), 801–810 (2018).
46. Gardiner, C. *et al*. Measurement of refractive index by nanoparticle tracking analysis reveals heterogeneity in extracellular vesicles. *J. Extracell. Vesicles* **3**, 25361, https://doi.org/10.3402/jev.v3.25361 (2014).
47. Chandler, W. L., Yeung, W. & Tait, J. F. A new microparticle size calibration standard for use in measuring smaller microparticles using a new flow cytometer. *J. Thromb. Haemost.* **9**, 1216–1224 (2011).
48. Pospichalova, V. *et al*. Simplified protocol for flow cytometry analysis of fluorescently labeled exosomes and microvesicles using dedicated flow cytometer. *J. Extracell. Vesicles* **4**, 25530, https://doi.org/10.3402/jev.v4.25530 (2015).
49. Bohren, C. F. & Nevitt, T. J. Absorption by a sphere: a simple approximation. *Appl. Opt.* **22**(6), 774–775 (1983).
50. Jaffe, J. S. A tomographic approach to inverse Mie particle characterization from scattered light. *Opt. Express* **15**(19), 12217–12229 (2007).
51. Lock, J. A. & Gouesbet, G. Generalized Lorenz-Mie theory and applications. *J. Quant. Spectrosc. Radiat. Transf.* **110**, 800–807 (2009).
52. Wiscombe, W. J. Improved Mie scattering algorithms. *Appl. Opt.* **19**(9), 1505–1509 (1980).
53. Bennet, H. S. & Rosasco, G. J. Resonances in the efficiency factors for absorption: Mie scattering theory. *Appl. Opt.* **17**(4), 491–493 (1978).
54. Tamimi, F. M., Tresguerres, I. & Jerez, L. B. A comparative study of 2 methods for obtaining platelet-rich plasma. *J. Oral Maxillofac. Surg.* **65**, 1084–1093 (2007).

Acknowledgements

We would like to thank Maria Gentile at Beckman Coulter for her support for the CytoFLEX and Life Science Research projects. This work was supported in part by a Discovery Grant and an Idea to Innovation (I2I) Grant by the Natural Sciences and Engineering Research Council of Canada (NSERC) to M.-A.L.

Author contributions

G.C.B., Y.Q.C., S.G. and M.-A.L. designed the experiments and methods. G.C.B., E.M., V.A.T. and T.M.R. prepared the samples and reagents. G.C.B. conducted all flow-cytometry experiments. G.C.B. and E.M. conducted the DLS experiments. G.C.B. analyzed the data and prepared the figures. G.C.B. wrote the manuscript. S.G., M.-A.L., and Y.Q.C. provided critical review of the manuscript. All authors reviewed the results and approved the final manuscript.

Competing interests

G.C.B., E.M. and S.G. are employees of Beckman Coulter, Inc. Y.Q.C. was the VP of Research and CTO of Beckman Coulter, Inc. M.-A.L. is the CEO and V.A.T. is the CSO of ViroFlow Technologies, Inc.

Additional information

Supplementary information is available for this paper at https://doi.org/10.1038/s41598-019-52366-4.

Correspondence and requests for materials should be addressed to S.G.

Reprints and permissions information is available at www.nature.com/reprints.

Publisher's note Springer Nature remains neutral with regard to jurisdictional claims in published maps and institutional affiliations.

Appendix 4

Curriculum Vitae

Tyler Renner

Language Skills

Language	Read	Write	Speak	Understand	Peer Review
English	Yes	Yes	Yes	Yes	

Degrees

2013/9 (2015/8) — Master's Thesis, Microbiology and Immunology, University of Ottawa
Degree Status: All But Degree

Supervisors: Dr. Marc-Andre Langlois

2015/9 - 2019/12 — Doctorate, Microbiology and Immunology, University of Ottawa
Degree Status: Completed
Thesis Title: **Uncovering the Complexities of a Simple Retrovirus: A Study of Glycosylated Gag and Flow Virometry**
Transferred to PhD without completing Masters?: Yes

Supervisors: Marc-André Langlois

Research Disciplines: Microbiology

Areas of Research: Viral Infections

Fields of Application: Biomedical Aspects of Human Health

2009/9 - 2013/4 — Bachelor's Honours, Biopharmaceutical Science, University of Ottawa
Degree Status: Completed

Recognitions

2019/12 — Faculty of Medicine Excellence Award for PhD Research (Canadian dollar)
University of Ottawa
Distinction

2019/10 — Trainee Award, Retropath 2019 (Canadian dollar)
RetroPath
Prize / Award

2019/7 — Travel Award, Mark Wainberg Fund - 2,500 (Canadian dollar)
Canadian Association for HIV Research
Prize / Award

2019/4 — Travel Award, American Society for Virology - 500 (Canadian dollar)
American Society for Virology (ASV)
Prize / Award

2019/3 — Nominated as top 5% in program to attend the CSHRF (Canadian dollar)
Canadian Student Health Research Forum
Distinction

2018/10	Best NanoScale Flow Cytometry Poster Award (Canadian dollar) University of Ottawa Prize / Award
2018/9 - 2019/8	Queen Elizabeth II graduate scholarships in science and technology (QEII - GSST) - 15,000 (Canadian dollar) University of Ottawa Distinction
2018/9 - 2019/8	Excellence Award - 7,500 (Canadian dollar) University of Ottawa Distinction
2018/4 - 2018/8	Admissions Scholarship - Doctorate - 3,000 (Canadian dollar) University of Ottawa Distinction
2018/3	Travel Award, Mark Wainberg Fund Canadian Association for HIV Research and ViiV Healthcare ULC Prize / Award
2018/3	Syed Sattar Award for Research Contributions (Canadian dollar) University of Ottawa Prize / Award
2017/12	Award of Excellence in Graduate Studies University of Ottawa Prize / Award
2017/5 - 2018/4	Queen Elizabeth II graduate scholarships in science and technology (QEII - GSST) - 15,000 (Canadian dollar) University of Ottawa Distinction
2017/5 - 2018/4	Excellence Scholarship - 7,500 (Canadian dollar) University of Ottawa Distinction
2017/3	2nd Place Seminar Presentation (Canadian dollar) University of Ottawa Prize / Award
2015/9 - 2017/4	Admission Scholarship - Doctorate - 15,000 (Canadian dollar) University of Ottawa Distinction
2015/6 - 2015/6	1st Place Poster Award The Canadian Society for Immunology Prize / Award Best Oral Poster Presentation in Competition Research Disciplines: Immunology Areas of Research: Viral Infections Fields of Application: Biomedical Aspects of Human Health

2015/6 - 2015/6	1st Place Poster Competetion Co-Author Canadian Cytometry and Microscopy Meeting Prize / Award Best Poster Award
	Research Disciplines: Immunology
	Areas of Research: Viral Infections
	Fields of Application: Biomedical Aspects of Human Health
2013/9 - 2015/8	Admission Scholarship - MSc - 15,000 (Canadian dollar) University of Ottawa Distinction
2013/4	Dean's Honour List University of Ottawa Distinction

User Profile

Researcher Status: Doctoral Student
Research Career Start Date: 2015/09/08
Engaged in Clinical Research?: No

Research Specialization Keywords: APOBEC3, HIV, NK Cells, Retroviruses

Disciplines Trained In: Microbiology, Biochemistry, Molecular Biology, Virology, Immunology, Chemistry

Research Disciplines: Immunology, Microbiology, Molecular Biology, Virology, Molecular Biology, Chemistry

Areas of Research: AIDS / HIV, Cellular Defense, Immune System, Viral Infections, Virus

Fields of Application: Biomedical Aspects of Human Health, Pathogenesis and Treatment of Diseases

Employment

2015/9 - 2019/8	Doctoral Candidate Biochemistry, Micriobiology and Immunology, Medicine / University of Ottawa / Roger Guindon, University of Ottawa Full-time
2013/9 - 2015/8	Master's Student Biochemistry, Microbiology and Immunology, Medicine, University of Ottawa Full-time
2013/4 - 2013/8	Research Assistant - Summer Student Biochemistry, Microbiology and Immunology, Medicine, University of Ottawa Full-time
2012/9 - 2013/4	Honour's Student Biochemistry, Microbiology and Immunology, Medicine, University of Ottawa Full-time
2012/4 - 2012/8	Research Assistant - Summer Student Biochemistry, Microbiology and Immunology, Medicine, University of Ottawa Full-time

Affiliations

The primary affiliation is denoted by (*)

(*) 2015/9	Doctoral Candidate, University of Ottawa
2013/9	Master's Student, Biochemistry, Microbiology and Immunology, University of Ottawa

Student/Postdoctoral Supervision

Bachelor's Honours [n=2]

Co-Supervisor	Matthew Greig (Completed) , University of Ottawa Student Degree Start Date: 2013/9 Student Degree Received Date: 2018/4 Project Description: Investigating the clinical effects of APOBEC3 deamination on the Long-Terminal-Repeats (LTRs) and potential implications on the virus replicative fitness. This impact is further investigated in vitro using replication-deficient compared to replication-competent viral strains.
2016/5 Co-Supervisor	Nebeyu Teshome (Completed) , University of Ottawa Student Degree Start Date: 2013/9 Student Degree Received Date: 2017/4 Thesis/Project Title: Analysis of HIV-1 LTRs for APOBEC3-Induced Mutations Project Description: Investigating the clinical effects of APOBEC3 deamination on the Long-Terminal-Repeats (LTRs) and potential implications on the virus replicative fitness. Present Position: Honours Student

Master's Thesis [n=5]

Co-Supervisor	Mariam Maltseva (In Progress) , University of Ottawa Student Degree Start Date: 2018/9 Project Description: Antigenic profiling of retroviruses.
Co-Supervisor	Andrew Norrie (In Progress) , University of Ottawa Student Degree Start Date: 2018/9 Project Description: Evaluation of Endogenous Retroviruses Impact on Existing Models
Co-Supervisor	Matthew Greig (In Progress) , University of Ottawa Student Degree Start Date: 2018/9 Project Description: Investigating the clinical effects of APOBEC3 deamination on the Long-Terminal-Repeats (LTRs) and potential implications on the virus replicative fitness. This impact is further investigated in vitro using replication-deficient compared to replication-competent viral strains.
2016/10 Co-Supervisor	Anna Fritzsche (Completed) , University of Konstanz Student Degree Start Date: 2016/10 Student Degree Received Date: 2017/4 Thesis/Project Title: Single-Virion Characterization of Host-Derived Antigens on HIV Particles by Flow Virometry Present Position: MSc Candidate

2014/9 Co-Supervisor	Cindy Lam (In Progress) , University of Ottawa Student Degree Start Date: 2015/9 Thesis/Project Title: Analysis of Impact of APOBEC3-Mediated Mutations on the Efficiency of HIV-1 LTRs and Potential Implications for Latency Project Description: Investigating the clinical effects of APOBEC3 deamination on the Long-Terminal-Repeats (LTRs) and potential implications on the virus replicative fitness. This impact is further investigated in vitro using replication-deficient compared to replication-competent viral strains. Present Position: MSc Candidate

Community and Volunteer Activities

2013/9	Volunteer, Let's Talk Science Volunteers with various scientific backgrounds enter the classroom of various age groups in order to engage the interests of youth with science.
2014/10 - 2018/10	Graduate Student Volunteer, University of Ottawa Assisting the Organizing Committee
2015/10 - 2016/4	Lead Student Representative, The Canadian Society for Immunology Leading and working as a team to organize trainee events to inspire networking within and outside of the immunology field.

Presentations

1. Vera Tang, Dylan Burger & Marc-Andre Langlois. (2019). Single viral particle resolution by small particle flow cytometry and its applications. RetroPath, Padova, Italy
   Main Audience: Researcher
2. Vera Tang, Anna Fritzsche, Mariam Maltseva & Marc-Andre Langlois. (2019). Single Particle Viral Surface Antigen Phenotyping and Quantification by Nanoscale Flow Cytometry. American Society for Virology, Minneapolis, Minnesota, United States
   Main Audience: Researcher
3. (2017). Investigations into Glyco-Gag: Unexpected Avenues. Annual Seminar Day in Biochemistry, Microbiology and Immunology., Ottawa, Canada
   Main Audience: Researcher
   Invited?: Yes, Keynote?: No
4. (2016). Barrier to Autointegration Factor Potentiates the Antiretroviral Effect of APOBEC3F/G Restriction Factors. Canadian AID / APOBEC Consortium 1st Annual Meeting, Ottawa, Canada
   Main Audience: Researcher
   Invited?: Yes, Keynote?: No
5. (2015). Barrier to Autointegration Factor 1 (BAF1) Potentiates the Antiretroviral Effect of APOBEC3F/G Restriction Factors.Annual Seminar Day in Biochemistry, Microbiology and Immunology., Ottawa, Canada
   Main Audience: Researcher
   Invited?: Yes, Keynote?: No
6. Tyler Renner, Munir Rahim, Andrew Makrigiannis and Marc?André Langlois. (2014). Role of APOBEC3-Induced Deamination in the Recognition of Retroviral Infection by Natural Killer Cells. Flow Cytometry Symposia Day - University of Ottawa, Canada
   Main Audience: Researcher
   Invited?: Yes, Keynote?: No

7. Tyler Renner, María Carla Rosales Gerpe, Cindy Lam, Munir Rahim, Andrew Makrigiannis and Marc-André Langlois. (2014). APOBEC3-Mediated Deamination Is Involved in the Recognition of Retrovirally Infected Cells by Natural Killer Cells. Annual Poster Day in Biochemistry, Microbiology and Immunology, Canada
   Main Audience: Researcher
   Invited?: Yes, Keynote?: No
8. Tyler Renner, María Carla Rosales Gerpe, Cindy Lam, Munir Rahim, Andrew Makrigiannis and Marc-André Langlois. (2014). APOBEC3-Mediated Deamination Is Involved in the Recognition of Retrovirally Infected Cells by Natural Killer Cells. Group for Research in Inflammation & Pathogenesis, Canada
   Main Audience: Researcher
   Invited?: Yes, Keynote?: No
9. Tyler Renner, Munir Rahim, Andrew Makrigiannis and Marc?André Langlois. (2013). Role of APOBEC3-Induced Deamination in the Recognition of Retroviral Infection by Natural Killer Cells. Annual Poster Day in Biochemistry, Ottawa, Canada
   Main Audience: Researcher
   Invited?: Yes, Keynote?: No, Competitive?: Yes

Publications

Journal Articles

1. Kaelan Gobeil Odai, Conor O'Dwyer, Rineke Steenbergen, Tyler A. Shaw, Tyler M. Renner, Peyman Ghorbani, Mojgan Rezaaifar, Shauna Han, Marc-André Langlois, Angela M. Crawley, Rodney S. Russell, John P. Pezacki , D. Lorne Tyrrell, Morgan D. Fullerton.In vitro hepatitis C virus infection and hepatic choline metabolism.Viruses.
   Revision Requested,
   Refereed?: Yes
2. Tyler Milston Renner, Vera A. Tang, Dylan Burger & Marc-Andre Langlois. (2019). Intact Viral Particle Counts Measured by Flow VirometryProvides Insight into the Infectivity and Genome Packaging Efficiency of the MoloneyMurine Leukemia Virus. Journal of Virology.
   Published,
   Refereed?: Yes
3. George C Brittain, IV, Yong Q Chen, Edgar Martinez, Vera A Tang, Tyler M Renner, Marc-André Langlois and Sergei Gulnik. (2019). A Novel Semiconductor-Based Flow Cytometer with Enhanced Light-Scatter Sensitivity for the Analysis of Biological Nanoparticles.Scientific Reports.
   Published,
   Refereed?: Yes
4. Hannah Ajoge*, Tyler M. Renner*, Marc-André Langlois# and Stephen D. Barr# *Co-First Authors. #Co-Senior Authors. (2019). Antiretroviral APOBEC3 cytidine deaminases alter HIV-1provirus integration site profiles.Nature Communications.
   Submitted,
   Refereed?: Yes
5. Tyler Milston Renner, Kasandra Belanger & Marc-Andre Langlois. (2018). Intact Virion Immunoprecipitations. Bio-Protocol.
   First Listed Author
   Published,
   Refereed?: Yes

6. Tyler Milston Renner*; Kasandra Bélanger*, Ph.D.; Laura Goodwin; Mark Campbell; Marc-André Langlois, Ph.D. *Contributed equally to work. (2018). Molecular Attributes Influencing LINE-1 Restriction by All Seven Human APOBEC3 Proteins. Virology.
Published,
Refereed?: Yes

7. Tyler Milston Renner, Kasandra Belanger & Marc-Andre Langlois. (2018). Viral core stability assay. Bio-Protocol.
First Listed Author
Published,
Refereed?: Yes

8. Dr. Vera A. Tang*, Tyler M. Renner*, Anna Fritzsche, Dylan Burger, Marc-Andre Langlois *Contributed equally to work. (2017). Single-Particle Discrimination of Retroviruses from Extracellular Vesicles by Nanoscale Flow Cytometry. Scientific Reports.7: Online-only.
Published,
Refereed?: Yes, Open Access?: Yes

9. Vera A. Tang, Tyler M. Renner, Oliver Varette, Fabrice Le Boeuf, Jiahu Wang, Jean-Simon Diallo, John C. Bell, Marc-André Langlois. (2016). Single-Particle Characterization of Oncolytic Vaccinia Virus by Flow Virometry.Vaccine.34(42): 5082-5089.
Published,
Refereed?: Yes

10. Rosales Gerpe MC*, Renner TM*, Bélanger K, Lam C, Aydin H, Langlois MA. *Contributed equally to work. (2015). N-linked glycosylation protects gammaretroviruses against deamination by APOBEC3 proteins.Journal of Virology.89(4): 2342-57.
Published, Canada
Refereed?: Yes
Number of Contributors: 6

11. Bélanger K, Savoie M, Aydin H, Renner TM, Montazeri Z, Langlois MA. (2014). Deamination intensity profiling of human APOBEC3 protein activity along the near full-length genomes of HIV-1 and MoMLV by HyperHRM analysis.Virology.448(5): 168-175.
Co-Author
Published,
Refereed?: Yes
Number of Contributors: 6

Working Papers

1. (Vera A. Tang, Anna K. Fritzsche, Tyler M. Renner, Dylan Burger, Edwin van der Pol, Joanne A. Lannigan, George C. Brittain, Joshua A. Welsh, Jennifer C. Jones, Marc-André Langlois.). (2019). Engineered Retroviruses as Fluorescent Biological Reference Particles for Small Particle Flow Cytometry. https://www.biorxiv.org/content/10.1101/614461v2.

Conference Publications

1. Tyler Renner, Munir Rahim, Andrew Makrigiannis and Marc-André Langlois.Role of APOBEC3-Induced Deamination in the Recognition of Retroviral Infection by Natural Killer Cells.Flow Cytometry Symposia Day. (October, 2014). Ottawa, Canada., ,
Poster
First Listed Author
Published

2. Tyler Renner, María Carla Rosales Gerpe, Kasandra Bélanger, Cindy Lam, Halil Aydin and Marc-André Langlois.N-Linked Glycosylation Protects Retroviruses from Mutagenesis by Human and Mouse APOBEC3 Proteins.Canadian Association for HIV Research. (May, 2015). Toronto, Canada., ,
   Poster
   First Listed Author
   Published

3. Tyler Renner, María Carla Rosales Gerpe, Cindy Lam, Munir Rahim, Andrew Makrigiannis and Marc-André Langlois.APOBEC3-Mediated Deamination Is Involved in the Recognition of Retrovirally Infected Cells by Natural Killer Cells.Group for Research in Inflammation & Pathogenesis. (August, 2014). Ottawa, Ontario., ,
   Poster
   First Listed Author
   Published

4. Tyler Milston Renner & Marc-Andre Langlois. **Barrier to Autointegration Factor (BAF) potentiates theantiretroviral effect of the APOBEC3 restriction factors.**Annual Poster Day in Biochemistry, Microbiology and Immunology - University of Ottawa. (May, 2018)., ,
   Poster
   First Listed Author
   Published

5. Vera Tang, Oliver Varette, Tyler M. Renner, Fabrice LeBoeuf, Jean-Simon Diallo, John Bell and Marc-André Langlois.Single-Particle Detection of Vaccinia Virus by Flow Cytometry.Canadian Cytometry and Microscopy Meeting. (June, 2015). Toronto, Canada., ,
   Poster
   Co-Author
   Published

6. Tyler M. Renner, Vera A. Tang & Marc-André Langlois.Retrovirus Surface Antigen Profiling By FlowVirometry.The Canadian Society for Immunology. (April, 2016). Ottawa, Canada., ,
   Poster
   First Listed Author
   Published

7. Vera A. Tang, Anna Fritzche, Tyler M. Renner, Fengxia Xiao, Joanne Lannigan, Desmond Pink, John D. Lewis, Dylan Burger, and Marc-André Langlois.Enveloped viruses as areference material for nanoscale flow cytometry.Congress of the International Society for Advancement of Cytometry (CYTO) (2018), Prague., ,
   Poster
   Co-Author
   Published

8. Anna K. Fritzsche, Vera Tang, Tyler M. Renner, and Marc-André Langlois.Assessmentof different classes of dyes to label enveloped viruses for nanoscale flowcytometry.Congress of the International Society for Advancement of Cytometry (CYTO) (2018), Prague., ,
   Poster
   Co-Author
   Published

9. Tyler Milston Renner & Marc-Andre Langlois. **Barrier to Autointegration Factor (BAF) potentiates theantiretroviral effect of the APOBEC3 restriction factors.**Canadian Association for HIV Research. (April 2018). Vancouver, Canada., ,
   Poster
   First Listed Author
   Published

10. Tyler M. Renner, Vera A. Tang & Marc-André Langlois.Retrovirus Surface Antigen Profiling By FlowVirometry.Canadian Association of HIV Research. (May, 2016). Winnipeg, Canada., ,
Poster
First Listed Author
Published

11. Tyler M. Renner, Vera A. Tang, Marc-Andre Langlois. Single-Particle Characterization: Discriminating Enveloped Viruses and Extracellular Vesicles by Flow Virometry. International Society for Extracellular Vesicles (ISEV). (May, 2017). Toronto, Canada., ,
Poster
First Listed Author
Published

12. Tyler Renner, Munir Rahim, Andrew Makrigiannis and Marc-André Langlois.Role of APOBEC3-Induced Deamination in the Recognition of Retroviral Infection by Natural Killer Cells.Annual Poster Day in Biochemistry - University of Ottawa. (April, 2013)., ,
Poster
First Listed Author
Published

13. Tyler Renner, María Carla Rosales Gerpe, Kasandra Bélanger, Cindy Lam, Halil Aydin and Marc-André Langlois.N-Linked Glycosylation Protects Retroviruses from Mutagenesis by Human and Mouse APOBEC3 Proteins.The Canadian Society for Immunology. (June, 2015). Winnipeg, Canada., ,
Poster
First Listed Author
Published

14. Tyler Renner, María Carla Rosales Gerpe, Cindy Lam, Munir Rahim, Andrew Makrigiannis and Marc-André Langlois.APOBEC3-Mediated Deamination Is Involved in the Recognition of Retrovirally Infected Cells by Natural Killer Cells.Annual Poster Day in Biochemistry, Microbiology and Immunology - University of Ottawa. (May, 2014)., ,
Poster
First Listed Author
Published

15. Tyler M. Renner, Vera A. Tang, Marc-Andre Langlois. Single-Particle Characterization: Discriminating Enveloped Viruses and Extracellular Vesicles by Flow Virometry. NanoScale Flow Cytometry Symposium (2018), ,
Poster
First Listed Author
Published

Intellectual Property

Patents

1. FLUORESCENT ENVELOPED VIRAL PARTICLES AS STANDARDS FOR NANOSALE FLOW CYTOMETRY. United States. United States Provisional Patent Appln No. 62/563,957. 2017/09/27.
Patent Status: Pending